University of Alberta

A MIXED WETTABILITY PORE SIZE DISTRIBUTION MODEL FOR THE ANALYSIS OF WATER TRANSPORT IN PEMFC MATERIALS

by

Pedro Abdiel Mateo Villanueva

A thesis submitted to the Faculty of Graduate Studies and Research in partial fulfillment of the requirements for the degree of **Master of Science**.

Department of Mechanical Engineering

Fall 2013
Edmonton, Alberta

To my dear family and friends

Abstract

Water management on proton exchange membrane fuel cells is one of the biggest issues that stop the effective commercialization of this promising technology. Due to water flooding, the performance of fuel cells decays rapidly at high current densities. To better design fuel cell electrodes, a mixed wettability pore-size distribution model was developed, and used to estimate the effective transport properties of dry and partially flooded fuel cell porous layers. Using this model, microporous layers and conventional cathode catalyst layers were studied. Results revealed that mass transport limitations can be significantly improved by controlling the wettability and microstructure of the electrodes.

Keywords: water transport, mass transport limitations, evaporation rates, fuel cell, microporous layer, two-phase flow, pore-size distribution

Acknowledgements

I would like to thank my family, specially my mother for her unconditional support 24 hours a day, seven days a week. Her hard work and discipline have always been my greatest source of inspiration; and I which some day I will be able to mimic her behaviour. Besides the time-zone difference, they could always find some time to give me advice and provide me with useful distractions during the long nights; Jaime and Mariella in particular. I will be always grateful for that... you are all my reasons.

I would like to thank all the amazing people I had the pleasure to meet in Edmonton. I would like to thank Samantha Millar (Sam) for being a late owl like myself, and Michael Moore (Mick) and Bijoy for the occasional soccer breaks. I will also like to thank Patrick Lohrmann for the MPL/GDL liquid breakthrough and permeation experiments, Lalit Pant for setting up my computer several times, and all the other ESDLab members I had the pleasure to work with during my tenure.

I would like to thank all my friends from *Entre Amigos*, for their prayers, wisdom, and periodic breaks as well. Their emotional support also played a key role during these years. Also, I will like to thank my old partners Vladimir, Rafael, Manuel and Omar for their useful perspectives about life and education and continuous moral support.

Finally, I would like to thank my supervisor, Dr. Marc Secanell, for all his time and effort. Not only research related topics, he also taught me important life lessons that I will likely remember for the rest of my days.

God bless you all!

Table of Contents

List of Tables

List of Figures

Nomenclature

English Letters

D_i	Diffusion coefficient of species i $(m^2 s^{-1})$
F	Total pore volume fraction of a wettability corresponding to a given PSD
f_k	Contribution of log-normal distribution k to total PSD
M_i	Molar mass of species i $(g\,mol^{-1})$
n	Number density of molecules (m)
r	Pore radius (m)
R_g	Universal gas constant $(8.314\ \ J\,K^{-1}\,mol^{-1})$
r_{Kn}	Average Knudsen radius of the layer (m)
r_k	Characteristic pore size of log-normal distribution k (m)
s_k	Spread of log-normal distribution k
T	Absolute temperature (K)
X	Porosity

Abbreviations

BET	Brunauer, Emmett and Teller
CCL	Cathode catalyst layer
CFD	Computational fluid dynamics
CL	Catalyst layers
DM	Diffusion media

GDL	Gas diffusion layer
GDM	Gas diffusion media
HOR	Hydrogen oxidation reaction
IP	Intrusion porosimetry
LBM	Lattice-Boltzmann method
MEA	Membrane electrode assembly
MIP	Mercury intrusion porosimetry
MPL	Microporous layer
MSP	Method of standard porosimetry
OCV	Open circuit voltage
ORR	Oxygen reduction reaction
PEM	Proton exchange membrane
PEMFC	Proton exchange membrane fuel cell
PNM	Pore network models
PSD	Pore-size distribution
PTFE	Polytetrafluoroethylene
WIP	Water intrusion porosimetry

Greek Letters

Ω_{ij}	Collision integral for species i and j
σ_{ij}	Collision diameter of gas species i and j (m)
σ_i	Molecular diameter of species i (m)

Subscripts and Superscripts

eff	Effective
HI	Hydrophilic pores
HO	Hydrophobic pores

Chapter 1

Introduction

1.1 Basic Fuel Cell Operation

Proton exchange membrane fuel cells (PEMFC) are energy conversion devices that produce electricity from chemical energy. The electrochemical reactions consist of combining hydrogen and oxygen (gas) to produce water, electricity, and heat, as described below:

$$\text{Anodic reaction:} \qquad 2H_2 \rightarrow 4H^+ + 4e^- \tag{1.1}$$

$$\text{Cathodic reaction:} \qquad O_2 + 4H^+ + 4e^- \rightarrow 2H_2O \tag{1.2}$$

$$\text{Overall reaction:} \qquad 2H_2 + O_2 \rightarrow 2H_2O \tag{1.3}$$

PEMFCs are a very promising alternative energy system for mobile (such as cellphones, calculators and other hand-held devices) and transportation applications (such as buses and smaller vehicles). Fuel cells usually have high efficiencies due to the electrochemical reactions (fuel cell systems are not limited by the Carnot efficiency that sets the efficiency levels for thermal systems) and they do not emit harmful by-products such as carbon monoxide, nitrous oxides and greenhouse gases when fuelled with hydrogen. Additionally, their modular design allows for the production of cells at any scale. The high cost of PEMFCs is however preventing the full commercialization of this promising technology.

Conventional PEMFCs are made of several porous layers, each one fulfilling a specific purpose. A diagram of a typical PEMFC showing the basic components is presented in Figure 1.1.

The proton exchange membrane (PEM) is the layer at the center of a PEMFC, and its thickness is usually around 30 μm. The PEM allows the protons to travel from anode to cathode while (ideally) blocking all the other species. The starting

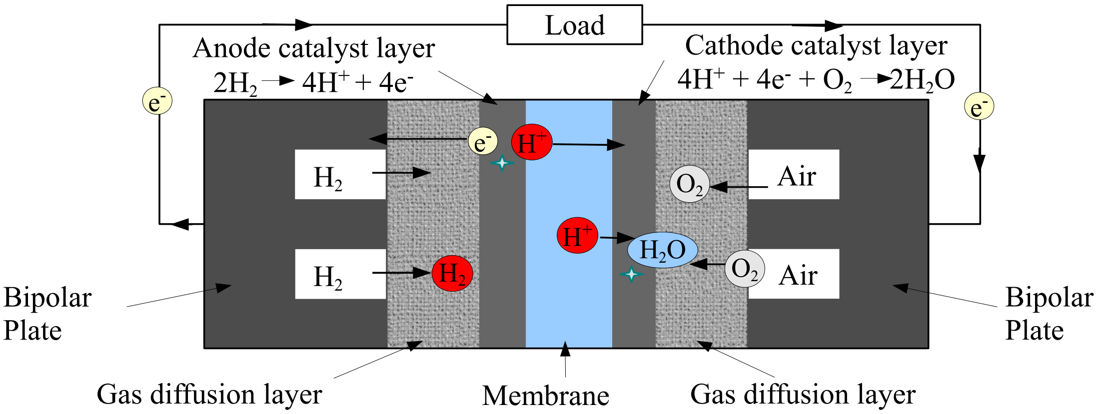

Figure 1.1 – Diagram showing the basic physical structure of conventional proton exchange membrane fuel cells [2].

point to create the PEM is a polymer known as polythetrafluoroethylene, or PTFE. The PTFE is a long and strongly hydrophobic polymer, which helps prevent water accumulation inside the cell. In order to achieve proton conduction, the PTFE backbone is treated with sulphonic acid, HSO_3, forming the perfluorosulfonated ionomer membrane (PFSI). Due to the ions present, this new material is often called ionomer. Sulphonic acid is hydrophilic, which means that inside the ionomer some regions will have affinity to liquid water [7]. Finally, as the hydrophilic regions inside the ionomer are filled with water, the sulphonic acid is diluted and there will be a weak attraction between the SO_3^- and the H^+ ions. Therefore, when the ionomer is properly hydrated, the H^+ ions can move without a lot of resistance within the membrane.

The catalyst layers (CL) are the porous electrodes at which the electrochemical reactions take place. In order to activate the anode and cathode electrochemical reactions, a catalyst is needed. Since the cathode reaction is slower than the anode reaction, more catalyst is needed in the cathode.

The catalyst must a) be selective in order to produce the desired product, b) have a good activity in order to make the reactions go as fast as possible, and c) must be resistant to contaminants. Platinum meets all these requirements for both the hydrogen oxidation reaction (HOR)and the oxygen reduction reaction (ORR). Usually, both the anode and the cathode electrodes contain platinum. Even though different manufacturing methods are reported [7, 8], the resulting (conventional) catalyst layers are usually made of carbon-supported platinum, which serves as the structural matrix for the catalyst, bounded by ionomer. The platinum particles are dispersed over the carbon particles, making the surface area of platinum that can be in contact with the reactants very large. The CL is treated with the ionomer in order to promote

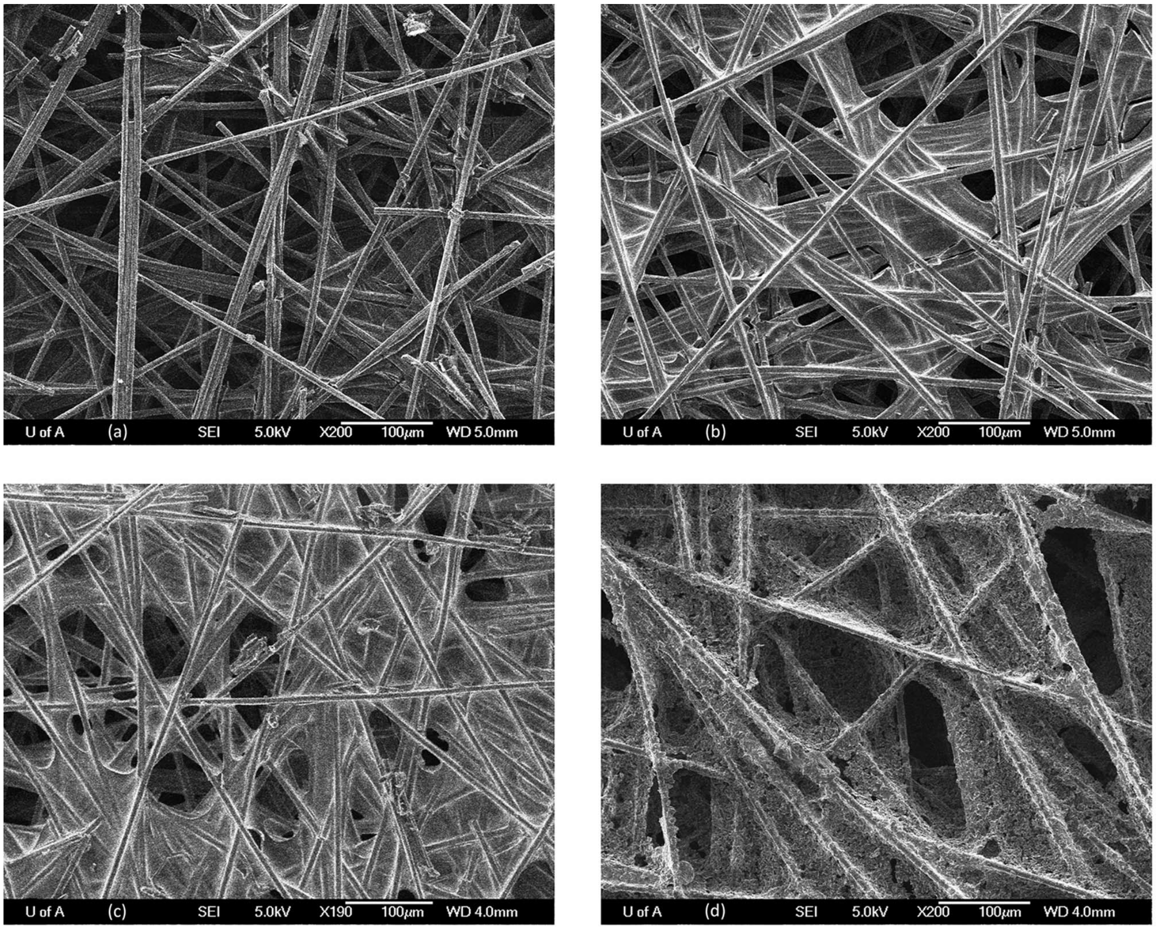

Figure 1.2 – Diagram showing the top views of conventional GDLs showing the structure and decrease in pore size for increased PTFE loading. (a) Untreated Toray GDL; (b) 5% PTFE Toray GDL; (c) 10% PTFE Toray GDL; (d) GDL side of SGL Sigracet 34BC. Reproduced with permission from Carrigy et al. 2012.

proton transport. The thickness of conventional catalyst layers is usually around 5-20 μm.

The gas diffusion layers (GDLs) are the porous layers that distribute the reactant gases uniformly on the surface of the catalyst layers and allow the product water to leave. GDLs are made of carbon fibre, carbon felt or carbon cloth. The basic structure of the GDL is an array of fibres that form pores, and are usually coated with PTFE to make them hydrophobic. The treatment with PTFE makes the GDL to display mixed wettability properties [9], and also changes the pore sizes of the GDL as presented in Figure 1.2 [10]. Usually, the thickness of the GDL is around 200-300 μm.

CL pore sizes are more than three orders of magnitude smaller than the GDL pore sizes, and this hinders liquid water transport, gas transport, and increases contact resistance between the CL and the GDL [11]. For this reason, an additional layer known as microporous layer (MPL) with pore sizes just slightly bigger than the catalyst layer is placed between the CL and the GDL. The structure of the MPL is similar to the structure of the catalyst layer, but it is made of PTFE and carbon, making it very hydrophobic. The MPL does not contain either ionomer or catalyst, and therefore this layer is not reactive. The thickness of the MPL, in most cases, is estimated to be between 20 and 40 μm [12, 13].

Finally, the bipolar plates allow to connect the cells in series, a useful characteristic when designing high-voltage fuel cell systems. The bipolar plates are responsible for taking the reactant gases and distributing them to the surface of the GDL. They also keep together the membrane electrode assembly, the name given to the combination of PEM, catalyst layers and reactant diffusion layers, and act as the current collectors (e.g. taking the electrons produced from the electrochemical reactions). Bipolar plates are usually made of graphite, but coated metals can be also used.

When the fuel cell is operating, water is generated in the cathode side. The water generated is proportional to the current produced, thus for large current densities liquid water may block the pores in the cathode side and preventing oxygen from reaching the reactive sites. The fuel cell requires a large pressure build-up to evacuate the water, therefore liquid water accumulates inside the cell. Since it is easier to evacuate water in vapour form than it is in liquid form, cell flooding could be prevented by enhancing the evaporation rates inside the cell. In order to increase the performance of conventional catalyst layers, their microstructure and wettability can be modified so that the layer itself can have a large liquid-gas interfacial surface area and thus enhance evaporation rates and mitigate mass transport losses due to water accumulation. For ultra-thin catalyst layers, volumetric water production rates are very high and the layer is too thin to evaporate the majority of the water. The wettability and microstructure of the MPL however can be modified instead in order to increase its water evaporation rates. Essentially, in the later case the MPL can be designed as a water shed and evaporative layer.

1.2 Motivation

Papageorgopoulos [14, 15] stated that the catalyst is the largest cost contributor for mid-range proton PEMFC stacks, and most of the funds approved for research and development of PEMFCs by the U.S. Department of Energy is dedicated to catalyst research and development. In Canada, a country-wide research network known as

The Catalyst Research for Polymer Electrolyte Fuel Cells (CARPE-FC) was recently formed to address the cost of PEMFCs.

In order to reduce the use of expensive catalyst, two alternatives are usually considered. The first alternative is to increase the cell performance for the same amount of catalyst (thus requiring fewer cells to meet specific power requirements). The second alternative involves decreasing the catalyst loading thus thickness of the catalyst layer without negatively impacting the performance (thus reducing the total amount of catalyst required to achieve any given power requirement). Regardless of the alternative, water accumulation must be minimized in order to avoid oxygen starvation and draw more current from the electrodes.

To increase the performance of conventional catalyst layers, their water management properties must be improved. Increasing the amount of current that is drawn from the catalyst layer increases the water generation rates (water generation rate is directly proportional to the current drawn from the cell). Therefore, evaporation inside the layer must be improved.

Ultra-thin catalyst layers have recently gained popularity due to improved catalyst utilization when compared to conventional electrodes [16, 17]. The thickness of a conventional cathode catalyst layer is $\sim 5 - 20\ \mu m$, while ultra-thin cathode catalyst layers have a thickness of $\sim 10 - 200\ nm$. The catalyst loading of conventional electrodes is around $0.4\, mg\, cm^{-2}$ [18], but can be as low as $0.05\, mg\, cm^{-2}$ for ultrathin catalyst layers [16]. The downside of this innovative technology is a sudden performance drop at high current densities (more than $1\ A/cm^2$) which may be due to water accumulation inside the catalyst layer induced by the higher volumetric water production rates.

Conventional catalyst layers and the MPL in ultra-thin electrodes must be designed to function as a water shedding layer or as an evaporative layer to overcome mass transport limitations by transforming all produced water to vapour before it floods either the GDL or the gas channels [16]. Therefore it is necessary to characterize the internal geometries of MPLs in a way such that they can be designed to fulfil specific this task. For conventional catalyst layers, MPLs that enhance evaporation rates will translate to better cell performance at high current densities if the catalyst layer cannot evaporate enough liquid water by itself. For the ultra-thin cathode catalyst layers that are likely to be fully flooded due to the high volumetric water generation rates, the MPL must act as an evaporative layer.

To understand two-phase water transport and predict its effects on cell performance, several macro-homogeneous models for MPLs and conventional catalyst layers have been implemented in the past [16, 19–28]. None of the models however included the effects of mixed wettability and microstructure on the two-phase effective transport properties of the layers. If the models used to describe conventional catalyst layers and MPLs cannot incorporate this information, layer design and layer optimization is impossible. The lack of such models is one of the key motivators for this study. This research intends to develop a framework in which the microstructure and wettability of the porous media required to increase performance of PEMFCs can be studied.

In attempting to design MPLs and conventional catalyst layers to improve liquid water transport, layer wettability and layer microstructure are essential factors to consider. To take into account the layer microstructure and wettability, a pore-size distribution (PSD) model is developed and used to characterize the geometry of MPLs and conventional catalyst layers. Experimental results completed by Martínez et al. [9] revealed that in general, the gas diffusion media (GDM) of PEMFCs cannot be defined by a unique wettability. They obtained PSDs for individual hydrophilic and hydrophobic pores. The individual hydrophilic and hydrophobic PSD functions are obtained from intrusion experiments with different working fluids, i.e. mercury and water.

To date, microporous layer and conventional catalyst layer models have either assumed a hydrophobic pore network or considered that hydrophilic and hydrophobic pores are distributed uniformly over the same pore-size distribution. Having hydrophilic and hydrophobic pores uniformly distributed over the same pore-sizes along gas diffusion media is very unlikely as recently shown by mercury/water intrusion experiments in gas diffusion layers [9]. Therefore performance optimization and re-design of microporous layers and conventional catalyst layers cannot be studied in detail with these models. Micro-structural properties of the layers must be fully represented prior to attempt further optimization studies.

Studying the effects of the hydrophilic and hydrophobic pore-size distributions on the effective transport properties of the MPL and catalyst layer might lead to the design of membrane electrode assemblies (MEA) with better reactant transport. The MPL and even the catalyst layer itself can be designed to act as an evaporative layer (enhance evaporation rates) or water shedding layer (hold water inside the MPL, evaporate as much as possible, and release after liquid pressure build-up is high enough in a quasi-periodic fashion) in order to boost electrode performance. This improvement on layer design is relevant regardless of the electrode technology used, and will allow to study the impact of wettability and micro-structure of the electrodes on performance and durability.

1.3 Literature Review

1.3.1 Porous Media Characterization

In this thesis, a mathematical model for GDLs, MPLs, and conventional CLs that is based on hydrophilic and hydrophobic pore-size distributions is developed. In this section, the methods available to obtain PSDs are studied and assessed as alternatives to measure PSDs. Researchers have used a variety of techniques to characterize the geometry of porous materials. Some of these techniques are described below.

Intrusion Porosimetry (IP)

In IP, different levels of pressure are applied to a porous sample immersed in a working fluid, and the intruded volume is recorded. Under the assumption that the porous sample is equivalent to an irregular, random array of cylindrical pores, the Young-Laplace equation (1.4) can be used to relate the controlled pressure that is forcing the fluid to invade the pores to a critical pore radius. Assuming that the contact angle of the interface between the working fluid and the porous material and the surface tension of the working fluid are known, the Young-Laplace equation can be used to obtain the pore radius r,

$$p_c = p_L - p_G = -\frac{2\,\sigma\,\cos(\theta)}{r} \tag{1.4}$$

$$r = -\frac{2\,\sigma\,\cos(\theta)}{p_c} \tag{1.5}$$

where p_c is the capillary pressure, p_L is the pressure of the liquid phase, p_G is the pressure of the gas phase (which is close to zero, because sample is evacuated prior to intrusion porosimetry tests), σ is the surface tension of the working fluid, θ is the contact angle of the working fluid, and r is an effective pore radius.

From the Young-Laplace equation, it can be observed that smaller pores will require larger pressures to force liquid to invade the pores if the fluid is non-wetting. If the fluid is wetting, then the sample will be invaded starting with the smaller pores. While performing IP tests, the pressure is gradually increased and the intruded volume of the working fluid entering the sample is recorded (using a non-wetting fluid). By relating the intruded volume to the intrusion pressure, which can then be related to a critical pore radius using the Young-Laplace equation, a PSD can be defined.

Since mercury is a non-wetting fluid for almost all materials, IP with mercury as the working fluid (MIP) is intended to enter the whole sample. Water, in the other hand, will fill the hydrophilic (HI) pores immediately and so IP with water as the working fluid (WIP) is intended to enter the hydrophobic (HO) pores in the sample. Therefore, a global PSD and a HO PSD can be directly obtained using IP. To obtain HI PSD, one can subtract the HO PSD from the global PSD and fully characterize the geometry of the sample.

There are several problems related to intrusion porosimetry. First, since pressure is being applied to the system, the risk of deforming the sample due to high pressures is present, as quoted by Martínez et al. [9]. Second, if a pore is made of hydrophilic walls surrounded by hydrophobic walls, pressure is needed to force the water to move through the hydrophobic sections, but will invade the hydrophilic sections immediately, thereby over-predicting the volume of hydrophilic pores. This situation may lead to liquid volume overestimation when WIP is used.

Method of Standard Porosimetry

The method of standard porosimetry (MSP) is based on the principle of capillary equilibrium [9, 29, 30]. If two samples, partially saturated by the same working fluid are put in contact, the system will eventually reach equilibrium, i.e. the capillary pressure for both samples will be the same at the contact interface. Therefore, if the capillary pressure distribution is known for one of the samples (e.g. a standard sample), a PSD can be obtained (using the Young-Laplace equation to correlate the capillary pressure to a critical pore radius). By removing a small amount of the working fluid from the standard sample (usually done by evaporation), a new equilibrium point can be achieved, and then a PSD can be obtained.

This technique is thus based on letting a known amount of fluid enter the samples freely, as opposed to forcing it (the case for IP). This means that for MSP, the working fluid must be wetting for at least a portion of the sample. Since Octane is wetting for almost all materials, MSP with Octane as the working fluid (MSP-O) generates a PSD for both hydrophilic and hydrophobic pores. Similarly, MSP with water as the working fluid (MSP-W) generates a PSD for the hydrophilic pores alone. The HO PSD can be obtained by subtracting the HI PSD from the global PSD

One problem with MSP-W is that if a pore consists on hydrophobic walls surrounding hydrophilic walls, MSP-W will never reach the hydrophilic portions of the pore. The reason is because the outer walls are hydrophobic, so pressure must be applied to the sample in order to have water enter the pores. This situation leads to potential volume underestimation when using MSP-W.

In addition, while pressures are not applied (as opposite to IP), some materials may expand (swell) in water (or any other wetting fluid), leading to unrealistic volume predictions from MSP-W as well.

BET Method

BET is a method generally used to estimate the surface area and PSD of porous materials [31]. Several sources have documented their findings about porous media characterization and PSD procedures using the BET method [32, 33, 33–35], and some compared the obtained distributions with those generated by other methods. For instance, Brown and Lard [35] compared the PSDs obtained by BET with those obtained from Mercury intrusion. Since Mercury intrusion needs large pressures to invade small pores, the walls corresponding to the larger pores are subjected to these pressures and they may collapse , sometimes leading to Mercury invading void space that under normal conditions is not accessible, or by deforming the pore and dividing one large pore into smaller pores. Joyner et al. [33] obtained very similar findings, and concluded that to obtain PSD functions for pores smaller than 30 nm the BET method can be used as it does not need large pressures to operate at this pore range, while for pore sizes larger than 30 nm intrusion methods can be used due to their simplicity.

Over the years; other versions of the BET method have been developed and implemented, including a graphic procedure [36] and an experimental procedure that involves the measurement of thermal conductivity of a mixture of an adsorbate gas and a diluent gas [37].

Conclusions

Due to the typical pore sizes of MPLs and GDLs (greater than 30 nm), the BET method unsuitable. Both the method of standard porosimetry and intrusion porosimetry can be used to obtain the PSD for MPL and GDL samples. Due to the simplicity of the experiments, equipment availability, and the duration of a typical test, intrusion porosimetry was selected as the method to obtain PSD measurements.

1.3.2 MPL Models

The MPL plays a key role on fuel cell performance [38–46], therefore in recent years many research groups have developed models to study them. Unfortunately, the current MPL models do not allow the implementation of a framework in which mixed wettability and micro-structural effects can be studied in order to design better performing MPLs.

Current MPL numerical modelling strategies have focused in three areas: macro-homogeneous models, micro-structural models, and pore-network models.

One of the most popular methods consists on image reconstruction of MPLs by using techniques such as X-ray tomography. This technique allows to reconstruct the internal microstructure of MPLs, but the hydrophilic and hydrophobic pores cannot be distinguished from the images, which makes it impractical to explore different MPL designs based on different hydrophilic and hydrophobic pores. Additionally, this technique requires a lot of computational power.

Other methods used to study MPLs are macro-homogeneous models, where the MPL is assumed to be a layer with uniform properties; and pore network models, where the MPL is reconstructed as an array of pores connected by throats of different sizes.

Macro-Homogeneous Models

Macro-homogeneous MPL models are very similar to macro-homogeneous conventional catalyst layer models previously described. Since the MPL is not a reactive layer there is no generation term in the governing equations for MPLs. Popular assumptions are isothermal conditions, effective transport properties obtained without information related to wettability and microstructure, and low gas velocities are used [12, 20, 44]. Such models are typically based on Fick's law and Darcy's law. While these models are relatively easy to solve, one disadvantage is that microstructural information of the MPL is not taken into account.

The result is usually a model in which the liquid and water vapour fluxed are included, but the wettability and microstructure effects on effective properties are usually completely neglected, or obtained from empirical relations.

Macro-homogeneous MPL models offer the advantage of requiring very low computational power, and have also the potential to incorporate the effects of mixed wettability and microstructure of the MPL.

The PSD model developed by Weber [3, 21] can also be applied to model MPLs and thus incorporate the effects of mixed wettability and microsructure. As for the cathode catalyst layer models, the major drawback of the MPL models formulated following Weber's approach is that the hydrophilic and hydrophobic network of pores are assumed to be uniformly distributed over the same pore sizes.

Pore Network Models

Because of the amount of computational power needed to perform direct numerical simulations, an alternative method gained popularity during the past decade, the pore network method (PNM). The PNM can be used to predict the capillary transport of liquid water through porous media. The main advantage of PNM is that it allows to create a structural representation of gas diffusion media without the computational burden associated with image reconstruction and full three-dimensional CFD simulations. Many researchers are widely using the PNM to conduct their research, see references [47–50]. Many theories are given to improve the quality of the gas diffusion media by designs adopting different pore network structures. Some of these are documented by Bazylak et al. [50], where pore networks with a radial biasing was found to decrease the liquid water saturation within the GDL network.

PNM are based on the principle of invasion percolation. In the PNM, the GDL/MPL is represented by a matrix of pores and connecting throats. The invasion percolation algorithm works as follows [47, 48]

- an invading phase (i.e. liquid water) enters the network (the section where the invading phase enters is known as inlet),
- the invading phase moves through the network, invading the throats with bigger radius first,
- once the invading phase reaches the first throat of the outlet face, the process stops and the liquid saturation can be obtained.

This process needs to be repeated several times to make sure the saturation found is, up to a certain degree of confidence, representative of the porous media being described. An error and uncertainty analysis is usually associated with PNM simulations of porous media.

Many scientific articles can be found about the use of PNM to model diffusion media (DM) in PEMFC, but not many can be found about the dramatic influence of PNM to the boundary conditions used at the entry of the MPL. Sinha and Wang [48] studied the liquid water movement and water flooding in a GDL. To include the boundary conditions, the GDL is assumed to be first saturated with air and the inlet face is in contact with a water reservoir providing a constant injection rate. Other documented studies, such as this completed by Markicevic et al. [47] do not include the inlet boundary conditions used to perform the numerical PNM simulations. Lee et al. [49] used the uniform flux boundary condition at the network inlet for his work. As will be shown, there is a possibility that neither of these articles offered a truly-representative description of what actually happens inside a PEMFC.

Wu et al. [51] showed that the boundary condition at the inlet of the MPL plays an essential role on the results obtained from PNM simulations of the MPL + GDL. If an inlet uniform pressure boundary condition (the inlet face is connected to a water reservoir, providing a uniform injection rate) is assumed, the liquid water saturation in the GDL is shown to drastically decrease when a MPL is included between the CL and the GDL. However, when using the uniform flux boundary condition (liquid water invading the network from different injection points) at the inlet of the MPL, the liquid saturation of the GDL is almost unaltered when comparing the profiles found with and without the MPL between the CL and the GDL. Therefore, a comprehensive study on the boundary conditions used for PNM and the results obtained applying PNM to PEMFC must be revised and corrected.

Also, using PNM simulations some of the effective properties impossible to obtain. For instance, the concepts of relative permeabilities are lost when using PNM simulations, and so is the liquid-gas interfacial surface area per unit volume.

The way in which PNM are first generated is by looking at images of the porous media and creating a pore network that matches some criteria observed from the images, such as porosity. However, there are infinite network configurations which can be assembled to match a given value of porosity, and the transport inside these network may be completely different.

Micro-Structural Models

Due to the strong correlation between capillary forces and liquid water transport, as mentioned by Wu et al. [51], continuum two-phase models for the MPL and the GDL usually under predict the liquid water saturation on the MPL. According to Wu et al. [51], this was part of the motivation to find different ways to solve porous media problems accurately. One of the first alternative methods was the direct numerical simulation (e.g. Lattice-Boltzmann simulations, Computational Fluid Dynamics, etc.) method.

Ostadi et al [52] used the Lattice-Boltzmann method to create 3-D reconstruction of MPLs and GDLs. Using X-ray nano-tomography and focused ion beam/scanning electron microscopy nano-tomography, properties such as porosity, characteristics lengths and 3D pore size distribution were determined; and the Lattice-Boltzmann method was used to obtain parameters such as the tortuosity and permeability. The Lattice-Boltzmann method was also successfully implemented by Hao and Cheng [53]. While not as common, CFD models for PEMFC layers have also been successfully implemented [54, 55]. The main drawback of these methods is the computational time and resources needed.

Conclusions

Based on this review, in this thesis we propose to use a macro-homogeneous approach to model the MPL and the cathode catalyst layer. The advantages of macro-homogeneous models over pore network models and micro-structural models are:

1. Computational time and computational resources required to obtain numerical solutions are low.
2. Macro-homogeneous models can be easily merged with pore-size distribution models in order to take wettability and microstructure into account.
3. Low coding time and easier code debugging.

1.3.3 Conventional Cathode Catalyst Layer Models

The electrochemical reactions, water generation, water phase change, heat generation, and diffusion of reactants (oxygen) and products (water vapour) all take place inside the catalyst layer. Due to the small pore sizes of conventional catalyst layers both binary and Knudsen diffusivity must be taken into account. Convective transport effects are also considered. Finally, effective transport properties such as the permeability and diffusivity are also related to the layer microstructure.

Because of the complexity of physical phenomena, cathode catalyst layer analysis is a cumbersome multi-physics problem. Most of the time, researchers make assumptions to simplify the cathode catalyst layer; such as considering isothermal conditions and thus neglecting heat transfer effects, and assuming that the effective transport properties can be obtained without looking at wettability and microstructure. Other popular assumptions are low gas velocities, so that the convective effects can be neglected.

After using one or more of the simplifying assumptions previously described, conventional cathode catalyst layer models can be grouped into two main categories: 1) macro-homogeneous models, where the catalyst layer is assumed to be a layer with averaged properties [56–60], and 2) agglomerates models, where the catalyst layer is idealized to be an array of spherical carbon agglomerates with platinum particles deposited on their surface [56, 61–67].

In both categories, water management is usually treated similarly: fluxes of liquid water and water vapour are included in the governing equations, and effective properties such as diffusion coefficients are assumed to be constant properties, or properties independent of wettability and microstructure. With such models, the effects of changing the wettability and microstructure of the catalyst layers cannot be studied.

Currently, very few cathode catalyst layer models include a pore-size distribution. Weber [3] and Lui and Eikerling [1] were among the pioneers on using PSD functions to characterize catalyst layers, but only Weber took mixed wettability into account. Weber's catalyst layer models take into account mixed wettability, but assume that the hydrophilic and hydrophobic pore networks are uniformly distributed along the same pore sizes. Liu and Eikerling's catalyst layer model does not include mixed wettability effects, but includes two modes: one corresponding to the primary pores and one corresponding to the secondary pores of the catalyst layer. The main difference between the cathode catalyst layer model we propose and previous PSD-based models is the ability of formulate a layer configuration with independent hydrophilic and hydrophobic networks, allowing for more flexibility and better layer representation.

1.4 Contributions

The novelty of this research is that different hydrophilic and hydrophobic wettability configurations for conventional catalyst layers and MPLs are studied in order to determine the optimal micro-structure of the cathode side. The main contributions are:

- the development of a mixed wettability pore-size distribution model that is used to estimate saturation and effective transport properties, such as permeability and effective diffusivity, for any porous material,
- the development of a mixed wettability MPL model that incorporates the proposed mixed wettability pore-size distribution model,
- the development of a conventional mixed wettability cathode catalyst layer model to examine the effect of adding a network of hydrophilic pores to a catalyst layer on cell performance,
- and a computational model for the cathode side of a PEMFC, using the proposed pore-size distribution model.

1.5 Structure of the Thesis

This research presents a model to estimate the effective transport properties of porous materials with mixed wettability, such as the MPL and the conventional catalyst layer of PEMFC. The basic operation of a PEMFC and an introduction to catalyst layer and MPL modelling is presented in Chapter 1. The description of the proposed pore-size distribution model, together with the experimental setup used to measure the global pore-size distribution of MPLs and GDLs, the validation of the effective properties estimated for conventional GDLs, and parametric studies of the effects of pore distribution and wettability are presented in Chapter 2. Chapter 3 described the governing equations and boundary conditions of the MPL model, including parametric studies about the effects of wettability on reactant transport. Chapter 4 contains the model description of the conventional catalyst layer model, including parametric studies on the effects of wettability on performance.

The final remarks of this work, including the conclusion, directions for future research and recommendations for industrial applications are presented in Chapter 5.

Chapter 2

Mixed Wettability Pore-Size Distribution Model

2.1 Introduction

In many disciplines that deal with porous media, such as electrochemistry and fuel cell modelling, oil reservoir characterization, and ground water extraction, it is of interest to find a way to estimate the effective transport properties based on the actual porous media in order to make good approximations of the transport mechanisms involved.

In many cases effective transport properties are obtained from empirical relations, which are based on experimental studies. It would be beneficial to develop mathematical models that can predict these properties for new materials when they are dry and wetted, as most experimental set-ups can measure these effective properties for dry conditions.

Pore-size distribution (PSD) models were introduced to estimate the effective transport properties of porous media under dry and wetted conditions [68, 69]. In PSD models, the change of cumulative pore volume (or pore volume fraction) based on pore sizes is represented by an algebraic function. This function is then used to estimate medium properties such as saturation, relative permeability, liquid-gas interfacial surface area per unit volume and Knudsen diffusivity. Weber [3, 21, 70] and Eikerling [60] pioneered this method in the area of fuel cell modelling.

PSD models use a family of functions to relate the change in cumulative volume of liquid invading a porous sample with an effective pore radius. This function is then used to estimate properties such as saturation, liquid and gas relative permeabilities, and liquid-vapour interfacial surface area. An infinite number of functions relating cumulative pore volume and pore radius can be used to fulfil this purpose. Log-normal distribution functions are commonly used because they were shown to represent the experimental values accurately [3, 21, 60, 70] and because analytical expressions can be obtained for saturation, liquid and gas relative permeabilities, and liquid-gas interfacial surface area after mathematical manipulation.

Weber implemented a PSD model that included the effects of mixed wettability to define porous materials. The basic form of the implemented PSD model is given as the sum of k log-normal distributions. This is given by

$$\frac{dX(r)}{dr} = \sum_k \left[\frac{f_k}{r\, s_k \sqrt{2\pi}} \exp\left(- \left[\frac{\ln(r) - \ln(r_k)}{s_k\sqrt{2}} \right]^2 \right) \right] \tag{2.1}$$

where f_k is the contribution of the log-normal distribution k to the total PSD, r_k is the characteristic pore size of the distribution k, s_k is the spread of the distribution k, and r is the pore radius. To represent mixed-wettability, Weber and Hickner [3, 21, 70] assumed that the hydrophilic and hydrophobic pores were distributed uniformly over the pore sizes. Therefore, the PSD functions for the hydrophilic and hydrophobic pores were represented by Equation (2.2) and Equation (2.3), respectively.

$$\frac{dX(r)_{HI}}{dr} = F_{HI} \sum_k \left[\frac{f_k}{r\, s_k \sqrt{2\pi}} \exp\left(- \left[\frac{\ln(r) - \ln(r_k)}{s_k\sqrt{2}} \right]^2 \right) \right] \tag{2.2}$$

$$\frac{dX(r)_{HO}}{dr} = F_{HO} \sum_k \left[\frac{f_k}{r\, s_k \sqrt{2\pi}} \exp\left(- \left[\frac{\ln(r) - \ln(r_k)}{s_k\sqrt{2}} \right]^2 \right) \right] \tag{2.3}$$

On these expressions, F_{HI} is the volume fraction corresponding to the hydrophilic pores and F_{HO} is the volume fraction corresponding to the hydrophobic pores. Note that $F_{HI} + F_{HO} = 1$. Figure 2.1 presents PSD functions for a porous material with the mixed wettability approach implemented by Weber [3, 21]. The global PSD is obtained by adding the hydrophilic (HI) and hydrophobic (HO) PSDs. Note that in this case for each pore radius there is a relative amount of hydrophilic and hydrophobic pores.

With this formulation Weber and Hickner [3, 21, 70] studied the effects of wettability and pore size on effective transport properties such as saturation, relative permeability, Knudsen radius (defined as the average pore size of the layers as indicated in Section 2.4.7), and liquid-gas interfacial surface area per unit volume. A shortcoming of this model is that porous media with distinct pore size distributions for hydrophilic and hydrophobic pores (i.e. a material with small hydrophilic pores and large hydrophobic pores) cannot be described.

Recently, Weber improved the PSD model by assuming that the contact angles that define the wettabilities of porous materials are distributed between 0°and 180°by

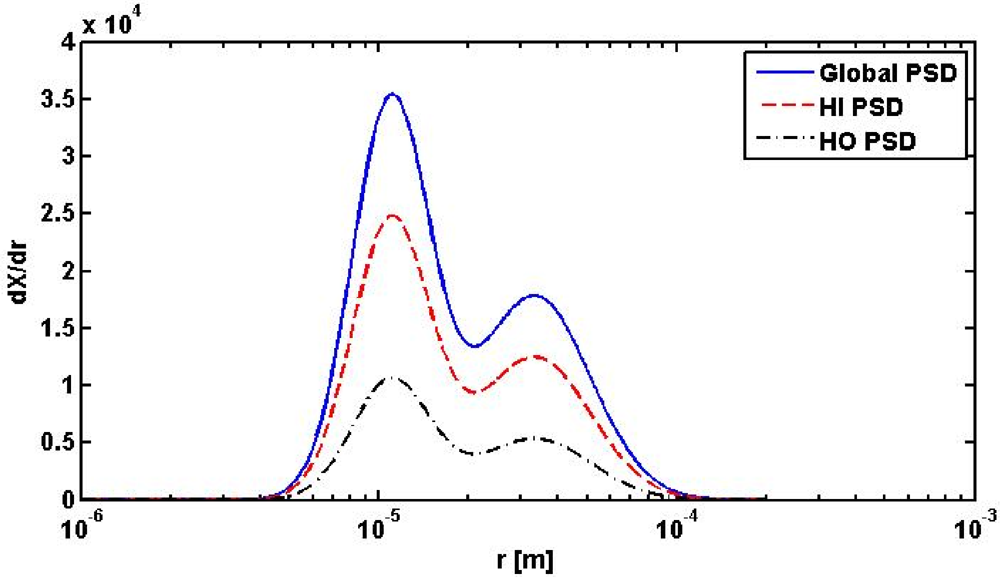

Figure 2.1 – Diagram showing global, hydrophilic and hydrophobic PSD functions from the mixed-wettability PSD model implemented by Weber, showing the assumption that hydrophilic and hydrophobic pores are distributed over the same range of pore sizes.

means of a contact angle distribution (CAD) [21]. Unlike PSDs, CADs cannot be measured, and therefore have to be assumed in advance or obtained by fitting the capillary pressure-saturation relationships [21].

Eikerling proposed a PSD model to describe conventional catalyst layers, and did not take mixed wettability into account. Instead, he looked at the pore size of primary pores (pores inside the carbon agglomerates) and secondary pores (pores between agglomerates) [60]. The proposed PSD model is also based on log-normal distributions, but the general form is more complex than the one presented by Weber [3, 21, 70]. Eikerling implemented the following bimodal PSD model:

$$\frac{dX_p(r)}{dr} = \frac{1 - X_{PtC} - X_{cl}}{\sqrt{\pi}\left[\ln(s_\mu) + \chi_M \ln(s_M)\right]} \frac{1}{r} \left(A + \chi_M B\right) \tag{2.4}$$

$$A = \exp\left[-\left(\frac{\ln(r) - \ln(r_\mu)}{\ln(s_\mu)}\right)^2\right] \tag{2.5}$$

$$B = \exp\left[-\left(\frac{\ln(r) - \ln(r_M)}{\ln(s_M)}\right)^2\right] \tag{2.6}$$

where X_{PtC} is the volume fraction of the solid platinum/carbon particles, X_{cl} is the volume fraction of ionomer, χ_M represents the relative contributions of primary and secondary pores, r_M is the radius at which the secondary pores are centred, r_μ is the radius at which the primary pores are centred, s_M is spread of the distribution corresponding to the secondary pores, and s_μ is spread of the distribution corresponding to the primary pores.

The PSD formulations for Weber et al. [3, 21, 70] and Eikerling [60] are very similar. The only considerable difference between the two PSD models is that Eikerling's uses the porosity of the media as a variable to define the PSD while Weber's PSD model does not. Additionally, the denominator inside the exponential terms on each model on Weber's PSD model is directly proportional to the distribution spread rather than to its natural logarithm. Both models are able to represent the experimental data reasonable well, but the advantage of Weber's PSD model is that allows to obtain analytical solutions for the effective properties, while Eikerling's PSD model does not and numerical integration must be used instead.

This research builds on top of the models above. Log-normal distributions can be used to accurately represent the PSDs of conventional catalyst layers and MPLs. Martínez et al. [9] revealed that the pore networks in gas diffusion media of PEMFCs can be characterized by two pore-size distributions that are not uniformly distributed over all pore sizes. Therefore, in this research a new PSD-based model is formulated that includes two PSDs rather than either one bi-modal distribution or two mixed wettability distributions that are uniformly distributed.

2.2 Model Description

A shortcoming of previous PSD models is that they cannot study the effects of individual hydrophilic and hydrophobic wettabilities if they are not uniformly distributed over the same pore sizes. However, it is likely that the PSD of HI and HO pores will be different [9]. Further, it would be beneficial to reduce the complexity of the CAD model by looking at a total PSD and a PSD corresponding to the wetting fluid, which is water in this particular case. Then, an accurate prediction of full and empty pores can be obtained. A PSD model with two independent wettabilities, each wettability associated with a contact angle, is proposed. The initial form of the PSD model takes the form:

$$\frac{dV(r)}{dr} = V_T \left\{ F_{HI} \sum_k \left[\frac{f_{HI,k}}{r\, s_{HI,k}\sqrt{2\pi}} E_{HI,k} \right] + F_{HO} \sum_k \left[\frac{f_{HO,k}}{r\, s_{HO,k}\sqrt{2\pi}} E_{HO,k} \right] \right\} \tag{2.7}$$

where the factors $E_{HI,k}$ and $E_{HO,k}$ are defined as:

$$E_{HI,k} = \exp\left(-\left[\frac{\ln(r) - \ln(r_{HI,k})}{s_{HI,k}\sqrt{2}}\right]^2\right) \tag{2.8}$$

$$E_{HO,k} = \exp\left(-\left[\frac{\ln(r) - \ln(r_{HO,k})}{s_{HO,k}\sqrt{2}}\right]^2\right) \tag{2.9}$$

where F_i is the fraction of the total volume corresponding to the pores with wettability i (either HI for hydrophilic pores, or HO for hydrophobic pores), V_T is the total volume of pores in the sample, $f_{i,k}$ is the contribution of the distribution k to the i PSD distribution, $r_{i,k}$ is the characteristic pore size of the distribution k into the i PSD, and $s_{i,k}$ is the spread of the distribution k into i PSD. This function represents the cumulative liquid volume of the pores as a function of pore radius r. The outer summation in Equation. 2.7 indicates that two functions corresponding to each one of the distinct wettabilities (hydrophilic and hydrophobic pores) are used to define the model; both functions have the same description but the parameters used to define them are independent.

Note that with respect to $f_{H,k}$, the PSD is linear. This will be important when defining the different PSD configurations tested in this study. Linearity with respect to $f_{H,k}$ means that commutative, associative, and distributive law can be used with the different modes of the PSD, if and only if the rest of the PSD parameters remain unchanged.

The change in cumulative pore volume fraction can be defined as:

$$\frac{dX(r)}{dr} = \frac{1}{V_T}\frac{dV(r)}{dr} \tag{2.10}$$

Equation (2.10) is the final form of the mixed wettability PSD model. Figure 2.2 shows the plot for the global, hydrophilic and hydrophobic PSD functions for the porous material used to generate Figure 2.1, assuming that 70% of the pores are hydrophilic and the other 30% are hydrophobic pores. The actual percentage of hydrophilic and hydrophobic pores for this example is irrelevant, the important aspect is to see the differences between the hydrophilic and hydrophobic pore-size distributions. Note that using the new formulation the hydrophilic and hydrophobic functions are allowed to be unrelated functions, as opposed to the ones observed in Figure 2.1.

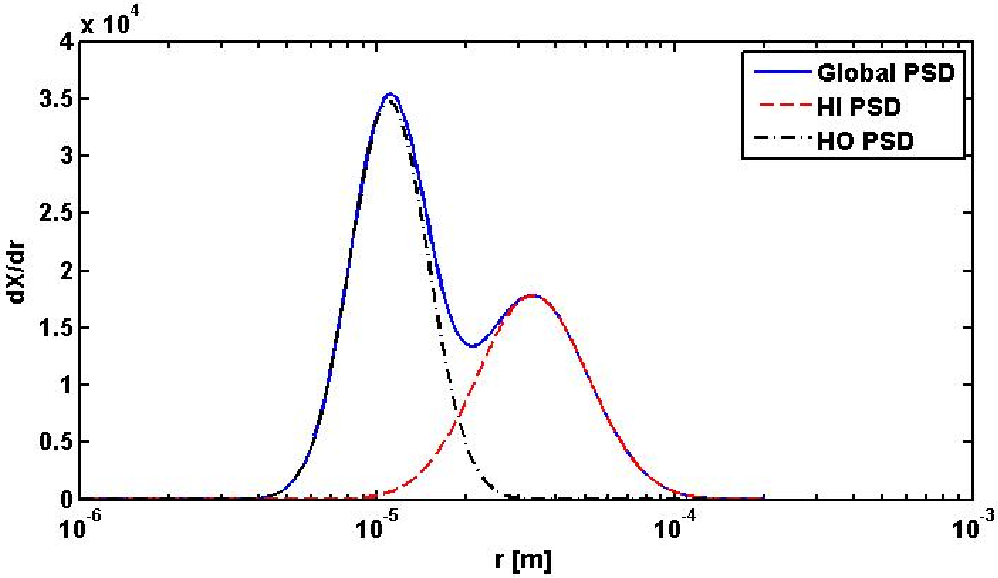

Figure 2.2 – Diagram showing global, hydrophilic and hydrophobic PSD functions from the proposed mixed-wettability PSD model, showing that the hydrophilic and hydrophobic pore networks are individual and not necessarily related.

2.3 Experimental Method and Fitting Procedure to Obtain PSD

2.3.1 Mercury Intrusion Porosimetry

Several researchers have used intrusion porosimetry (IP) to study the structure and wettability behaviour of powders and porous materials [9, 71–73]. Because mercury is hydrophobic for most materials, the contact angle is approximately constant, and evaporation rates are low for very low pressures, researchers use MIP to obtain global properties (independent of material wettability) of porous structures such as fuel cell gas diffusion media [9, 74], cement-based materials [75], and petroleum reservoirs [69]. For mercury at room temperature, the surface tension is taken to be $0.480\, N\, m^{-1}$ and the contact angle is taken to be 140°. Even though this is an intrusion experiment, we assume the contact angle to be static; we do not consider the effects of advancing or receding contact angles and instead assume that the contact angles remain constant during intrusion.

Using mercury, Martínez et al. [9] documented IP results for two of the gas diffusion media (DGM) commonly used in PEMFC. In IP, different levels of pressure are applied to a working fluid in which the sample is immersed. The intruded volume is recorded as the injection pressure is gradually increased. Under the assumption that the porous sample is equivalent to an array of cylindrical pores, the Young-

Figure 2.3 – PoreMaster 33 intrusion porosimeter, manufactured by Quantachrome Instruments.

Laplace equation can be used to relate the controlled pressure that is forcing the fluid to invade the pores to a critical pore radius. The Young-Laplace equation can be used to obtain an effective, critical pore radius [3, 21]. Based on its contact angle, mercury is a non-wetting fluid for most materials.

In this thesis, IP measurements with mercury as the working fluid have been performed on SGL Sigracet 34BA (GDL) and SGL Sigracet 34BC (GDL and MPL). To perform the IP measurements for this work a *PoreMaster 33* intrusion porosimeter, manufactured by Quantachrome Instruments, was used. Prior to the analysis, the porosimeter was calibrated using the manufacturer standards. The *PoreMaster 33*, shown in Figure 2.3, is capable of applying pressures of up to 227.53 MPa (33000 $psia$), which in turn allows for pore size measurements ranging from 950 to 0.0064 μm when mercury is used as the working fluid.

In our experiments, between 0.1 and 0.25 grams of sample are dried by placing in an oven at 80°C from 5 to 10 hours to ensure that irreducible saturation and humidity is removed prior to the intrusion experiments. The samples are then placed inside a sample cell (penetrometer) and vacuumed. Vacuuming the samples is a vital step in our experiments because since the capillary pressure is defined as the difference of

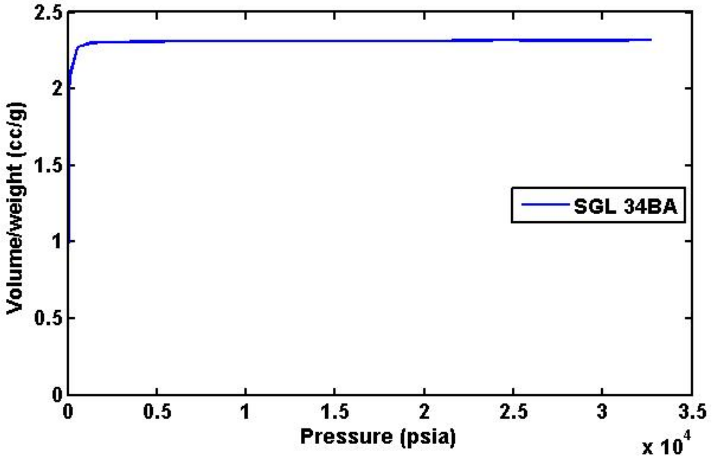

Figure 2.4 – Raw data from mercury intrusion porosimetry for SGL 34BA.

liquid and gas pressures, $p_c = p_L - p_G$, vacumming the sample ensures that the gas pressure is vanishingly small and therefore $p_c \approx p_L$. During the process of removing the samples from the oven and transferring them to the PoreMaster, humid air may re-enter the samples, but due to the short exposure time is assumed that water is removed after vacuuming the samples.

When the gas pressure is down to 1.35 Pa ($\sim$ 10 mTorr), mercury is injected into the sample cell. As the mercury injection pressure is gradually increased, the intruded volume normalized by sample mass is recorded. The applied pressure and intruded volume can then be post-processed to obtain the PSD corresponding to all the pores of the sample. To relate the capillary pressure to an effective pore size, the Young-Laplace equation is used.

An example of the raw data from mercury intrusion porosimetry (intruded volume normalized by sample weight in terms of applied pressure) for the SGL Sigracet 34BA GDL and for the SGL Sigracet 34BC composite GDL + MPL are presented in Figure 2.4 and Figure 2.5, respectively.

Multiplying by the corresponding sample mass and finding the rate of change of the intruded volume with respect to the pore radius (related to the applied pressure by the Young-Laplace equation), a PSD that shows the change in cumulative pore volume with respect to pore size can be obtained,

$$\frac{dV}{dr} = \frac{V^{n+1} - V^{n}}{r^{n+1} - r^{n}} \tag{2.11}$$

Finally, this PSD can be normalized by the total intruded volume. With this step, the cumulative pore volume fraction X is obtained,

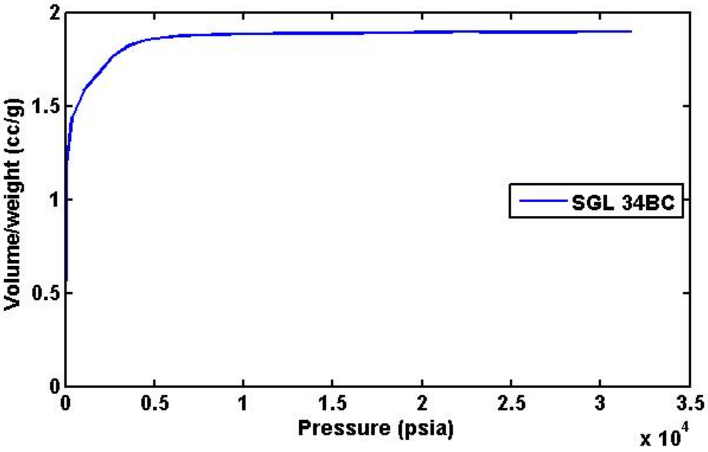

Figure 2.5 – Raw data from mercury intrusion porosimetry for SGL 34BC.

$$\frac{dX}{dr} = \frac{1}{V_T}\frac{dV}{dr} \tag{2.12}$$

where V is the cumulative pore volume and V_T is the total intruded volume. The final post-processed PSD functions for one SGL 34BA and two 34BC samples are shown in Figure 2.6. The SGL 34BC is very similar to the SGL 34BA GDL, but a microporous layer was applied to one of the sides of the GDL. The smaller pore sizes corresponding to the MPL can be observed in Figure 2.6 in the 1 $\mu m - 10nm$ range. IP tests were performed several times, and consistent results were always obtained.

To highlight the pore-sizes and have a visual representation of the percentage of pores and their pore sizes, the *PoreMaster 33* reports the PSD as:

$$\frac{dX}{d(\log(r))} \tag{2.13}$$

plotted against the pore-size logarithmic scale. However, since $d(\log(r)) \propto r^{-1}dr$ we express the PSD as

$$r\frac{dX}{dr} \tag{2.14}$$

plotted against the pore-size logarithmic scale.

Figure 2.7 presents the PSD for the SGL 34BC obtained in-house using intrusion porosimetry, and PSD functions for composite GDL-MPL layers reported by Martínez et al. [76]. Two GDL-MPL composite materials are reported from Martinez and co-workers: a) a Toray TGP-H-060 coated with an MPL with 10% PTFE in the GDL, and b) a Toray TGP-H-060 coated with an MPL with 40% PTFE in the GDL. Note that the distributions for small pores (MPL) agrees very well with the two additional

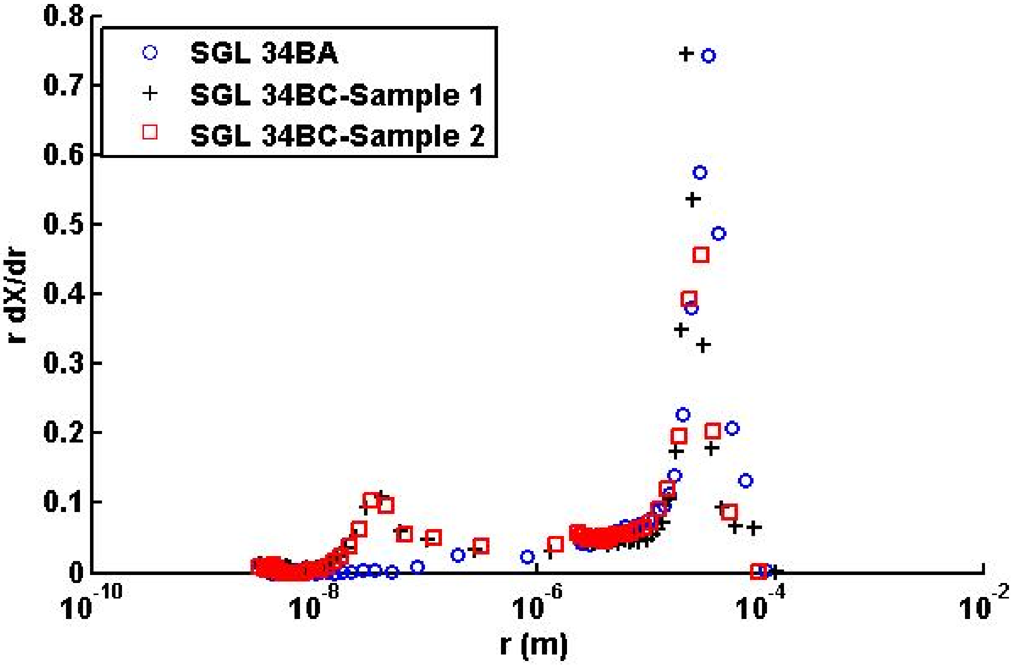

Figure 2.6 – Discrete PSD function from mercury intrusion porosimetry for SGL 34BA and SGL 34BC samples.

distributions presented, but the distribution corresponding to the GDL does not. Several factors influence the PSD for GDLs:

- GDL classification. Luo et al. [5] showed that there is a difference in pore sizes between carbon cloth and carbon paper GDLs. The same can be then expected from carbon paper and carbon felt GDLs. Toray GDLs are carbon paper, while SGL Sigracet are carbon felt.

- Wet proofing. It is clear that wet proofing changes the porosity of GDLs, but the behaviour of wet proofing of SGL Sigracet GDLs on pore-size distribution could not be found.

2.3.2 Water Intrusion Porosimetry

The proposed PSD model requires a total PSD and a PSD obtained using the working fluid in the GDL/MPL, and catalyst layers. In this case, the working fluid is water. Water intrusion porosimetry has been documented in the past by researchers studying the hydrophobic properties of different materials [9, 73, 77]. The idea of WIP is very similar to MIP, but in this case the intruding fluid is water.

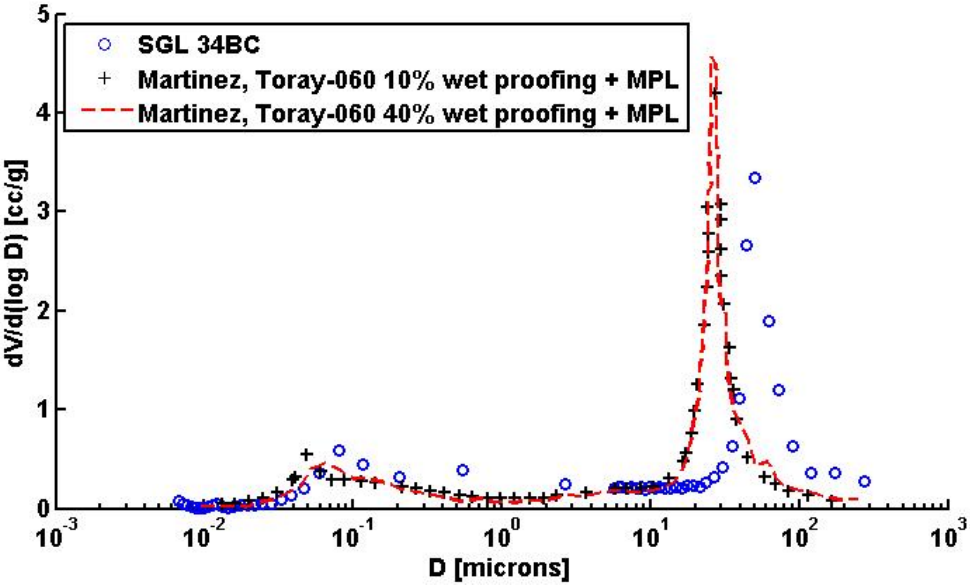

Figure 2.7 – PSD functions corresponding to GDL-MPL composite layers.

The sample preparation for WIP is the same as for MIP. After weighting the sample and placing it inside an oven at 80°C from 5 to 10 hours to ensure that irreducible saturation and humidity is removed prior to the intrusion experiments, the sample is placed inside a chamber and is vaccumed. After the gas pressure is vanishingly small, water is injected. With this procedure, all the hydrophilic pores will be ideally filled. As liquid pressure is systematically increased then water will invade the hydrophobic pores as dictated by the Young-Laplace Equation.

The process to obtain the PSD corresponding to hydrophobic pores from WIP data is the same used to obtain the global PSD from MIP data. With a global PSD and a hydrophobic PSD, a hydrophilic PSD can be obtained by subtracting the two. A diagram showing the methodology used to develop the PSD model from experimental data is shown in Fig. 2.8. The values for surface tension and contact angle for both mercury and water are assumed to be constant through the experiment.

With the Quantachrome *PoreMaster 33* intrusion porosimeter, is not possible to perform WIP following the procedure outlined in this section. Since mercury invades the penetrometer cell during the experiment, keeping the sample under vacuum and surrounded by water is very complicated. Thus, WIP data is outside the scope of the current project.

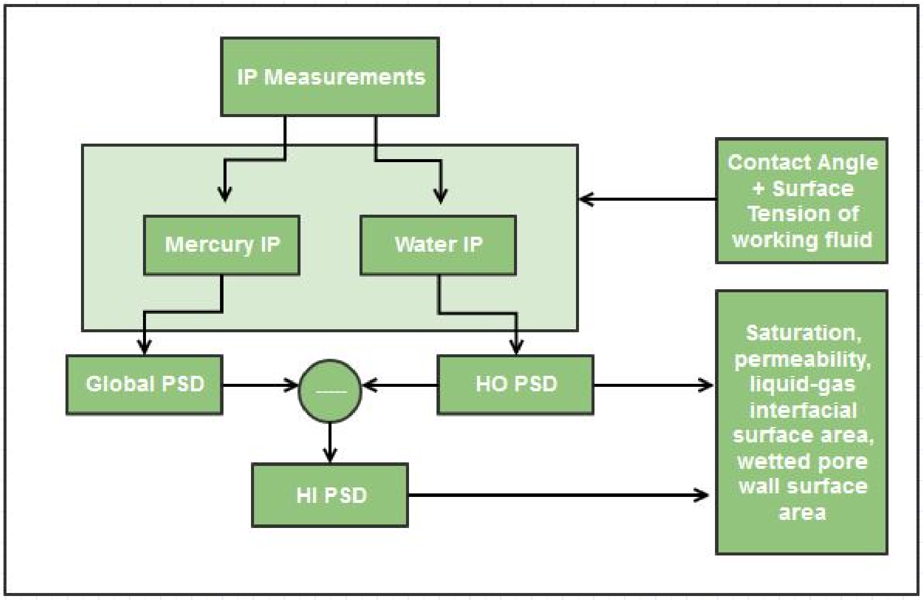

Figure 2.8 – Diagram showing the experimental procedure used to measure PSD functions from porous media samples.

2.3.3 Fitting Procedure

Using experimental data, a discrete form of the PSD can be obtained as previously explained. Next, the parameters that determine the PSD in Equation (2.7) need to be obtained. To accomplish this, the parameters s_k, r_k and $f_{H,k}$ are obtained by solving the least-squares parameter fitting problem below:

$$\begin{aligned} Minimize \quad & \sum_{i=1}^{Np} \left[\frac{\Delta X_i}{\Delta r_i} - \sum_k \left(\frac{F_H \, f_{H,k}}{r_i \, s_{H,k} \sqrt{2\pi}} E_{H,k,i} \right) \right]^2 \\ s.t. \quad & 0 \leq f_k \leq 1 \\ & 0 < s_k \leq 5 \\ & 0 < r_k \leq 1 \times 10^{-3} m \\ & \sum_k f_{H,k} = 1 \end{aligned} \tag{2.15}$$

and

$$E_{H,k,i} = \exp\left(- \left[\frac{\ln(r_i) - \ln(r_{H,k})}{s_{H,k}\sqrt{2}} \right]^2 \right) \tag{2.16}$$

The bounds for s_k are arbitrary, and are given between 0 and 5 because during the fitting process for MPLs and GDLs the values for s_k were always inside this range.

Pore sizes of MPLs and GDLs are known to be well below the millimetre scale, and thus the constraints for distribution radius is between 0 and 1×10^{-3} m. Since the PSD is a normalized function that represents the cumulative volume fraction of porous samples, no distribution weight $f_{H,k}$ can be greater that 1, and the sum of the weights of all distributions k must be exactly unity.

The least-squares parameter estimation problem was solved in Matlab, using the solver LSQNONLIN. Convergence issues are a common product of the developed algorithm to solve the problem. The Matlab least-squares method is gradient-based, therefore the location of local optimal solutions is common. Care has to be taken in order to provide an appropriate solution. In the future, global optimization techniques such as genetic algorithms (GA) or simulated annealing (SA) could be used to improve the present least-squares parameter estimation.

2.4 Effective Properties

This section highlights the different effective properties that can be estimated from the pore-size distribution of porous media. The complete derivation of the expressions presented in this section can be found in Appendix A.

2.4.1 Saturation

The saturation of a porous medium can be obtained by integrating the change of cumulative pore volume fraction as a function of effective pore radius over the whole pore size domain, where the critical pore radius is obtained using the capillary pressure of the sample. With the hydrophilic and hydrophobic PSD functions previously described, these integrals can be analytically defined, leading to an expression of the form:

$$S = S_{HI} + S_{HO} = \int_{0}^{r_{c,HI}} \frac{dX(r)_{HI}}{dr}\, dr + \int_{r_{c,HO}}^{\infty} \frac{dX(r)_{HO}}{dr}\, dr \tag{2.17}$$

For the hydrophilic pores, the limits of integration go from a pore size of zero to the critical pore size corresponding to the hydrophilic pores since small pores will fill up first. For the hydrophobic pores, the integration limits go from the critical pore size corresponding to the hydrophobic pores to a pore size of infinity as large HO pores fill up first.

Integrating the previous equations as shown in Appendix A.1 can be found that the saturation for the hydrophilic and hydrophobic pores, respectively, is given as:

$$S_{HI} = F_{HI} \sum_k \frac{f_{HI,r,k}}{2} \left[1 + \operatorname{erf}\left(\frac{\ln(r_{c,HI}) - \ln(r_{HI,k})}{s_{HI,k}\sqrt{2}}\right)\right] \tag{2.18}$$

$$S_{HO} = F_{HO} \sum_k \frac{f_{HO,k}}{2} \left[1 - \operatorname{erf}\left(\frac{\ln(r_{c,HO}) - \ln(r_{HO,k})}{s_{HO,k}\sqrt{2}}\right)\right] \tag{2.19}$$

2.4.2 Saturated Permeability

Darcy's law predicts that the mean velocity through any porous media depends on the pressure gradient along the media:

$$u_{mean} = -\frac{k}{\mu}\frac{dp}{dx} \tag{2.20}$$

where k is the permeability of the media, and μ is the dynamic viscosity of the fluid. The solutions from the Newtonian viscous flows equations through circular cross sections (Poiseuille flow) [78] predict the mean velocity inside a pore to be:

$$u_{mean} = -\frac{r^2}{8\mu}\frac{dp}{dx} \tag{2.21}$$

where r is the radius of the cross section. Therefore, for a single circular capillary we have that the absolute permeability is given as:

$$k = \frac{r^2}{8} \tag{2.22}$$

Since PSD models assume that the porous media is represented as an array of straight capillaries, integration is needed in order to take into account the effects of all the pores. For that, we can take into account how all the pores fill out with water. The absolute permeability can be found from:

$$k = \int_0^\infty \frac{r^2}{8}\frac{dX}{dr}dr \tag{2.23}$$

When obtaining the PSD from intrusion porosimetry measurements, the porous material is assumed to be an array of straight cylindrical pores as shown in Figure 2.9. Interconnectivity effects, which play an important role to define some of the internal physical properties of the layer, are lost. Thus, assuming that the porous layer is sliced into sections of the same cross-sectional area and then the slices are randomly put back together, the effects of the interconnectivity of the pores can be recovered. To accomplish this, statistics is used.

In order to account for interconnectivity, suppose that an array of straight cylindrical capillaries is sliced into several sections, as assumed by Bear [68]. These sections

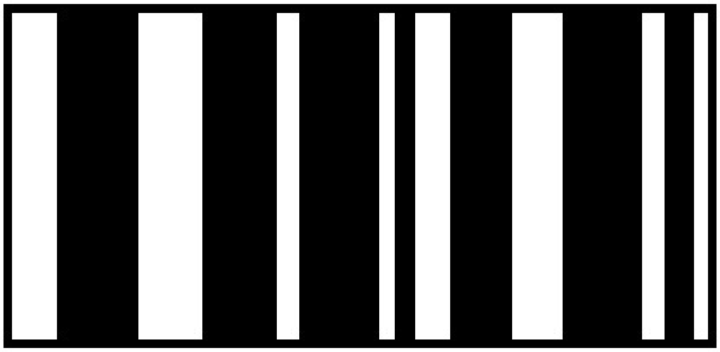

Figure 2.9 – Diagram showing porous material represented as an array of straight capillaries.

are randomly arranged and reassembled as shown in Figure 2.10. In any slice area A of this latter geometry, the area occupied by liquid water is given by:

$$A_{Liq} = \varepsilon_o \, A \, S_e \tag{2.24}$$

where ε_o is the porosity of the material and S_e is the effective saturation, which is used because previously most researchers considered that the effects of residual liquid saturations cannot be explained using the PSD functions and thus the saturation levels were corrected. As will be explained in Section 2.5.5, the effects of residual liquid saturation can be explained by considering the PSD of the media to be of mixed wettability. The effective saturation is defined as:

$$S_e = \frac{S - S_o}{1 - S_o} \tag{2.25}$$

where S_o is the liquid residual saturation of the medium. For our studies, we assume that $S_o = 0$ and therefore $S_e = S$.

Any slice contains the same area occupied by liquid water. However, some portions of these areas may not be connected, due to the random interconnection of the pores between each slice. Using statistical analysis, the probability of having a point on the interface between two neighbouring slices which also lies on liquid water is given by [3]:

$$P_1 = \frac{\varepsilon_o \, S_e}{\lambda} \tag{2.26}$$

where λ represents a factor that takes into account the interconnection of the pores. λ must always be greater than unity. The probability that a point lies in two wet slices simultaneously is given as:

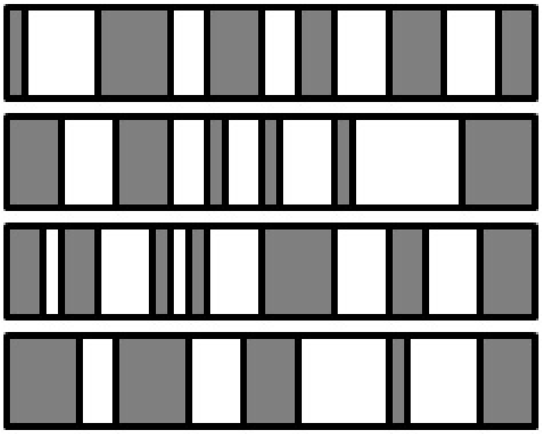

Figure 2.10 – Diagram showing sliced and randomly reconstructed array of capillaries to incorporate effects of pore microstructure on effective properties.

$$P_2 = P_1\,P_1 = \left[\frac{\varepsilon_o\,S_e}{\lambda}\right]^2 \tag{2.27}$$

Combining the previous equations, it can be shown that the absolute permeability of a fully saturated porous medium can be estimated from the mixed wettability PSD model by assuming that all pores contribute to transport, and that the sample is fully saturated:

$$k_{sat} = \left[\frac{\varepsilon_o}{\lambda}\right]^2 \int_0^\infty \frac{r^2}{8}\frac{dX(r)}{dr}dr \tag{2.28}$$

Solving the integral as shown in Appendix A.2, the saturated permeability is given as:

$$k_{sat} = \frac{1}{8}\left[\frac{\varepsilon_o}{\lambda}\right]^2 \sum_k \exp\left(-2\,s_k^2\right) r_k^2 f_k \tag{2.29}$$

2.4.3 Liquid Relative Permeability

The liquid relative permeability of a porous materials characterises how easily the liquid phase can move through the porous media at different saturation levels. If the permeability of the liquid phase is defined as k_L and the saturated permeability of the media is k_{sat}, then the liquid relative permeability is defined as:

$$k_{r,L} = \frac{k_L}{k_{sat}} \tag{2.30}$$

where k_{sat} is given by Equation (2.29). Unlike the saturated permeability, the liquid permeability k_L depends on the capillary pressure.

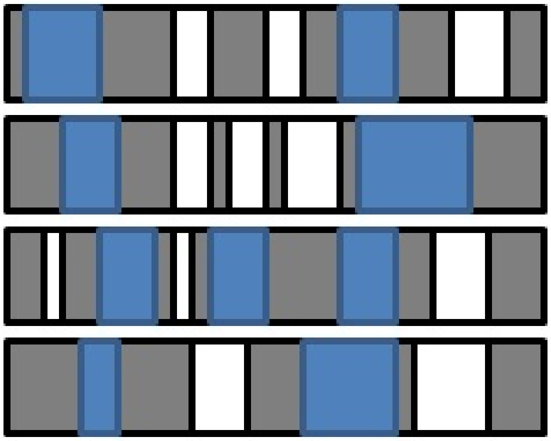

Figure 2.11 – Diagram showing a partially flooded, sliced and randomly reconstructed array of capillaries to incorporate effects of pore microstructure on effective properties.

Under the same assumptions of randomly sliced and re-arranged bundle of capillaries, the liquid relative permeability of a porous material can be estimated from the PSD model as:

$$k_{r,L} = \frac{\frac{1}{8}\left[\frac{\varepsilon_o\, S_e}{\lambda}\right]^2 \left[\int_0^{r_{c,HI}} r^2 \frac{dX(r)_{HI}}{dr} dr + \int_{r_{c,HO}}^{\infty} r^2 \frac{dX(r)_{HO}}{dr} dr\right]}{\frac{1}{8}\left[\frac{\varepsilon_o}{\lambda}\right]^2 \int_0^{\infty} r^2 \frac{dX(r)}{dr} dr} \tag{2.31}$$

where the numerator represents the permeability of the liquid phase corresponding to the hydrophilic and hydrophobic pores, and the denominator represents the saturated permeability previously defined. The integration limits for the numerator of Equation (2.31) are the same as the ones used to define the saturation and S_e is obtained using Equation (2.25).

Also, since the liquid permeability depends on the capillary pressure, the probability function used to define the effects of pore geometry and interconnectivity depends on the effective saturation. A diagram showing an example of a partially saturated reconstructed porous medium is presented in Figure 2.11.

Integrating the numerator of Equation (2.31) as shown in Appendix A.2 leads to:

$$k_{L,HI} = \frac{F_{HI}}{16}\left[\frac{\varepsilon_o\, S_e}{\lambda}\right]^2 \sum_k \exp\left(-2\, s_{HI,k}^2\right) r_{HI,k}^2 f_{HI,k} \left[\operatorname{erf}\left(\frac{\ln\left(r_{c,HI}\right) - \ln\left(r_{HI,k}\right)}{s_{HI,k}\sqrt{2}} - s_{HI,k}\sqrt{2}\right) + 1\right] \tag{2.32}$$

for the hydrophilic pores. Similarly, for the hydrophobic pores the liquid permeability is found from:

$$\begin{aligned} k_{L,HO} =& \frac{F_{HO}}{16} \left[\frac{\varepsilon_o \, S_e}{\lambda} \right]^2 \sum_k \exp\left(-2\, s^2_{HO,k}\right) r^2_{HO,k} f_{HO,k} \\ & \left[-\text{erf}\left(\frac{\ln\left(r_{c,HO}\right) - \ln\left(r_{HO,k}\right)}{s_{HO,k}\sqrt{2}} - s_{HO,k}\sqrt{2} \right) + 1 \right] \end{aligned} \tag{2.33}$$

The total liquid relative permeability is obtained by adding the relative contributions of both networks

$$k_{r,L} = \frac{k_{L,HI} + k_{L,HO}}{k_{sat}} \tag{2.34}$$

2.4.4 Gas Relative Permeability

The gas relative permeability can be interpreted as the permeability of the non-wetting phase (gas phase) in both the hydrophilic and hydrophobic pore networks. Therefore, the expressions used are the same as the ones used to obtain the final expression to estimate the liquid relative permeability but the integration limits corresponding to the hydrophilic and hydrophobic pores are inverted (hydrophilic contributions are obtained by integrating from $r_{c,HI}$ to ∞, while the hydrophobic contributions are obtained by integrating from 0 to $r_{c,HO}$) and the probability of two slices filled with the gas phase is given as:

$$P_1 = \frac{\varepsilon_o \, (1 - S_e)}{\lambda} \tag{2.35}$$

Thus, the gas relative gas permeability can be found from:

$$k_{r,G} = \frac{k_{G,HI} + k_{G,HO}}{k_{sat}} \tag{2.36}$$

where the hydrophilic gas permeability is given as:

$$\begin{aligned} k_{G,HI} =& \frac{F_{HI}}{16} \left[\frac{\varepsilon_o \, (1 - S_e)}{\lambda} \right]^2 \sum_k \exp\left(-2\, s^2_{HI,k}\right) r^2_{HI,k} f_{HI,k} \\ & \left[-\text{erf}\left(\frac{\ln\left(r_{c,HI}\right) - \ln\left(r_{HI,k}\right)}{s_{HI,k}\sqrt{2}} - s_{HI,k}\sqrt{2} \right) + 1 \right] \end{aligned} \tag{2.37}$$

and the hydrophobic gas permeability is given as:

$$k_{G,HO} = \frac{F_{HO}}{16} \left[\frac{\varepsilon_o \left(1 - S_e\right)}{\lambda} \right]^2 \sum_k \exp\left(-2\, s^2_{HO,k}\right) r^2_{HO,k} f_{HO,k} \left[\operatorname{erf}\left(\frac{\ln\left(r_{c,HO}\right) - \ln\left(r_{HO,k}\right)}{s_{HO,k}\sqrt{2}} - s_{HO,k}\sqrt{2} \right) + 1 \right] \tag{2.38}$$

$$k_{r,G} = \frac{k_G}{k_{sat}} = \frac{1}{8} \left[\frac{\varepsilon_o \left(1 - S_e\right)}{\lambda} \right]^2 \frac{\displaystyle\int_0^{r_{c,HO}} r^2 \frac{dX(r)_{HO}}{dr} dr + \int_{r_{c,HI}}^{\infty} r^2 \frac{dX(r)_{HI}}{dr} dr}{\displaystyle\frac{1}{8} \left[\frac{\varepsilon_o}{\lambda} \right]^2 \int_0^{\infty} r^2 \frac{dX(r)}{dr} dr} \tag{2.39}$$

2.4.5 Liquid-Gas Interfacial Surface Area per Unit Volume

The expression used to estimate the liquid-gas interfacial surface area per unit volume from the proposed mixed wettability PSD model is based on empirical relations and geometrical considerations used to represent the actual area available for evaporation as closely as possible. The information that we know with certainty for the surface area per unit volume between the liquid and the gas phases is:

1. must be zero when the porous medium is completely unsaturated,
2. must be zero when the porous medium is completely saturated, and
3. there must be a maximum value for a saturation value between zero and one.

Based on these known facts, and assuming that the lost information about pore interconnectivity can be recovered using statistics; the liquid-gas interfacial surface area per unit volume corresponding to the hydrophilic pores is estimated by looking at the cross sectional area of the pores. If pores are assumed to be cylindrical, we assume that phase changes will occur only in the circular cross sectional area of the capillaries.

The cross-sectional area of a single capillary is given as:

$$area = \pi r^2 \tag{2.40}$$

On the previous expression, was assumed that one end cap of the pore is always in contact with water, and therefore only the area of one end cap is used to estimate the liquid-gas interfacial surface area per unit volume. This assumption is justified by considering the specific application for which the model is developed. If the PSD model is used to model a GDL or an MPL in contact with a catalyst layer, liquid water will move from the catalyst layer to the MPL/GDL, therefore we can approximate that is water is uniformly distributed inside the catalyst layer, one end of the MPL/GDL will be in contact with liquid water during cell operation.

The pore volume is given as:

$$Volume = \pi r^2 \, L = a \, L \tag{2.41}$$

where L is the length of the pore. Using these expressions, the ratio of cross sectional area over volume is given as:

$$\frac{area}{Volume} = \frac{1}{L} \tag{2.42}$$

In order to take into account that some of the pores will be either filled with liquid water or empty, the previous expression is integrated for the pore sizes that are filled, based on the PSD model. In integral form, the wetted pore surface area per unit volume for all the wetted pores can be defined as:

$$\frac{a(r)}{V_T} = \int_0^{r_{c,HI}} \frac{1}{L}\frac{dX_{HI}}{dr} dr + \int_{r_{c,HO}}^{\infty} \frac{1}{L}\frac{dX_{HO}}{dr} dr \tag{2.43}$$

Eikerling [60] documented that for conventional catalyst layers, a linear relation between pore size and average pore length. The suggested form is given as:

$$L = M \, r \tag{2.44}$$

where M is assumed to be 4. This value may be linked to the material used to fabricate layers, but for this thesis is assumed that $M = 4$. The cross sectional area of the pores per unit volume is defined as:

$$\frac{a(r)}{V_T} = \int_0^{r_{c,HI}} \frac{1}{4\,r}\frac{dX(r)_{HI}}{dr} dr + \int_{r_{c,HO}}^{\infty} \frac{1}{4\,r}\frac{dX(r)_{HO}}{dr} dr \tag{2.45}$$

Integrating as shown in Appendix A.4, the cross sectional area per unit volume corresponding to the hydrophilic pores can be found from:

$$\frac{a(r)_{HI}}{V_T} = F_{HI} \sum_k \frac{f_{k,HI} \exp\left(\frac{s_{k,HI}^2}{2}\right)}{8\, r_{k,HI}} \left[1 + \text{erf}\left(\frac{\ln(r_{cr}) - \ln(r_{k,HI})}{s_{k,HI}\sqrt{2}} + \frac{s_{k,HI}\sqrt{2}}{2}\right)\right] \tag{2.46}$$

The effects of pore interconnectivity can be included using a probability function Pb such that,

$$\frac{a(r)_{HI}}{V_T} = Pb\,F_{HI} \sum_k \frac{f_{k,HI} \exp\left(\frac{s_{k,HI}^2}{2}\right)}{8\, r_{k,HI}} \left[1 + \operatorname{erf}\left(\frac{\ln(r_{cr}) - \ln(r_{k,HI})}{s_{k,HI}\sqrt{2}} + \frac{s_{k,HI}\sqrt{2}}{2}\right)\right] \tag{2.47}$$

For the hydrophobic pores the cross sectional area per unit volume can be estimated from an expression of the form:

$$\frac{a(r)_{HO}}{V_T} = Pb\,F_{HO} \sum_k \frac{f_{k,HO} \exp\left(\frac{s_{k,HO}^2}{2}\right)}{8\, r_{k,HO}} \left[1 - \operatorname{erf}\left(\frac{\ln(r_{cr}) - \ln(r_{k,HO})}{s_{k,HO}\sqrt{2}} + \frac{s_{k,HO}\sqrt{2}}{2}\right)\right] \tag{2.48}$$

Therefore, the expression for the liquid-vapour interfacial surface area per unit volume corresponding to all the pores is given by:

$$a(r)_T = \frac{a(r)}{V_T} = \frac{a(r)_{HI}}{V_T} + \frac{a(r)_{HO}}{V_T} \tag{2.49}$$

Choosing the correct probability function is essential for the predictions to be physically accurate. To estimate this probability function, we propose that the ratio between the wetted cross sectional area and the maximum cross sectional area of the pores can be used. The cumulative cross sectional area of all the capillaries per unit volume (in integral form) was previously defined in Equation (2.45).

The maximum cross sectional area can also be defined in terms of the PSD. To accomplish this, we integrate over all the pores. The total pore cross sectional area is then given by:

$$a_{max} = \sum_k \frac{f_k \exp\left(\frac{s_k^2}{2}\right)}{8\, r_k} \left[1 + \operatorname{erf}\left(\frac{\ln(\infty) - \ln(r_k)}{s_k\sqrt{2}} + \frac{s_k\sqrt{2}}{2}\right)\right] \tag{2.50}$$

Since $\ln(\infty) = \infty$ and $\operatorname{erf}(\infty) = 1$,

$$a_{max} = \sum_k \frac{f_k \exp\left(\frac{s_k^2}{2}\right)}{4\, r_k} \tag{2.51}$$

With these expressions the ratio of the cumulative cross sectional area of the liquid-invaded pores and the total cross sectional area of all the pores is defined as:

$$a(r)_L = \frac{a(r)_c}{a_{max}} \tag{2.52}$$

where the prefix L represents the liquid phase. Similarly, the ratio of the cross sectional area of empty capillaries (capillaries where the gaseous phase is present) and the total cross sectional area is given as:

$$a(r)_G = 1 - \frac{a(r)_c}{a_{max}} \tag{2.53}$$

The product of the previous two expressions can be used to define the probability function that represents the likehood of having a liquid-gas interface,

$$Pb = a(r)_L \, a(r)_G = \frac{a(r)_c}{a_{max}} \left(1 - \frac{a(r)_c}{a_{max}}\right) \tag{2.54}$$

Therefore, the specific liquid-gas interfacial surface area per unit volume corresponding to the hydrophilic pores can be found from an expression of the form:

$$\frac{a(r)_{HI}}{V_T} = \frac{a(r)_c}{a_T} \left(1 - \frac{a(r)_c}{a_T}\right) \frac{a(r)_{HI}}{V_T} \tag{2.55}$$

For the hydrophobic pores, the specific liquid-gas interfacial surface area per unit volume takes the form:

$$\frac{a(r)_{HO}}{V_T} = \frac{a(r)_c}{a_T} \left(1 - \frac{a(r)_c}{a_T}\right) \frac{a(r)_{HO}}{V_T} \tag{2.56}$$

Adding the hydrophilic and hydrophobic distributions the final expression to estimate the liquid-gas interfacial surface area per unit volume can be expressed as:

$$a_{LV} = \frac{a(r)_{HI}}{V_T} + \frac{a(r)_{HO}}{V_T} \tag{2.57}$$

Figure 2.12 presents the probability Pb as a function of saturation level for a conventional carbon felt GDL. The figure illustrates that the profile of the probability function goes to zero for either an unsaturated GDL, or a completely saturated GDL. This is the desired behaviour of interfacial surface area. The probability function has a maximum value between saturation values of zero and unity. Also note that the maximum value is very close to a zero saturation, but this will depend on PSD and wettability. The PSD used to represent the GDL is presented in Table 2.1. For the

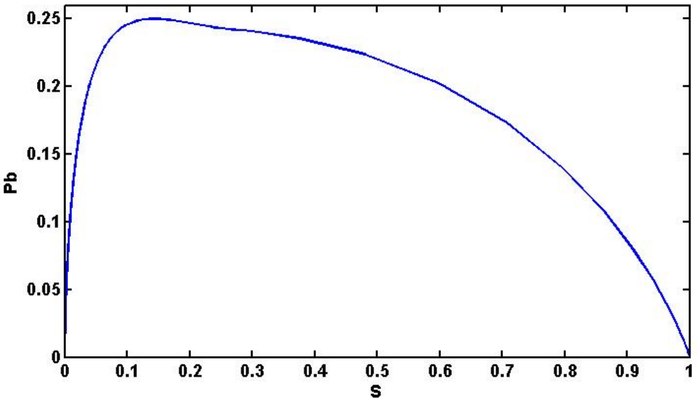

Figure 2.12 – Probability function plotted against layer saturation for a conventional carbon felt GDL.

Table 2.1 – Fitting parameters used to define PSD for SGL Sigracet 34BA GDL.

Variable	Value
f_k	$[0.72,\ 0.28]$
$r_k\ [\mu m]$	$[34,\ 14.2]$
s_k	$[0.35,\ 1]$

test case, the pores centred around $14.2 \mu m$ are assumed to be hydrophilic, and the rest of the GDL is assumed to be hydrophobic. The hydrophilic and hydrophobic static contact angles were assumed to be 80^o and 100^o, respectively.

Figure 2.13 presents the estimated liquid-vapor interfacial surface area per unit volume profile as a function of saturation. The interfacial surface area goes to zero when all the pores are free of liquid water, and when all the pores are full of liquid water. A maximum value of interfacial surface area per unit volume is observed for saturations in the range of 0.2 and 0.8.

2.4.6 Wetted Pore Wall Surface Area

Since the porous materials are assumed to be an array of straight cylindrical micro and nanopores, the total surface area of the pores would be the same as the lateral surface area of cylinders.

The lateral surface area of a cylinder can be found from:

$$a_{Lateral} = 2\,\pi\,r\,L \tag{2.58}$$

Therefore the ratio of lateral surface area to volume for a straight capillary is given

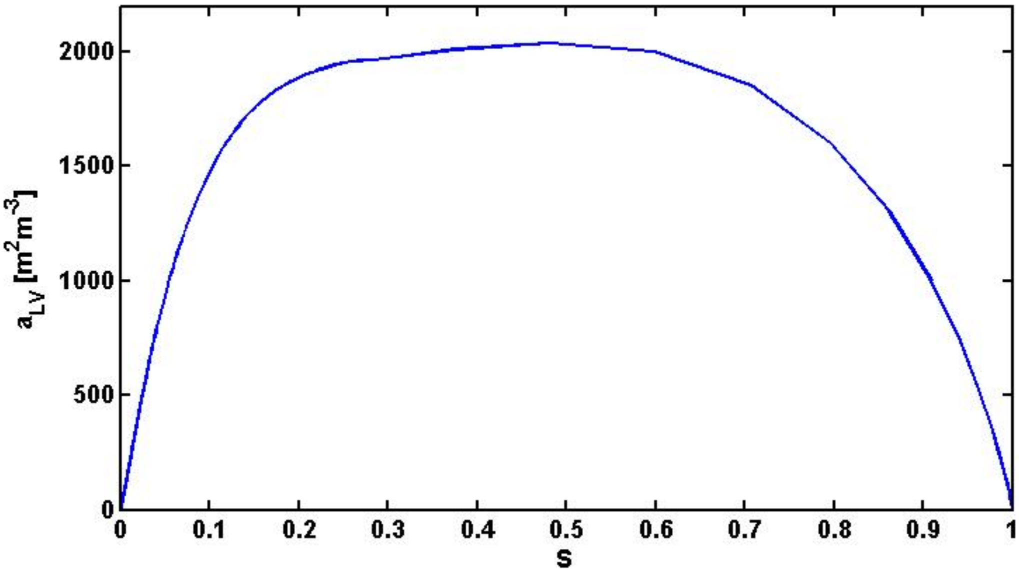

Figure 2.13 – Liquid-vapor interfacial surface area per unit volume for a conventional carbon felt GDL plotted against saturation, neglecting effects of pore interconnectivity factor λ.

as:

$$\frac{a_{Lateral}}{Volume} = \frac{2}{r} \tag{2.59}$$

Integrating the latter expression in order to incorporate all the pores that constitute the bundle of capillaries, and by taking into account the filling of pores due to capillary pressure, the lateral surface area per unit volume of porous materials can be found from the PSD model as:

$$a_{wall} = \int_0^\infty \frac{a_{Lateral}}{V_T} = \int_0^{r_{c,HI}} \frac{2}{r}\frac{dX(r)_{HI}}{dr}\,dr + \int_{r_{c,HO}}^\infty \frac{2}{r}\frac{dX(r)_{HO}}{dr}\,dr \tag{2.60}$$

Integrating as shown in Appendix A.3, the total surface area per unit volume can be found as:

$$a_{wall,HI} = \sum_k \frac{F_{HI}\, f_{k,HI}}{r_{k,HI}} \exp\left(\frac{s_{k,HI}^2}{2}\right) \left[1 + \operatorname{erf}\left(\frac{\ln(r_{c,HI}) - \ln(r_{k,HI})}{s_{k,HI}\sqrt{2}} + \frac{s_{k,HI}}{\sqrt{2}}\right)\right] \tag{2.61}$$

for the hydrophilic pores, and

$$a_{wall,HO} = \sum_k \frac{F_{HO}\, f_{k,HO}}{r_{k,HO}} \exp\left(\frac{s_{k,HO}^2}{2}\right) \left[1 - \mathrm{erf}\left(\frac{\ln(r_{c,HO}) - \ln(r_{k,HO})}{s_{k,HO}\sqrt{2}} + \frac{s_{k,HO}}{\sqrt{2}}\right)\right] \tag{2.62}$$

for the hydrophobic pores. The total pore walls surface area per unit volume can be found, using the PSD model, as:

$$a_{wall} = a_{wall,HI} + a_{wall,HO} \tag{2.63}$$

2.4.7 Average Knudsen Radius

To characterize the dominant diffusion mode, the average Knudsen radius of the porous media must be estimated. The Knudsen radius is defined as the effective pore radius used to define the Knudsen number and the Knudsen diffusivity. By geometrical considerations, the average radius of a pore can be estimated from the lateral area and volume of a pore as:

$$r = 2\frac{Volume}{a_{Lateral}} \tag{2.64}$$

and using the PSD model, the average Knudsen radius can be estimated from:

$$r_{Kn}(r) = 2\frac{V(r)}{a_{wall}(r)} = 2\frac{\frac{1}{V_T}\frac{dV(r)}{dr}}{\frac{1}{V_T}\frac{da_{wall}(r)}{dr}} \tag{2.65}$$

By integrating over the whole range of pore sizes, the average Knudsen radius can be found as:

$$r_{Kn} = 2\frac{\int_{r_{crit}}^{\infty} \frac{1}{V_T}\frac{dV_{HI}(r)}{dr}dr + \int_0^{r_{crit}} \frac{1}{V_T}\frac{dV_{HO}(r)}{dr}dr}{\int_{r_{crit}}^{\infty} \frac{1}{V_T}\frac{da_{wall,HI}(r)}{dr}dr + \int_0^{r_{crit}} \frac{1}{V_T}\frac{da_{wall,HO}(r)}{dr}dr} \tag{2.66}$$

Note that the numerator of Equation (2.66) is similar to the equation for total saturation presented in Equation 2.17, but the integration limits for hydrophilic and hydrophobic pores are switched. The reason for this is that Knudsen diffusivity is related to transport of gases; if the pores are filled with liquid water then gas transport cannot take place. Gas transport takes place only is the pores are not filled with the wetting phase, and thus instead of looking at how many pores are filled one must look at how many pores are empty. A similar analogy can be made from the similarity between the denominator of Equation (2.66) and the final expression used to estimate the wetted pore wall surface area, i.e. Equation (2.63).

Thus, a final expression to estimate the average Knudsen radius of porous sample based on the proposed PSD model can be presented as:

$$r_{Kn} = \frac{C_1 + C_2}{C_3 + C_4} \tag{2.67}$$

where,

$$C_1 = F_{HI} \sum_k \frac{f_{HI,r,k}}{2} \left[1 - \text{erf} \left(\frac{\ln(r_{c,HI}) - \ln(r_{HI,k})}{s_{HI,k}\sqrt{2}} \right) \right] \tag{2.68}$$

$$C_2 = F_{HO} \sum_k \frac{f_{HO,k}}{2} \left[1 + \text{erf} \left(\frac{\ln(r_{c,HO}) - \ln(r_{HO,k})}{s_{HO,k}\sqrt{2}} \right) \right] \tag{2.69}$$

$$C_3 = \sum_k \frac{F_{HI}\, f_{k,HI}}{r_{k,HI}} \exp \left(\frac{s_{k,HI}^2}{2} \right) \left[1 - \text{erf} \left(\frac{\ln(r_{c,HI}) - \ln(r_{k,HI})}{s_{k,HI}\sqrt{2}} + \frac{s_{k,HI}}{\sqrt{2}} \right) \right] \tag{2.70}$$

$$C_4 = \sum_k \frac{F_{HO}\, f_{k,HO}}{r_{k,HO}} \exp \left(\frac{s_{k,HO}^2}{2} \right) \left[1 + \text{erf} \left(\frac{\ln(r_{c,HO}) - \ln(r_{k,HO})}{s_{k,HO}\sqrt{2}} + \frac{s_{k,HO}}{\sqrt{2}} \right) \right] \tag{2.71}$$

2.4.8 Diffusivity

The smallest pores of conventional catalyst layers and MPLs are in the range of 10 to 100 nm. At atmospheric pressure, the Knudsen number in this pore range is of the order of 1.0 to 10, indicating that the gas flow is in the molecular-Knudsen transition regime [10, 79]. In this regime, both binary and Knudsen diffusion must be taken into account.

The binary diffusion coefficient of species i into species j is obtained using Equation (2.72) [80].

$$D_{ij} = \frac{3}{16\, n\, \sigma_{ij}^2 \Omega_{ij}} \left[\frac{2\, R_g\, T}{\pi} \left(\frac{1}{M_i} + \frac{1}{M_j} \right) \right]^{1/2} \tag{2.72}$$

where n is the number density of the molecules, σ_{ij} is the collision diameter of the two molecules, R_g is the universal gas constant, T is the absolute temperature, and Ω_{ij} is the collision integral (a factor that depends on the intermolecular forces between the molecules, and is of order unity). The collision diameter is given as

$$\sigma_{ij} = \frac{\sigma_j + \sigma_i}{2} \tag{2.73}$$

where σ_i and σ_j are the molecular diameters of the two interacting species. The collision integral can be approximated using an expression of the form:

$$\Omega_{ij} = \frac{1.06036}{\overline{T}^{0.1561}} + \frac{0.193}{e^{0.47635\overline{T}}} + \frac{1.03587}{e^{1.52996\overline{T}}} + \frac{1.76474}{e^{3.89411\overline{T}}} \tag{2.74}$$

$$\overline{T} = \frac{T\,k_B}{\sqrt{\epsilon_i \epsilon_j}} \tag{2.75}$$

where $\overline{T}$ is a dimensionless temperature, k_B is the Boltzmann constant ($k_B = 1.38065 \times 10^{-23}\ J/K$) and ϵ_i is the molecular characteristic energy of component i.

The Knudsen diffusion coefficient of species i is found from Equation (2.76) [80].

$$D_i^K = \frac{2\,r_{Kn}}{3}\sqrt{\frac{8\,R_g\,T}{\pi\,M_i}} \tag{2.76}$$

where r_{Kn} is the average Knudsen pore radius (estimated from the PSD model), M_i is the molar mass of species i, .

In order to combine the effects of binary and Knudsen diffusivity and obtain an absolute diffusion coefficient, the Bosanquet equation is used [81],

$$D_i^{abs} = \left[\frac{1}{D_{ij}} + \frac{1}{D_i^K}\right]^{-1} \tag{2.77}$$

To obtain the effective diffusion coefficients, the most common approach is to use the Bruggeman approximation [82], where the effective diffusivity is calculated as:

$$D_i^{abs,eff} = D_i^{abs}\left[\varepsilon\,(1-S)\right] \tag{2.78}$$

where ε is the layer porosity and S is the layer saturation.

2.5 Results and Discussions

2.5.1 PSD for GDLs

To obtain the global PSD corresponding to a GDL, a sample of SGL Sigracet 34BA carbon paper GDL was tested using mercury intrusion porosimetry as described in Section 2.3. The expressions presented in Section 2.4 are used to estimate the effective transport properties. The basic raw data from MIP for the SGL Sigracet 34BA carbon paper GDL is presented in Figure 2.14.

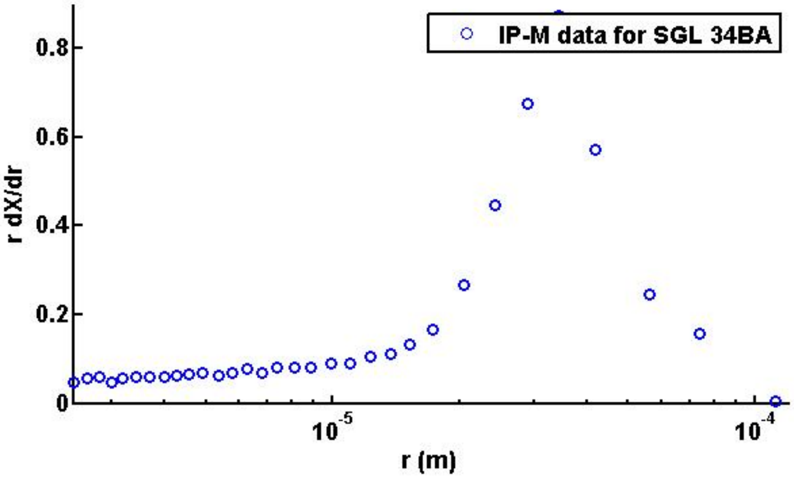

Figure 2.14 – Data points for MIP corresponding to the SGL Sigracet 34BA carbon paper GDL.

Using the least-squares optimization algorithm described in Section 2.3, the MIP experimental data points were fitted to the PSD model. Figure 2.15 illustrates the fit on top of the experimental data points corresponding to the global PSD for a GDL. For the GDL PSD, pore sizes smaller than 1 μm were neglected.

2.5.2 PSD for MPLs and Conventional Catalyst Layers

The PSD for an MPL is obtained by comparing the PSDs for SGL Sigracet 34BA and 34BC samples. As previously described, the SGL Sigracet 34BC is a carbon paper GDL coated with an MPL on one side (GDL-MPL composite layer). In order to obtain the PSD for the MPL only, the PSD corresponding to the GDL-MPL composite layer can be obtained, and then the PSD of the GDL portion can be subtracted, leaving the PSD corresponding to the MPL only.

The experimental MIP data for the SGL Sigracet 34BC GDL-MPL composite layer is presented in Figure 2.16. The distribution corresponding to the MPL can be clearly observed for pore sizes in the range of $10 - 100\,nm$.

Since the raw data from intrusion porosimetry is a set of discrete points, the PSDs from the SGL Sigracet 34BA and 34BC cannot be directly subtracted as discrete points will not be on the same location for the samples.

After subtracting the PSD of the SGL Sigracet 34BA from the PSD of the SGL Sigracet 34BC and fitting the points to the PSD model, the PSD for an MPL is presented in Figure 2.17, and Table 2.2 presents the list of fitting parameters used to define it.

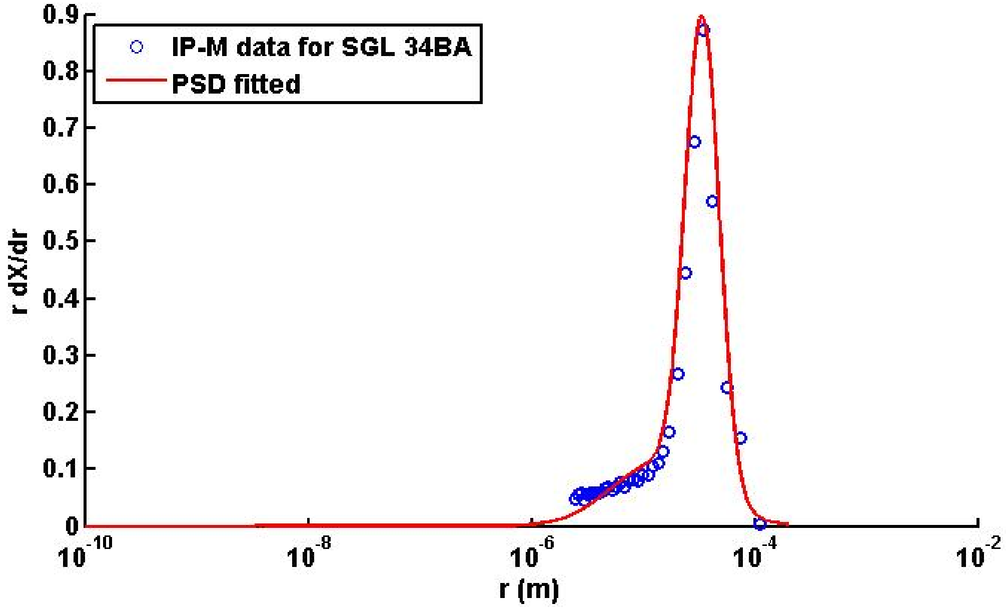

Figure 2.15 – Data points for MIP corresponding to the SGL Sigracet 34BA carbon paper GDL, and fitted PSD.

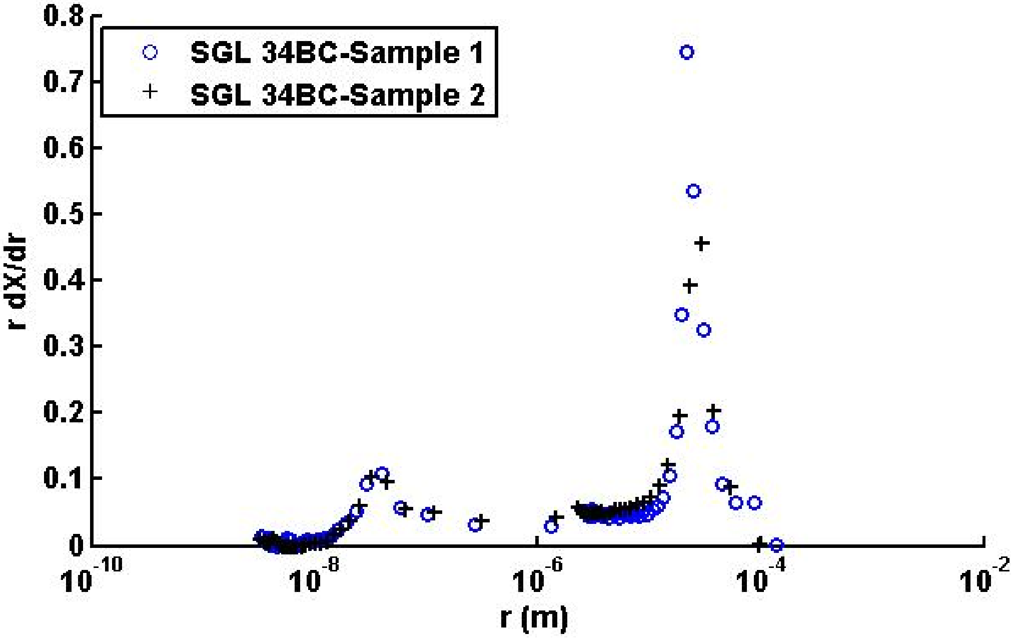

Figure 2.16 – Data points for MIP corresponding to the SGL Sigracet 34BA carbon paper GDL.

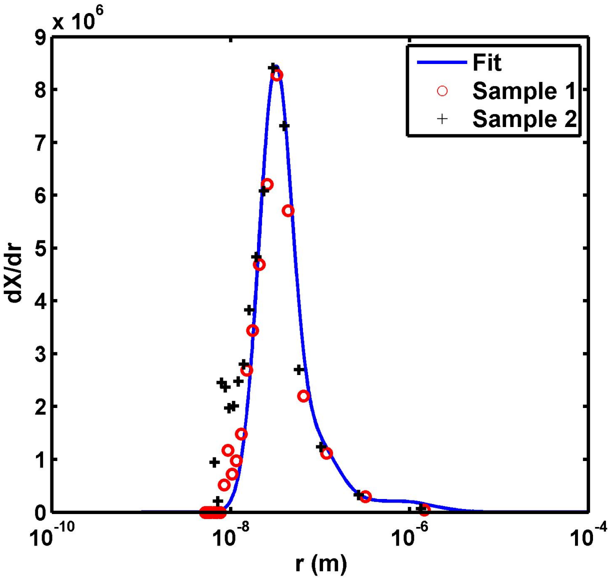

Figure 2.17 – Diagram showing experimental data points corresponding to two different samples used to define PSD for typical MPL, with fitted log-normal distribution.

Table 2.2 – Fitting parameters to define PSD for typical MPL, obtained from IP analysis of SGL Sigracet 34BA and 34BC.

Mode Number (k)	f_k	r_k $[nm]$	s_k
1	0.31	38.2	0.43
2	0.18	125	0.55
3	0.1	500	0.65
4	0.05	1200	0.45
5	0.36	2000	0.75

One downside of this technique is that if the MPL has cracks, there is no way to separate them from the post-processed results. MPL cracks will show up as a pore size distribution, which may lead to overestimation of MPL transport properties.

Only the global PSD is measured with MIP. In order to study the effects of mixed wettability of the MPL, several artificial PSD configurations are tested. The different configurations are given in Table 2.3. The different PSD configurations will allow us to determine the optimal distribution of HI and HO pores in the MPL.

Specific wettabilities are created by assigning PSD modes to HI pores and, if a partial PSD is needed, one PSD mode into two, keeping the PSD spread s_k and the radius r_k at which the mode is centred the same, as initially discussed in Section 2.2. The notation of small pores and large pores indicates that the PSD is taken from

Table 2.3 – PSD functions for the MPL configurations tested in this study.

MPL number	Percent HI pores	Percent HO pores
1	0	100
2	10 (small pores)	90 (large pores)
3	20 (small pores)	80 (large pores)
4	30 (small pores)	70 (large pores)
5	40 (small pores)	60 (large pores)
6	50 (small pores)	50 (large pores)
7	10 (large pores)	90 (small pores)
8	20 (large pores)	80 (small pores)
9	30 (large pores)	70 (small pores)
10	40 (large pores)	60 (small pores)
11	50 (large pores)	50 (small pores)

Table 2.4 – Parameters to define PSD for MPL 2.

HI Mode Number (k)	f_k	r_k $[nm]$	s_k
1	0.1	38.2	0.43

HO Mode Number (k)	f_k	r_k $[nm]$	s_k
1	0.21	38.2	0.43
2	0.18	125	0.55
3	0.1	500	0.65
4	0.05	1200	0.45
5	0.36	2000	0.75

the the smallest r_k to the largest r_k. For example, an MPL with 10 percent small hydrophilic pores mean that starting from zero, pore sizes corresponding to one or more modes with the smallest r_k are taken as hydrophilic until exactly 10% of the total pore volume corresponds to hydrophilic pores. For reference, Table 2.4 presents the PSD used to define an MPL with 10% of the pore volume corresponds to small hydrophilic pores.

2.5.3 Validation of Effective Properties Estimated with Previous PSD Models

In this section, results obtained from the PSD-based model are compared to the PSD model previously developed by Weber [3, 21]. The PSD functions for GDL and

Table 2.5 – Fitting parameters to define PSD for catalyst layer used for validation of saturation.

Mode Number (k)	f_k	r_k [μm]	s_k
1	0.5	0.2	1.2
2	0.5	0.05	0.5

Table 2.6 – Fitting parameters to define PSD for GDL used for validation of saturation.

Mode Number (k)	f_k	r_k [μm]	s_k
1	1	6	0.5

catalyst layer proposed by Weber are implemented in our model, and the results are compared.

Saturation

The selected PSDs used to perform this validation study correspond to a conventional catalyst layer and a GDL used by Weber [3]. The PSD for the catalyst layer is presented in Table 2.5. The hydrophilic and hydrophobic contact angles are assumed to be 80 and 100°, respectively. 30% of the pore volume is assumed to correspond to hydrophilic pores.

The PSD for the GDL is presented in Table 2.6. For this layer, the hydrophilic and hydrophobic contact angles are assumed to be 45 and 110°, respectively. The porosity is reported to be 0.6, and 60% of the pores are assumed to be hydrophilic, as selected by Weber [3].

Figure 2.18 presents the saturation profile of the catalyst layer against capillary pressure from the original source [3] and from the implementation of the PSD model in this thesis. The two profiles agree very well, revealing that the implemented PSD model matches the original formulation to estimate saturation for the catalyst layer.

Figure 2.19 presents the saturation profile of the GDL layer against capillary pressure. For small capillary pressures the profiles agree very well. However, the predicted saturation for large capillary pressures is slightly lower when compared to the values reported.

The PSD model proposed by Weber [3, 21] accounts for residual saturation inside the layers. On his formulation, the residual liquid saturation is defined as:

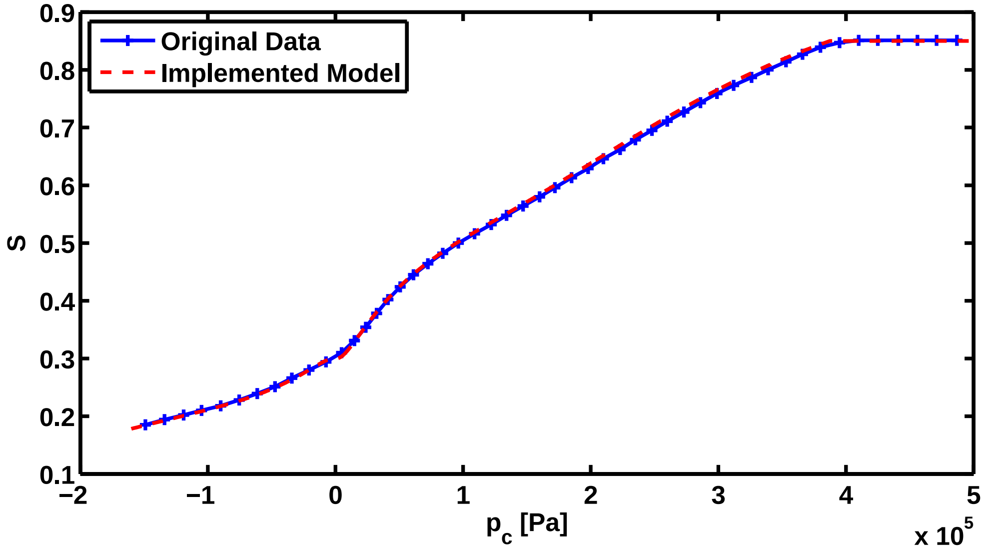

Figure 2.18 – Saturation versus capillary pressure profiles for CL reported by Weber, compared with the implemented Weber's PSD model [3].

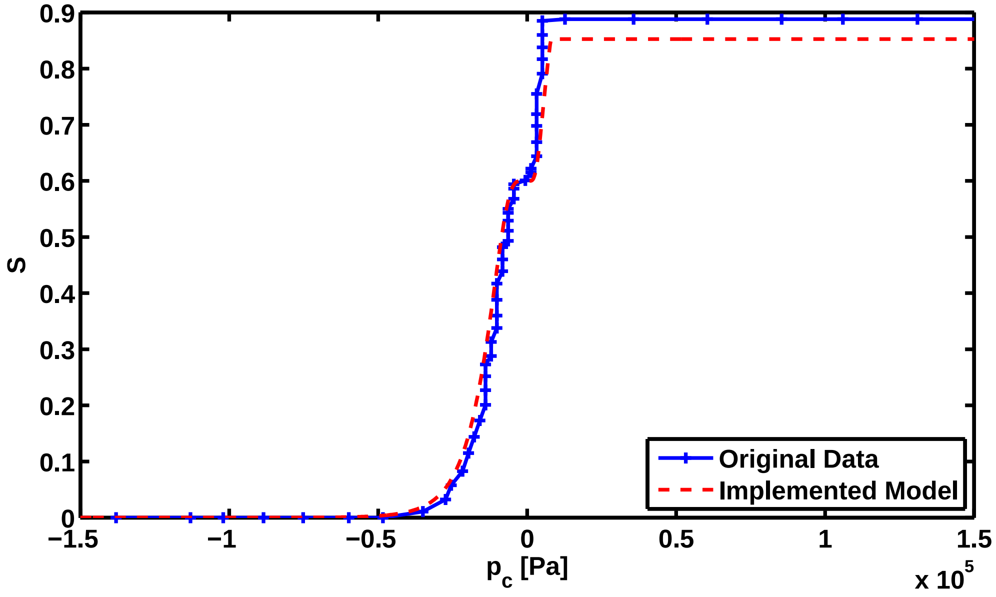

Figure 2.19 – Saturation versus capillary pressure profiles for GDL reported by Weber, compared with the implemented Weber's PSD model [3].

$$S_o = -5.3202\varepsilon^5 + 17.062\varepsilon^4 - 21.706\varepsilon^3 + 13.692\varepsilon^2 - 4.816\varepsilon + 0.9989 \tag{2.79}$$

where ε is the porosity of the layer. Using this value, the saturation of the layers is corrected as:

$$Saturation = S \qquad (S \leq S_g) \tag{2.80}$$

$$Saturation = S_g \qquad (S > S_g) \tag{2.81}$$

where S_g is the gas residual saturation, defined as:

$$S_g = 1 - S_o \qquad (S_o \leq 0.15) \tag{2.82}$$

$$S_g = 0.85 \qquad (S_o > 0.15) \tag{2.83}$$

For a porosity value of 0.3 corresponding to the catalyst layer, the residual liquid saturation is 0.3256. From the previous expressions, the residual gas saturation will be 0.85, which will set the limit for the maximum layer saturation.

For the GDL, the residual liquid saturation predicted is 0.14, which means that the residual gas saturation must be 0.86. However, the data provided by Weber indicates that the residual gas saturation for the GDL must be 0.89.

2.5.4 Validation with Experimental Data

Prior to using the PSD model to formulate GDL, MPL and CCL models that take into account individual wettability and microstructure, it is important to know how accurate are the measured PSDs, and how accurate are the estimated effective properties of the layers. Thus, validation data for some of the effective properties estimated is presented. Experimental data for MPL and CL is scarce, therefore the majority of the validation will be performed for the GDL case. The GDL PSD parameters are given in Table 2.1.

Pore-Size Distribution for GDLs

In order to validate the PSD obtained from the Sigracet SGL 34BA in this study, PSD obtained from other researchers for common GDLs was used [5, 6, 46, 83–85]. Note that, unfortunately, PSD data for the GDL we have is unavailable in the literature.

Figure 2.16 shows that the pore sizes of the SGL 34BA GDL are centred around a radius of 35 μm. The mean mode location, minimum pore size, and maximum pore

Table 2.7 – Summary of PSD functions for GDLs, presenting the main mode center, and approximation for minimum and maximum pore sizes.

Main mode	Min. Pore	Max. Pore	GDL Type	Ref.
$20\mu m$	$1\mu m$	$100\mu m$	Toray TGP-H-060	[5]
$100\mu m$	$1\mu m$	$220\mu m$	Carbon cloth, E-Tek	[5]
$100\mu m$	$10\mu m$	$200\mu m$	Composite GDL-MPL	[85]
$13\mu m$	$1\mu m$	$100\mu m$	Toray TGP-H-090	[84]
$15\mu m$	$1\mu m$	$200\mu m$	Toray TGP-H-090	[83]
$34\mu m$	N/A	$90\mu m$	Toray TGP-H-060	[6]
$35\mu m$	N/A	$100\mu m$	SGL 34BA	This study

size for typical GDLs are presented in Table 2.7. The pore sizes obtained from MIP for GDLs are within the same range for all GDLs considered.

Note the slight differences between the reported PSD values from different researchers. While Cheung et al. [84] and Fairweather et al. [83] report maximum pore sizes of 100-200 μm for the Toray-090 GDL, Gostick et al. [86] reports values of 20 microns. With pores centred between 30 and 40 μm and a maximum pore size of just over 100 μm, the PSD obtained for the SGL Sigracet 34BA GDL agrees very well with the data presented by Koido et al. [6] and Luo et al. [5].

Saturation Profiles for GDLs

Saturation versus capillary pressure profiles for GDL reported by Shi et al. [87] and Gostick et al. [88] are compared to the estimated profiles from the proposed PSD model, assuming that 30% of the pore volume corresponds to hydrophilic pores, and these are among the smallest pores of the GDL. The assumption regarding the amount of HI pores is based on the information documented by Martínez et al. [9] where hydrophilic pores for GDLs are usually the smallest pores. The reason for choosing a hydrophilic volume fraction of 30% is to match the experimental data presented by Shi et al. [87], where the saturation level is around 0.3 when the capillary pressure is zero.

The results for the comparison are shown in Figure 2.20. Gostick [88] obtained an empirical expression to obtain saturation versus capillary pressure profiles for different Toray and SGL Sigracet GDLs. However, negative capillary pressures are

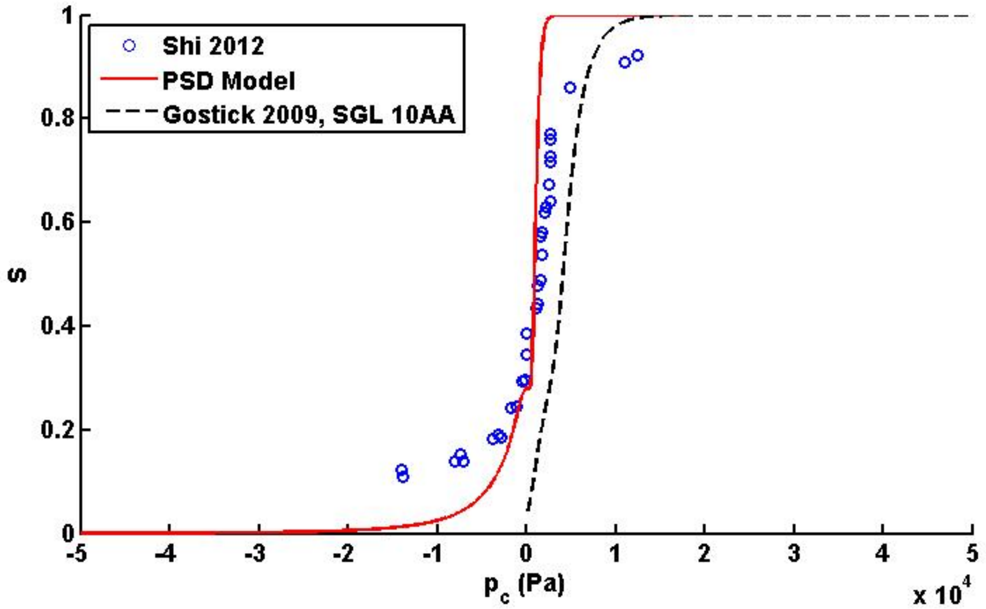

Figure 2.20 – Saturation versus capillary pressure profiles for different GDLs reported. Data of Shi et al obtained for Toray TGP 090, original source Fairweather et al. [4].

not considered by the empirical expressions.

Figure 2.20 shows that the results obtained from the PSD with 30% small hydrophilic pores in Table 2.1 agrees with experimental data. The values agree reasonably well considering that the PSD used for the model is not for the same GDL used for the experimental study. Full agreement was not expected, but different GDL samples must have similar behaviour.

Due to the large pores of the GDL, the saturation increases sharply for small capillary pressures. This is reproduced well by the model. The non-zero experimental saturation values for negative capillary pressures presented by Shi et al. [87] could be achieved by changing the PSD and contact angles of the hydrophilic and hydrophobic pores. Adding larger hydrophilic pores, for instance, will make the saturation profiles for negative capillary pressures from the proposed mixed wettability PSD model similar to the profile measured by Shi et al. [87]. Therefore, the proposed PSD model can be effectively used to estimate saturation for GDLs.

Saturated Permeability of GDLs

Using Equation (2.29), the permeability for the SGL Sigracet 34BA GDL was estimated and compared with reported values. By using a value of $\lambda = 2.26$, the estimated permeability agrees reasonably well with other reported data, as can be

Table 2.8 – Permeability values reported for GDLs, $\lambda = 2.26$.

Value, m^2	GDL type	Reference
9×10^{-12} (in-plane/thru-plane)	SGL 34BA	This work
8×10^{-12} (in-plane)	Avcarb P75T	[4]
9×10^{-12} (in-plane)	Toray 060	[6]
9×10^{-12} (in-plane)	Toray 060	[5]
6.5×10^{-12} (thru-plane)	Toray 060	[5]
2.74×10^{-11} (thru-plane)	SGL 34BA	[89]
1.54×10^{-11} (thru-plane)	SGL 34BA	[10]
1.10×10^{-11} (thru-plane)	Toray 090	[10]

seen from Table 2.8.

Carrigy et al. [10] reported the permeability values for the SGL Sigracet 34BA GDL to be 1.54×10^{-11} m^2. If the value of λ is set to 1.325, the proposed PSD model is able to reproduce this value.

Saturated Permeability of MPLs

From the SGL Sigracet 34BA GDL and 34BC GDM, the permeability of the MPL was also estimated. However, when matching the MPL permeability value with the measurements reported by Pant et al. for the same GDM [89], the required λ was smaller than one. The estimated value from the PSD model, neglecting the effects of λ was 1.34×10^{-14} m^2, while the measured value from Pant et al. was 1.39×10^{-13} m^2. Using this information, the model requires $\lambda = 9.64 \times 10^{-2}$ in order to match the experimental values. The estimated MPL permeability is one order of magnitude smaller than the measured value.

Having a λ value smaller than unity means that by assuming the porous media is an array of straight cylindrical pores for a given pore volume, the inter-connectivity of the cylindrical pores is larger than the inter-connectivity of the original porous sample, which is unrealistic.

SEM images of the SGL Sigracet 34BC composite layer presented in Figure 2.21a reveals that the MPLs have cracks after they are coated on top of the GDL, while Figure2.21b reveals that coated MPLs can penetrate on the GDL. The under-prediction of the permeability by the PSD model compared to measured MPL permeability values may be due to cracks and/or larger pores, which are not accounted for in the PSD model since they cannot be differentiated from the MPL. Therefore, in this study $\lambda = 1$ is used.

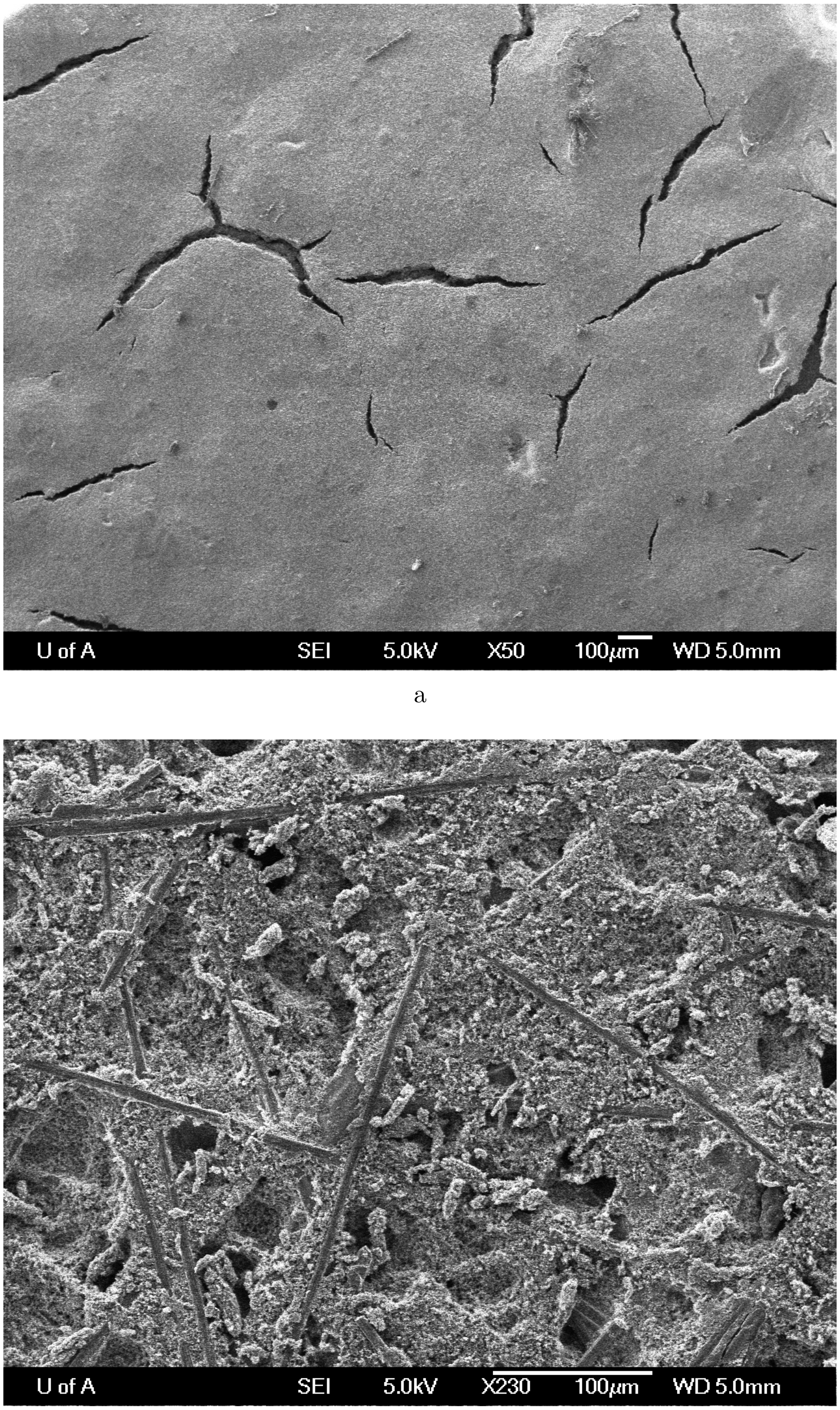

Figure 2.21 – a) MPL side corresponding to SGL Sigracet 34BC. b) MPL coated on Toray 060 with 20% PTFE.

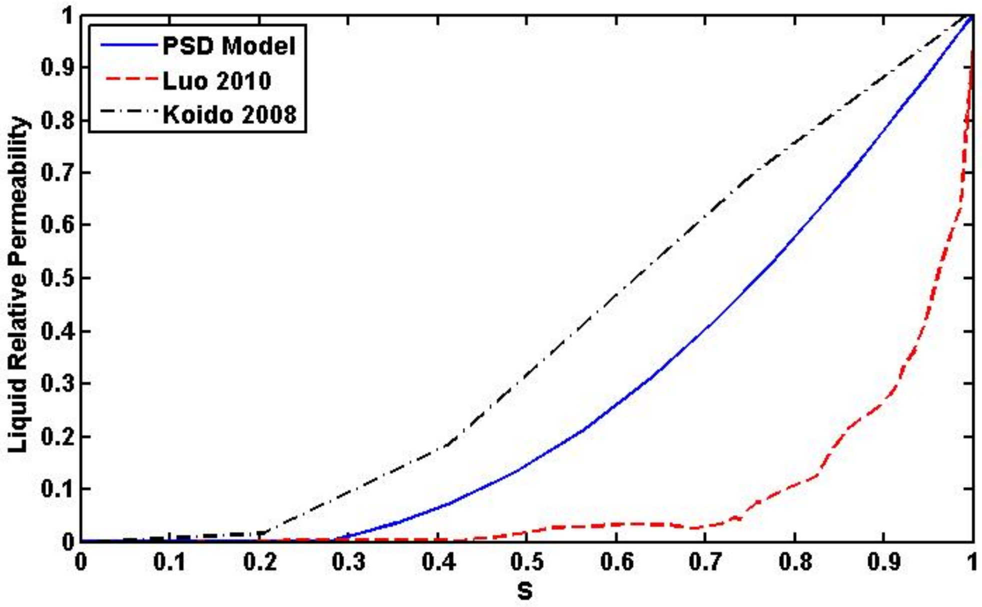

Figure 2.22 – Validation of liquid relative permeability for GDLs with experimental data from Lou et al. [5] (Toray 060 GDL) and Koido et al. [6] (Toray 060 GDL).

Relative Permeabilities for GDLs

The predicted relative permeability of the SGL Sigracet 34BA carbon felt GDL was compared to experimental relative permeabilities. Data from Lou et al. [5], and Koido et al. [6], both for the Toray 060 carbon paper GDL, was used. Figure 2.22 and Figure 2.23 show the liquid relative permeability and gas relative permeability, respectively. Figure 2.23 shows that the proposed PSD model tends to over-predict the gas relative permeability, while the liquid relative permeability fall in between the reported values. One explanation for this is that the morphologies of SGL Sigracet GDLs and Toray GDLs is different, and thus effective properties may deviate for both GDL types.

Diffusivity for GDLs

Recently, Pant et al. [89] reported values for effective oxygen diffusivity under dry conditions. This information can be used to validate effective diffusivity coefficients. Since the effective diffusivity is related to the average Knudsen radius obtained, a general idea of how reasonable the estimated average Knudsen radius is, as well as the way in which the effective diffusivity is computed.

For GDLs, the relative small velocities and pore sizes indicate that Knudsen effects

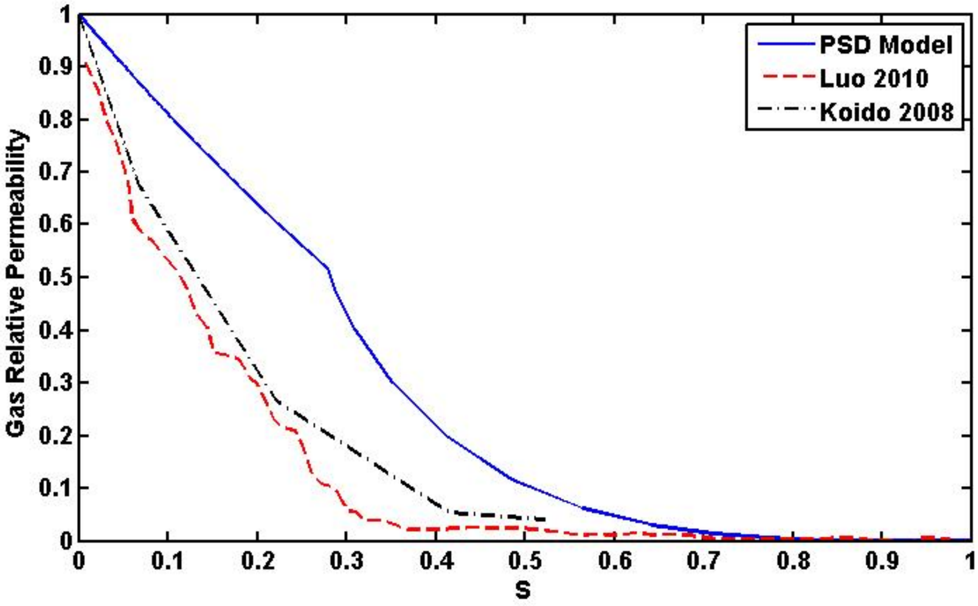

Figure 2.23 – Validation of gas relative permeability for GDLs with experimental data from Lou et al. [5] (Toray 060 GDL) and Koido et al. [6] (Toray 060 GDL).

are unimportant, and binary diffusion is the dominant diffusion transport mode. For MPLs pore sizes are smaller than for GDLs, and both binary and Knudsen effects are important and must be taken into account.

For MPLs, the measured oxygen Knudsen diffusivity for an MPL was $3.3 \times 10^{-5}\ m^2 s^{-1}$ for unsaturated conditions. Using the estimated average Knudsen radius, the Knudsen diffusivity estimated from the proposed PSD model was $5.76 \times 10^{-5}\ m^2 s^{-1}$, and the combined effect of binary and Knudsen oxygen diffusion for MPLs was estimated to be $1.9 \times 10^{-5}\ m^2 s^{-1}$. The value reported by Pant et al. [89] for MPLs is $3.3 \times 10^{-5}\ m^2 s^{-1}$. All values are within the same range, which reveals that the proposed PSD model can be used to obtain reasonable estimates of Knudsen diffusivity for GDMs.

Measurements of the effective diffusivity of species through MPLs and GDLs in terms of saturation level are very cumbersome. Therefore, effective diffusivity values at different saturation values have not yet been reported in the literature.

2.5.5 Impact of Mixed Wettability Pore-Size Distribution on Effective Properties for MPLs and CCLs

In this section, the effects of mixed wettability for an MPL, which PSD was obtained from MIP on the SGL Sigracet 34BA and 34BC GDM, are studied.

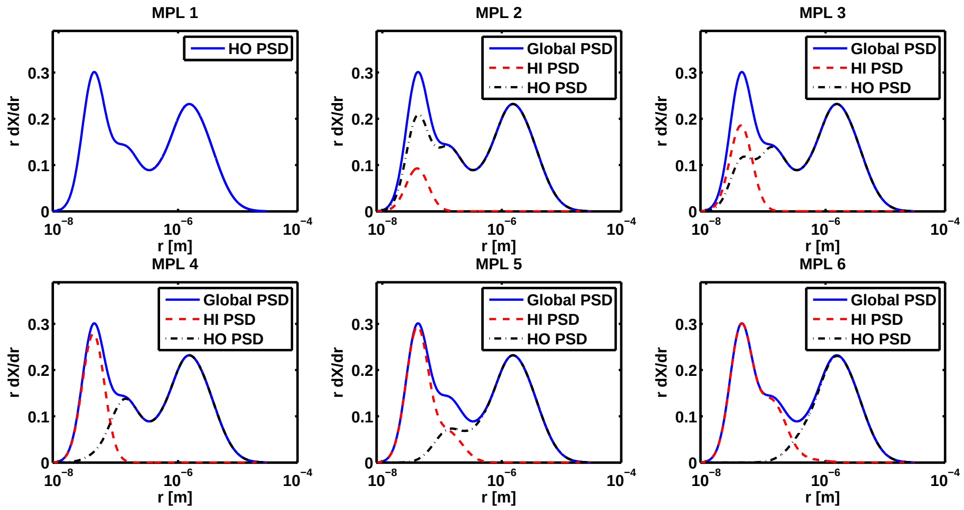

Figure 2.24 – Diagram showing global PSD and PSD of all the tested MPL configurations, multiplied by the pore radius, corresponding to the small hydrophilic pores.

The PSD functions for the MPL configurations that will be studied are shown in Figure 2.24 and Figure 2.25. Figure 2.24 shows the cases for MPLs with small hydrophilic pores. Figure 2.25 shows the cases for MPLs with large hydrophilic pores. Note that the global PSD function remains the same, but the fractions of hydrophilic and hydrophobic pores change.

Effects of Hydrophilic and Hydrophobic Pore Volume Fractions

In this section, the effects of the MPL hydrophilic and hydrophobic volume fractions on effective properties are studied. For the parametric studies, the hydrophilic contact angle is assumed to be 80°and the hydrophobic contact angle is assumed to be 100°. In the following subsections further studies will also analyse the effect of contact angle.

Figure 2.26 shows the saturation profiles plotted against capillary pressure for each of the MPL configurations in Figure 2.24. Figure 2.27 presents the saturation profiles for the MPL configurations in Figure 2.25. Figure 2.26 shows that the saturation level for MPL 1 remain zero for negative capillary pressure values. For the next five configurations, MPL 2 to MPL 6, non-zero saturations are observed for negative capillary pressures due to the existence of hydrophilic pores. Also, as the fraction of hydrophilic pores increases the saturation at zero capillary pressure increases accordingly, because all hydrophilic pores will be filled for a zero capillary pressure.

As the volume fraction of small hydrophilic pores increases, the hydrophobic pores

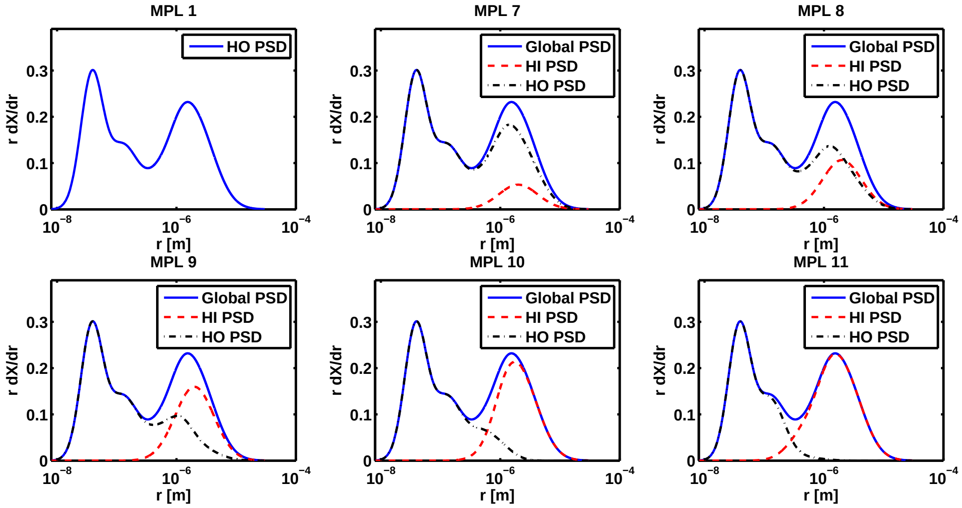

Figure 2.25 – Diagram showing global PSD and PSD of all the tested MPL configurations, multiplied by the pore radius to better see differences, corresponding to the large hydrophilic pores.

become larger on average, which causes the saturation profiles for positive capillary pressure to approach a value of one with lower capillary pressures. Therefore, MPLs with large volume fractions of small hydrophilic pores will flood at lower capillary pressures than MPLs with fractions of large hydrophilic pores.

Several researchers used the concept of residual liquid saturation to account for water retention until very large negative capillary pressures [3, 21]. It can be seen from the proposed mixed wettability PSD model that the same behaviour can be observed as it is assumed that the porous material has a network of small hydrophilic pores.

Figure 2.27 shows that when the hydrophilic pores are on average much larger than the hydrophobic pores, saturation profiles are not as severely affected by pore volume fractions. Since the hydrophobic pores are smaller on average, saturation profiles for positive capillary pressures are very similar for each of the tested MPL configurations. Also, due to the large size of hydrophilic pores, saturation profiles for negative capillary pressure remain near zero until a pressure of around -1×10^{-5} Pa, when pores start to fill.

The liquid relative permeability for the tested MPLs plotted against capillary pressure are presented in Figures 2.28 and 2.29. When the MPL is saturated or nearly saturated, liquid transport will benefit the most as the dominant phase. If the MPL contains small hydrophilic pores then for saturations lower than the total fraction of hydrophilic pores liquid transport will not be very effective because liquid

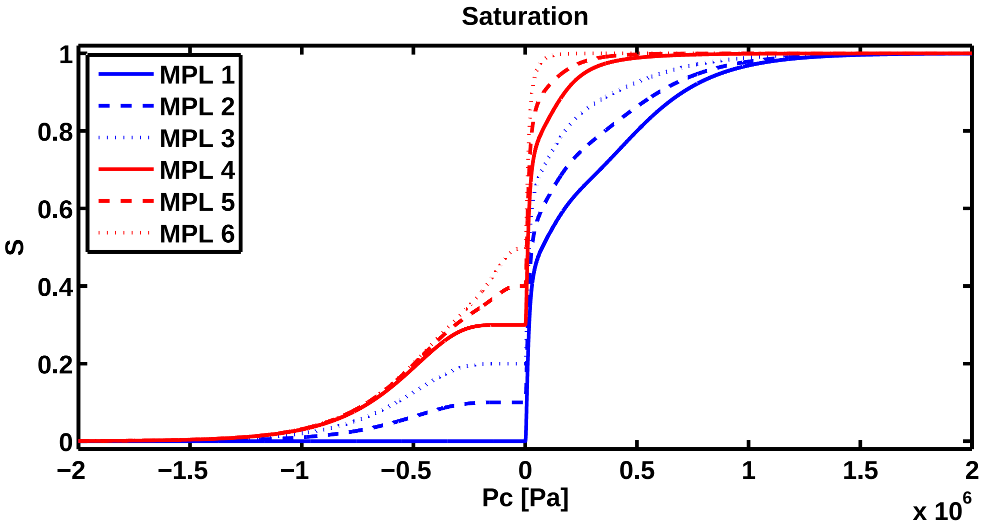

Figure 2.26 – Saturation profiles for tested MPL cases with small hydrophilic pores plotted against capillary pressure.

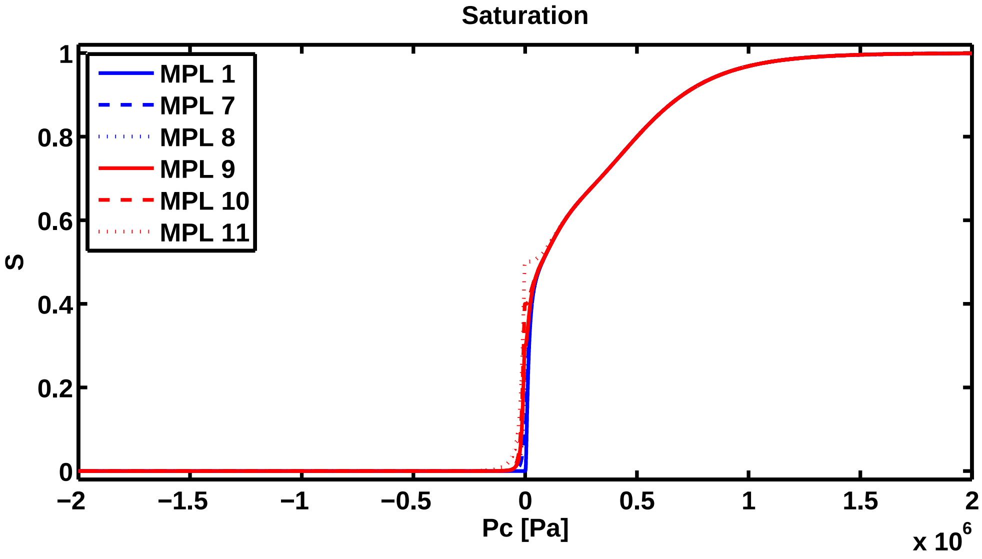

Figure 2.27 – Saturation profiles for tested MPL cases with large hydrophilic pores plotted against capillary pressure.

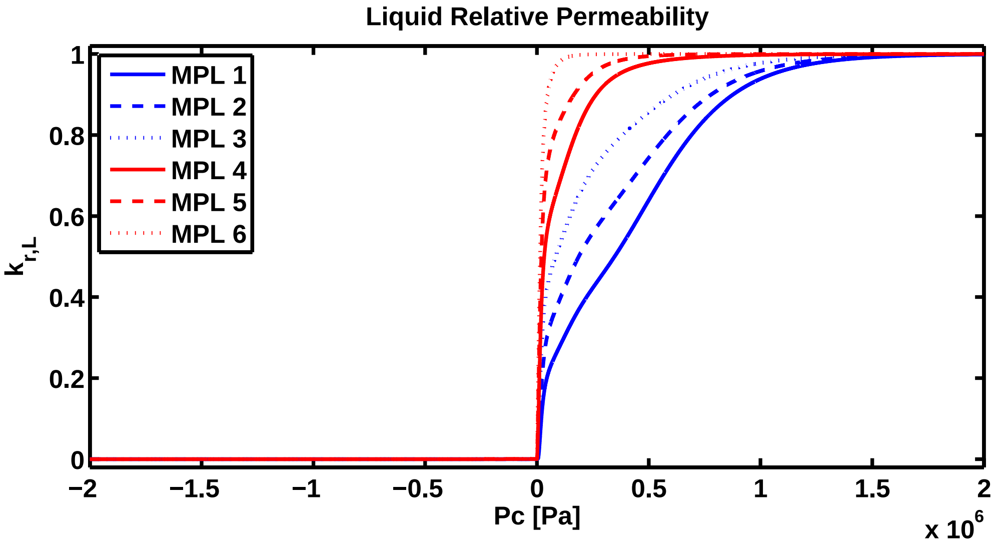

Figure 2.28 – Liquid relative permeability profiles for tested MPL cases with small hydrophilic pores plotted against capillary pressure.

permeability is proportional to pore size, and hydrophilic pore sizes are small for these configurations.

Large fractions of small hydrophilic pores are better for liquid transport in MPLs, as seen from Figure 2.28. If the MPL contains large fractions of small hydrophilic pores, the hydrophobic pores become larger on average. Since the capillary pressure required to force water to enter into large hydrophobic pores is lower than that required if the hydrophobic pores were small, liquid transport benefits from large fractions of small hydrophilic pores.

Figure 2.29 reveals that when the hydrophilic pores are large, liquid permeability profiles do not change drastically for different pore volume fractions since the hydrophilic pores fill only near zero capillary pressure where a sudden increment in liquid relative permeability is observed. Similar effects were found for saturation profiles in Figure 2.27.

The gas relative permeability for the tested MPLs plotted against capillary pressure are presented in Figure 2.30 and Figure 2.31. The gas relative permeability behaves in the opposite way of the liquid relative permeability. For gas transport to be enhanced, pores must be completely unsaturated. Thus, the gas relative permeability has its maximum value when the saturation is zero. That is why, as Figure 2.30 and Figure 2.31 reveal, a completely hydrophobic MPL will have the best gas relative permeability.

As observed from Figure 2.30 and Figure 2.31, even though a fully hydrophobic MPL will have the best gas transport, MPLs with very large fractions of large

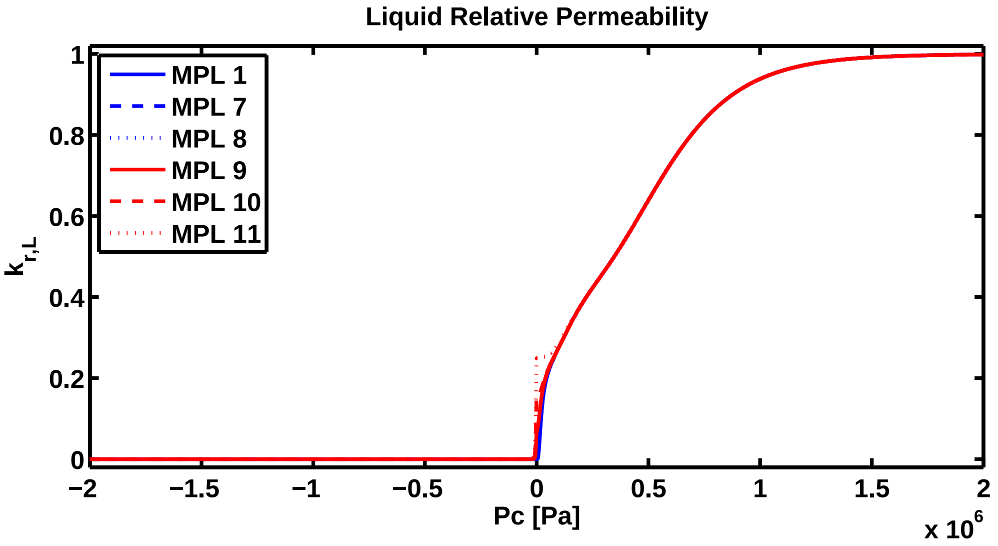

Figure 2.29 – Liquid relative permeability profiles for tested MPL cases with large hydrophilic pores plotted against capillary pressure.

hydrophilic pores and MPLs with small fractions of small hydrophilic pores, tend to have relatively high values of gas relative permeabilities. For MPLs with very large fractions of small hydrophilic pores, the gas relative permeability is reduced at negative capillary pressures.

The average Knudsen radius, which is used to determine the value of the Knudsen diffusivity of MPLs and conventional catalyst layers, for the MPL configurations studied are presented in Figure 2.32 and Figure 2.33, plotted against capillary pressure. For large negative capillary pressures, where the saturation is zero, the Knudsen radius must be the same for all MPL configurations.

Interesting results are revealed once hydrophilic pore volume fractions are studied. Figure 2.32 reveals that if small hydrophilic pores are added to a porous medium, these pores will start to fill at negative capillary pressures as described by the Young-Laplace equation. Since the filling of the hydrophilic pores will begin with the smallest pore sizes, the average Knudsen radius will increase, as only the largest hydrophilic pores will remain empty. At a zero capillary pressure all the hydrophilic pores will be filled, and the filling of the hydrophobic pores will begin. The filling of the hydrophobic pores will start from the largest pores, which means that the average Knudsen radius on the regime of positive capillary pressures will decrease with increasing capillary pressure.

Figure 2.33 reveals that when large hydrophilic pores are added to a porous medium, the Knudsen radius profiles do not change drastically, and remain similar to the profile obtained for the fully hydrophobic MPL configuration.

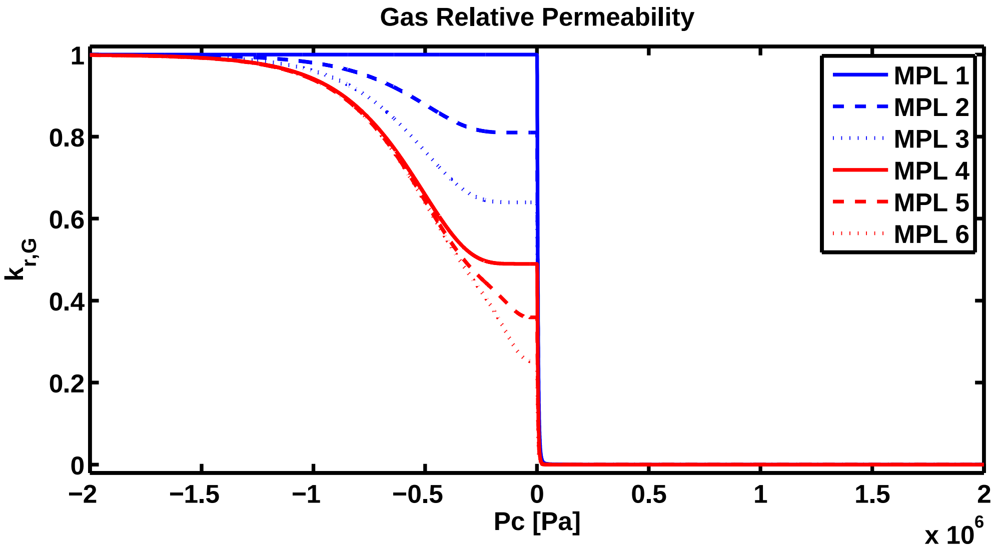

Figure 2.30 – Gas relative permeability profiles for tested MPL cases with small hydrophilic pores plotted against capillary pressure.

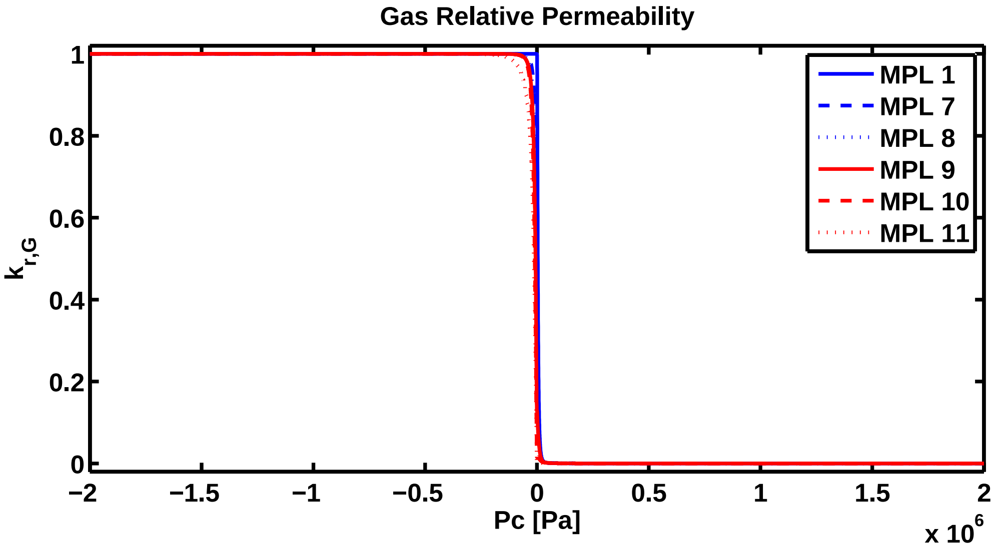

Figure 2.31 – Gas relative permeability profiles for tested MPL cases with large hydrophilic pores plotted against capillary pressure.

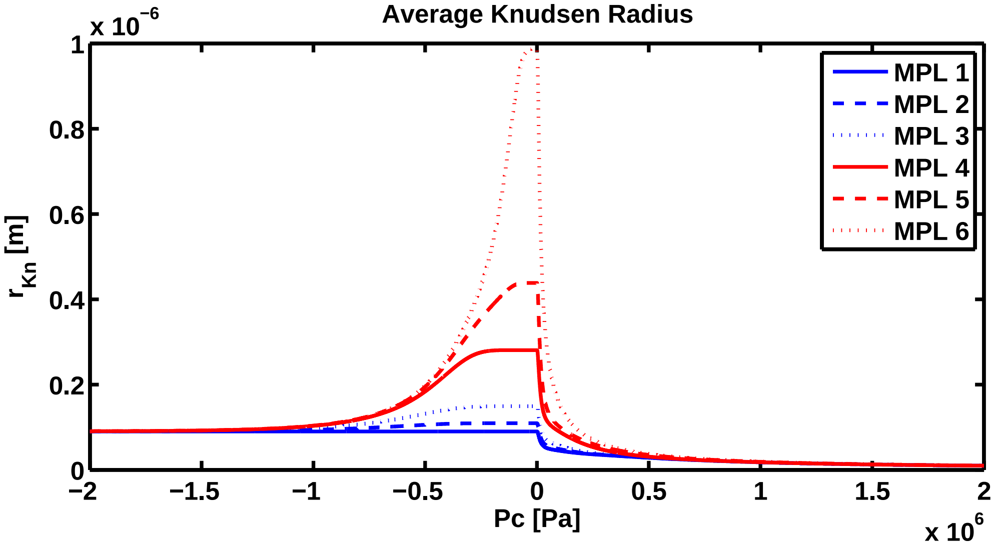

Figure 2.32 – Knudsen radius profiles for tested MPL cases with small hydrophilic pores, plotted against capillary pressure.

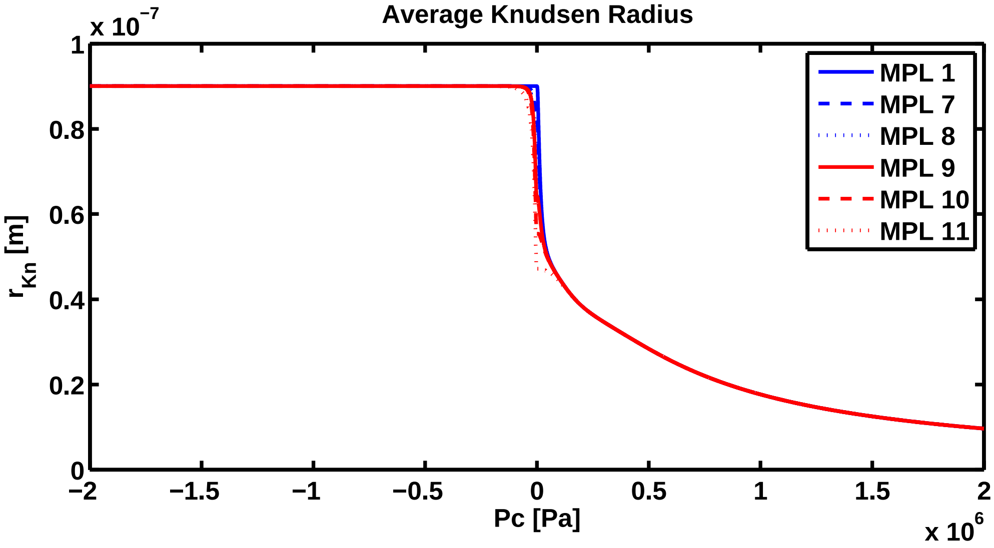

Figure 2.33 – Knudsen radius profiles for tested MPL cases with large hydrophilic pores, plotted against capillary pressure.

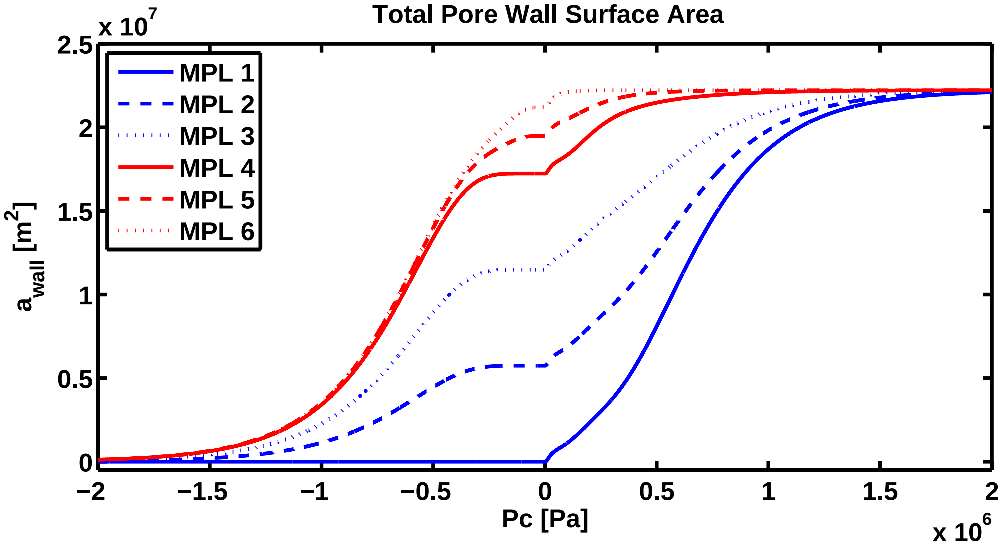

Figure 2.34 – Wetted pore wall surface area profiles for tested MPL cases with small hydrophilic pores, plotted against capillary pressure.

The pore wall surface area profiles, which may be used to define the effective active area of conventional catalyst layers plotted against capillary pressure, are presented in Figure 2.34 and Figure 2.35. When all the pores are saturated, the surface area of the pore walls in contact with liquid water is the same, thus all MPL test cases display the same value for very large capillary pressures. Since the estimated pore surface area is related with the filling of the pores, at a given capillary pressure the value of pore wall surface area benefits from the inclusion of large fractions of small hydrophilic pores, as these will be easy to fill with the liquid phase.

When the hydrophilic pores are large the profiles for the pore wall surface area are very similar. To better appreciate the differences, Figure 2.35 presents the wetted pore wall surface area for MPL configurations 7 through 11, using a smaller range for the capillary pressures used. Also, can be seen that the value of wetted pore wall surface area for a zero capillary pressure increases with an increasing fraction of hydrophilic pores.

The profiles of liquid-gas interfacial surface area per unit volume profiles plotted against capillary pressure and saturation are presented in Figure 2.37 through Figure 2.40. The liquid-gas interfacial surface area per unit volume affect the rate of evaporation inside the MPL. In order to design the MPL and the catalyst layer as evaporative layers, this value must be maximized. For all MPL configuration, the profiles show a maximum value. Additionally, for all MPL configurations the maximum values for the interfacial surface area per unit volume are very similar. Additionally, the profiles go to zero for an unsaturated MPL and a saturated MPL.

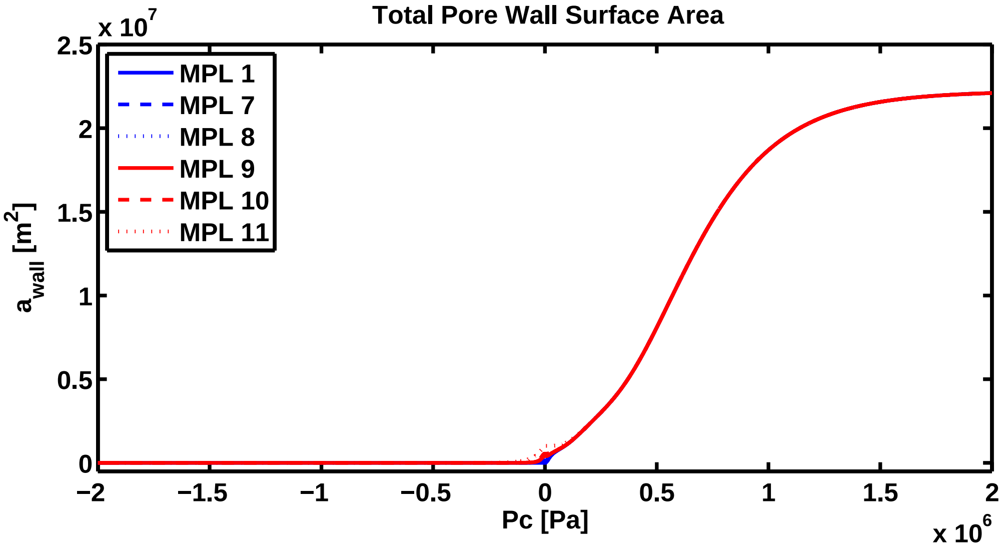

Figure 2.35 – Wetted pore wall surface area profiles for tested MPL cases with large hydrophilic pores, plotted against capillary pressure.

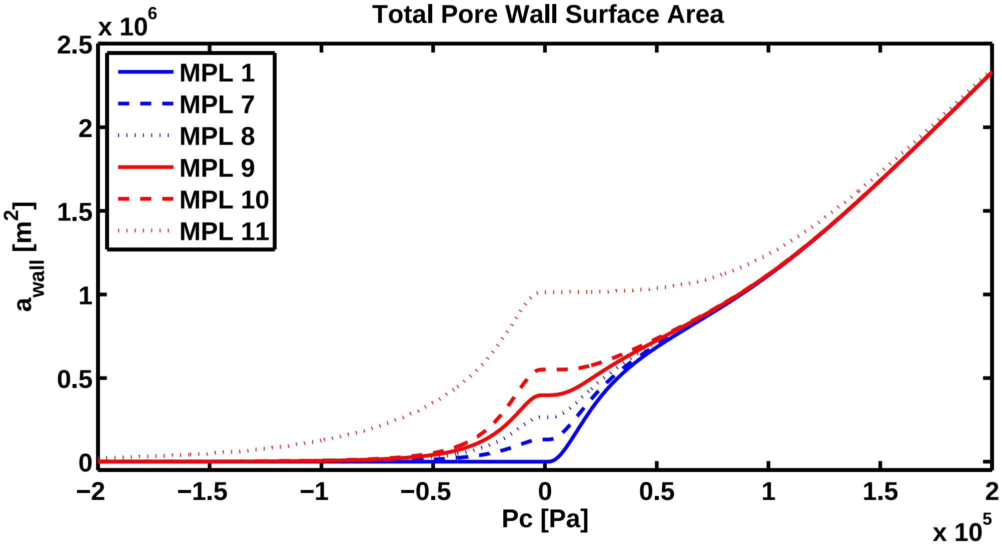

Figure 2.36 – Wetted pore wall surface area profiles for tested MPL cases with large hydrophilic pores, plotted against capillary pressure, using smaller capillary pressure ranges to better appreciate the differences.

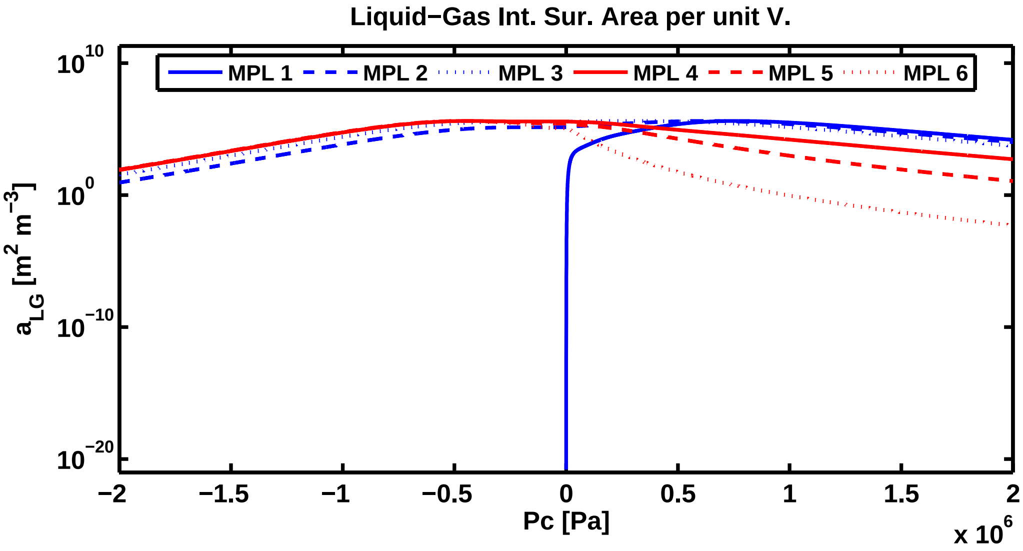

Figure 2.37 – Liquid-gas interfacial surface area per unit volume profiles for tested MPL cases with small hydrophilic pores, plotted against capillary pressure.

Figure 2.39 shows that MPL 3 and MPL 4 would be the optimal choice for MPLs where saturation levels are between 0% and 80%. MPL configurations 5 and 6 are better at enhancing evaporation rates for saturations between 0 to 30%.

For relatively small positive capillary pressures, MPL 3 is unarguably the best configuration to enhance evaporation rates. As observed from Figure 2.37, MPL 3 displays a maximum value for liquid-gas interfacial surface area per unit volume at a very small capillary pressure. During normal operation the capillary pressure inside the layers of a PEMFC are not dramatically large, as the liquid and gas pressures are very close in magnitude. This reveals that configurations such as the one described by MPL 3 will be preferred when designing MPLs to enhance evaporation rates while minimizing the adverse effects on gas transport due to flooding that result from adding a hydrophilic network of pores to a hydrophobic MPL configuration (minimizing the hit on gas transport produced by adding hydrophilic pores).

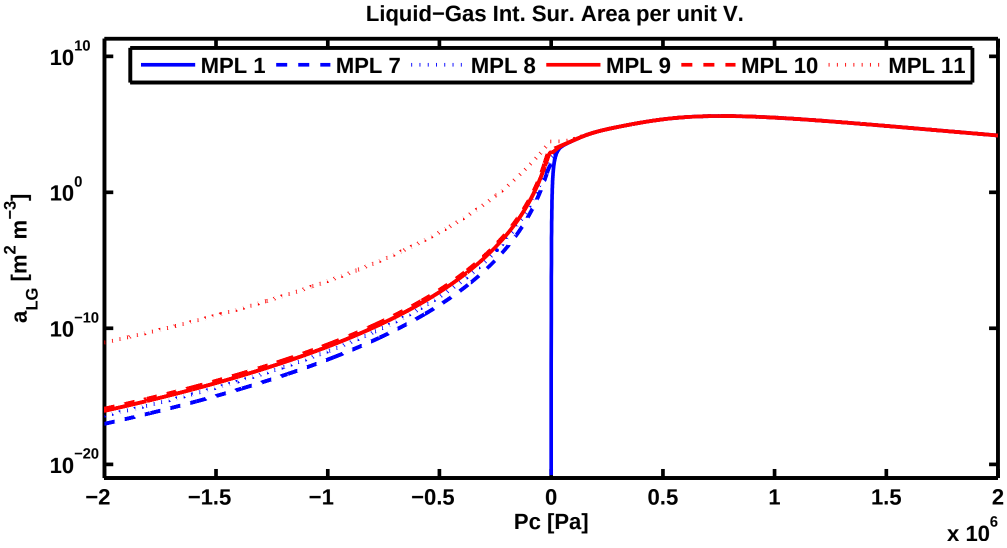

Figure 2.38 – Liquid-gas interfacial surface area per unit volume profiles for tested MPL cases with large hydrophilic pores, plotted against capillary pressure.

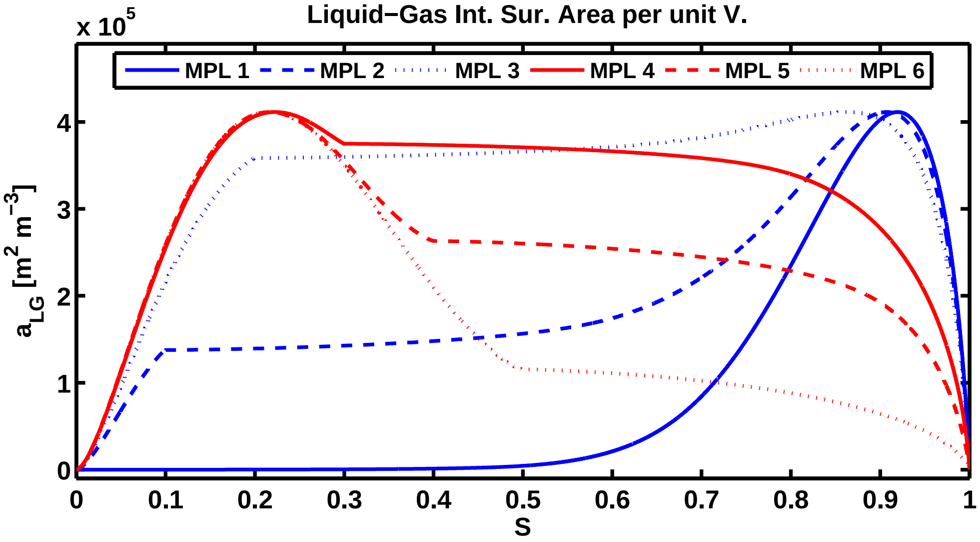

Figure 2.39 – Liquid-gas interfacial surface area per unit volume profiles for tested MPL cases with small hydrophilic pores, plotted against saturation.

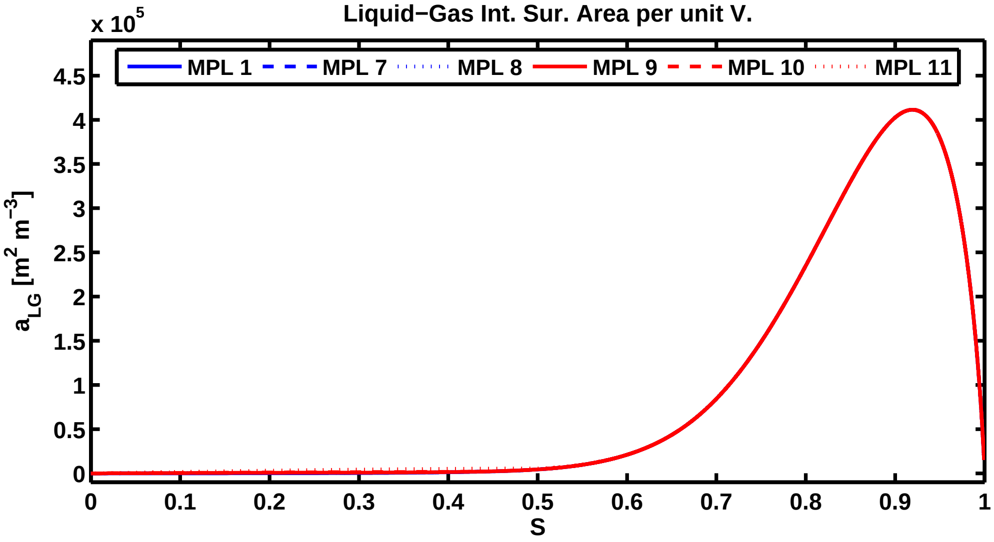

Figure 2.40 – Liquid-gas interfacial surface area per unit volume profiles for tested MPL cases with large hydrophilic pores, plotted against saturation.

Effects of Hydrophilic and Hydrophobic Contact Angles

To look at the effects of the contact angles on the effective properties predicted by the PSD model two MPL configurations will be used. From the previous study, MPL 3 will be the best configuration to enhance evaporation rates at low capillary pressures. Therefore, the effects of HI and HO contacts angles for MPL 3 will be studied. To have a comparison and study the effects of pore size and wettability, MPL 8 (MPL configuration where 20% of the pores are hydrophilic, but they are among the largest pores of the MPL) will be also analysed. The parametric studies for the hydrophilic and hydrophobic contact angles are outlined in Table 2.9.

The saturation profiles for MPL 3 and MPL 8 are presented in Figures 2.41 and 2.42. For negative capillary pressures the saturation level for MPL 3 decreases as the hydrophilic contact angle approaches 90°. For positive capillary pressures the

Table 2.9 – Parametric studies for hydrophilic and hydrophobic contact angles of MPL 3 and MPL 10.

MPL Case	Hydrophilic contact angle	Hydrophobic contact angle
1	70°	110°
2	75°	105°
3	80°	100°
4	85°	95°

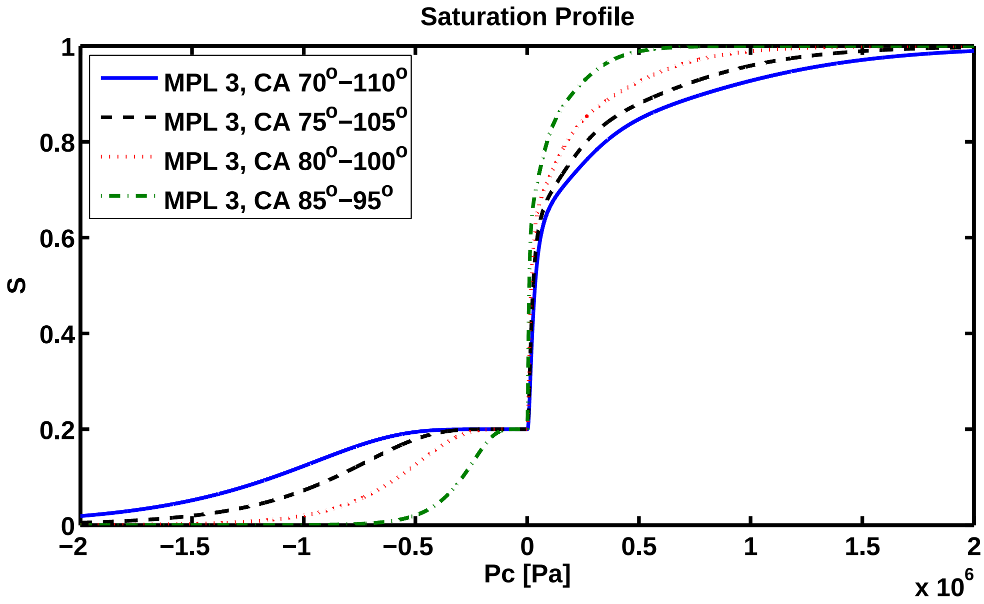

Figure 2.41 – Saturation profiles for MPL 3, varying hydrophilic and hydrophobic contact angles.

saturation level corresponding to MPL 3 increases as the hydrophobic contact angle approaches 90°.

Figure 2.42 reveals that the saturation level of MPL 8 for negative capillary pressures remains close to zero, regardless of contact angle. For positive capillary pressures, the saturation level of MPL 8 increases as the hydrophobic contact angle approaches 90°.

The liquid relative permeability profiles plotted against capillary pressure for MPL 3 and MPL 8 are presented in Figure 2.43. Due to the similarities between liquid saturation and liquid relative permeability, very similar results are found between the two for positive capillary pressures. The most notable difference is that since the liquid relative permeability is multiplied by a term that scales as saturation squared, for negative capillary pressures where saturations are small the liquid relative permeability is close to zero.

The gas relative permeability profiles are shown in Figure 2.44. For both small and large hydrophilic pores and negative capillary pressures, the gas relative permeability increases as the hydrophilic contact angle gets closer to 90°. For small and large pores hydrophilic pores in conditions of positive capillary pressures, the gas relative permeability increases as the hydrophobic contact angle becomes larger; which means that better transport of reactant gases is achieved if the contact angle for the hydrophobic pore network gets closer to 180°.

The profiles of liquid-gas interfacial surface area per unit volume plotted against

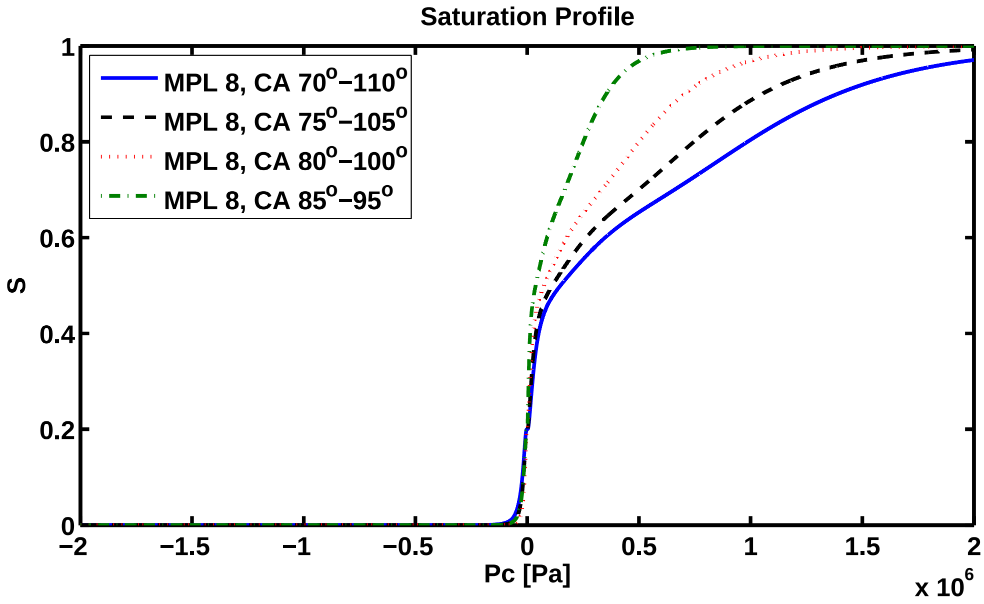

Figure 2.42 – Saturation profiles for MPL 8, varying hydrophilic and hydrophobic contact angles.

capillary pressure are presented in Figure 2.45. As the layers become less hydrophilic (hydrophilic contact angle gets closer to 90°) and more hydrophobic (hydrophobic contact angle gets closer to 180°), the profiles spread more over the capillary pressure. For the cases where the both contact angles are very close to 90°, the interfacial surface area profiles become narrower, which means that the evaporation rates will be more susceptible to changes when the capillary pressure changes.

2.5.6 Impact of Mixed Wettability Pore-Size Distribution on Effective Properties for GDLs

In this section, the effects of mixed wettability and microstructure for a GDL, whose PSD was obtained from MIP on the SGL Sigracet 34BA, are studied. The trends are similar to the ones observed for MPLs, and thus not all parametric studies will be presented.

In order to study the effects of hydrophilic and hydrophobic pore networks on GDL effective transport properties, 11 GDL configurations were tested: a completely hydrophobic GDL, 5 GDL configurations with small hydrophilic pores, and 5 GDL configurations with large hydrophilic pores. The GDL configurations with small hydrophilic pores are presented in Figure 2.46, while the GDL configurations with large hydrophilic pores are presented in Figure 2.47.

Assuming hydrophilic and hydrophobic contact angles of 45 and 110°, the satu-

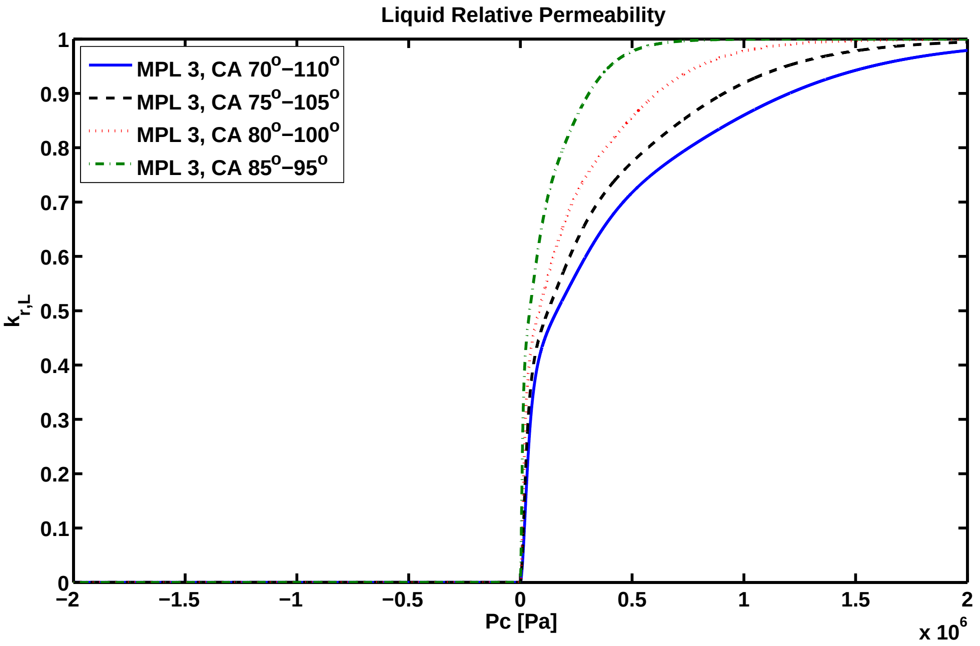

a) MPL 3.

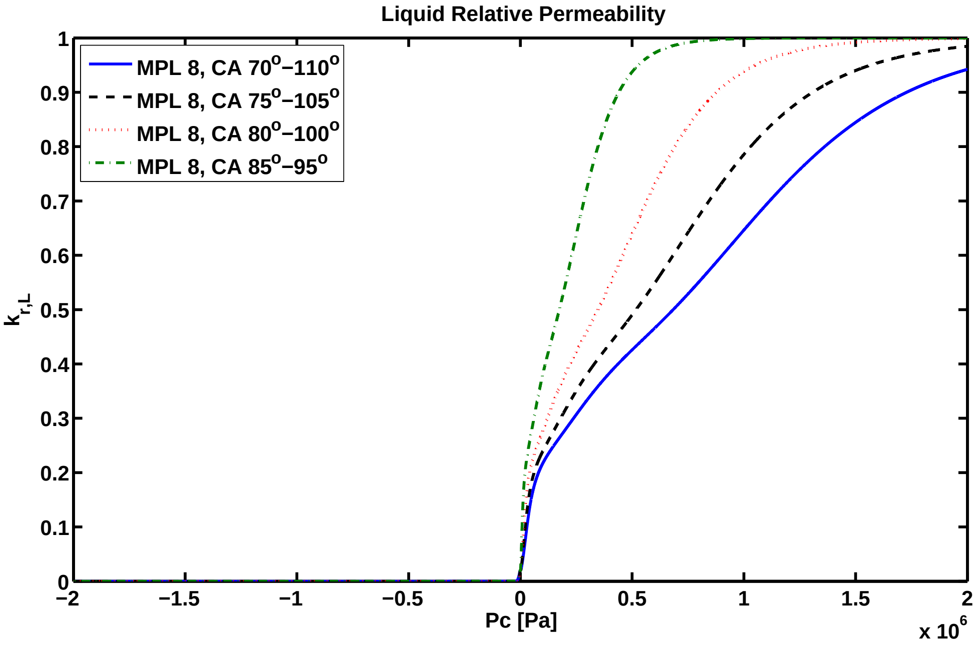

b) MPL 8.

Figure 2.43 – Liquid relative permeability profiles for MPL 3 and MPL 8, varying hydrophilic and hydrophobic contact angles.

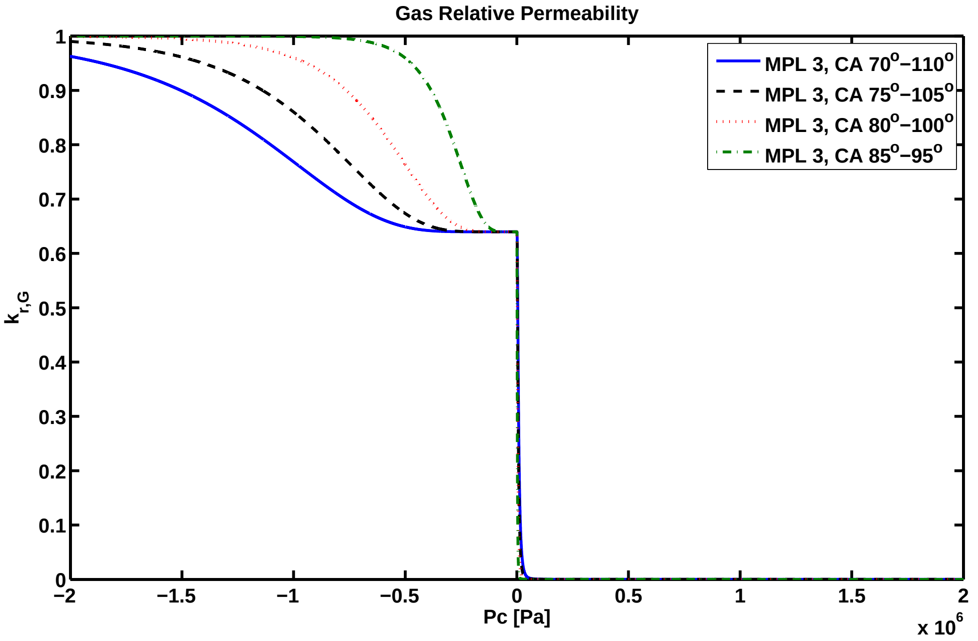

a) MPL 3.

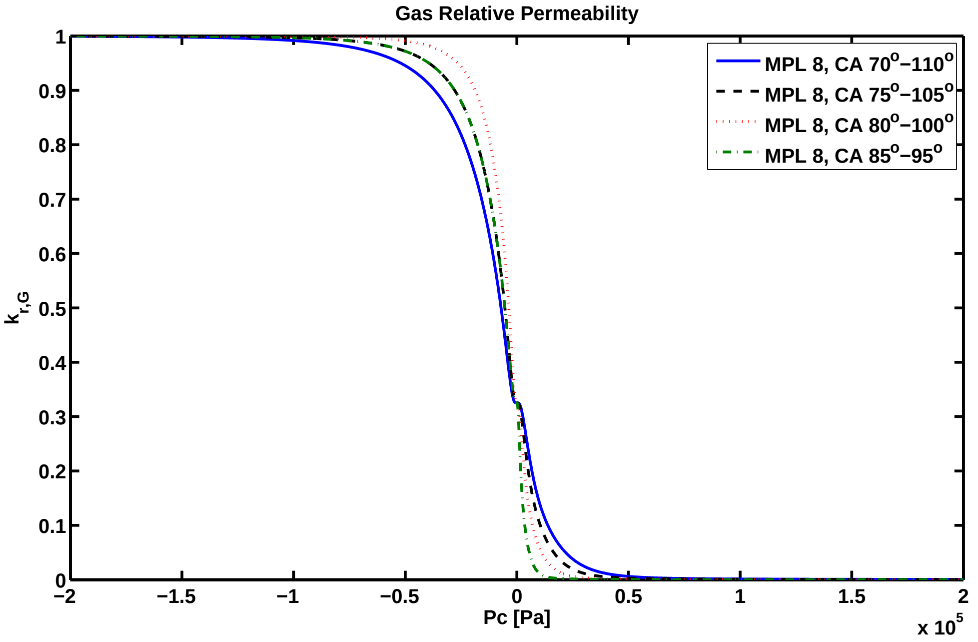

b) MPL 8.

Figure 2.44 – Gas relative permeability profiles for MPL 3 and MPL 8, varying hydrophilic and hydrophobic contact angles.

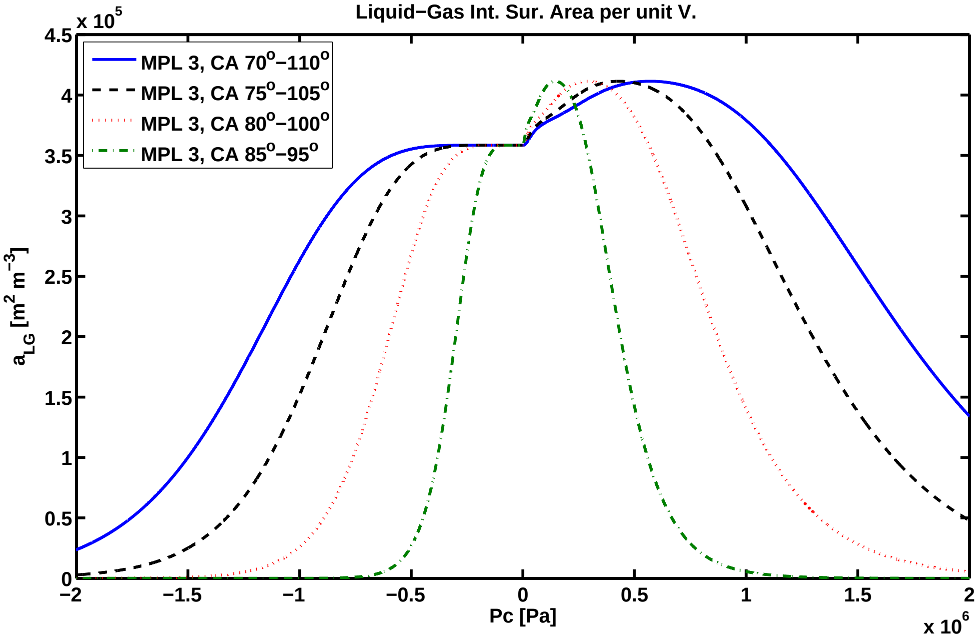

a) MPL 3.

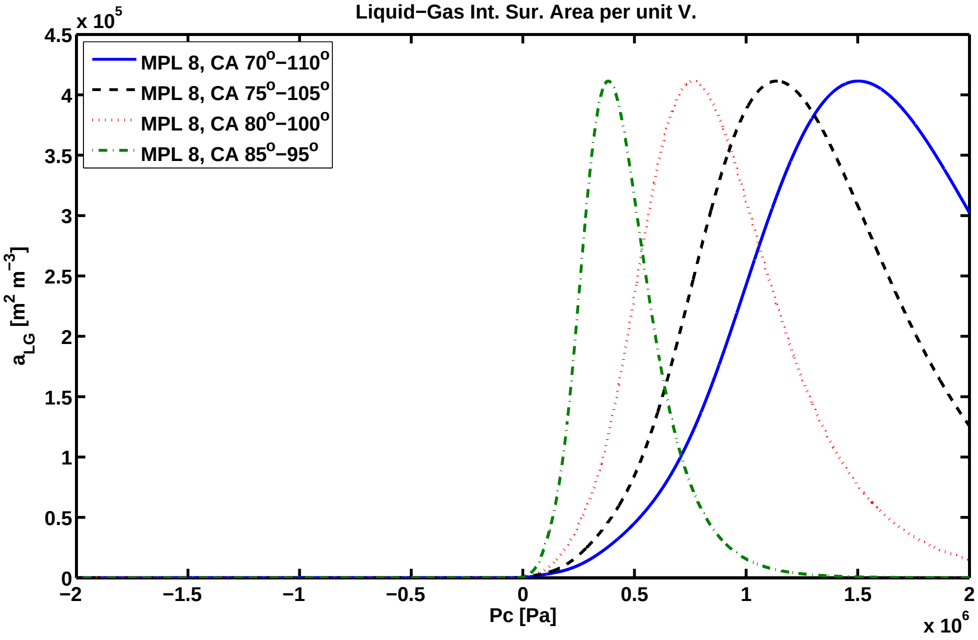

b) MPL 8.

Figure 2.45 – Liquid-gas interfacial surface area per unit volume profiles for MPL 3 and MPL 8, varying hydrophilic and hydrophobic contact angles.

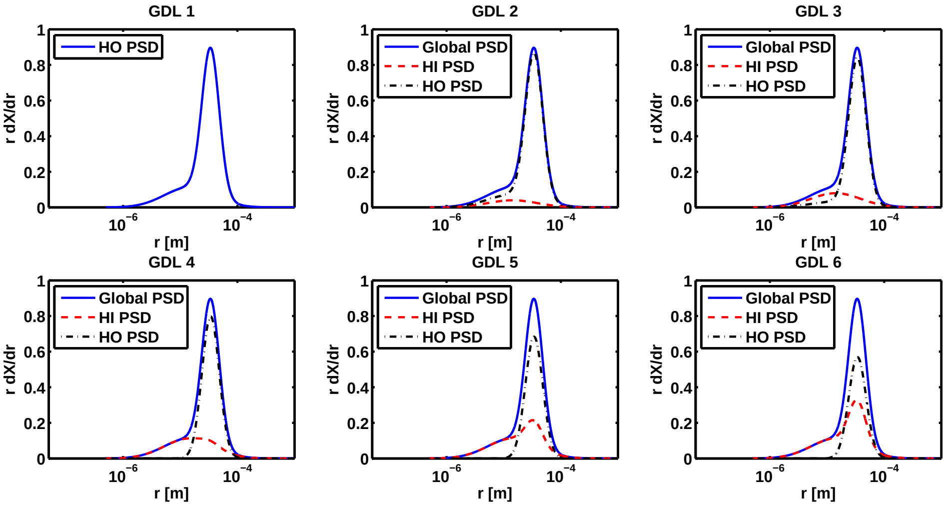

Figure 2.46 – Diagram showing global PSD and PSD of all the tested GDL configurations, multiplied by the pore radius, corresponding to the small hydrophilic pores.

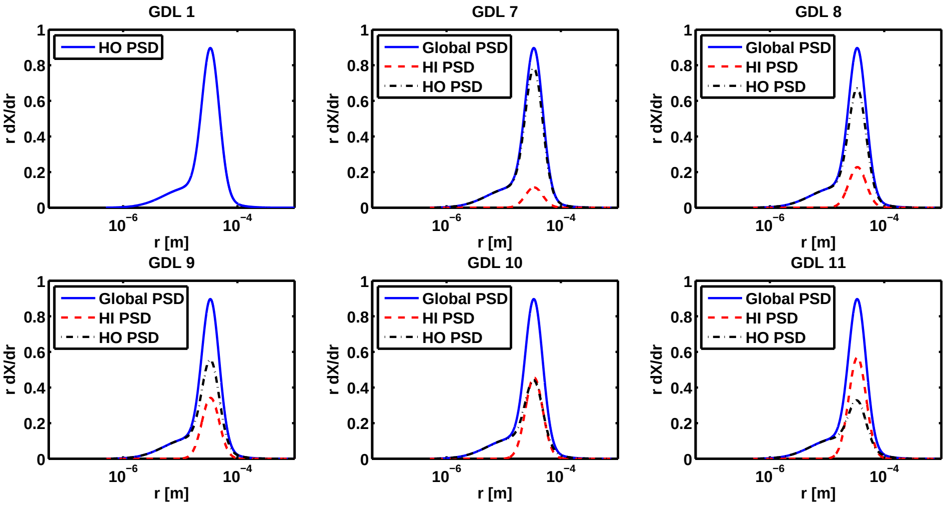

Figure 2.47 – Diagram showing global PSD and PSD of all the tested GDL configurations, multiplied by the pore radius to better see differences, corresponding to the large hydrophilic pores.

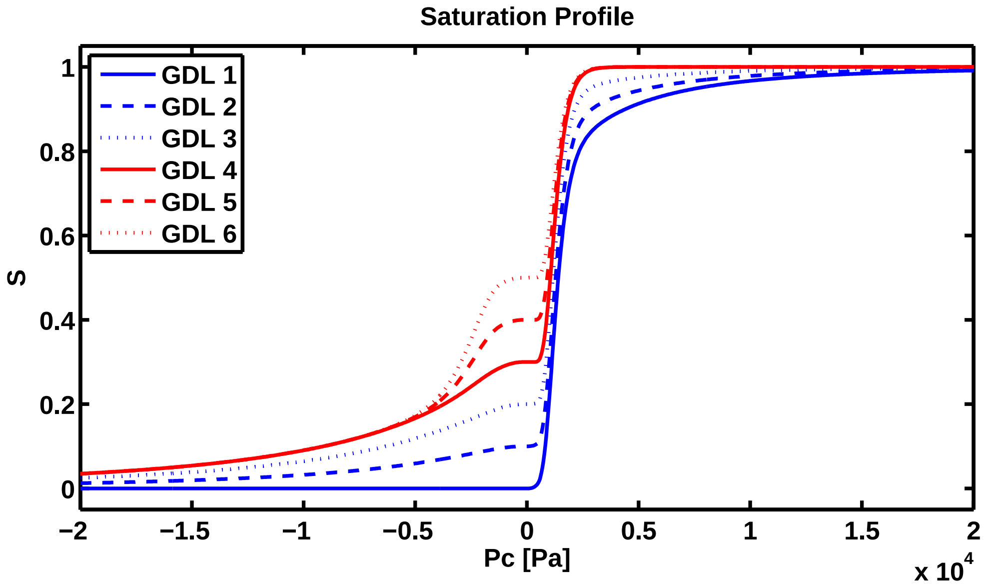

Figure 2.48 – Saturation profiles for tested GDL cases with small hydrophilic pores plotted against capillary pressure.

ration profiles for the GDLs presented in Figure 2.46 are displayed in Figure 2.48. Similarly, the saturation profiles corresponding to the GDL configurations shown in Figure 2.47 are presented in Figure 2.49.

Figure 2.48 reveals that when small hydrophilic pores are added to a GDL, the saturation profiles corresponding to both positive and negative capillary pressures are closely related with the amount of hydrophilic pores of the layer. However, when the network of hydrophilic pores added to the GDL corresponds to large pores, the saturation profiles for positive capillary pressures are not too sensitive to the amount of hydrophilic pores added.

The liquid relative permeability profiles for the GDLs presented in Figure 2.46 are displayed in Figure 2.50. Similarly, the saturation profiles corresponding to the GDL configurations shown in Figure 2.47 are presented in Figure 2.51. Similar to the MPL configurations, large hydrophilic pores cause the liquid relative permeability profiles for positive capillary pressures to be almost independent of hydrophilic pore fractions, while for negative capillary pressures it changes accordingly.

The gas relative permeability profiles corresponding to the GDL configurations presented in Figure 2.46 and Figure 2.47 are shown in Figure 2.52 and Figure 2.53, respectively. The size of the hydrophilic pore fractions only impacts the profile for negative capillary pressures. However, note that the gas relative permeability benefits from small fractions of hydrophilic pores.

The liquid-gas interfacial surface area per unit volume, and pore wall surface area

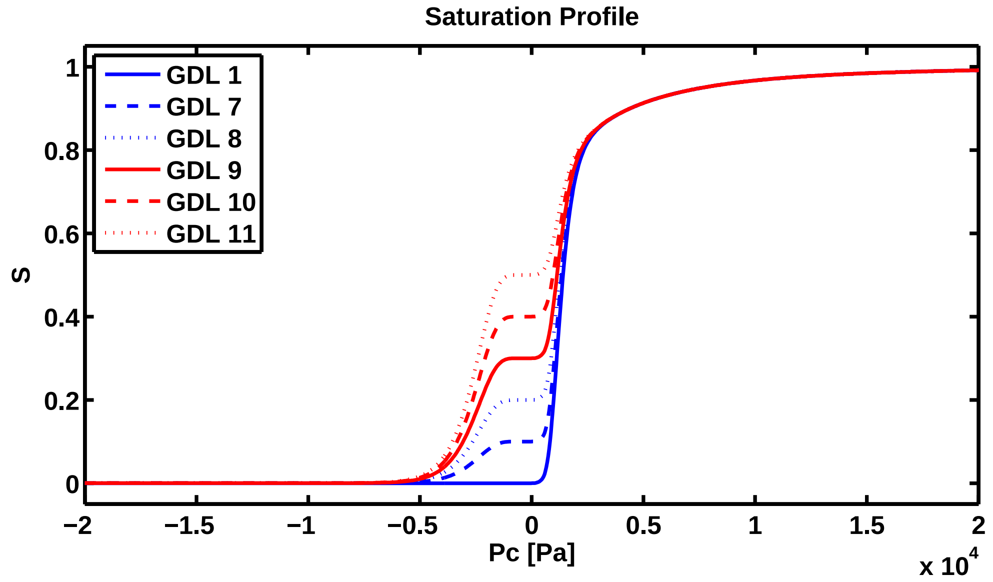

Figure 2.49 – Saturation profiles for tested GDL cases with large hydrophilic pores plotted against capillary pressure.

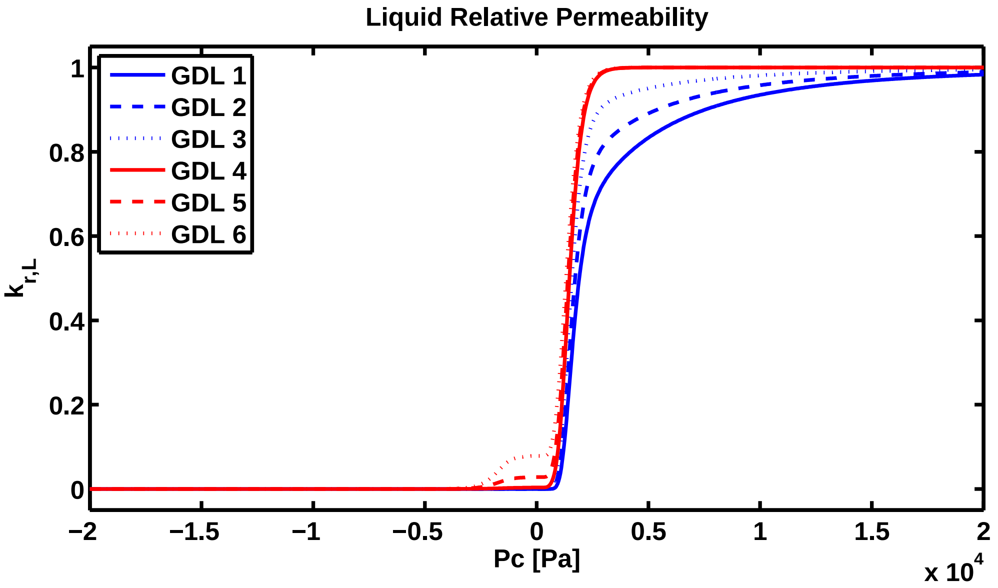

Figure 2.50 – Liquid relative permeability profiles for tested GDL cases with small hydrophilic pores plotted against capillary pressure.

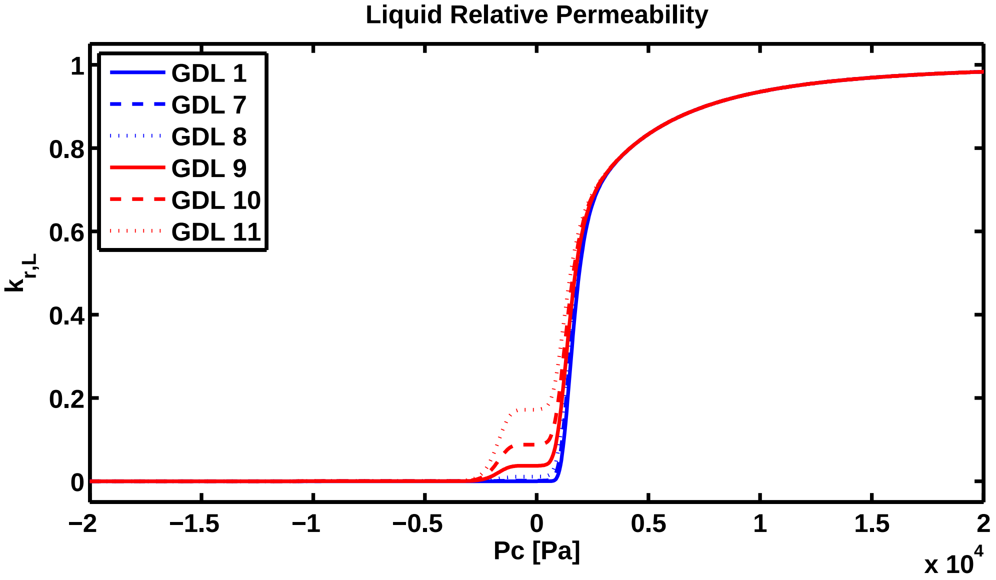

Figure 2.51 – Liquid relative permeability profiles for tested GDL cases with large hydrophilic pores plotted against capillary pressure.

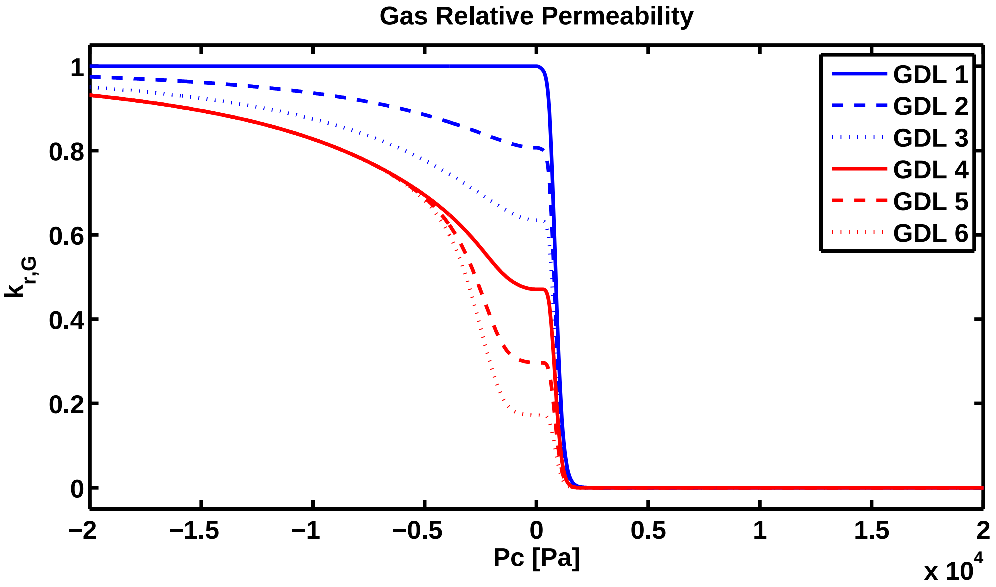

Figure 2.52 – Gas relative permeability profiles for tested GDL cases with small hydrophilic pores plotted against capillary pressure.

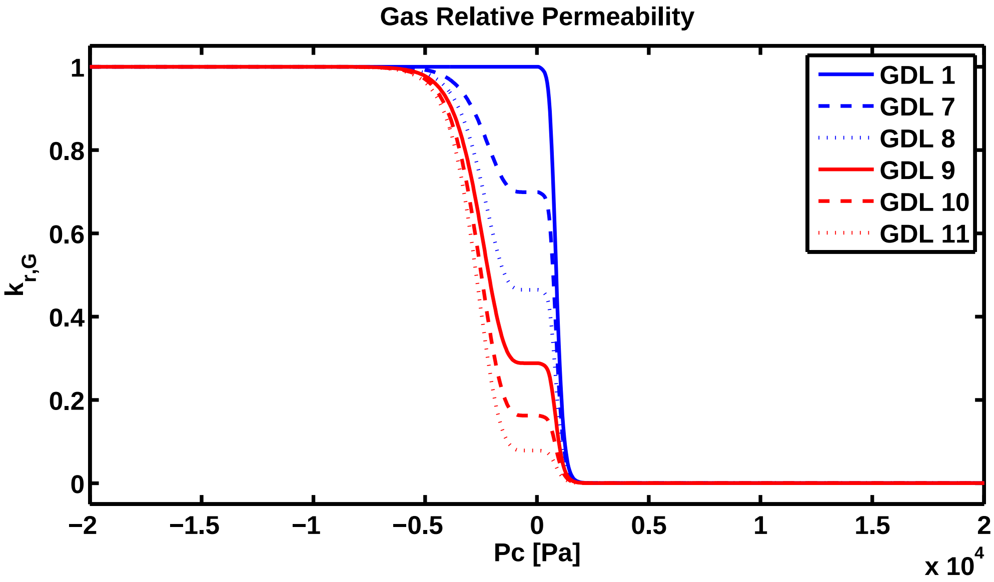

Figure 2.53 – Gas relative permeability profiles for tested GDL cases with large hydrophilic pores plotted against capillary pressure.

per unit volume, are not discussed here and instead are presented in Appendix B.

2.5.7 Conclusions

The proposed mixed wettability PSD model was used to represent a Sigracet SGL 34BA GDL, and estimate the corresponding transport properties. Is was observed that properties such as saturation, liquid relative permeability, gas relative permeability, and saturated permeability estimated from the PSD model agree well with experimental data for other conventional GDLs, such as Toray 060 and Toray 090.

Using the SGL 34BA and the SGL 34BC, the PSD corresponding to an MPL was obtained. For MPLs, the agreement between the predicted transport properties and experimental data is not as good as for the GDL cases. The reason for this is the uncertainty of actual MPL microstructure. As shown in this Chapter, when MPLs are coated on top of a GDL cracks of considerable sizes can be observed, leading to larger than expected pore sizes. Additionally, the MPLs may also penetrate inside the GDL, leading to difficulties to separate the two layers when performing experiments.

From the parametric studies presented in this section, it was found that the MPL with best gas transport properties is a fully hydrophobic MPL. This result was expected, because a fully hydrophobic MPL will tend to have lower saturations, and therefore the gas relative permeability and diffusivity will be optimal.

However, due to the lack of hydrophilic pores, the liquid-gas interfacial surface area per unit volume for a fully hydrophobic layer is very small, leading to low evaporation rates. When hydrophilic pores are added, clusters of liquid water are created within the MPL and the interfacial surface area increases substantially while saturation remains low.

For MPL conditions where saturations are relatively low and capillary pressures are close to zero, MPL 3 (MPL with 20% of total volume corresponding to small hydrophilic pores) and MPL 4 (MPL with 30% of total volume corresponding to small hydrophilic pores) are the best options to enhance evaporation rates.

In general, evaporation rates from MPL 4 are the best, but the gas relative permeability and effective gas diffusivity decreases with the increasing fraction of hydrophilic pores. As observed from Figure 2.37, the liquid-gas interfacial surface area per unit volume for MPL 3 and MPL 4 for a capillary pressure of zero are relatively close, but from Figure 2.30 and Figure 2.31 can be observed that the gas relative permeability for MPL 3 is significantly better than for MPL 4, which means that gas transport will be better for MPL 3 than for MPL 4.

Given the benefits of enhanced evaporation and the quality of gas transport, MPL 3 will be the best MPL configuration to enhance evaporation while minimising the impact of the added hydrophilic pores to the overall gas transport.

Additionally, the choice for optimal contact angle must be balanced between the gas relative permeability and the liquid-gas interfacial surface area per unit volume. While for low capillary pressures the liquid-gas interfacial surface area per unit volume will benefit from MPL configurations with hydrophilic and hydrophobic contact angles close to 90°, the gas relative permeability benefits from hydrophilic contact angles close to 90°and hydrophobic contact angles far from 90°.

Chapter 3

Microporous Layer (MPL) Model

3.1 Model Description

3.1.1 Model Formulation

Using the mixed wettability formulation introduced by the proposed PSD model, a two-phase model for MPLs was defined in order to incorporate the effects of wettability and microstructure. The assumptions and conditions used to develop the mathematical model are summarized as follows:

1. One-dimensional.
2. Steady-state.
3. Isothermal.
4. Air is an infinite dilute mixture where nitrogen is assumed to be the solvent while water vapour and oxygen are assumed to be the solutes. Solute-solute interactions are considered negligible.
5. Convective transport effects are important.
6. Binary and Knudsen diffusion both take place inside the layer, and can be obtained using Bosanquet approximation, defined by Equation (2.77).

The mass conservation of the liquid and gas phases are given by the following expressions:

$$\nabla \cdot (\rho_L \vec{u}_L) = S_{LG} M_{H_2O} \tag{3.1}$$

$$\nabla \cdot (\rho_G \vec{u}_G) = -S_{LG} M_{H_2O} \tag{3.2}$$

where ρ_L and ρ_G are the mass densities for the liquid water and the gas phase, respectively; $\vec{u}_L$ and $\vec{u}_G$ are the liquid and gas velocities; S_{LG} is the evaporation-condensation conversion term; and M_{H_2O} is the molar mass of water. The evaporation-condensation conversion rate is defined as:

$$S_{LG} = k^{evap} a_{LG} \left[p_V - p^{sat}(r) \right] \tag{3.3}$$

where k^{evap} is the evaporation rate constant, a_{LG} is the liquid-gas interfacial surface area per unit volume obtained from Chapter 2, p_V is the water vapour pressure, $p^{sat}(r)$ is the corrected saturated water vapour pressure (that takes into account the effect of pore size on saturated vapour pressure). $p^{sat}(r)$ is defined by the Kelvin equation [3] as:

$$p^{sat}(r) = p^{sat} \exp\left(-\frac{2\,\sigma\, \cos(\theta)}{r} \frac{M_G}{R_g\, T\, \rho_G} \right) \tag{3.4}$$

where p^{sat} is the saturated vapour pressure and M_G is the molar mass of the gas phase. Note that using the Young Laplace equation, the corrected saturated vapour pressure can be written in terms of the capillary pressure as:

$$p^{sat}(p_c) = p^{sat} \exp\left(\frac{p_c\, M_G}{R_g\, T\, \rho_G} \right) \tag{3.5}$$

For flow through porous media, Darcy's law can be used to define the conservation of linear momentum as a simplification of the full set of Navier-Stokes equations. Using Darcy's law, the momentum conservation of the liquid and the gas phase are given, respectively, as:

$$\vec{u}_L = -\frac{k_{sat}\, k_{rL}}{\mu_L} \nabla p_L \tag{3.6}$$

$$\vec{u}_G = -\frac{k_{sat}\, k_{rG}}{\mu_G} \nabla p_G \tag{3.7}$$

where k_{sat} is the absolute permeability of the porous media , p_L is the liquid water pressure, and p_G is the gas pressure. Absolute and relative permeabilities are estimated using the PSD model in Chapter 2.

Using the molar conservation of individual species in the gas phase, the conservation of molar water vapour flux is given as:

$$\nabla \cdot \vec{N}_V = -S_{LG} \tag{3.8}$$

while the conservation for the oxygen molar flux is defined as:

$$\nabla \cdot \vec{N}_{O_2} = 0 \tag{3.9}$$

Assuming that the gas phase is an infinite dilute solution, the oxygen flux is defined as:

$$\vec{N}_{O_2} = -D^{eff}_{O_2,MPL} \nabla c_{O_2} + c_{O_2} \vec{u^*}_G \tag{3.10}$$

where $D^{eff}_{O_2,MPL}$ is the effective oxygen diffusion coefficient of the MPL, c_{O_2} is the oxygen concentration, and $\vec{u^*}_G$ is the molar velocity of the gas phase. The molar velocity is obtained from the ratio of total molar flux and total concentration. $D^{eff}_{O_2,MPL}$ is obtained with the PSD model from the expressions provided in Section 2.4.8.

Similarly, the molar flux of water vapour is defined as:

$$\vec{N}_V = -D^{eff}_{V,MPL} \nabla c_V + c_V \vec{u^*}_G \tag{3.11}$$

where $D^{eff}_{V,MPL}$ and c_V are the effective diffusion coefficient and concentration of water vapour, respectively. $D^{eff}_{V,MPL}$ is also obtained with the PSD model from the expressions provided in Section 2.4.8.

A summary of all the governing equations is presented in Table 3.1. Even though the governing equations were written in a general form in three dimensional notation, the model implementation is only one dimensional. Properties such as permeability and effective diffusivity cannot be easily defined in three dimensions, and thus only a one-dimensional approach is considered in this thesis.

To solve the boundary value problem, the solver BVP5C from the Matlab libraries was used. To solve the system of ordinary differential equations, the absolute and relative tolerances were set to 1×10^{-5}.

3.1.2 Boundary Conditions

To solve the proposed MPL model, eight boundary conditions are needed. The fluxes and current density are related to an overpotential value by means of a Tafel equation, which dictates the relation between current density, oxygen concentration and cell overpotential.

The MPL is assumed to be paired with a cathode catalyst layer. Water is generated in the catalyst layer and travels to the MPL. Therefore, the liquid pressure and the liquid flux are prescribed at the interface between the MPL and the catalyst layer. Similarly, the oxygen flux is prescribed at the catalyst layer interface. The liquid velocity entering the MPL from the catalyst layer is given as:

Table 3.1 – Summary of the governing equation of the MPL for a PEMFC.

Variable	Governing Equation MPL
$\vec{u}_L$	$\nabla \cdot (\rho_L \vec{u}_L) = S_{LG}\, M_{H_2O}$
$\vec{u}_G$	$\nabla \cdot (\rho_G \vec{u}_G) = -S_{LG}\, M_{H_2O}$
$\vec{N}_{O_2}$	$\nabla \cdot \vec{N}_{O_2} = 0$
$\vec{N}_V$	$\nabla \cdot \vec{N}_V = -S_{LG}$
p_L	$\vec{u}_L = -\dfrac{k_{sat}\, k_{r,L}}{\mu_L} \nabla p_L$
p_G	$\vec{u}_G = -\dfrac{k_{sat}\, k_{r,G}}{\mu_G} \nabla p_G$
c_{O_2}	$\vec{N}_{O_2} = -D^{eff}_{O_2,N_2} \nabla c_{O_2} + c_{O_2} \vec{u}^*_G$
c_V	$\vec{N}_V = -D^{eff}_{V,N_2} \nabla c_V + c_V \vec{u}^*_G$

$$\vec{u}_L\big|_{x=0} = \frac{i_{tot}\, M_{H_2O}}{2\, F\, \rho_L} \tag{3.12}$$

where i_{tot} is the total volumetric current density generated from the catalyst layer. The water transport across the membrane is ignored due to the uncertain contribution of electro-osmotic drag and back diffusion. The total current is obtained from:

$$i_{tot} = \int_0^{L_{UTCL}} i_c(x)\, dx \tag{3.13}$$

where i_c is the local current density, which is defined as a function of the cell overpotential as:

$$i_c = i_0 \frac{p_{O_2}}{p_{O_2}^{ref}} \exp\left[-\frac{\alpha_c\, F}{R_g\, T}\eta\right] A_{eff} \tag{3.14}$$

where $p_{O_2}^{ref}$ is the reference oxygen partial pressure, i_0 is the exchange current density, α_c is the cathodic transfer coefficient, η is the cell overpotential, F is the Faraday constant, and A_{eff} is the effective area of catalyst per cubic centimetre of electrode, found from the expression provided by Wang et al. [16],

$$A_{eff} = \frac{3\, \mu_{Pt}}{\rho_{Pt}\, r_{Pt}\, L_{UTCL}} \tag{3.15}$$

where μ_{Pt} is the platinum loading of the ultrathin cathode catalyst layer (amount of Platinum used per squared centimetre of electrode), ρ_{Pt} is the density of Platinum, r_{Pt} is the average radius of a Platinum particle, and L_{UTCL} is the thickness of the ultrathin cathode catalyst layer.

The liquid pressure at the catalyst layer interface is written as:

$$p_L\big|_{x=0} = p_L^{CL} \tag{3.16}$$

where p_L^{CL} is the liquid water pressure value of the catalyst layer. The liquid pressure boundary condition is set to the MPL liquid breakthrough pressure, which was measured experimentally to be near $6\, kPa$.

The oxygen flux entering the MPL is given by Faraday's law as:

$$\vec{N}_{O_2}\Big|_{x=0} = -\frac{i_{tot}}{4\, F} \tag{3.17}$$

The model assumes that water cannot evaporate at the catalyst layer interface, and correspondingly the water vapour flux is set to zero at the catalyst layer interface.

Since all fluxes are prescribed at the catalyst layer interface, the total gas velocity is also prescribed at the catalyst layer interface. The gas velocity entering the MPL is given as:

$$\vec{u}_G|_{x=0} = -\frac{i_{tot}\, M_G\, R\, T}{4\, F\, p_o} \tag{3.18}$$

where p_o is the total gas pressure.

The water vapour flux at the catalyst layer interface is prescribed as:

$$\vec{N}_V\Big|_{x=0} = 0 \tag{3.19}$$

Assuming that the gas pressure remains constant inside the gas channels and GDL, the gas pressure is prescribed as a boundary condition at the interface of the MPL with the GDL:

$$p_G|_{x=L_{MPL}} = p_o \tag{3.20}$$

where p_o is the gas channel pressure.

The boundary condition at the GDL/MPL interface accounts for the mass transport losses in the GDL. Oxygen has to travel from the channel to the MPL via the GDL, therefore the oxygen boundary condition is defined in terms of the oxygen partial pressure as:

$$c_{O_2}|_{x=L_{MPL}} = \frac{p_{O_2}}{R_g T} \tag{3.21}$$

and therefore, the oxygen boundary condition is defined in terms of the channel oxygen partial pressure $p^o_{O_2}$ as:

$$c_{O_2}|_{x=L_{MPL}} = \frac{p_{O_2}}{R_g T} = \frac{p^o_{O_2}}{R_g T} - \frac{L_{GDL}\, i_{tot}}{4\, F\, D_{O_2,GDL}\left[(1 - S_{GDL})\, \varepsilon_{GDL}\right]^{1.5}} \tag{3.22}$$

where $p^o_{O_2}$ is the oxygen partial pressure inside the gas channels, given as $0.21\,(p_o - p^o_V)$. p^o_V is the vapour pressure at the GDL interface. The second term for the oxygen concentration boundary condition in Equation (3.22) represents the oxygen diffusion through the GDL. This term takes into account the concentration losses due to GDL diffusion. The expression $\left[(1 - S_{GDL})\, \varepsilon_{GDL}\right]^{1.5}$ represents the effective oxygen diffusion coefficient of the GDL, given by the Bruggeman approximation [82]. The GDL saturation, S_{GDL}, comes from the PSD model, using the information from Table 2.6 and the capillary pressure at the interface between the MPL and the GDL, and assuming that 30% of the smallest pores are hydrophilic. L_{GDL} is the length of the

GDL, $D_{O_2,GDL}$ is the oxygen diffusion inside the GDL, S_{GDL} is the saturation of the GDL at the MPL-GDL interface, and ε_{GDL} is the porosity of the GDL

Similarly, the vapour pressure boundary condition is prescribed at the interface between the MPL and the GDL. The boundary condition used take the following form:

$$c_V\big|_{x=L_{MPL}} = \frac{p_V^o}{R_g T} + \frac{N_V^L\, L_{GDL}}{D_{V,GDL}\left[(1 - S_{GDL})\,\varepsilon_{GDL}\right]^{1.5}} \tag{3.23}$$

where p_V^o is the water vapour pressure at the gas channels, N_V^L is the water vapour flux at the MPL-GDL interface, and $D_{V,GDL}$ is the water vapour diffusion coefficient inside the GDL. Since the mean pore size of GDLs is around 40 μm and the operating pressures are usually in the order of one atmosphere, the effects of Knudsen diffusion can be neglected. Assuming an infinite dilute solution, the oxygen and water vapour diffusion coefficients are given by the binary diffusion coefficients of oxygen-nitrogen and vapour-nitrogen, respectively.

In order to prevent the model from evaporating more water than the water that is available from the catalyst layer, the liquid and vapour fluxes are monitored. If the liquid water velocity is less than or equal to zero (or when the vapour flux is equal to the liquid flux inside the MPL) the liquid-vapour conversion rate is set to $S_{LG} = 0$. Once all the water reaches vapour form there is no need to solve for water transport. The assumption of $S_{LG} = 0$ reveals that:

$$p_V - p^{sat} \exp\left(\frac{p_c\, M_G}{R_g\, T\, \rho_G}\right) = 0 \tag{3.24}$$

From the previous expression, the value of capillary pressure required to satisfy this condition can be obtained,

$$p_c = \frac{R_g T \rho_G}{M_G} \ln\left(\frac{p_V}{p^{sat}}\right) \tag{3.25}$$

and this new value can be used to define the layer saturation, relative permeabilities, and all other parameters related to the PSD model. This new definition of capillary pressure will cause a sharp change on the solution profiles, and will cause instability and slow convergence rates.

The cell voltage can be found from

$$V_{cell} = E^o - i_{tot}\, L_{mem} \sigma_{mem}^{-1} + \eta_0 \tag{3.26}$$

where E^o is the open circuit voltage of the cell, L_{mem} is the length of the membrane, σ_{mem} is the membrane ionic conductivity, and η_0 is the cell overpotential at the

Table 3.2 – MPL boundary conditions.

Variable	GDL/MPL	MPL/UTCCL
$\vec{u}_L$	-	$\dfrac{i_{tot}\,M_{H_2O}}{2\,F\,\rho_L}$
$\vec{u}_G$	-	$-\dfrac{i_{tot}\,M_G\,R_g\,T}{4\,F\,p_o}$
$\vec{N}_{O_2}$	-	$-\dfrac{i_{tot}}{4\,F}$
$\vec{N}_V$	-	0
p_L	-	p_L^{CL}
p_G	p_o	-
c_{O_2}	$\dfrac{p^o_{O_2}}{R_gT} - \dfrac{L_{GDL}\,i_{tot}}{4\,F\,D_{O_2,GDL}\,\left[(1-S_{GDL})\,\varepsilon_{GDL}\right]^{1.5}}$	-
c_V	$\dfrac{p^o_V}{R_gT} + \dfrac{N^L_V\,L_{GDL}}{D_{V,GDL}\,\left[(1-S_{GDL})\,\varepsilon_{GDL}\right]^{1.5}}$	-

membrane interface.

Assuming large overpotentials, the exchange current density i_0, reference oxygen partial pressure $p_{O_2}^{ref}$, and open circuit voltage OCV were obtained from the data documented by Parthasarathy et al. [90]. Interpolating this data to an operating temperature of 75^oC, the obtained parameters were:

$$\begin{aligned} i_0 &= 1.0174 \times 10^{-8}\, A\, cm^{-2} \\ E^o &= 1.1958\, V \\ p_{O_2}^{ref} &= 5\, atm \end{aligned} \tag{3.27}$$

A summary of the model parameters for the MPL model is presented in Table 3.3.

3.2 Results and Discussions

3.2.1 MPL Performance

Polarization Curves

Polarization curves for MPL configurations 1 to 6 is presented in Figure 3.1. Due to the high values of capillary pressure, the saturation at the GDL interface is very high (GDL flooding), which causes early mass transport limitations for MPL 1. MPL configurations 2 to 6 show better performance in comparison, and the reason is because the added network of hydrophilic pores increases interfacial surface area per unit volume and therefore increase evaporation rates inside the MPL.

For MPL configurations with added hydrophilic pores, it can be observed that the current density will increase up to a point in which a sudden bifurcation will take place, and a very low limiting current density will appear. As current density increases so will the water production rates. There will be a point in which the water production rates will surpass the water evaporation rates, and GDL flooding will take place, which results in the bifurcation observed.

As predicted from the previous section, MPL 3 shows the best performance among the MPL configurations, closely followed by MPL 4. Due to the lack of hydrophilic pores, MPL 1 is the worst performer layer.

Polarization curves for the MPL configurations with hydrophilic fractions of large pores (MPL 7 to MPL 11), are presented in Figure 3.2. The polarization curve for MPL 1 is also shown for comparison. Note that due to the large size of the hydrophilic pores, evaporation rates are not enhanced significantly and therefore the performance of these MPLs is low when compared to the curves shown in Figure 3.1.

Table 3.3 – Summary of model parameters for MPL model.

Parameter	Value	Reference
T	75^oC	-
F	$96485\,C\,mol^{-1}$	-
R_g	$8.314\,J\,mol^{-1}K^{-1}$	-
k^{evap}	-	-
p^o	$101325\,Pa$	-
i_0	$1.0174 \times 10^{-8}\,A\,cm^{-2}$	[90]
E^o	$1.1958\,V$	[90]
$p_{O_2}^{ref}$	$5\,atm$	[90]
σ_{mem}	$0.067\,S\,cm^{-1}$	[16]
L_{mem}	$0.005\,cm$	[16]
μ_{Pt}	$0.3\,mg\,cm^{-2}$	[16]
ρ_{Pt}	$21.5\,g\,cm^{-3}$	[16]
r_{Pt}	$5.5\,nm$	[16]
L_{GDL}	$250\,\mu m$	
L_{MPL}	$50\,\mu m$	
ε_{GDL}	-	
ε_{MPL}	-	

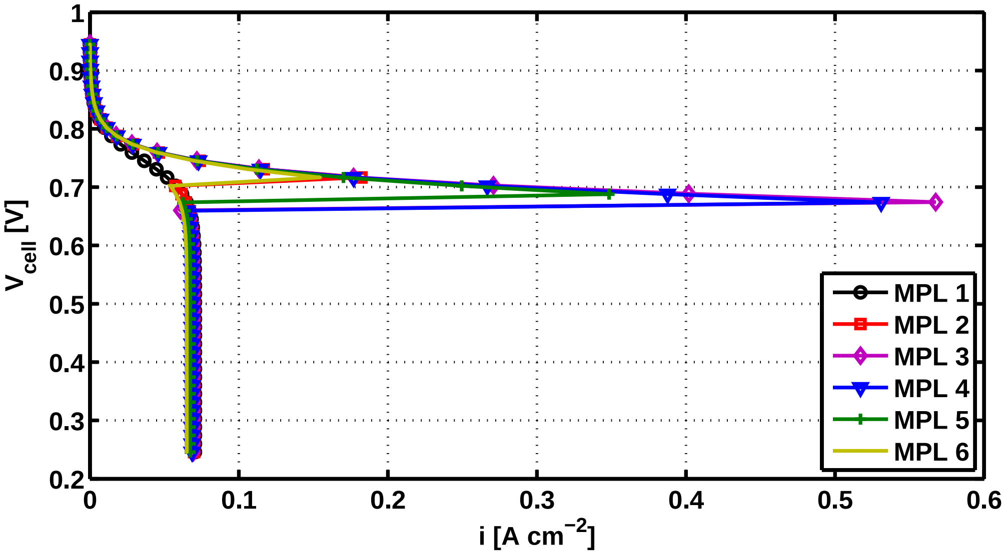

Figure 3.1 – Polarization curves for MPL configurations 1 through 6, showing the effects of hydrophilic pore fractions with small pores on cell performance.

MPL 1, and MPL 7 to 11 are always wetted, and thus these configurations are prone to GDL flooding. MPL 2 to 6 are dry for low current densities, and become wetted at moderately high current densities; leading to an increase in cell performance.

Internal Solution Profiles

From the previous analysis was observed that for MPLs with small hydrophilic pores a solution bifurcation occurs due to the enhanced evaporation rates of the MPLs. When current densities are small the liquid water generated at the catalyst layer travelling through the MPL is evaporated, but once water generation surpasses water evaporation rates then the GDL floods and mass transport limitations take place.

In order to gain additional insight, solution profiles along the MPL were obtained. Profiles are obtained for MPL 3, which is the best performing MPL as indicated by Figure 3.1. In order to look at the evolution of the solution profiles, current densities of 0.026 (Point 1), 0.04 (Point 2), 0.46 Acm^{-2} (Point 3) corresponding to the dry model; and 0.027 Acm^{-2}(Point 4), corresponding to the wet MPL model and the limiting current case, were selected. For this MPL configuration, the liquid breakthrough pressure is assumed to be 9000 Pa and the evaporation rate constant assumed to be 0.0005 $m^{-3}s^{-1}$.

The normalized water vapour flux profiles corresponding to the different current densities is presented in Figure 3.3. As appreciated, the first three points are in the regime where the evaporation rates surpass the water generation rates of the catalyst

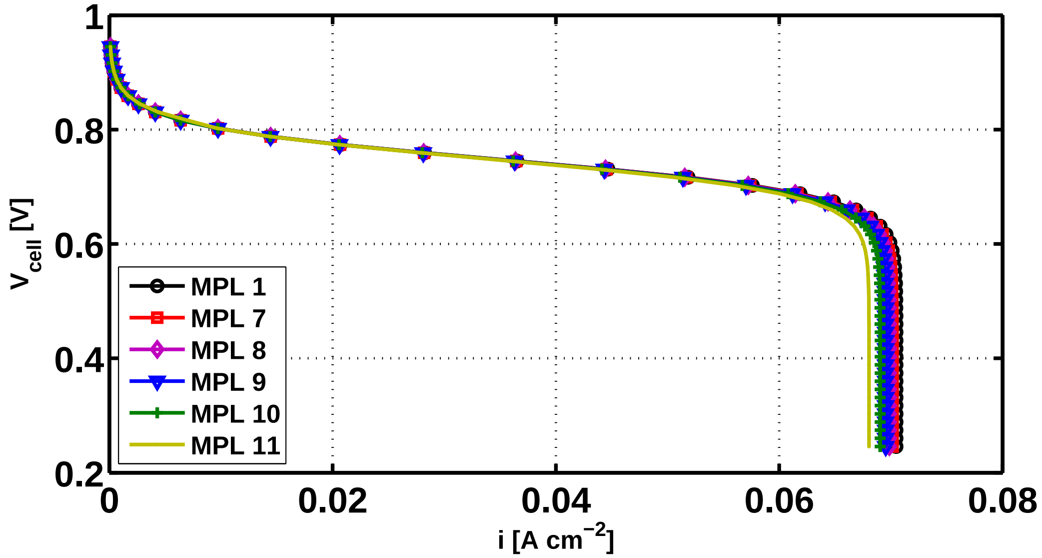

Figure 3.2 – Polarization curves for MPL configurations 1, and 7 through 11, showing the effects of hydrophilic pore fractions with large pores on cell performance.

layer, thus the produced liquid water turns into vapour immediately. For Point 4, however, toward the end of the catalyst layer the water production rates surpass the liquid evaporation rates, and thus the liquid phase exists.

The capillary pressure profiles along MPL 3 for the selected current densities are presented in Figure 3.4. When the evaporation rates are slower than the water production rates, the capillary pressure remains almost constant along the MPL due to the size of the MPL pores and the relative small capillary pressure values. However, for the dry MPL cases (where all the liquid water generated turns into water vapour), a sharp and pronounced drop in capillary pressure is observed. This drop in capillary pressure corresponds to a saturation level where only the small hydrophilic pores are filled with liquid water.

When all the water is evaporated, the capillary pressure is obtained from Equation (3.25). At this point, the only pores with liquid water will be the smallest hydrophilic pores, and that is why the obtained capillary pressure from Equation (3.25) turns out to be a relatively large negative number. This substantial change in capillary pressure will change the effective properties accordingly.

The saturation profile along MPL 3 for the different current densities are presented in Figure 3.5. As expected from Figure 3.4, the saturation decreases, from 0.35 to 0.2, when the liquid water is evaporated completely to a critical value given by the Kelvin equation, as described by Equation (3.25). Due to the small sizes of the hydrophilic pores, a capillary pressure of -20 kPa dictates a layer saturation of 20%, which is the

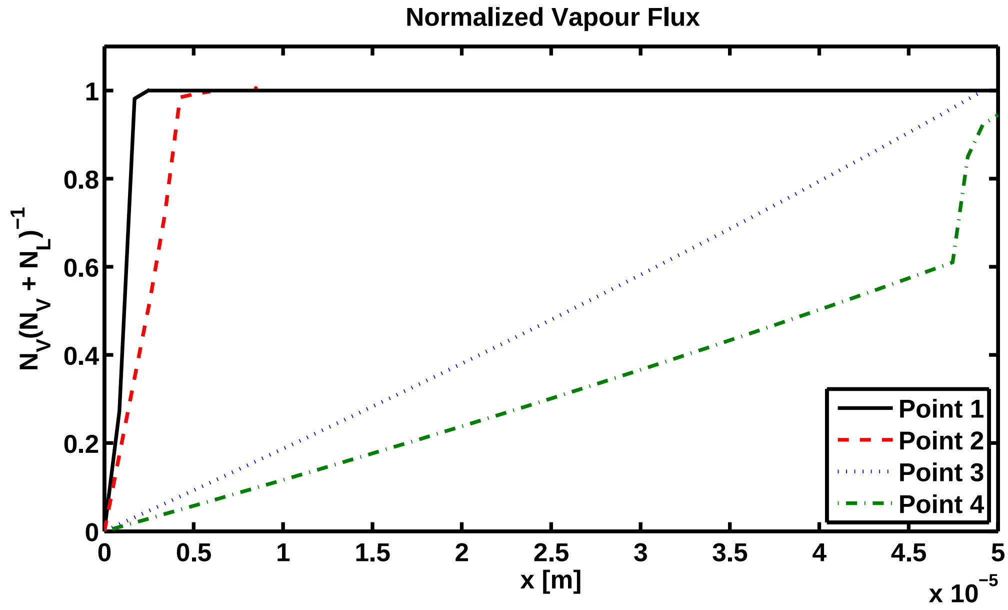

Figure 3.3 – Profiles of the normalized water vapour flux along MPL 3 for different current densities.

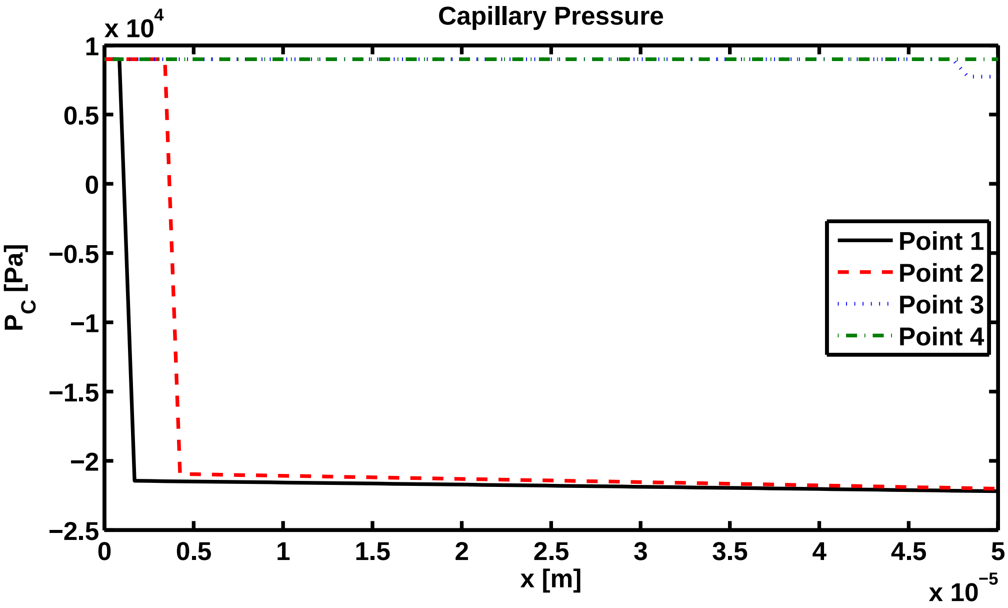

Figure 3.4 – Capillary pressure profiles along MPL 3 for different current densities.

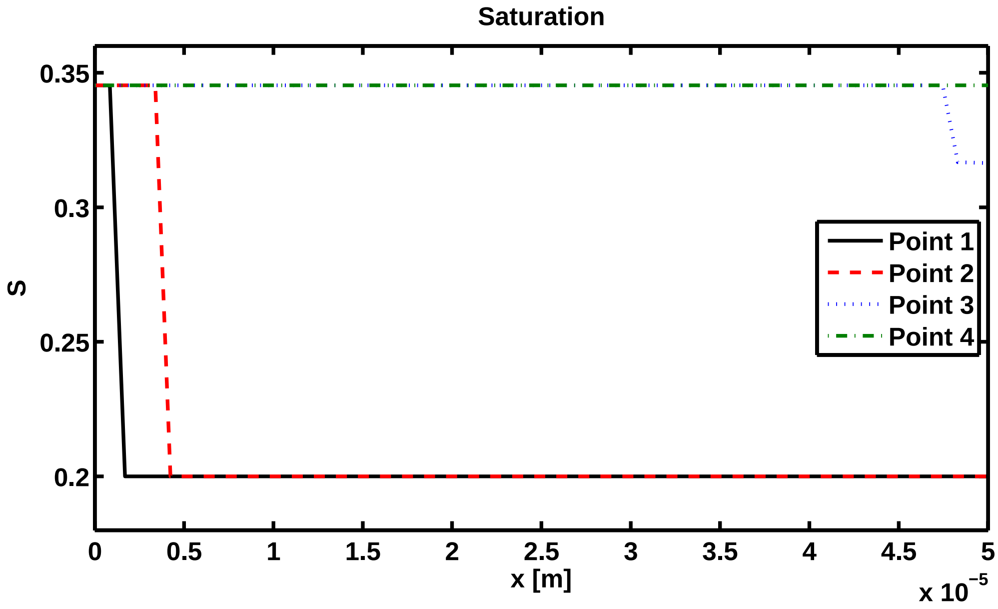

Figure 3.5 – Saturation profiles along MPL 3 for different current densities.

fraction of hydrophilic pores contained in MPL 3. When the evaporation rates are slower than the water production rates, the MPL saturation remains almost constant along the layer.

The liquid and gas relative permeabilities are presented in Figure 3.6 and Figure 3.7, respectively. When the MPL is running dry, the liquid relative permeability decreases to zero due to the low saturation values, while the gas relative permeability is enhanced. When the MPL is running wet, the liquid relative permeability is moderately enhanced (from 0 to around 0.1), but the gas relative permeability is severely decreased (from 0.65 to 0.08).

The liquid-gas interfacial surface area per unit volume profiles along the MPL are presented in Figure 3.8. Similar to the other effective properties studied, the decrease in saturation for the dry MPL cases leads to slightly lower interfacial surface area when compared to the wet MPL counterparts. The interfacial surface area only decreases by 0.61% if the MPL is running dry.

As previously mentioned, the reason for the solution bifurcation shown in Figure 3.1 is because since liquid water is entering the GDL and the capillary pressure is near 9 kPa, the GDL floods and mass transport limitations in the GDL lead to low oxygen concentrations at the MPL/GDL interface. The described scenario can be observed from the oxygen pressure profiles along the MPL, shown in Figure 3.9. The first thing to notice is that the oxygen pressure gradients are very modest, due to the low current densities studied and the high oxygen diffusivity inside the MPL.

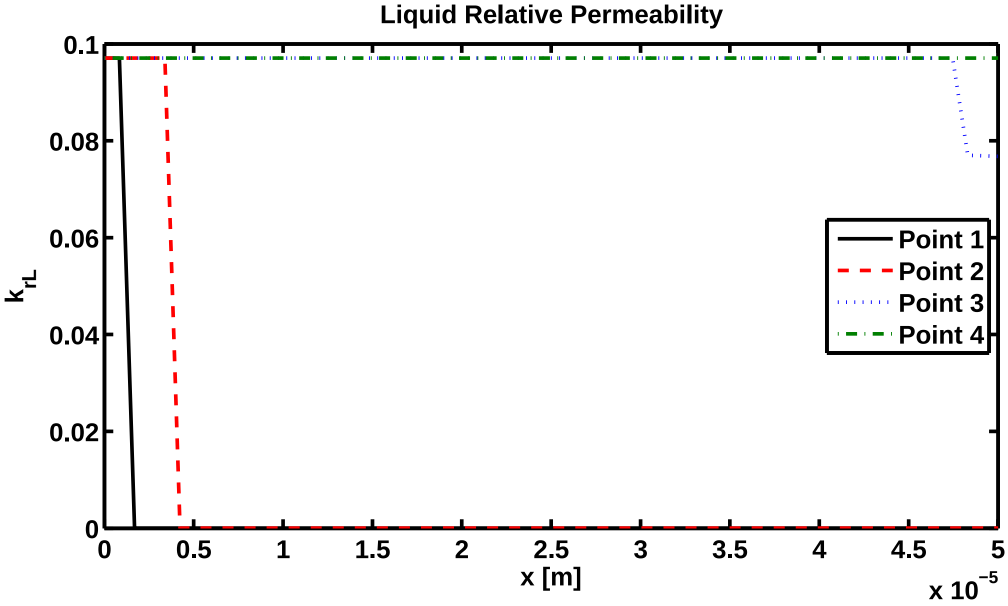

Figure 3.6 – Liquid relative permeability profiles along MPL 3 for different current densities.

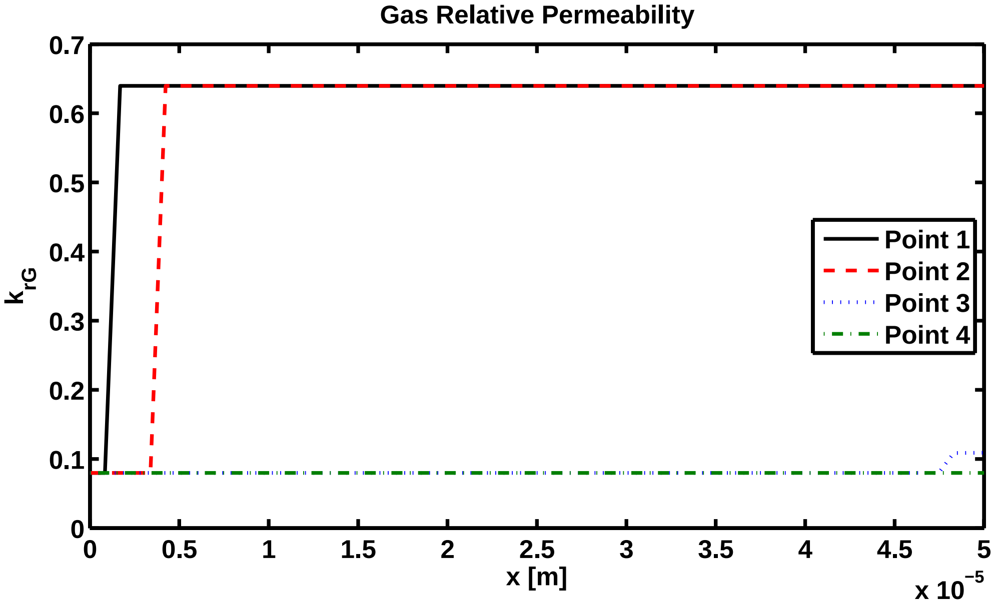

Figure 3.7 – Gas relative permeability profiles along MPL 3 for different current densities.

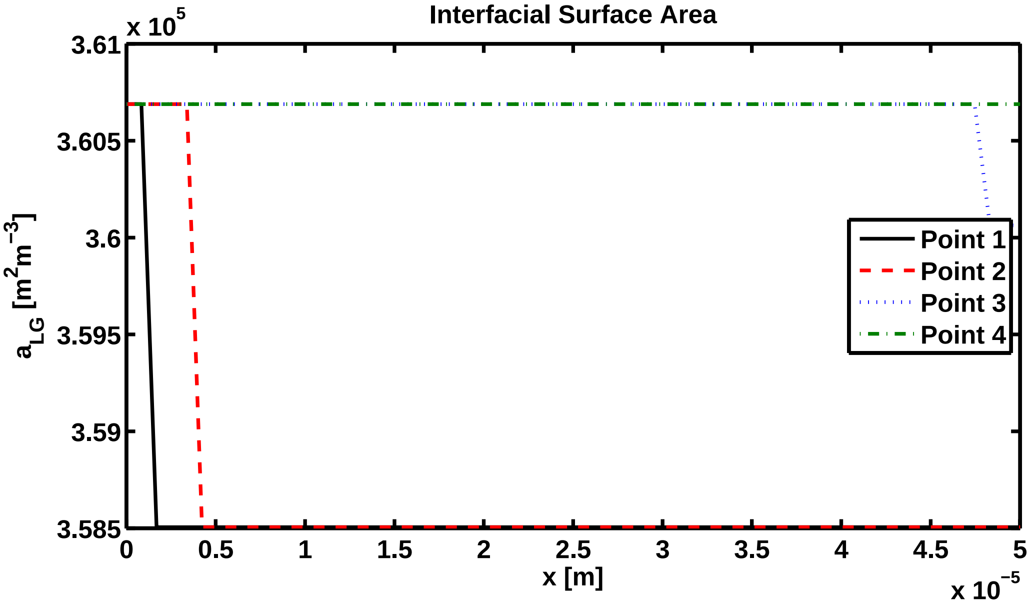

Figure 3.8 – Liquid-gas interfacial surface area profiles along MPL 3 for different current densities.

However, the profiles corresponding to dry MPLs have a much higher oxygen partial pressure than the wet MPL at the MPL-GDL interface. When the liquid water is not evaporated, the capillary pressures of the layer will lead to a GDL saturation of 0.95, which leads to the small limiting currents observed in the polarization curve for this MPL configuration.

The vapour pressure profiles along MPL 3 are presented in Figure 3.10. Due to the way in which the vapour concentration boundary conditions are implemented, the value of the vapour pressure increases with current density because water generation is directly proportional to current generation, and most the water generated is turning into vapour. For the first three points, the vapour pressure increases with current density accordingly. For Point 4, even though the current density value is similar to the one corresponding to Point 2, the vapour pressure is higher due to the high GDL saturations corresponding to the larger capillary pressure of Point 4.

Finally, the evaporation-condensation conversion rate along MPL 3 at different current densities is presented in Figure 3.11. Negative values of this term indicate that water is evaporated; and a value of zero indicates that at that point all the liquid water has been transformed to vapour, and thus no more water can be evaporated. For Point 1 and Point 2, all the water generated is quickly evaporated and thus the evaporation-condensation conversion term goes to zero very early along the MPL. For Point 3, water is evaporated along most of the MPL, and all the produced water is finally evaporated near the MPL/GDL interface. For Point 4, the evaporation-

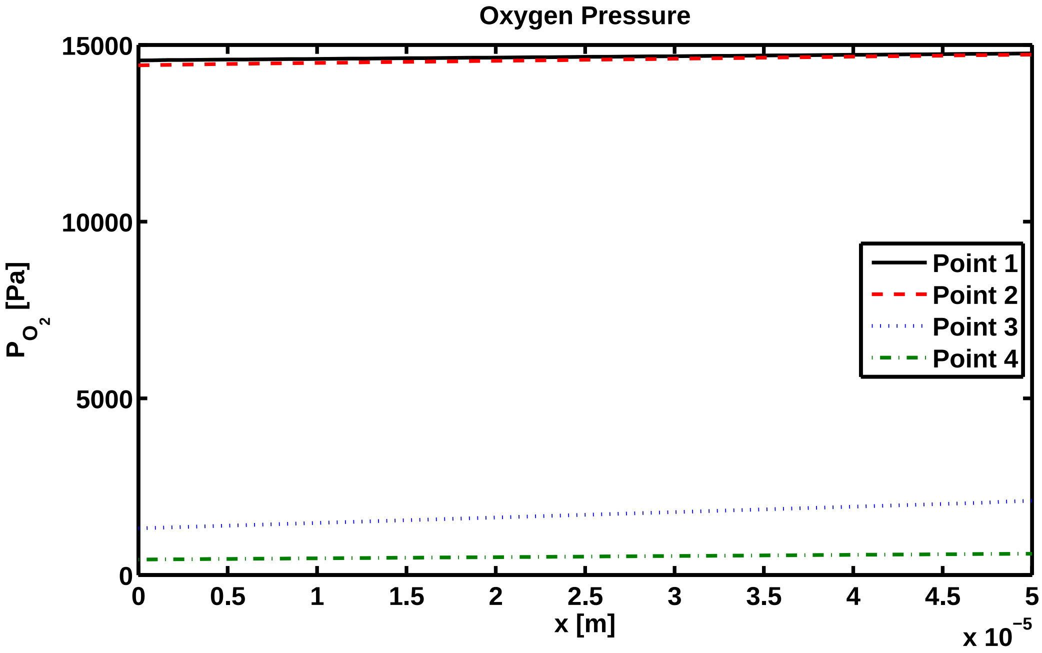

Figure 3.9 – Oxygen partial pressure profiles along MPL 3 for different current densities.

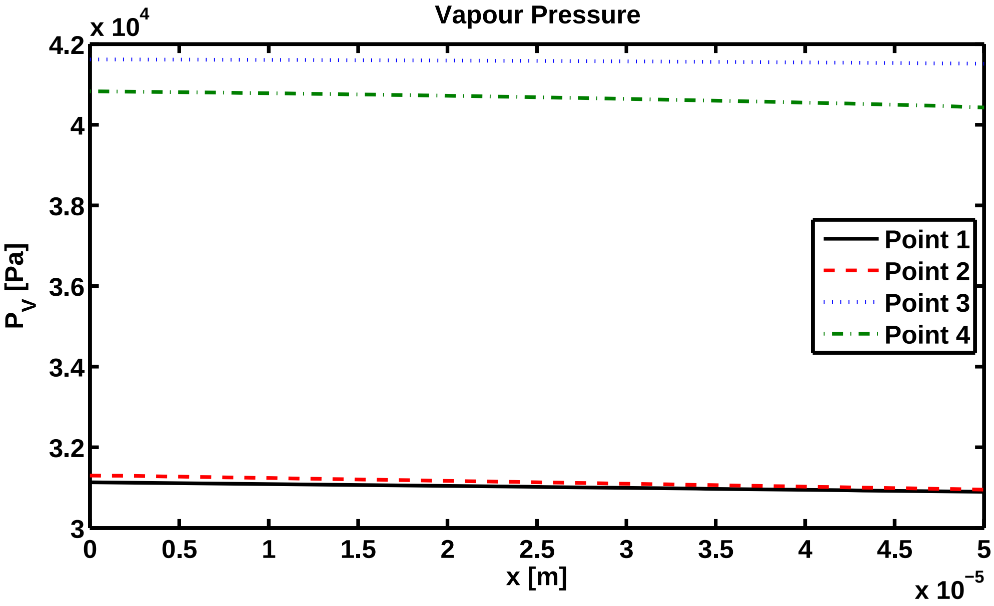

Figure 3.10 – Water vapour partial pressure profiles along MPL 3 for different current densities.

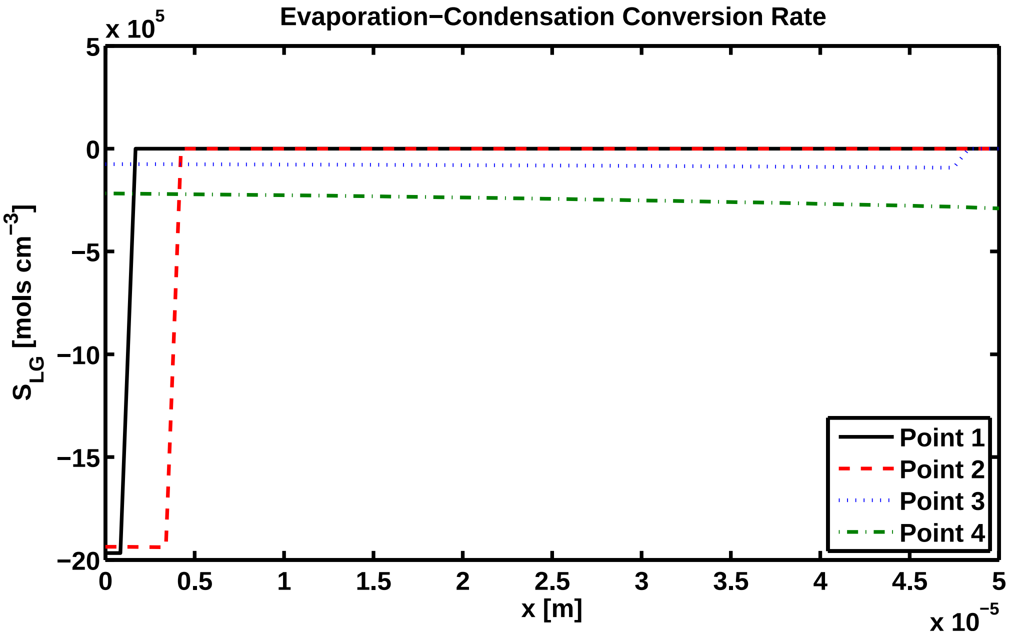

Figure 3.11 – Evaporation-condensation conversion rate term S_{LG} for MPL 3 at different current densities.

condensation conversion term is always negative because the MPL cannot evaporate all the water, so there is always liquid to available for evaporation.

3.2.2 Effects of Liquid Pressure Boundary Condition

The effects of liquid pressure boundary condition are closely related to overall cell performance. Mass transport limitations occurs when the GDL saturation is high enough that reactant concentration at the MPL-GDL interface is low. GDL saturation is controlled by the capillary pressure at the GDL-MPL interface, which depends on the value of liquid pressure.

If the liquid breakthrough pressure at the catalyst layer-MPL interface is 4 kPa (instead of 9 kPa), the polarization curves for MPL 2 to MPL 6 are presented in Figure 3.12. By decreasing the liquid breakthrough pressure, the capillary pressure at the MPL-GDL interface is reduced, and thus mass transport limitations are alleviated.

A polarization curve corresponding to MPL 1 cannot be obtained for this configuration, because the capillary pressure will be negative near the GDL interface, and due to the lack of hydrophilic pores the liquid relative permeability and the interfacial surface area will be zero; but liquid water is still being produced at the catalyst layer, leading to non-physical conditions for the models. A transient model is needed for this case, where the water accumulation inside the hydrophobic catalyst layer will lead to higher capillary pressures for the MPL/GDL interface.

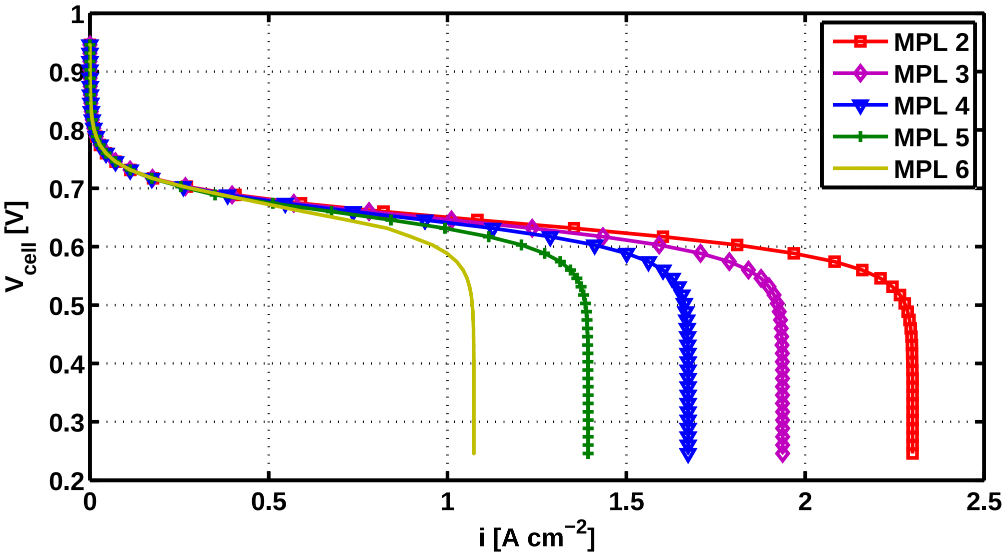

Figure 3.12 – Polarization curves for MPL configurations 2 through 6, showing the effects of hydrophilic pore fractions with small pores on cell performance, using liquid breakthrough pressure of 4 kPa.

Additionally, can be clearly observed that if GDL flooding does not take place, the more hydrophobic MPLs perform better. This is due to the lower saturation levels (lower fractions of hydrophilic pores), leading to larger limiting currents.

Using 4 kPa as the MPL liquid breakthrough pressure, polarization curves for MPL 7 to MPL 11 are presented in Figure 3.13. Results are very similar to the ones shown in Figure 3.12, revealing that if GDL flooding does not take place, the size of hydrophilic pores is irrelevant, and MPL saturation level is the only important factor that determines cell performance.

3.2.3 Summary and Parametric Studies

Polarization Curves

In order to analyse the combined effects of MPL liquid breakthrough pressure and evaporation rate constant, the MPL model was implemented using values of 0.0001, 0.0005, and 0.001 $m^{-3}s^{-1}$. For each value of evaporation rate, the liquid breakthrough pressure was assumed to be 4000, 6000, and 9000 Pa.

The polarization curves for evaporation rates of 0.0001, 0.0005, and 0.001 $m^{-3}s^{-1}$ are presented in Figures 3.14, 3.15 and 3.16 respectively. This study verifies that the evaporation rates and cell performance are not enhanced when the hydrophilic pores are large if compared to the hydrophobic pores. An exception to the last claim is MPL 11, corresponding to an evaporation rate of 0.001 $m^{-3}s^{-1}$ and an MPL liquid

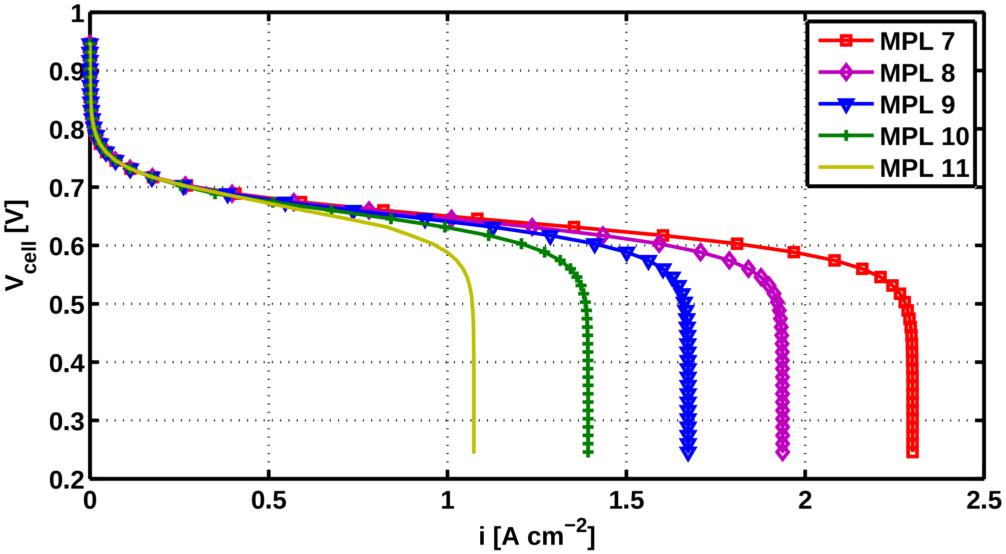

Figure 3.13 – Polarization curves for MPL configurations 7 through 11, showing the effects of hydrophilic pore fractions with large pores on cell performance, using liquid breakthrough pressure of 4 kPa.

breakthrough pressure of $9000\,Pa$, where a slight performance increase prior to the mass transport limitation region is observed but due to the high capillary pressure the limiting current is less than $0.03\,Acm^{-2}$, which makes this MPL configuration impractical for any real application.

As mentioned in Section 3.2.1, the performance for cells with low evaporation rates benefits the hydrophobic MPLs. However, by looking at MPL 3 and MPL 4 in Figure 3.16, one can clearly obtain better cell performance than MPL 1 thanks to the larger evaporation rates.

Is observed that the mass limited current density does not change with MPL configuration. However, for MPL 3 and MPL 4 all the water is evaporated and that translates into a maximum current density of over $0.75\,Acm^{-2}$, larger than the mass limited current density. By comparison, the completely hydrophobic MPL 1 can just go over $0.7\,Acm^{-2}$ before encountering the mass transport limitation region.

Additionally, recall from Figure 2.39 and Figure 2.37 that the liquid-gas interfacial surface area per unit volume corresponding to MPL 3 and MPL 4 are very similar. However, for very low saturations and capillary pressures the interfacial surface area of MPL 4 is higher than the interfacial surface area of MPL 3. In Figure 3.16 MPL 4 outperforms MPL 3 when the liquid breakthrough pressure is $6000\,Pa$ because since the evaporation rate constant is high the saturation of the MPL drops, and thus the performance of MPL 4 becomes better than the performance of MPL 3. This situation

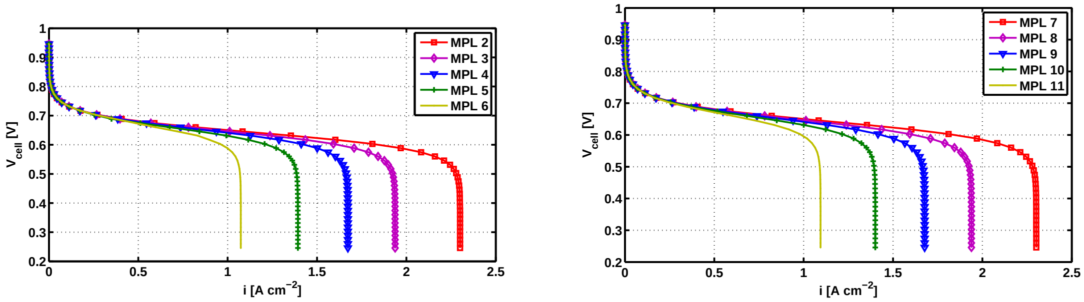

a) Liquid breakthrough 4000 Pa b) Liquid breakthrough 4000 Pa

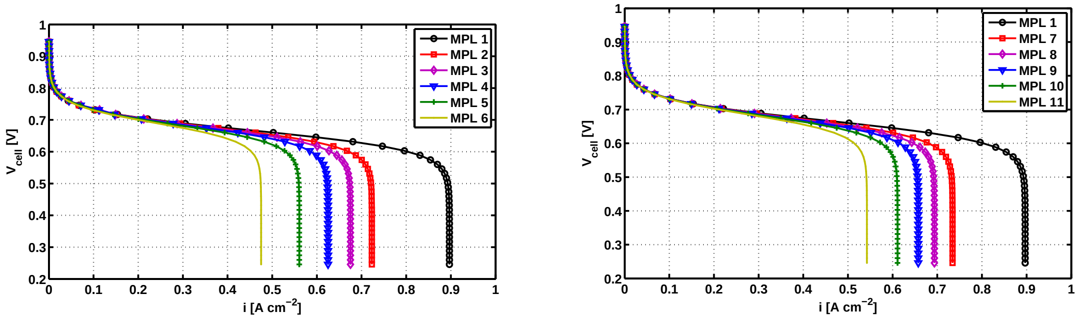

c) Liquid breakthrough 6000 Pa d) Liquid breakthrough 6000 Pa

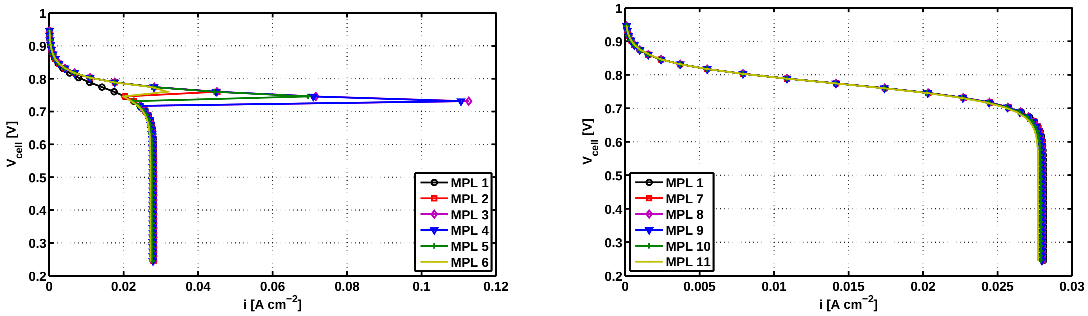

e) Liquid breakthrough 9000 Pa f) Liquid breakthrough 9000 Pa

Figure 3.14 – Polarization curves for different MPL configurations and different liquid breakthrough pressures, evaporation rate constant of 0.0001 $m^{-3}s^{-1}$

does not occur for a liquid breakthrough pressure of $9000\,Pa$ because saturation is slightly higher for the capillary pressures of the MPL.

Internal Solution Profiles

For this study, MPL 2 was selected because it offers modest evaporation enhancement and the cell performance is not too far off the completely hydrophobic MPL. The MPL liquid breakthrough pressure is $9000\,Pa$, and the evaporation rate constant is $0.001\,m^{-3}s^{-1}$, which is the value at which performance bifurcation starts to occur for MPL 2. The obtained polarization curve for this MPL configuration is presented in Figure 3.17. The presented polarization curve illustrates two points at which internal profiles were obtained. Point 1 corresponds to a current density of around $0.12\,Acm^{-2}$ where the liquid water evaporates; while Point 2 corresponds to the last point of the polarization curve, where water generation rates are higher than evaporation rates, therefore liquid water travels to the GDL and flooding takes place. The current density corresponding to GDL mass transport limitations for this test configuration is $0.07\,Acm^{-2}$.

The capillary pressure profile corresponding to the selected points is presented in Figure 3.18. Even though the current density corresponding to Point 1 and Point 2 are very similar, the capillary pressure profiles are vastly different. This is because Point 1 corresponds to the dry MPL regime, while Point 2 corresponds to the wet MPL regime.

The saturation profiles corresponding to the capillary pressures presented in Figure 3.18 are presented in Figure 3.19. As discussed in Section 3.2.1, saturation levels for dry conditions are always lower than the levels of the wet conditions. For the GDL, the saturation values are 0 and 0.95 for the dry and wet regimes, respectively.

The reason why the current density for the selected points in the polarization curve is similar can be explained by looking at the oxygen partial pressure profiles along the MPL, presented in Figure 3.20. Even though the overpotential for Point 1 is $0.45\,V$ and for Point 2 is $0.95\,V$, the amount of water going to the GDL hinders the gaseous transport considerably at very large overpotentials.

3.3 Conclusions

From the parametric studies performed on the MPL model, is observed that the cell performance is strongly linked to the MPL liquid breakthrough pressure. Mass transport limitations are improved if the MPL liquid breakthrough pressure is small. Interestingly, the limiting layer is not the MPL but the GDL instead.

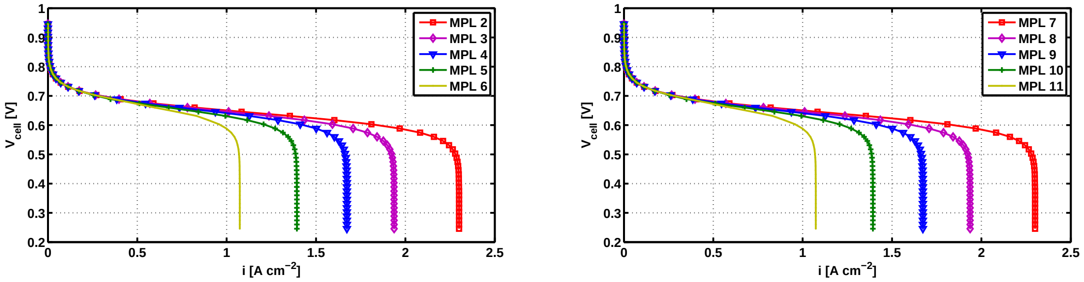

a) Liquid breakthrough 4000 Pa b) Liquid breakthrough 4000 Pa

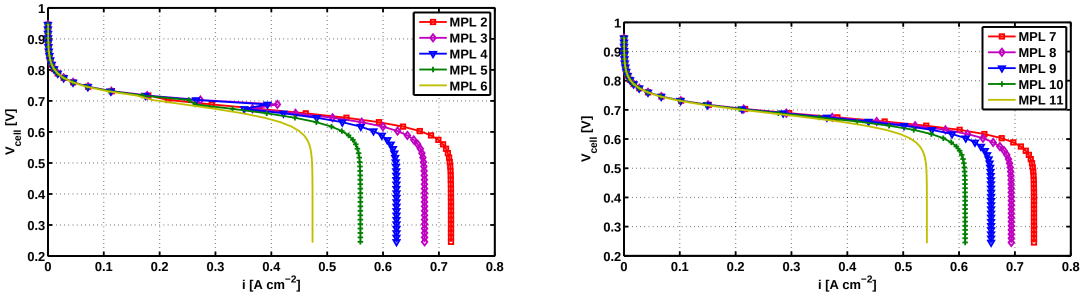

c) Liquid breakthrough 6000 Pa d) Liquid breakthrough 6000 Pa

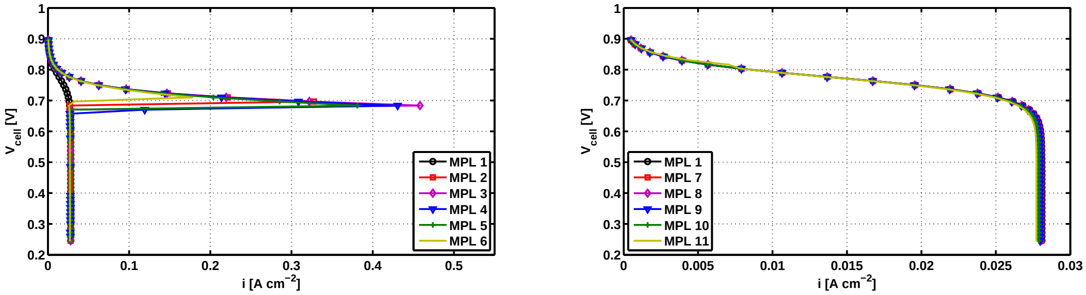

e) Liquid breakthrough 9000 Pa f) Liquid breakthrough 9000 Pa

Figure 3.15 – Polarization curves for different MPL configurations and different liquid breakthrough pressures, evaporation rate constant of $0.0005\,m^{-3}s^{-1}$

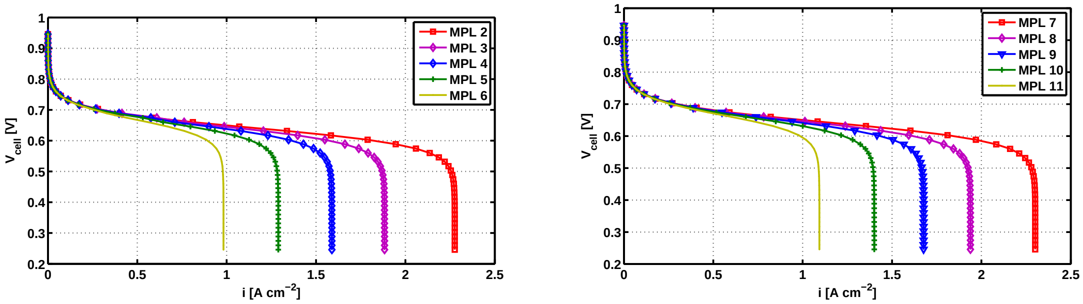

a) Liquid breakthrough 4000 Pa

b) Liquid breakthrough 4000 Pa

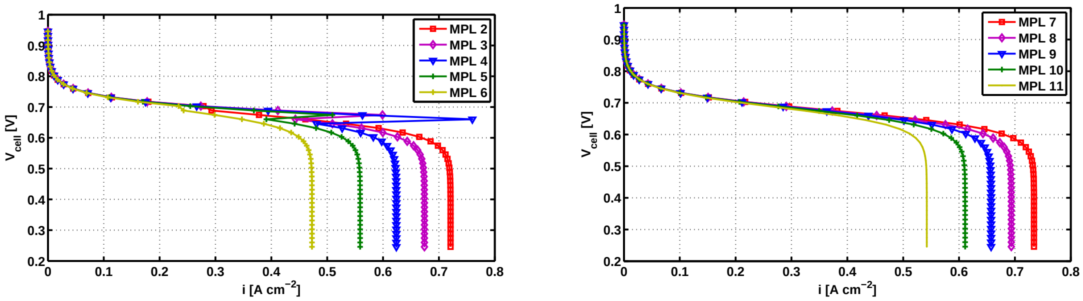

c) Liquid breakthrough 6000 Pa

d) Liquid breakthrough 6000 Pa

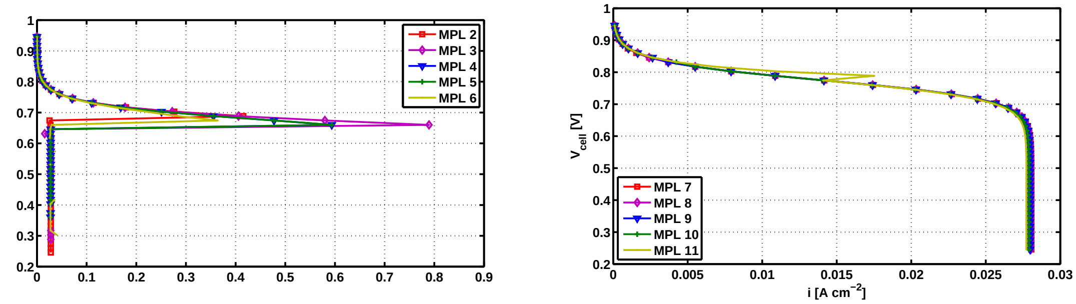

e) Liquid breakthrough 9000 Pa

f) Liquid breakthrough 9000 Pa

Figure 3.16 – Polarization curves for different MPL configurations and different liquid breakthrough pressures, evaporation rate constant of $0.001\,m^{-3}s^{-1}$

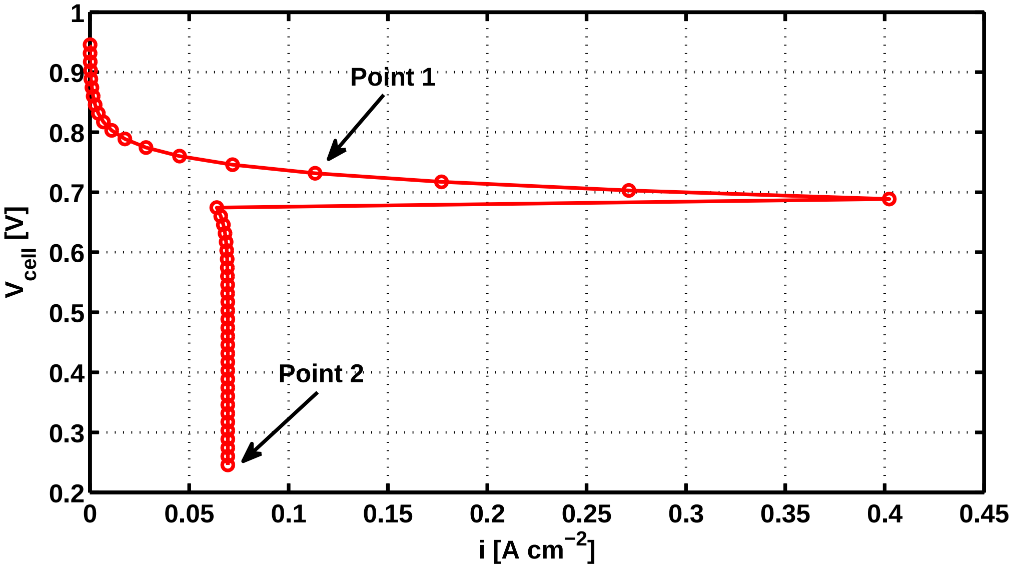

Figure 3.17 – Polarization curve for MPL 2, using liquid breakthrough pressure of 9000 Pa and evaporation rate of 0.001 $m^{-3}s^{-1}$.

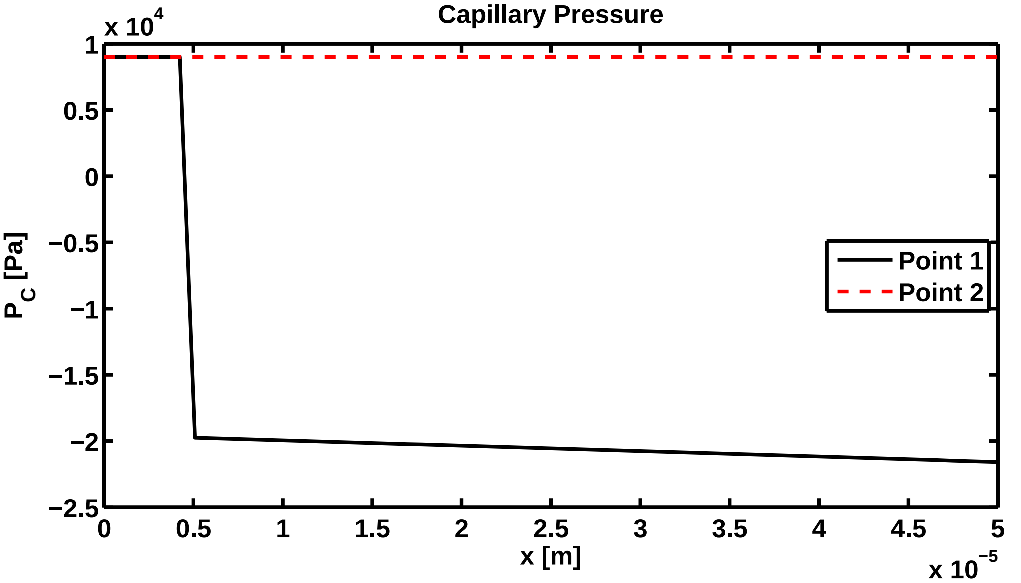

Figure 3.18 – Capillary pressure profiles for MPL 2, using liquid breakthrough pressure of 9000 Pa and evaporation rate of 0.001 $m^{-3}s^{-1}$.

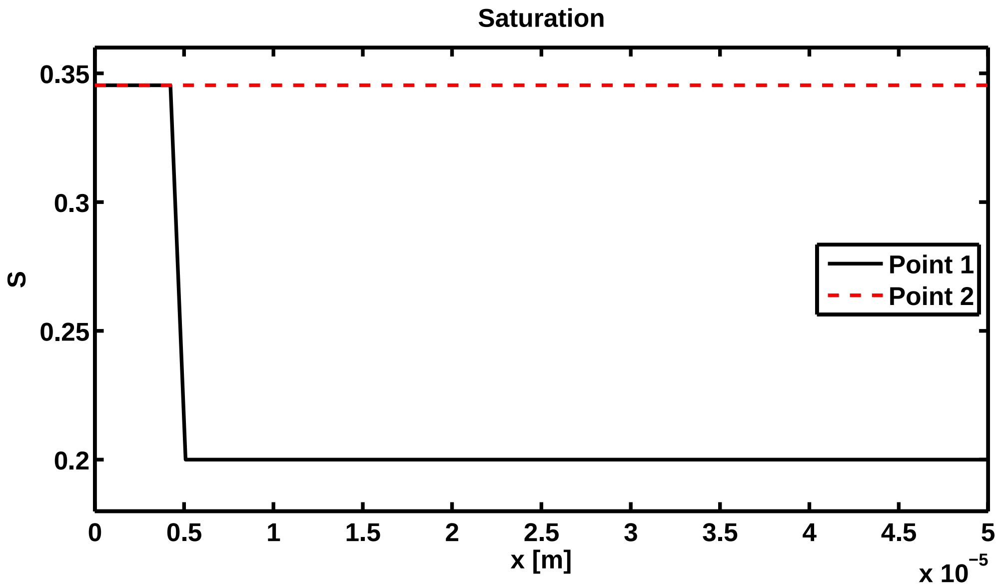

Figure 3.19 – Saturation profiles for MPL 2, using liquid breakthrough pressure of $9000\,Pa$ and evaporation rate of $0.001\,m^{-3}s^{-1}$.

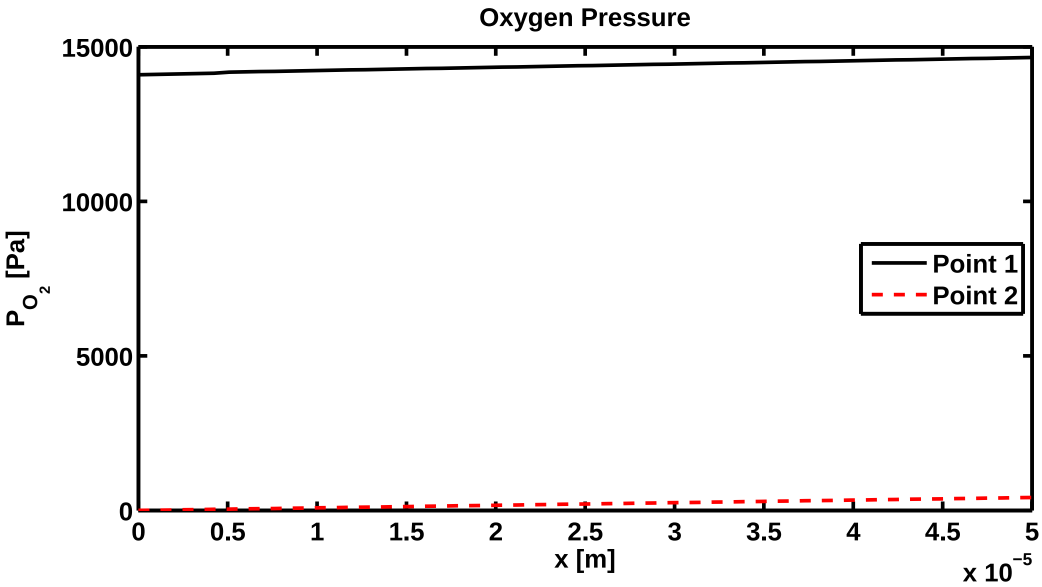

Figure 3.20 – Oxygen pressure profiles for MPL 2, using liquid breakthrough pressure of $9000\,Pa$ and evaporation rate of $0.001\,m^{-3}s^{-1}$.

When the MPL liquid breakthrough pressure is large, then the capillary pressure profile inside the MPL will be large. Due to the large pore sizes of the GDL, even a capillary pressure slightly above atmospheric pressure will promote GDL flooding. This effect can lead to very small current densities, such as the results obtained for MPLs with different pore morphology where the liquid pressure was assumed to be $9000\,Pa$ presented in Figure 3.14, Figure 3.15 and Figure 3.16.

When evaporation rates and the catalyst liquid breakthrough pressures are small, hydrophobic MPLs are the best performers, due to the lower saturations and higher gas relative permeabilities. For high evaporation rates, the cell performance is linked to the MPL morphology.

Adding small hydrophilic pores to the MPL increases the liquid-vapour interfacial surface area dramatically; this reveals that is MPLs are designed with networks of hydrophilic pores their performance will be superior than the performance of hydrophobic MPLs by delaying the onset of GDL flooding.

Chapter 4

CCL Model

4.1 Model Description

4.1.1 Model Formulation

A two-phase flow conventional cathode catalyst layer model (CCL) was implemented based on the previous MPL model.

Due to the lack of CCL samples to perform MIP and obtain a PSD and the fact that CCL PSDs look similar to the MPL PSD obtained [3], it was assumed that the PSD for the MPL could be also used as the PSD for a conventional catalyst layer. Due to the similarities of the fabrication methods of MPLs and CCLs, and the similarities in thickness and porosity, this assumption is justified.

The assumptions and conditions used to develop the proposed cathode catalyst layer model are:

1. One-dimensional.
2. Steady-state.
3. Isothermal.
4. Air can be taken as an infinite dilute solution of oxygen and water in nitrogen.
5. Convective transport effects are important.
6. Binary and Knudsen diffusion take place inside the layer.
7. Cathode side consists only of a catalyst layer and a GDL.
8. Water is produced in liquid form.

In a CCL, the mass conservation of the liquid and gas phases can be written as:

$$\nabla \cdot (\rho_L \vec{u}_L) = S_{LG} M_{H_2O} + \frac{i}{2\,F} M_{H_2O} \tag{4.1}$$

$$\nabla \cdot (\rho_G \vec{u}_G) = -S_{LG} M_{H_2O} - \frac{i}{4\,F} M_{O_2} \tag{4.2}$$

where i is the local current density, M_{O_2} is the molar mass of oxygen, and S_{LG} is given by Equation (3.3).

The conservation of water vapour in moles is given as:

$$\nabla \cdot \vec{N}_V = -S_{LG} \tag{4.3}$$

The conservation of oxygen and protons are given by:

$$\nabla \cdot \vec{N}_{O_2} = -\frac{i}{4\,F} \tag{4.4}$$

$$\nabla \cdot \vec{N}_{H^+} = -\frac{i}{F} \tag{4.5}$$

Using Darcy's law, the momentum conservation of the liquid and gas phases are given as:

$$\vec{u}_L = -\frac{k\,k_{rL}}{\mu_L} \nabla p_L \tag{4.6}$$

$$\vec{u}_G = -\frac{k\,k_{rG}}{\mu_G} \nabla p_G \tag{4.7}$$

The oxygen flux is defined as:

$$\vec{N}_{O_2} = -D^{eff}_{O_2,CCL} \nabla c_{O_2} + c_{O_2} \vec{u^*}_G \tag{4.8}$$

where $D^{eff}_{O_2,CCL}$ is the effective oxygen diffusion coefficient of the conventional cathode catalyst layer obtained using Equation (2.78) and $\vec{u^*}_G$ is the molar velocity defined by the ratio of total molar gas flux and total concentration:

$$\vec{u^*}_G = \frac{\vec{N}_{N_2} + \vec{N}_V + \vec{N}_{O_2}}{p_G} R_g\,T \tag{4.9}$$

The molar flux of water vapour is defined as:

$$\vec{N}_V = -D^{eff}_{V,CCL} \nabla c_V + c_V \vec{u^*}_G \tag{4.10}$$

where $D^{eff}_{V,CCL}$ is the effective diffusion coefficient of water vapour inside the catalyst layer.

To define the proton flux, the proton conductivity of Nafion can be written as:

$$\vec{N}_{H^+} = -\frac{\sigma_{Nafion}}{F} \nabla \eta \tag{4.11}$$

where σ_{Nafion} is the Nafion proton conductivity and η is defined as the positive overpotential,

$$\eta = E^{eq} + \phi_{el} - \phi_{Pt} \tag{4.12}$$

where E^{eq} is the equilibrium potential from the oxygen reduction reaction, ϕ_{el} is the potential of the electrolyte, and ϕ_{Pt} is the potential of the metal, which is assumed constant due to the much higher conductivity.

Finally, the local current is defined as:

$$i = i_0 \, A_{eff} \left(\frac{p_{O_2}}{p^{ref}_{O_2}} \right) \exp \left(\frac{\alpha_c \, F \, \eta}{R_g \, T} \right) \tag{4.13}$$

The parameters used to define the local current are the same ones defined in Section 3.1.2. The governing equations for the CCL are summarized in Table 4.1.

When all the liquid water generated is evaporated, the CCL model is reformulated in order to take into account the absence of a flowing, continuously connected liquid phase. The proposed technique is that when the liquid velocity is zero and the water generation term is smaller than the water evaporation term, the evaporation term and the water generation term must balance to zero,

$$S_{LG} + \frac{i}{2\,F} = 0 \tag{4.14}$$

Expanding the terms of the previous equation using Equation (3.3), the capillary pressure for the dry conditions is given by:

$$p_c = \frac{R_g \, T \, \rho_G}{M_G} \ln \left(\frac{i}{2\,F\,k^{evap}\,a_{LG}\,p^{sat}} + \frac{p_V}{p^{sat}} \right) \tag{4.15}$$

Equation (4.15) is an implicit equation, because the capillary pressure is required to calculate i and a_{LG}. The liquid pressure is then obtained by adding the gas pressure and the capillary pressure. Due to the presence of the water generation term, convergence rate of the dry CCL model is better than the convergence rates of the dry MPL model.

Table 4.1 – Summary of the governing equation of the CCL for a PEMFC.

Variable	Governing Equation CCL
$\vec{u}_L$	$\nabla \cdot (\rho_L \vec{u}_L) = S_{LG}\, M_{H_2O} + \frac{i}{2\,F} M_{H_2O}$
$\vec{u}_G$	$\nabla \cdot (\rho_G \vec{u}_G) = -S_{LG}\, M_{H_2O} - \frac{i}{4\,F} M_{O_2}$
$\vec{N}_{O_2}$	$\nabla \cdot \vec{N}_{O_2} = -\frac{i}{4\,F}$
$\vec{N}_V$	$\nabla \cdot \vec{N}_V = -S_{LG}$
p_L	$\vec{u}_L = -\frac{k_{sat}\, k_{r,L}}{\mu_L} \nabla p_L$
p_G	$\vec{u}_G = -\frac{k_{sat}\, k_{r,G}}{\mu_G} \nabla p_G$
c_{O_2}	$\vec{N}_{O_2} = -D^{eff}_{O_2,N_2} \nabla c_{O_2} + c_{O_2} \vec{u}^*_G$
c_V	$\vec{N}_V = -D^{eff}_{V,N_2} \nabla c_V + c_V \vec{u}^*_G$
$\vec{N}_{H^+}$	$\nabla \cdot \vec{N}_{H^+} = -\frac{i}{F}$
η	$\vec{N}_{H^+} = -\frac{\sigma_{Nafion}}{F} \nabla \eta$

For this model, similar to the MPL model, the implementation is also one-dimensional, the reason being the difficulty to define permeability, effective diffusivity, and the approach used to model the dried layer using a three-dimensional approach.

The solver used to obtain a numerical solution for the CCL model was BVP5C, from the Matlab library. Both the absolute and relative tolerances were set to 1×10^{-5}.

4.1.2 Boundary Conditions

To define the boundary conditions for the conventional catalyst layer model, electro-osmotic drag and water back diffusion across the membrane are neglected and therefore the flux of liquid water is zero. Assuming that the membrane is impermeable to gases, the fluxes of water vapour, oxygen, and all gaseous species are also zero at the interface between the cathode catalyst layer and the PEM. In summary:

$$N_V|_{x=0} = 0 \tag{4.16}$$

$$N_{O_2}|_{x=0} = 0 \tag{4.17}$$

$$u_G|_{x=0} = 0 \tag{4.18}$$

$$u_L|_{x=0} = 0 \tag{4.19}$$

The liquid pressure depends on the interplay between the anode and the cathode. In this case, it is taken as a known value at the PEM-catalyst layer interface:

$$p_L|_{x=0} = p_L^{mem} \tag{4.20}$$

where p_L^{mem} is a pressure value for the liquid pressure at the catalyst layer-membrane interface.

At the interface between the catalyst layer and the GDL, the gas pressure is assumed to be the total pressure in the gas channels,

$$p_G|_{x=L_{CCL}} = p^o \tag{4.21}$$

Implicitly, this equation assumes that the gas pressure drop along the GDL is given by Darcy's law, but due to the large GDL permeability values the pressure gradient is small.

Similarly, the oxygen and vapour concentration boundary conditions are defined as:

$$c_{O_2}|_{x=L_{CCL}} = \frac{p^o_{O_2}}{R_g T} - \frac{L_{GDL}\, i_{tot}}{4\, F\, D_{O_2,GDL} \left[(1 - S_{GDL})\, \varepsilon_{GDL}\right]^{1.5}} \tag{4.22}$$

$$c_V|_{x=L_{CCL}} = \frac{p_V^o}{R_g T} + \frac{N_V^L\, L_{GDL}}{D_{V,GDL}\left[(1 - S_{GDL})\, \varepsilon_{GDL}\right]^{1.5}} \tag{4.23}$$

where the second term on the right for both boundary conditions account for mass transport losses in the GDL, as explained in Chapter 3.

Since there is no electrolyte outside the CCL, the proton flux must be zero at the interface with the GDL:

$$N_{H^+}|_{x=L_{CCL}} = 0 \tag{4.24}$$

Finally, the cell overpotential is defined at the interface of the CCL and the GDL,

$$\eta|_{x=L_{CCL}} = \eta_L \tag{4.25}$$

The summary of the boundary conditions used for the CCL model is presented in Table 4.2. The additional parameters used to define the model are presented in Table 4.3

4.2 Results and Discussions

4.2.1 Comparison with Previous Models

The model formulated by Liu and Eikerling [1] for conventional cathode catalyst layer is based on PSD functions, and the formulation is very similar to the model proposed in this chapter. The transport properties are however, calculated differently. The model presented by Lui and Eikerling assumes a bimodal hydrophilic PSD, with a contact angle of 88°. The main differences between the two models are:

1. Knudsen diffusion coefficient and Knudsen radius: even though the expression used by Liu and Eikerling to estimate the Knudsen diffusion coefficients has the same form of Equation (2.76), they use a critical radius instead of the average Knudsen radius of the layer. This critical radius is not estimated from the PSD model, and is independent of saturation. Additionally, the exact value used for the simulations is not specified by Liu and Eikerling. In this case, a value of $30\,nm$ is used.

2. The expression used to estimate the effective diffusion coefficients as a function of saturation is different than the one implemented and used in this thesis. Having a bimodal PSD distributions used to represent the primary and secondary pores of a conventional cathode catalyst layer, Liu and Eikerling assume that

Table 4.2 – CCL boundary conditions.

Variable	CCL/PEM	CCL/GDL
$\vec{u}_L$	0	-
$\vec{u}_G$	0	-
$\vec{N}_{O_2}$	0	-
$\vec{N}_V$	0	-
p_L	p_L^{mem}	-
p_G	-	p_o
c_{O_2}	-	$\dfrac{p_{O_2}^o}{R_g T} - \dfrac{L_{GDL}\, i_{tot}}{4\, F\, D_{O_2,GDL}\, \left[(1 - S_{GDL})\, \varepsilon_{GDL}\right]^{1.5}}$
c_V	-	$\dfrac{p_V^o}{R_g T} + \dfrac{N_V^L\, L_{GDL}}{D_{V,GDL}\, \left[(1 - S_{GDL})\, \varepsilon_{GDL}\right]^{1.5}}$
$\vec{N}_{H^+}$	-	0
η	-	η_L

Table 4.3 – Summary of model parameters for CCL model.

Parameter	Value	Reference
α_c	1	[16]
T	75^oC	-
F	$96485\,C\,mol^{-1}$	-
R_g	$8.314\,J\,mol^{-1}K^{-1}$	-
k^{evap}	-	-
A^{eff}	2.6×10^5	[60]
p^o	$101325\,Pa$	-
i_0	$1.0174 \times 10^{-8}\,A\,cm^{-2}$	[90]
E^o	$1.1958\,V$	[90]
$p_{O_2}^{ref}$	$5\,atm$	[90]
σ_{mem}	$0.067\,S\,cm^{-1}$	[16]
L_{mem}	$0.005\,cm$	[16]
L_{CCL}	$15\,\mu m$	[16]
L_{GDL}	$250\,\mu m$	
ε_{GDL}	-	
ε_{CCL}	-	

the smallest pores do not contribute to gas transport. The expressions used to estimate the effective diffusion coefficients used for this comparison study has the following form:

$$D_{eff} = D_0 \frac{(X_p - X_\mu - X_c)^{2.4}}{(1 - X_c)^2 (X_p - X_c)^{0.4}} + D_{res} \qquad \text{if } S < \frac{X_\mu}{X_p} \tag{4.26}$$

$$D_{eff} = D_0 \frac{[(1 - S)X_p - X_c]^{2.4}}{(1 - X_c)^2 (X_p - X_c)^{0.4}} + D_{res} \qquad \text{if } S \geq \frac{X_\mu}{X_p} \tag{4.27}$$

where D_0 is the Knudsen diffusion coefficient, X_p is the volume fraction of void space of the catalyst layer, X_μ is the volume fraction of primary pores, X_c is the percolation threshold in the random network of secondary pores, and D_{res} is a residual diffusion coefficient.

3. Liu and Eikerling assumed that the exchange current density changes as a function of saturation. Additionally, the exchange current density is also related to a factor that takes into account the effective catalyst utilization. The local exchange current density implemented for the validation study has the following form:

$$i_0 = f_1 \, i_0^* \frac{a_{wall}}{a_{wall}^{max}} \frac{f_2}{X_{el}} \Gamma \tag{4.28}$$

where f_1 is a constant that represents the combined effect of platinum surface area and platinum loading, i_0^* is the generic exchange current density, a_{wall} is the wetted pore wall surface area obtained from the PSD model using Equation (2.63), a_{wall}^{max} is the total pore wall surface area obtained from the PSD model, f_2 is a constant that accounts for the reduction of platinum utilization due to the random and partially saturated porous structure, X_{el} is the volume fraction of the electrolyte phase for the catalyst layer, and Γ represents the platinum utilization factor. Since the value used for platinum utilization was not documented by Liu and Eikerling, a value of one was used.

4. Liu and Eikerling have an extra source term on the water conservation equation. Their model accounts for water generation due to the electrochemical reaction, an evaporation term, and a term that is intended to take electro-osmotic drag into account. Thus, the conservation of the liquid phase implemented for the validation study is given as:

Table 4.4 – Summary of model parameters for CCL model comparison [1].

Parameter	Value	Reference
D_{res}	$2 \times 10^{-10}\, m^2 s^{-1}$	[1]
f_1	250	[1]
f_2	0.1	[1]
i_0^*	$3.03 \times 10^{-9}\, A\, cm^{-2}$	[1]
n_{eo}	0 to 1.2	Assumed
p_G	$3\, atm$ to 1.2	[1]
p_L	$0.25\, atm$ to 1.2	[1]
T	60°C	[1]
X_p	0.37	[1]
X_μ	0.124	[1]
X_M	0.246	[1]
X_c	0.1	[1]
X_{el}	0.31	[1]
Γ	1	Assumed

$$\nabla \cdot (\rho_L \vec{u}_L) = S_{LG} M_{H_2O} + \frac{i}{F} M_{H_2O} \left(n_{eo} + \frac{1}{2} \right) \tag{4.29}$$

where n_{eo} is the electro-osmotic drag coefficient. The value of this coefficient is not specified by Liu and Eikerling. A value of unity is assumed. Electro-osmotic drag is only taken into account when comparing the model to the one implemented by Liu and Eikerling.

The values for all the constants required for the validation study are summarized in Table 4.4, using the parameters documented by Liu and Eikerling [1] as the source where applicable.

In order to compare the results, the liquid pressure boundary condition at the membrane/catalyst layer interface must be set to $0.25\, atm$, and the total gas pressure

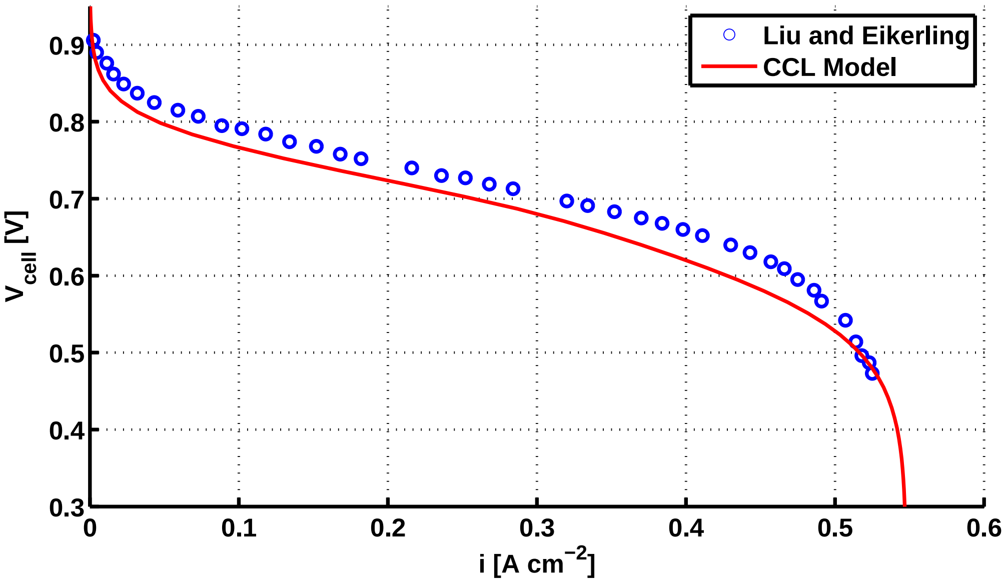

Figure 4.1 – Polarization curve corresponding the model implemented by Liu and Eikerling plotted against the curve obtained from the proposed CCL model.

must be set to $3\,atm$. The oxygen partial pressure at the GDL/channel interface is set to $0.63\,atm$. The catalyst layer length is set to $10\,\mu m$.

The bimodal PSD functions used to represent the catalyst layer are centred around radii of $3\,nm$ and $30\,nm$, each one with a spread of 2. The contact angle for both PSD modes is set to 88°, making the CCL completely hydrophilic.

The polarization curve for a GDL diffusion coefficient of $7.7 \times 10^{-4}\ cm^2\,s^{-1}$ is presented in Figure 4.1. Results from Lui and Eikerling are presented as discrete points because they were extracted from the original journal article. The differences between the polarization curve originally presented by Liu and Eikerling and the polarization curve obtained from this study arises because the implemented model is not completely described by the original source, as previously discussed. Another difference, which triggers most of the inconsistencies between the reported results from our implementation and the original source is the saturation profile inside the CCL.

The saturation profile along the CCL documented by Liu and Eikerling is presented in Figure 4.2, together with the saturation profile obtained from our implementation for a current density of $0.5\ A\,cm^{-2}$. An additional saturation profile, corresponding to the limiting current case, is also presented in order to appreciate the large saturation change along the CCL under there conditions.

The saturation profiles for the implemented model remains almost constant through the CCL, while the saturation profile shown by Liu and Eikerling is slightly lower than the saturation profiles obtained from our model implementation. Another difference is that the CCL saturation is the highest at the interface CCL/GDL for the model implemented by Liu and Eikerling, while for our model this interface corresponds to the lowest layer saturation. More discussion will be added later about this issue.

Additionally, with the PSD used to represent the CCL the absolute permeability estimated from the model is of the order of $1 \times 10^{-21}\ m^2$, and the total liquid permeability is of the order of $1 \times 10^{-27}\ m^2$. This small permeability value combined with very small liquid relative permeability, cause very large liquid pressure gradients along the layer and may potentially cause severe convergence issues for the model. Moreover, values found in the literature are several orders of magnitude larger than that obtained from this PSD. Eikerling [60] reported values of the order $1 \times 10^{-18}\ m^2$ for the total liquid permeability, using a very similar PSD and similar contact angle. Given that the expression used in this thesis has been shown to reproduce other results in the literature, see Section 2.5, there might be an error on the relative permeability calculations presented in article [60]. In order to compare the model in this thesis to those reported by Liu and Eikerling in reference [1], the values used for the comparison in this section are taken as $1 \times 10^{-18}\ m^2$, i.e. in the same order as the value documented by Eikerling, and is obtained from the PSD and multiplying the estimated permeability by a constant in order to keep the liquid pressure gradients small.

The plots of liquid relative permeability are presented in Figure 4.4. For large negative capillary pressures, the liquid relative permeability is almost zero, and then increases rapidly to 1.0 at a near zero capillary pressure. However, since the liquid pressure boundary condition is much smaller than the gas pressure boundary conditions, the liquid relative permeability profiles inside the CCL will be very close to zero. Very similar profiles for liquid permeability were reported by Eikerling [60].

The gas relative permeability, plotted against capillary pressure, is presented in Figure 4.5. As expected from a completely hydrophilic layer, the gas relative permeability goes to zero when the capillary pressure is greater to or equal to zero. However, values of gas relative permeability are larger than the values of liquid relative permeabilities for this layer configuration. Gas pressure gradients are relatively small inside the layer.

The liquid relative permeability is several orders of magnitude smaller than the gas relative permeability, which reveals that the changes in capillary pressure will be mostly dominated by the changes in liquid pressure. Since liquid pressure should

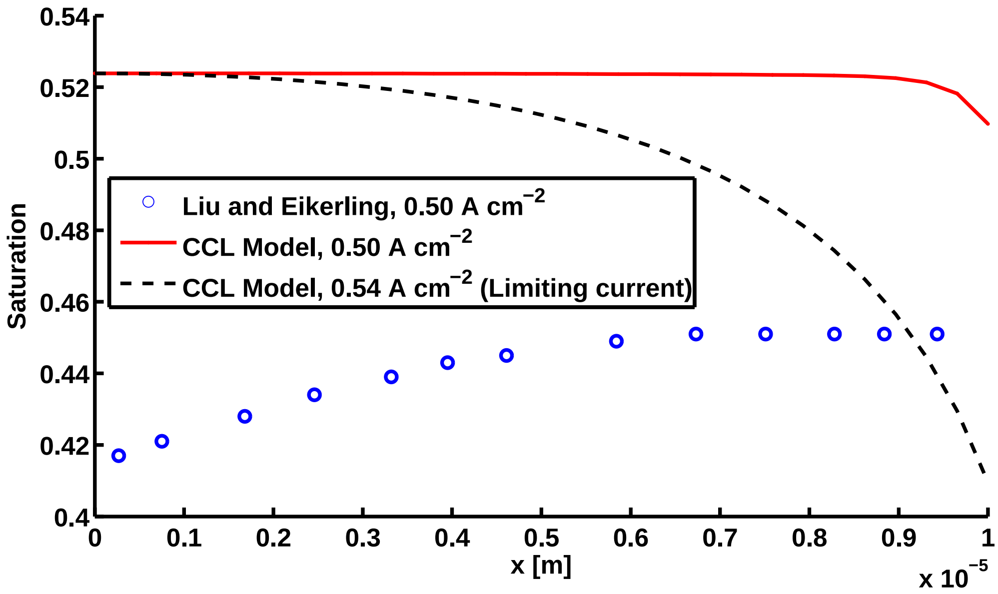

Figure 4.2 – Saturation profiles along CCL for model implemented by Liu and Eikerling (2008) and the implementation of a similar model developed for this thesis.

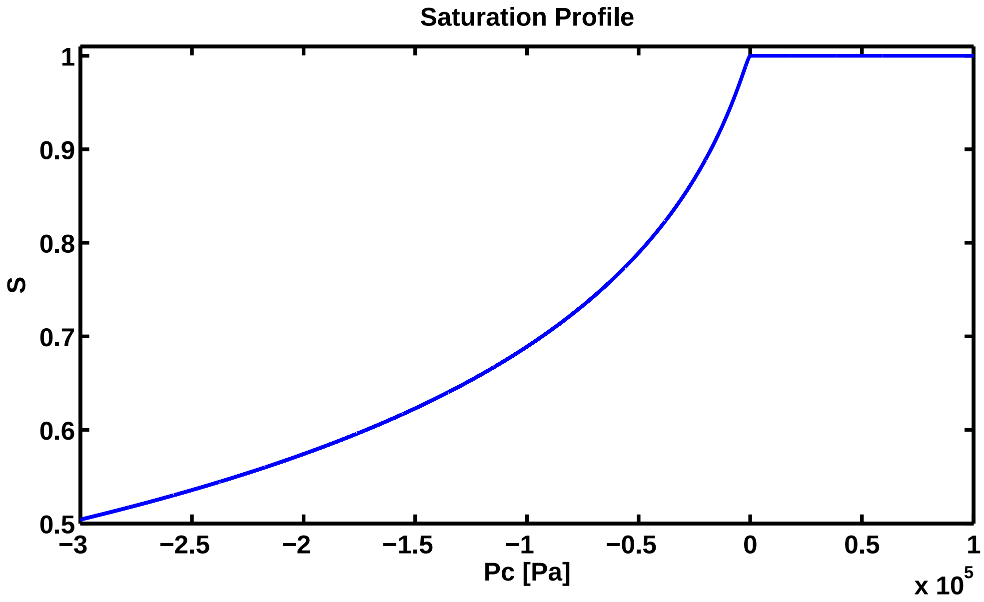

Figure 4.3 – Saturation profiles plotted against capillary pressure for the CCL used during the validation process.

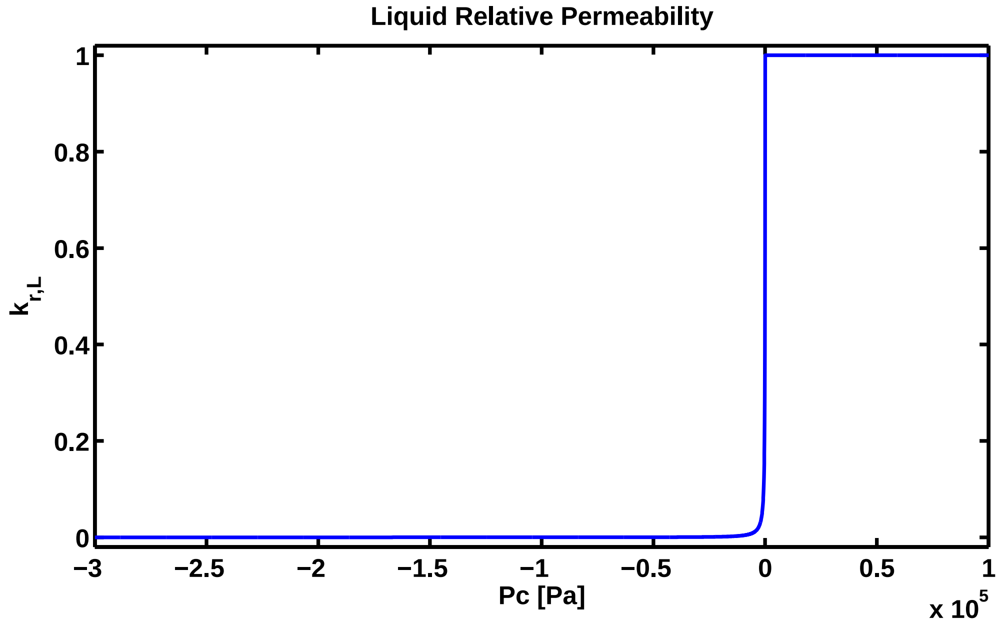

Figure 4.4 – Liquid relative permeability profiles plotted against capillary pressure for the CCL used during the validation process.

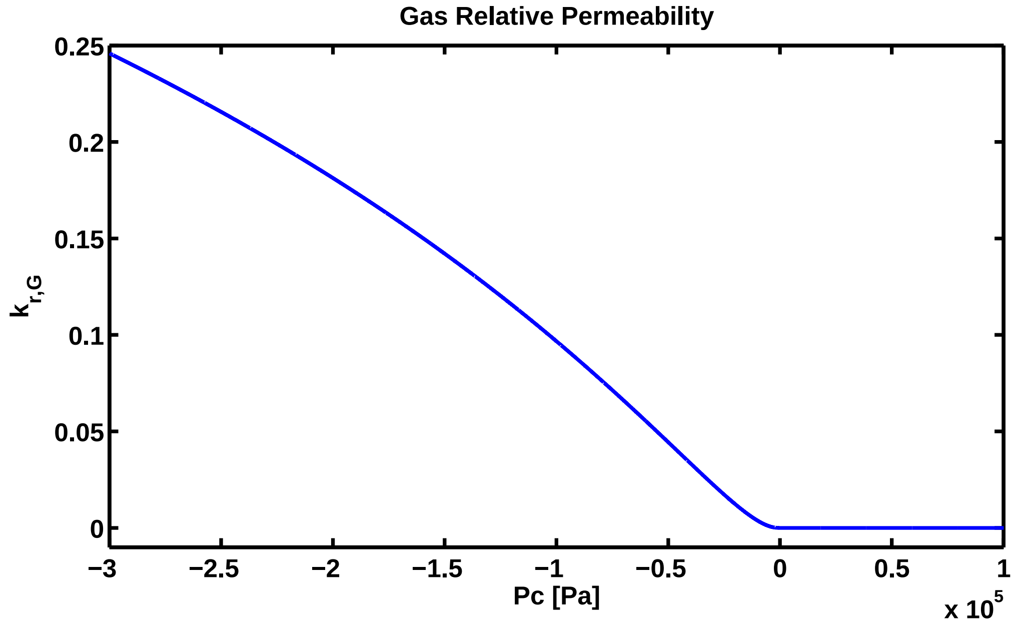

Figure 4.5 – Gas relative permeability profiles plotted against capillary pressure for the CCL used during the validation process.

decrease in order to create water movement through the layer, the saturation profiles along the layer should also decrease accordingly. Therefore, the saturation profiles presented by Liu and Eikerling [1] do not seem to match with the model expectation, and the profiles do not meet the zero velocity boundary condition implemented in the model because there is a noticeable capillary pressure gradient at the PEM/CCL interface.

The oxygen partial pressures from the two models, plotted for current densities of approximately 0.2, 0.31, and $0.4\,A\,cm^{-2}$ are shown in Figure 4.6. Note that for all the cases, the implementation of the model developed by Liu and Eikerling always underpredicts the oxygen profiles from the original source, leading to oxygen depletion inside the catalyst layer. Since other solution profiles, such as capillary pressure, overpotential, or proton flux are not provided, comparing all the predicted results is difficult.

The capillary pressure profiles for the implemented CCL model is presented in Figure 4.7, for current densities of 0.2, 0.31, and 0.4 $A\,cm^{-2}$. The maximum value for the capillary pressure is at the interface PEM/CCL, where the liquid pressure is the greatest. The profiles of liquid and gas pressure along the CCL, for the same current densities, are presented in Figure 4.8. Since the liquid pressure boundary condition is set to $0.25\,atm$ at the PEM/CCL interface, the gas pressure boundary condition is set to $3.0\,atm$ at the CCL/GDL interface, and the liquid relative permeability is very low, the capillary pressure stays always negative. Additionally, due to the low liquid relative permeability values, the liquid pressure gradients required to transport the water out of the layer produce negative liquid pressures, which is a non-physical scenario. This non-physical scenario is, however, likely to occur due to the large difference between the liquid and the gas pressure boundary conditions.

Additionally, note that due to the differences in relative permeability values, the liquid pressure gradient are much larger than the gas pressure gradients. This indicates that the saturation profiles along the layer should decrease toward the GDL interface rather than increase as shown by Liu and Eikerling [1].

Using the boundary conditions suggested by Liu and Eikerling, the saturation profiles inside the catalyst layer will be high, leading to very low effective diffusion coefficients. The low values of effective oxygen diffusion cause the oxygen partial pressures to drop very fast along the catalyst layer.

In order to obtain results, Liu and Eikerling must use a very low liquid pressure boundary condition. The reason for this is to avoid a fully saturated catalyst layer, originated from positive capillary pressures. Since this model does not take into account mixed wettability, both the liquid relative permeability and the effective

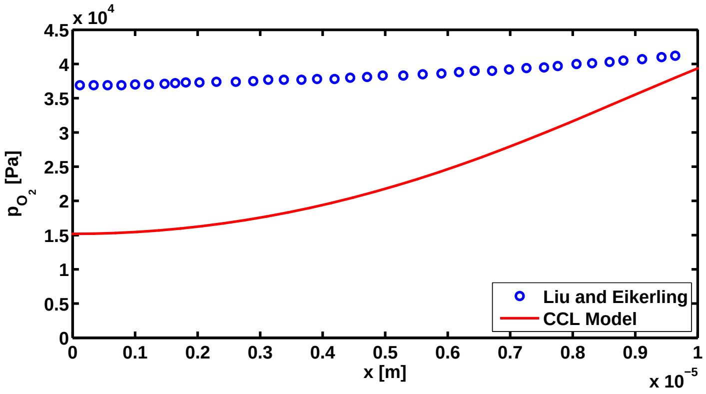

a) Current density appx. $0.2\,A\,cm^{-2}$

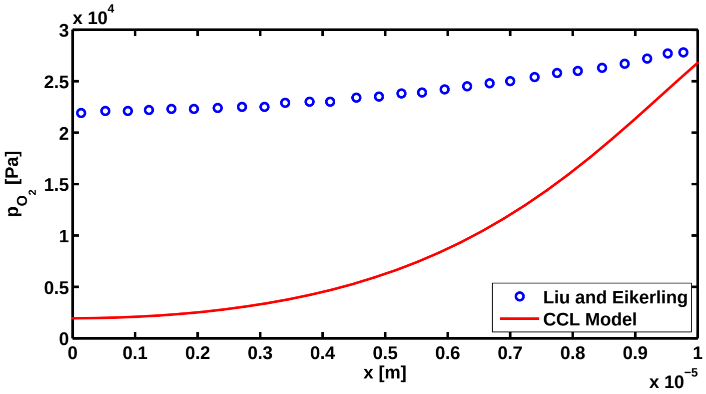

b) Current density appx. $0.3\,A\,cm^{-2}$

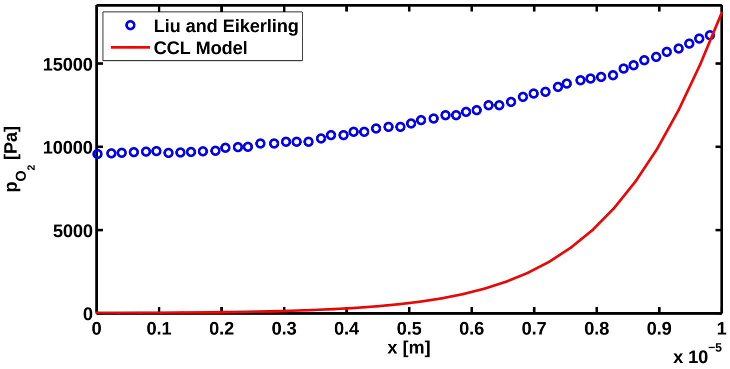

c) Current density appx. $0.4\,A\,cm^{-2}$

Figure 4.6 – Oxygen partial pressure profiles along cathode catalyst layer at different current densities.

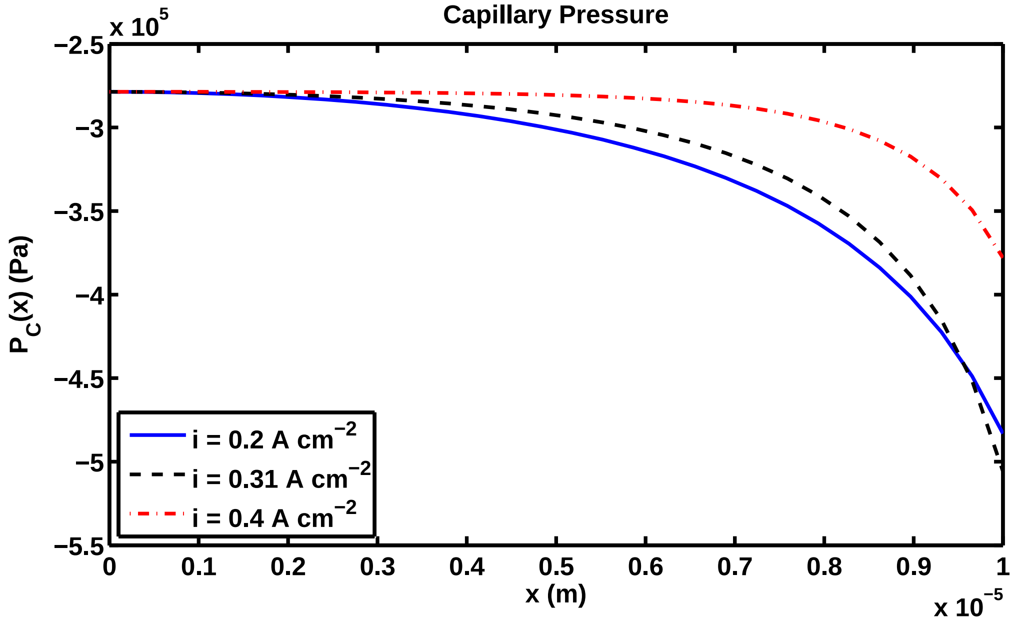

Figure 4.7 – Capillary pressure profiles along the CCL corresponding to the validation configuration.

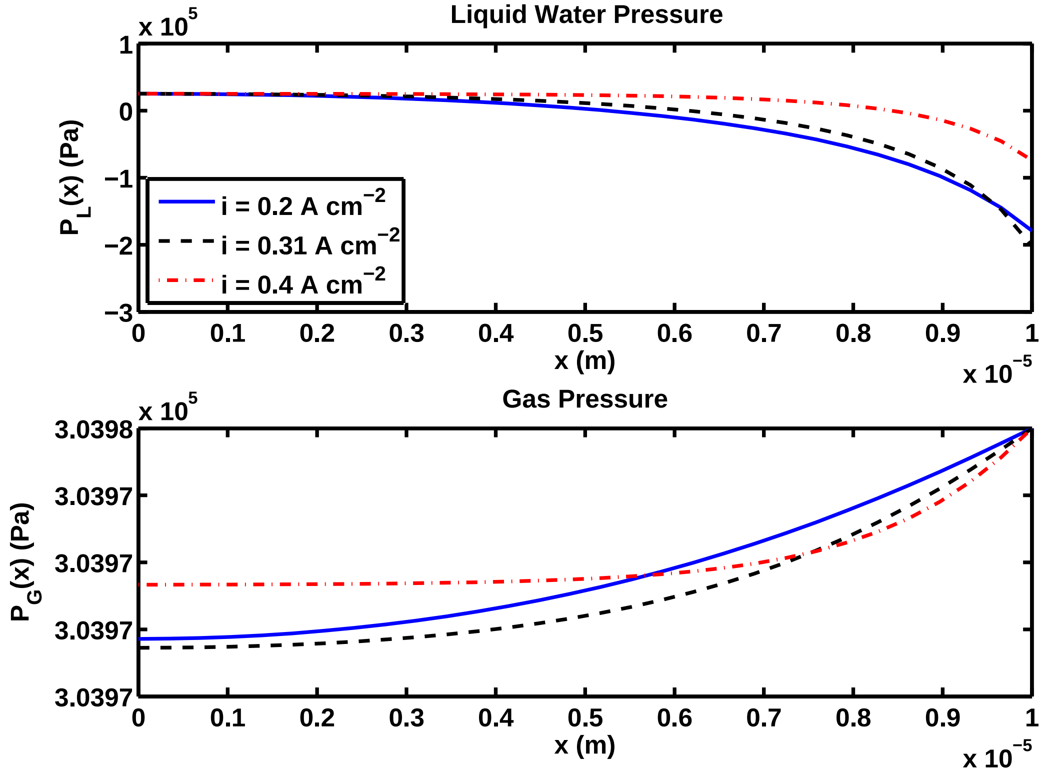

Figure 4.8 – Liquid and gas pressure profiles along the CCL corresponding to the validation configuration.

diffusivity values go to zero for positive capillary pressures. Our proposed model, on the other hand, is able to reproduce these kind of conditions.

To summarize, the model implemented by Liu and Eikerling [1] is similar to the CCL model implemented in this thesis. However, the boundary conditions used by Liu and Eikerling cannot simulate what happens inside the cathode of a PEMFC. If the total gas pressure is $3\,atm$ during operation, the liquid pressure cannot be $0.25\,atm$ inside the layer. Additionally, given the small value of liquid permeability and the low liquid pressure, the results presented by Liu and Eikerling are questionable in the sense that the liquid pressure profiles (which are nor included in the original reference) will likely be negative toward the interface of the CCL with the GDL. Moreover,the model implemented by Liu and Eikerling seems to over predict the liquid permeability, because based on a similar PSD with the same contact angle, the estimated liquid permeability from the proposed PSD model is several orders of magnitude smaller than the value reported by Eikerling [60].

4.2.2 Catalyst Layer Performance

A total of eleven CCL configurations were tested to determine the optimal wettability and microstructure of conventional cathode catalyst layers. The PSD used are illustrated in Figure 2.24 and Figure 2.25. The description of the layer configurations is presented in Table 4.5.

Table 4.5 – PSD functions for the GDL configurations tested in this study.

CCL number	Percent HI pores	Percent HO pores
1	0	100
2	10 (small pores)	90 (large pores)
3	20 (small pores)	80 (large pores)
4	30 (small pores)	70 (large pores)
5	40 (small pores)	60 (large pores)
6	50 (small pores)	50 (large pores)
7	10 (large pores)	90 (small pores)
8	20 (large pores)	80 (small pores)
9	30 (large pores)	70 (small pores)
10	40 (large pores)	60 (small pores)
11	50 (large pores)	50 (small pores)

The polarization curves for the eleven CCL configurations, using a liquid pressure boundary condition of $p^o + 6000\,Pa$ and evaporation rate constants of $0.0005\,m^{-3}s^{-1}$,

$0.005\,m^{-3}s^{-1}$, and $0.05\,m^{-3}s^{-1}$ are presented in Figure 4.9. The selected liquid breakthrough pressure value is selected because it corresponds to the GDL liquid breakthrough pressure measured in-house. The values of evaporation rate constants used for this section were chosen based on the magnitude of the evaporation-condensation conversion rate; in such a way that by using the same PSD the behaviour of layers with evaporation rates smaller than the water production rates (promoting layer flooding) and evaporation rates larger than the water production rates (alleviating flooding).

Additionally, three different values of evaporation rate constants were used in order to gain understanding of the effects of this parameters on cell performance. Currently, a lot of uncertainty exists regarding the value of evaporation rate constant, and therefore we used different values to examine the impact of this parameter.

The first feature that can be noticed is that for an evaporation rate of $0.0005\,m^{-3}s^{-1}$, no significant performance increase can be observed between the different CCL configurations, and the completely hydrophobic CCL is the best performing configuration due to the slightly lower saturation, caused by the lack of hydrophilic pores and leading to a slightly higher limiting current when compared to the other ten configurations.

For evaporation rates of $0.005\,m^{-3}s^{-1}$ and $0.05\,m^{-3}s^{-1}$, CCL configurations 3, 4, and 5 offer a very similar performance, which is superior to the performance of the hydrophobic CCL configuration. CCL 3 is the best performing layer for both evaporation rate constants. This reveals that due to the higher evaporation rates obtained from the addition of small hydrophilic pores, adding up to 20% of the total pore volume fraction of the CCL, cell performance can be greatly increased.

Due to the enhanced liquid-gas interfacial surface area of the mixed wettability CCLs, very large current densities can be achieved, past what would be the limiting current density of the layer. The reason is because since evaporation rates are large enough to keep up with the water production rates of the layers, keeping the GDL unsaturated. Once water starts to invade the large pores of the GDL, the current density decreases rapidly to the corresponding limiting current.

Taking a closer look at CCL 3, Figure 4.10 presents the polarization curves obtained under two different liquid pressure boundary conditions: $p^o + 6000\,Pa$ and $p^o + 4000\,Pa$. For each liquid pressure boundary condition, three values of evaporation rate constants are used: 0.0005, 0.005, and $0.05\,m^{-3}s^{-1}$. It can be observed that under conditions of high evaporation, the performance increase of CCL 3 is substantial, allowing to draw current densities up to five times larger than the mass-transport limited current density.

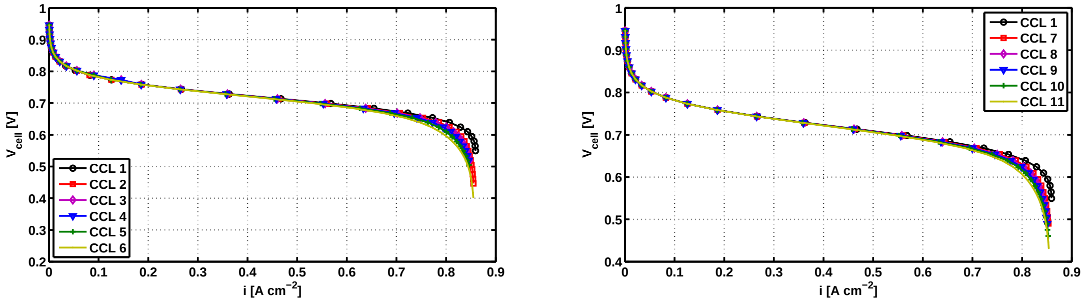

a) Liquid breakthrough 6000 Pa, $k^{evap} = 0.0005\,m^{-3}s^{-1}$.

b) Liquid breakthrough 6000 Pa, $k^{evap} = 0.0005\,m^{-3}s^{-1}$.

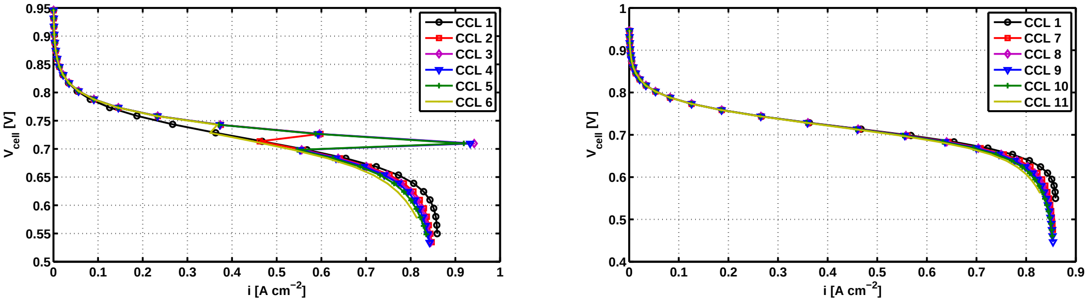

c) Liquid breakthrough 6000 Pa, $k^{evap} = 0.005\,m^{-3}s^{-1}$.

d) Liquid breakthrough 6000 Pa, $k^{evap} = 0.005\,m^{-3}s^{-1}$.

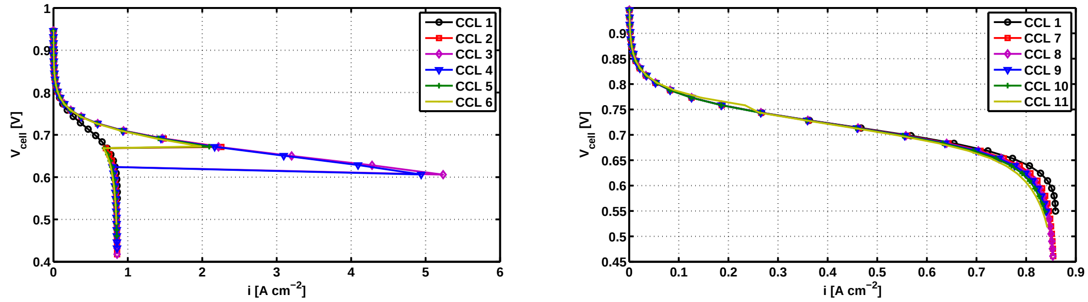

e) Liquid breakthrough 6000 Pa, $k^{evap} = 0.05\,m^{-3}s^{-1}$.

f) Liquid breakthrough 6000 Pa, $k^{evap} = 0.05\,m^{-3}s^{-1}$.

Figure 4.9 – Polarization curves for CCL configurations using different evaporation rate constants.

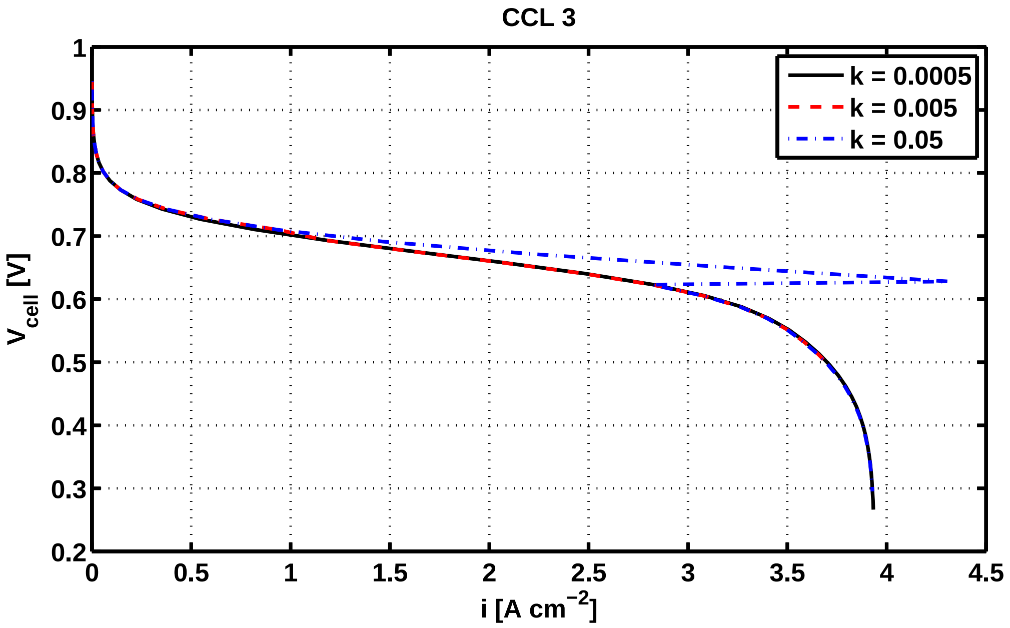

a) Liquid breakthrough 4000 Pa

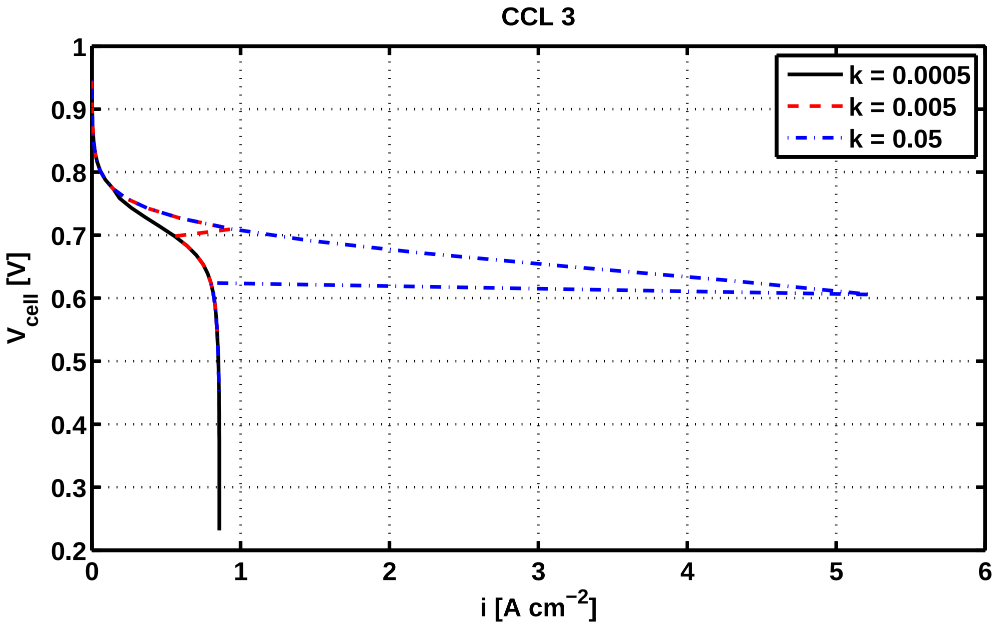

b) Liquid breakthrough 6000 Pa

Figure 4.10 – Polarization curves for CCL 3 using different liquid breakthrough pressures and evaporation rate constants.

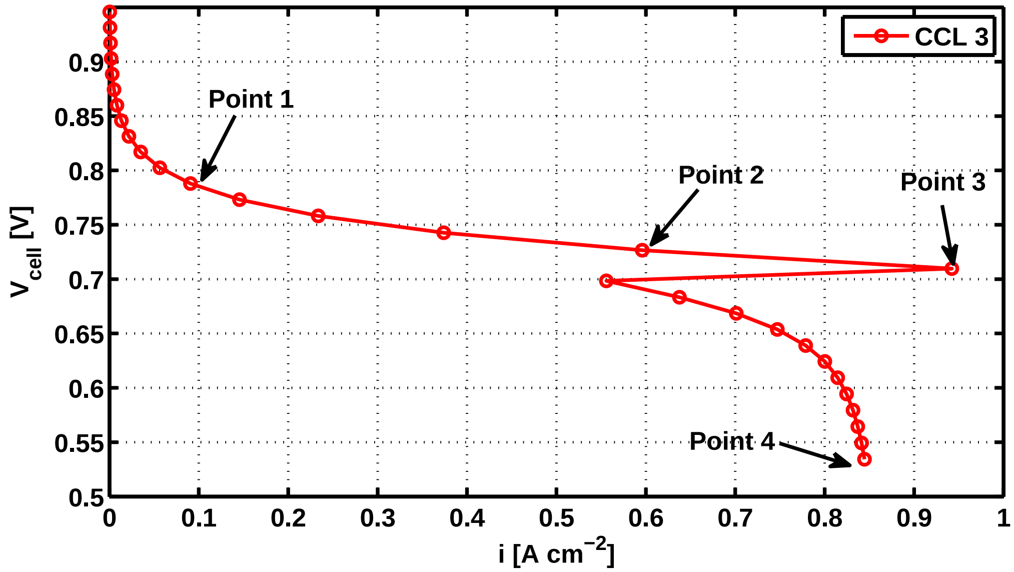

Figure 4.11 – Polarization curve for CCL 3, for a liquid pressure boundary condition of $p^o + 6000\,Pa$ and evaporation rate constant of $0.005\,m^{-3}s^{-1}$.

4.2.3 Reactant Profiles Inside the Electrode

To analyse the solution profiles inside the layer, CCL 3 was used. The tested configuration includes a CCL liquid breakthrough pressure of $6000\,Pa$ and an evaporation rate constant of $0.005\,m^{-3}s^{-1}$. Four points along the polarization curve were examined: Point 1 corresponds to a current density of $0.10\,A\,cm^{-2}$, Point 2 corresponds to a current density of $0.60\,A\,cm^{-2}$, Point 3 corresponds to a current density of $0.95\,A\,cm^{-2}$, and Point 4 corresponds to a current density of $0.85\,A\,cm^{-2}$. The selected points and polarization curve are presented in Figure 4.11.

The total water vapour flux normalized by the total amount of water (liquid and vapour) present in the layer is presented in Figure 4.12. As expected from Figure 4.11, all the liquid water produced from the electrochemical reaction is removed by evaporation for the first three points. Not being able to evaporate all the liquid water that is produced, mass transport limitations finally take over for Point 4.

The capillary pressure profiles for the selected points of CCL 3 are presented in Figure 4.13. The capillary pressure for Point 1, Point 2 and Point 3 is negative because for these cases all the liquid water is evaporated and thus the capillary pressure is obtained from Equation (4.15). Since CCL 3 has a volume fraction of small hydrophilic pores of 20%, the capillary pressure for the first three points is negative. This negative capillary pressure corresponds to the smallest hydrophilic pores which are filled with liquid water, but the liquid water lost all connectivity and thus is not

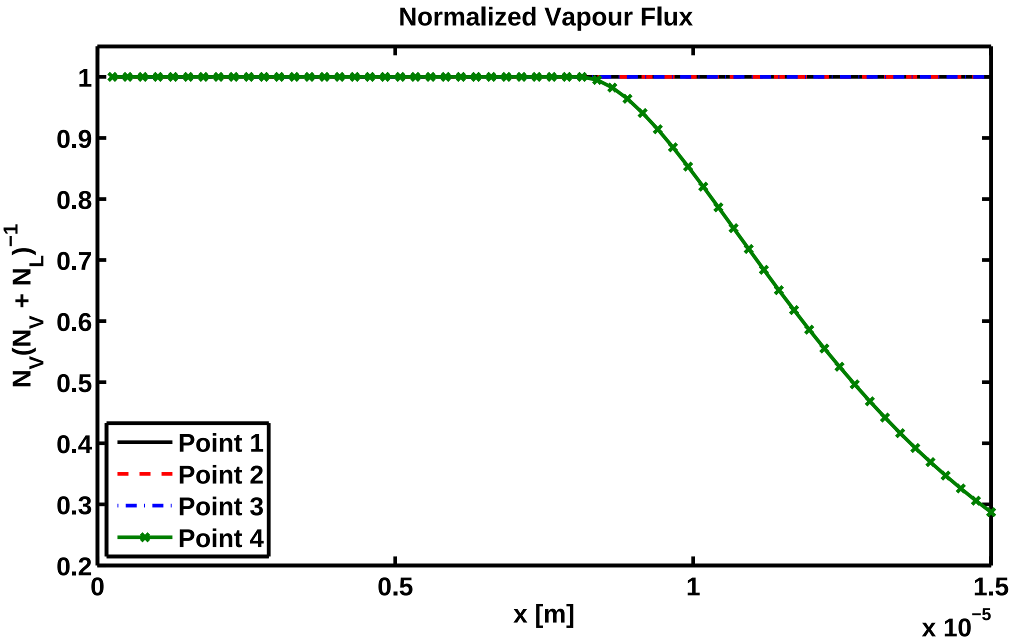

Figure 4.12 – Normalized water vapour flux for CCL 3, for a liquid pressure boundary condition of $p^o + 6000\,Pa$ and evaporation rate constant of $0.005\,m^{-3}s^{-1}$.

a flowing phase. As expected, the capillary pressure is related to the amount of liquid water that is produced from the electrochemical reactions: the capillary pressure becomes more negative when the current density becomes smaller due to the reduced liquid-gas interfacial surface area needed to evaporate the produced water.

An additional consideration from this catalyst layer configuration is the saturation of the GDL. When all the water is evaporated, the GDL saturation is zero. For Point 4, where the liquid water is not completely evaporated and the capillary pressure is near $6000\,Pa$, the GDL saturation is 0.8; which means that most of the losses corresponding to Point 4 arise from GDL flooding. The behaviour of these profiles is also different than the behaviour obtained for MPLs. For MPLs, saturation tends to decrease when the layer is dry because no water production exists. For CCLs, the saturation increases when the layer is dry because water is still being produced along the layer.

The saturation profiles along the catalyst layer are shown in Figure 4.14. For the first three points in the polarization curve, where all the liquid water evaporates, the saturation has an almost constant value of 0.2, which corresponds to the saturation of the hydrophilic pores only. For Point 4, the saturation jumps from 0.2 to around 0.28 rapidly because the layer cannot evaporate all the liquid water produced and it accumulates to create the required pressure gradient to evacuate it to the GDL.

The oxygen partial pressure profiles are presented in Figure 4.15. From the figure

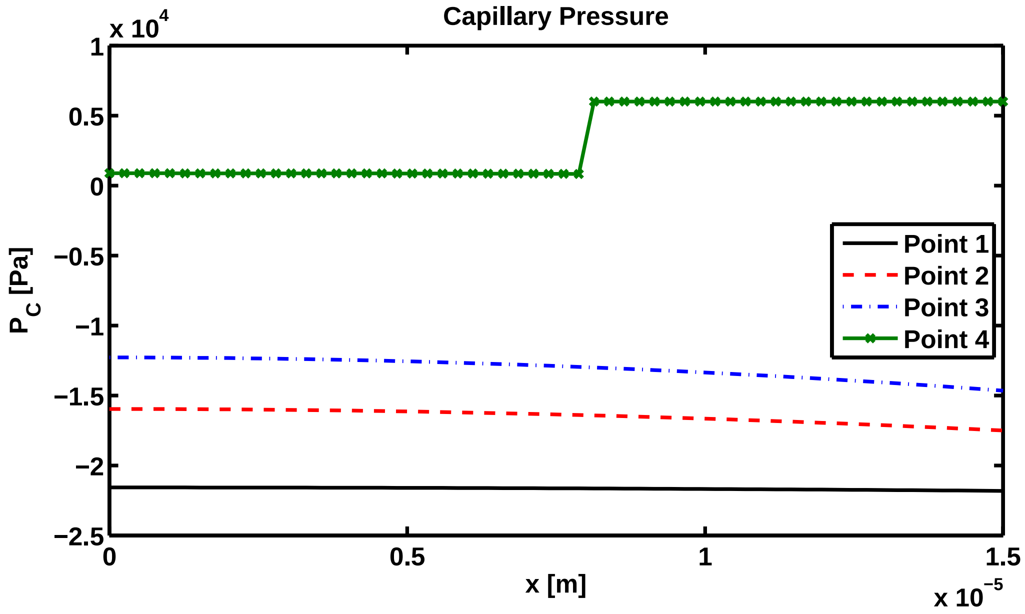

Figure 4.13 – Capillary pressure profiles for CCL 3 at four different current densities, for a liquid pressure boundary condition of $p^o + 6000\,Pa$ and evaporation rate constant of $0.005\,m^{-3}s^{-1}$.

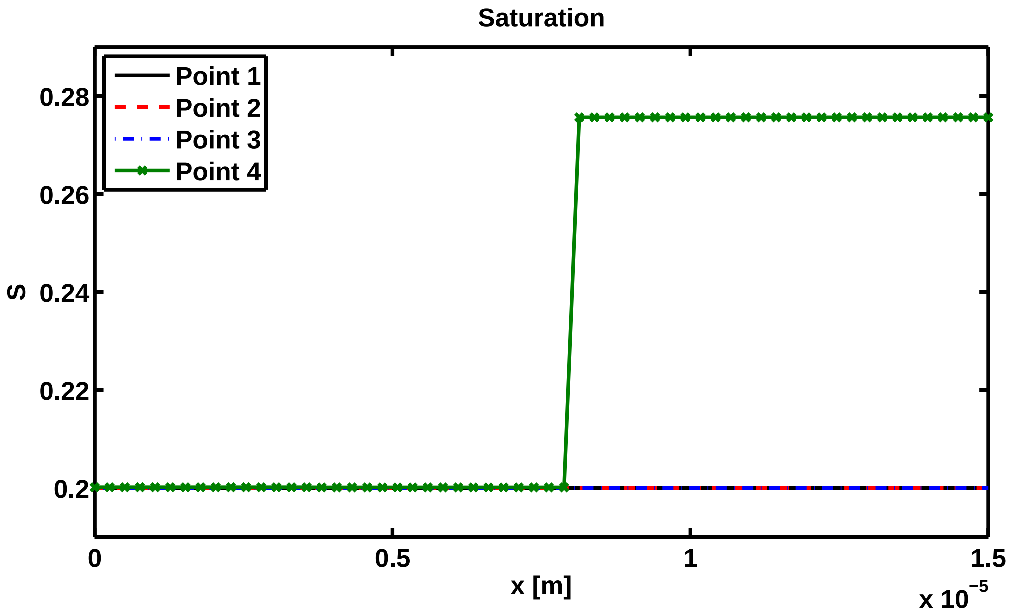

Figure 4.14 – Saturation profiles for CCL 3 at four different current densities, for a liquid pressure boundary condition of $p^o + 6000\,Pa$ and evaporation rate constant of $0.005\,m^{-3}s^{-1}$.

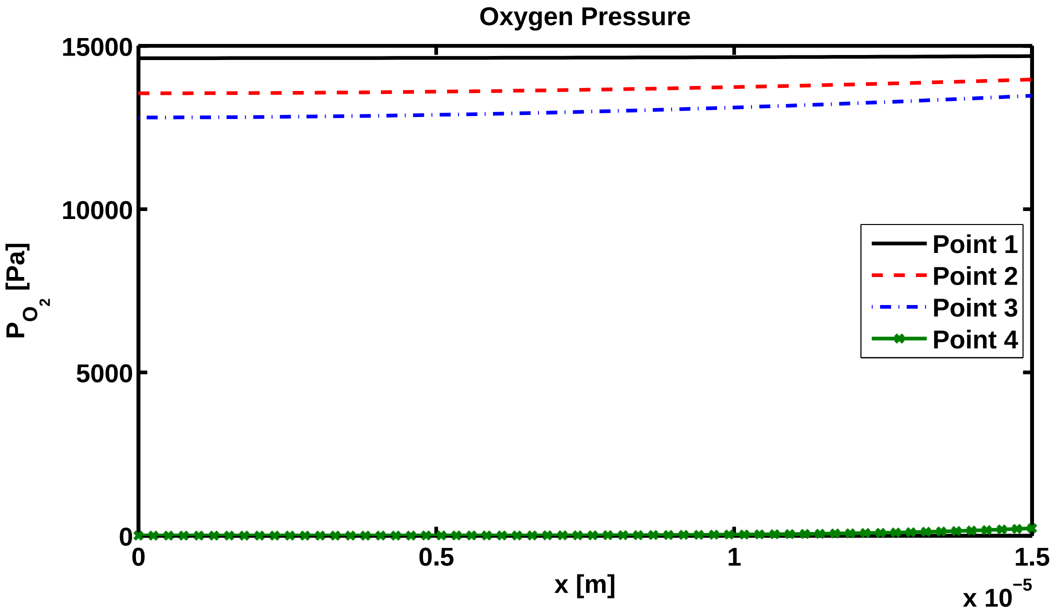

Figure 4.15 – Oxygen partial pressure profiles for CCL 3 at four different current densities, for a liquid pressure boundary condition of $p^o + 6000\,Pa$ and evaporation rate constant of $0.005\,m^{-3}s^{-1}$.

can be observed that the mass limiting layer for this configuration is the GDL rather than the catalyst layer, because the oxygen pressure gradients remain small but the oxygen boundary condition decreases rapidly unless the produced water is successfully evaporated. The lack of evaporation and the high capillary liquid pressures lead to GDL flooding. For the first three points, the layer exhibits very low losses inside the GDL, and small losses inside the catalyst layer as well. Point 4, on the other hand, exhibits very high losses inside the GDL, and small losses inside the cathode catalyst layer itself.

The vapour pressure solution profiles along the catalyst layer is shown in Figure 4.16. The vapour pressure increases as the vapour flux increases. Since the vapour boundary condition depends not only on the amount of current produced but also on the GDL saturation, the pressure profile for Point 4 is higher than for the other three points, as one can expect from the higher GDL saturation corresponding to this point in the polarization curve.

The electrochemical reaction term i/F for the selected CCL configuration is presented in Figure 4.17. For Point 1, Point 2 and Point 3, the oxygen reduction reaction is uniformly distributed along the CCL. For Point 4, due to oxygen depletion, most of the oxygen reduction reaction occurs near the CCL/GDL interface.

The profiles corresponding to the proton flux are presented in Figure 4.18. As the total current density approaches the limiting current, the proton flux gradients

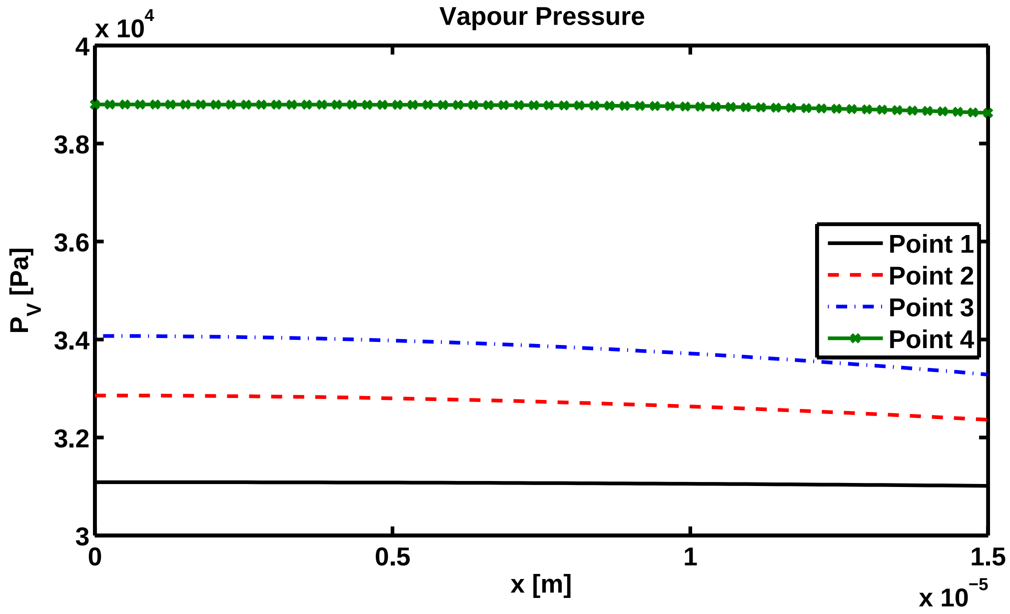

Figure 4.16 – Vapour partial pressure profiles for CCL 3 at four different current densities, for a liquid pressure boundary condition of $p^o + 6000\,Pa$ and evaporation rate constant of $0.005\,m^{-3}s^{-1}$.

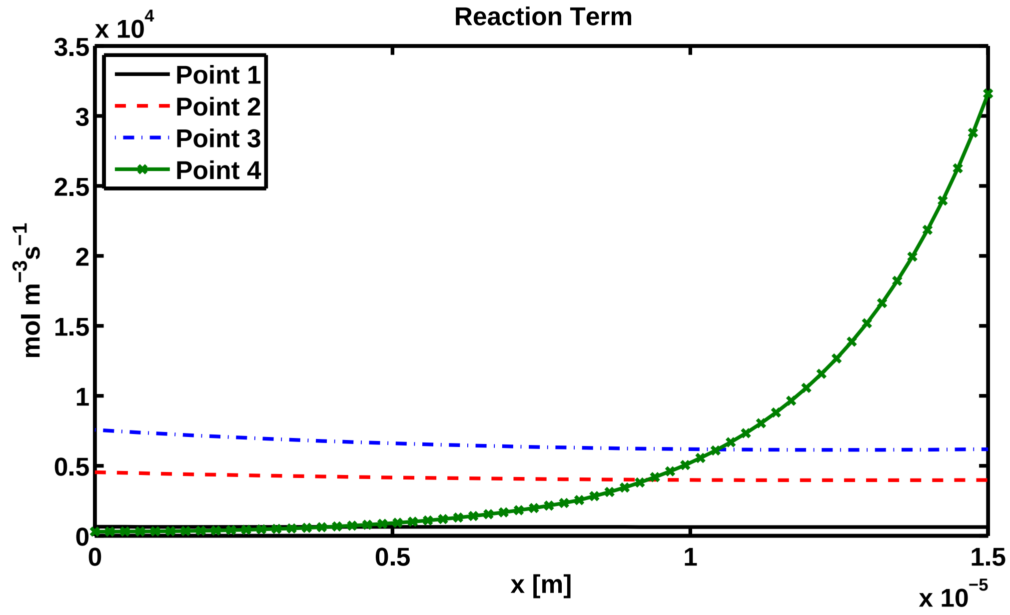

Figure 4.17 – Electrochemical reaction term for CCL 3 at four different current densities, for a liquid pressure boundary condition of $p^o + 6000\,Pa$ and evaporation rate constant of $0.005\,m^{-3}s^{-1}$.

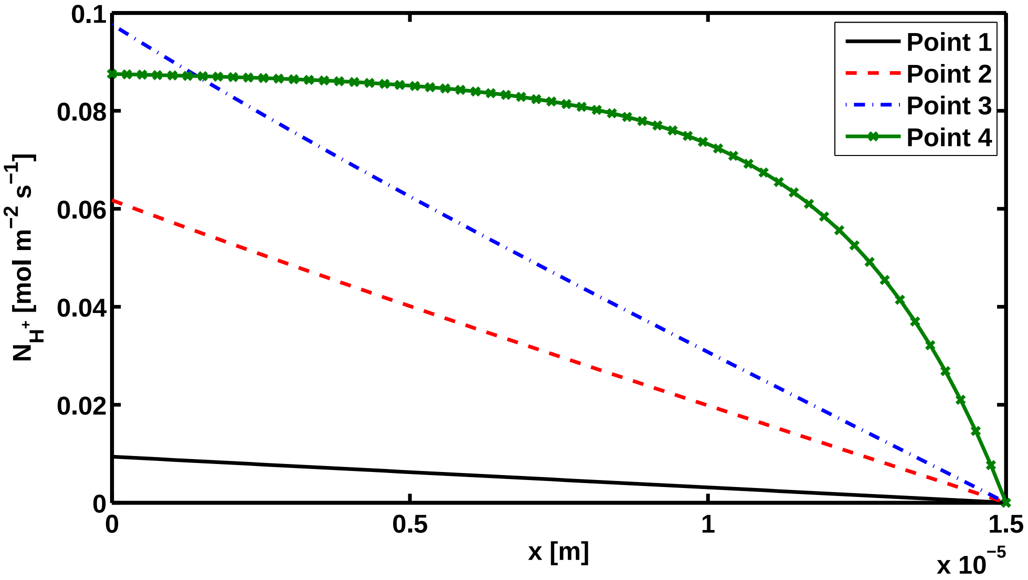

Figure 4.18 – Proton flux profiles for CCL 3 at four different current densities, for a liquid pressure boundary condition of $p^o + 6000\,Pa$ and evaporation rate of $0.005\,m^{-3}s^{-1}$.

near the interface CCL/GDL become larger. This behaviour causes the model to be unstable for very large overpotentials. When the produced water is completely evaporated, the proton flux profiles are almost linear; while if the produced water is not evaporated and the cell approaches limiting current, the proton fluxes becomes more concave-down.

4.3 Conclusions

The proposed cathode catalyst layer model shows that fuel cell performance can be significantly enhanced by controlling the wettability and microstructure of the electrodes.

A catalyst layer with a pore volume fraction of 20% very small hydrophilic pores will increase evaporation rates considerably, leading to maximum achievable current densities of up to five times larger values than the current density obtained from a fully hydrophobic catalyst layers under the right conditions. The increased performance is due to mitigation of GDL flooding. Similar findings were obtained for MPLs in Chapter 3. The optimal electrode configuration consists of layers with very small hydrophilic pores, and a hydrophilic pore volume fraction between 20 and 30%.

The model indicates that the mass transport limited current density is dramatically affected by the liquid pressure at the membrane/catalyst layer interface. Higher pressures causes higher capillary pressures, which promote GDL flooding. The liquid water pressure at the PEM/CCL interface depends on the interplay between the anode and cathode water transport, and it is outside of the scope of this work. Further research is needed to integrate this model to a complete MEA model.

Chapter 5

Conclusions and Future Work

5.1 Conclusions

This thesis proposes a framework for studying mixed wettability PEMFC layers using a PSD model. By controlling the microstructure and wettability of the catalyst layer and the MPL, evaporation rates can be greatly enhanced. Higher evaporation rates allow to draw more current from the cells by reducing mass transport limitation losses.

With the PSD model, the effects of mixed wettability and microstructure on effective transport properties was studied. It was observed that the effective transport properties vary significantly with layer wettability; and that properties such as liquid-gas interfacial surface area per unit volume and wetted pore wall surface area can be increased by several orders of magnitude by controlling the layer wettability and microstructure.

Designing MPLs for ultra-thin electrodes with 20 and 30% of the total pore volume fraction corresponding to small hydrophilic pores revealed that evaporation rates can be significantly enhanced. These electrode configurations allow the PEMFC performance curves to have two very distinct regimes: one regime where all the produced water is evaporated, and another regime where the produced water cannot be completely removed by evaporation. For optimal cell performance, the preferred operation regime is the dry regime. Manufacturing this kind of MPLs commercially could be achieved by selecting a hydrophobic carbon support, and adding small hydrophilic particles (such as silica particles) to create a mixed wettability environment.

When the cells operate on the wet regime, the mass transport limitation losses is strongly related to the liquid breakthrough pressure of the MPL. In general, MPL liquid breakthrough pressure must be as low as possible to avoid premature mass transport limitations. However, one piece of information missing with this assumption is the flooding of the gas channels; more information is needed to determine in which conditions the gas channels flood, causing severe mass transport limitation losses.

From the developed MPL model, it can be observed that the mass transport limitations of PEMFC arise due to GDL flooding almost exclusively. If the water generated is not completely evaporated, liquid water will invade the GDL. Due to the large pores of the GDL (from 10 to 100 μm), even capillary pressures of 4000 to 6000 Pa can significantly increase layer saturation and severely hinder gaseous transport.

Finally, the developed MPL model revealed that the performance of ultra-thin electrodes can be further improved by coupling them with mixed wettability MPLs. The results from this thesis revealed that evaporation rates of partially hydrophilic MPLs can be greatly enhanced when compared to completely hydrophobic MPLs, and therefore these MPLs can handle the high volumetric water production rates associated with ultra-thin catalyst layers. With better platinum utilization and improved water management properties, ultra-thin electrodes coupled with mixed wettability MPLs could help achieve the cost reduction goal required to make this innovative technology more attractive as a power source for mobile applications and for the automotive industry.

The proposed mixed wettability CCL model revealed that CCLs with small hydrophilic pores also cause a significant performance increase with respect to single wettability CCLs. CCLs with 20% of the total pore volume fraction corresponding to small hydrophilic pores showed a significant increase of liquid-gas interfacial surface area per unit volume, causing GDL flooding mitigation. Similar to the MPL, the CCL also exhibits two very distinct regimes of operation: one regime where all the produced water is evaporated and the cell performance is the greatest, and another regime where the produced water cannot be completely removed by evaporation and the cell performance decays.

5.2 Future Work

Future work on the mixed wettability PSD formulation should include validation data for the estimated effective transport properties under dry and partially wet conditions. A lot of information is available about GDLs, but information about MPLs and conventional catalyst layers is very limited.

Additionally, some of the effective properties estimated from the PSD model are not typically documented, but it may be possible to design experimental set-ups to measure them. Such is the case of the combined effects of the liquid-gas interfacial surface area per unit volume and evaporation rate constant. Also, BET analysis can be used to measure and validate the total pore wall surface area (wetted pore wall surface area for a fully saturated layer).

For instance, in a controlled environment where relative humidity and the temperature can be measured and controlled, an experimental set-up could consist of a closed system where one side of a porous sample is in contact with liquid and another side is in contact with air. If liquid is slowly injected by applying a known liquid pressure, evaporation inside the layer will take place and the relative humidity of the air opposite to the injection side of the layer will increase. This change in relative humidity will reveal how much water evaporated, and this can be ultimately used to measure the combined effect of liquid-gas interfacial surface area per unit volume and evaporation rate constant. However, with the described system will b hard to know what the layer saturation is.

After looking at the benefits of having mixed wettability CCLs and MPLs, the two models can be merged into a cathode model, where both the CCL and the MPL are evaporative layers. An additional model improvement is to remove the steady-state and isothermal assumptions, to study the effects of cell temperature and drying, and to study the time it takes for the liquid pressure to build up to the MPL/GDL breakthrough pressure.

References

[1] Liu, J., and Eikerling, M., 2008. “Model of cathode catalyst layers for polymer electrolyte fuel cells: The role of porous structure and water accumulation”. Electrochimica Acta, **53** (13) , pp. 4435 – 4446.

[2] Miller, S. M., 2013. Analysis of an open-cathode fuel cell stack in an enclosure for varying operating conditions. Master’s thesis, University of Alberta.

[3] Weber, A. Z., 2004. *Modeling Water Management in Polymer-Electrolyte Fuel Cells*. PhD thesis, University of California, Berkeley.

[4] Fairweather, J. D., Cheung, P., St-Pierre, J., and Schwartz, D. T., 2007. “A microfluidic approach for measuring capillary pressure in {PEMFC} gas diffusion layers”. Electrochemistry Communications, **9** (9) , pp. 2340 – 2345.

[5] Luo, G., Ji, Y., Wang, C.-Y., and Sinha, P. K., 2010. “Modeling liquid water transport in gas diffusion layers by topologically equivalent pore network”. Electrochimica Acta, **55** (19) , pp. 5332 – 5341.

[6] Koido, T., Furusawa, T., and Moriyama, K., 2008. “An approach to modeling two-phase transport in the gas diffusion layer of a proton exchange membrane fuel cell”. Journal of Power Sources, **175** (1) , pp. 127 – 136.

[7] Laramine, J., , and Dicks, A., 2003. *Fuel Cell Systems Explained*, 2nd ed. Wiley & Sons, Cambridge.

[8] Litster, S., and McLean, G., 2004. “PEM Fuel Cell Electrodes”. Journal of Power Sources, **130** (1-2) May , pp. 61–76.

[9] Martínez, M. J., Shimpalee, S., Zee, J. W. V., and Sakars, A. V., 2009. “Assessing methods and data for Pore-Size Distribution of PEMFC gas-diffusion media”. Journal of the Electrochemical Society, **156** (5) , pp. B558–B564.

[10] Carrigy, N. B., Pant, L. M., Mitra, S., and Secanell, M., 2013. "Knudsen Diffusivity and Permeability of PEMFC Microporous Coated Gas Diffusion Layers for Different Polytetrafluoroethylene Loadings". Journal of The Electrochemical Society, **160** (2) , pp. F81–F89.

[11] Rajalakshmi, N., and Dhathathreyan, K., 2007. "Catalyst layer in {PEMFC} electrodes?fabrication, characterisation and analysis". Chemical Engineering Journal, **129** (1?3) , pp. 31 – 40.

[12] Weber, A. Z., and Newman, J., 2005. "Effects of microporous layers in polymer electrolyte fuel cells". Journal of The Electrochemical Society, **152** (4) , pp. A677–A688.

[13] SGL Group, 2012. SGL Group Official Website. www.sglgroup.com/cms/international/home/ index.html, August.

[14] Papageorgopoulos, D., 2009. "Fuel cell technologies".

[15] Papageorgopoulos, D., 2010. "Status of DOE EERE's fuel cell research and development efforts".

[16] Wang, Q., Eikerling, M., Song, D., and Liu, Z.-S., 2007. "Modeling of ultrathin two-phase catalyst layers in pefcs". Journal of The Electrochemical Society, **154** (6) , pp. F95–F101.

[17] Debe, M. K., 2010. *Novel catalysts, catalysts support and catalysts coated membrane methods.* John Wiley & Sons, Ltd.

[18] Liu, C.-Y., and Sung, C.-C., 2012. "A review of the performance and analysis of proton exchange membrane fuel cell membrane electrode assemblies". Journal of Power Sources, **220** (0) , pp. 348 – 353.

[19] Chun, J. H., Park, K. T., Jo, D. H., Kim, S. G., and Kim, S. H., 2011. "Numerical modeling and experimental study of the influence of gdl properties on performance in a pemfc". International Journal of Hydrogen Energy, **36** (2) , pp. 1837 – 1845.

[20] Wang, X., and Nguyen, T. V., 2008. "Modeling the effects of the cathode microporous layer on the performance of a pem fuel cell". ECS Transactions, **16** (2) , pp. 3–12.

[21] Weber, A. Z., 2010. "Improved modeling and understanding of diffusion-media wettability on polymer-electrolyte-fuel-cell performance". Journal of Power Sources, **195** (16) , pp. 5292–5304.

[22] Marr, C., and Li, X., 1999. "Composition and performance modelling of catalyst layer in a proton exchange membrane fuel cell". Journal of Power Sources, **77** (1) , pp. 17 – 27.

[23] Zamel, N., and Li, X., 2010. "Non-isothermal multi-phase modeling of pem fuel cell cathode". International Journal of Energy Research, **34** (7) , pp. 568–584.

[24] Min, C.-H., 2010. "A novel three-dimensional, two-phase and non-isothermal numerical model for proton exchange membrane fuel cell". Journal of Power Sources, **195** (7) , pp. 1880 – 1887.

[25] Weber, A. Z., and Newman, J., 2006. "Coupled thermal and water management in polymer electrolyte fuel cells". Journal of The Electrochemical Society, **153** (12) , pp. A2205–A2214.

[26] Khajeh-Hosseini-Dalasm, N., Fushinobu, K., and Okazaki, K., 2010. "Phase change in the cathode side of a proton exchange membrane fuel cell". Journal of Power Sources, **195** (20) , pp. 7003 – 7010.

[27] Afshari, E., Jazayeri, S., and Mollayi Barzi, Y., 2010. "Effect of water phase change on temperature distribution in proton exchange membrane fuel cells". *Heat and Mass Transfer,* **46** , pp. 1295–1305. 10.1007/s00231-010-0647-x.

[28] Pasaogullari, U., and Wang, C.-Y., 2005. "Two-phase modeling and flooding prediction of polymer electrolyte fuel cells". Journal of The Electrochemical Society, **152** (2) , pp. A380–A390.

[29] Gostick, J. T., Fowler, M. W., Ioannidis, M. A., Pritzker, M. D., Volfkovich, Y., and Sakars, A., 2006. "Capillary pressure and hydrophilic porosity in gas diffusion layers for polymer electrolyte fuel cells". Journal of Power Sources, **156** (2) , pp. 375 – 387.

[30] Gostick, J., Ioannidis, M., Fowler, M., and Pritzker, M., 2010. "Characterization of the capillary properties of gas diffusion media". In *Modeling and Diagnostics of Polymer Electrolyte Fuel Cells*, C.-Y. Wang and U. Pasaogullari, Eds., Modern Aspects of Electrochemistry. Springer New York, pp. 225–254.

[31] Brunauer, S., Emmett, P. H., and Teller, E., 1938. “Adsorption of gases in multimolecular layers”. Journal of the American Chemical Society, **60** (2) , pp. 309–319.

[32] Kruk, M., Jaroniec, M., and Sayari, A., 1997. “Application of large pore mcm-41 molecular sieves to improve pore size analysis using nitrogen adsorption measurements”. Langmuir, **13** (23) , pp. 6267–6273.

[33] Joyner, L. G., Barrett, E. P., and Skold, R., 1951. “The determination of pore volume and area distributions in porous substances. ii. comparison between nitrogen isotherm and mercury porosimeter methods”. Journal of the American Chemical Society, **73** (7) , pp. 3155–3158.

[34] Barrett, E. P., Joyner, L. G., and Halenda, P. P., 1951. “The determination of pore volume and area distributions in porous substances. i. computations from nitrogen isotherms”. Journal of the American Chemical Society, **73** (1) , pp. 373–380.

[35] Brown, S. M., and Lard, E. W., 1974. “A comparison of nitrogen and mercury pore size distributions of silicas of varying pore volume”. Powder Technology, **9** (4) , pp. 187 – 190.

[36] Bhambhani, M. R., Cutting, P. A., Sing, K. S. W., and Turk, D. H., 1972. “Analysis of nitrogen adsorption isotherms on porous and nonporous silicas by the bet and [alpha]s methods”. Journal of Colloid and Interface Science, **38** (1) , pp. 109 – 117.

[37] Nelsen, F. M., and Eggertsen, F. T., 1958. “Determination of surface area. adsorption measurements by continuous flow method”. Analytical Chemistry, **30** (8) , pp. 1387–1390.

[38] Tseng, C.-J., Lou, S.-K., Yan, Y.-Y., and Sung, L.-Y., 2005. “Gas diffusion layer and microporous layer for PEMFC”. In Proceedings International Hydrogen Energy Congress and Exhibition, Istambul, Turkey.

[39] Ismail, M., Damjanovic, T., Ingham, D., Ma, L., and Pourkashanian, M., 2010. “Effect of polytetrafluoroethylene-treatment and microporous layer-coating on the in-plane permeability of gas diffusion layers used in proton exchange membrane fuel cells”. Journal of Power Sources, **195** (19) , pp. 6619 – 6628.

[40] Gostick, J. T., Ioannidis, M. A., Fowler, M. W., and Pritzker, M. D., 2009. "On the role of the microporous layer in pemfc operation". Electrochemistry Communications, **11** (3) , pp. 576 – 579.

[41] Atiyeh, H. K., Karan, K., Peppley, B., Phoenix, A., Halliop, E., and Pharoah, J., 2007. "Experimental investigation of the role of a microporous layer on the water transport and performance of a pem fuel cell". Journal of Power Sources, **170** (1) , pp. 111 – 121.

[42] Pharoah, J. G., Peppley, B., Atiyeh, H., Halliop, E., Karan, K., and Phoenix, A., 2006. "Investigating the role of a microporous layer on the water transport and performance of a pemfc". ECS Transactions, **3** (1) , pp. 1227–1237.

[43] Kitahara, T., Konomi, T., and Nakajima, H., 2010. "Microporous layer coated gas diffusion layers for enhanced performance of polymer electrolyte fuel cells". Journal of Power Sources, **195** (8) , pp. 2202 – 2211.

[44] Nishiyama, E., and Murahashi, T., 2011. "Water transport characteristics in the gas diffusion media of proton exchange membrane fuel cell - role of the microporous layer". Journal of Power Sources, **196** (4) , pp. 1847 – 1854.

[45] Park, S., Lee, J.-W., and Popov, B. N., 2006. "Effect of carbon loading in microporous layer on pem fuel cell performance". Journal of Power Sources, **163** (1) , pp. 357 – 363. Special issue including selected papers presented at the Second International Conference on Polymer Batteries and Fuel Cells together with regular papers.

[46] Tseng, C.-J., and Lo, S.-K., 2010. "Effects of microstructure characteristics of gas diffusion layer and microporous layer on the performance of pemfc". Energy Conversion and Management, **51** (4) , pp. 677 – 684.

[47] Markicevic, B., Bazylak, A., and Djilali, N., 2007. "Determination of transport parameters for multiphase flow in porous gas diffusion electrodes using a capillary network model". Journal of Power Sources, **171** (2) , pp. 706 – 717.

[48] Sinha, P. K., and Wang, C.-Y., 2007. "Pore-network modeling of liquid water transport in gas diffusion layer of a polymer electrolyte fuel cell". Electrochimica Acta, **52** (28) , pp. 7936 – 7945.

[49] Lee, K.-J., Nam, J. H., and Kim, C.-J., 2009. "Pore-network analysis of two-phase water transport in gas diffusion layers of polymer electrolyte membrane fuel cells". Electrochimica Acta, **54** (4) , pp. 1166 – 1176.

[50] Bazylak, A., Berejnov, V., Markicevic, B., Sinton, D., and Djilali, N., 2008. "Numerical and microfluidic pore networks: Towards designs for directed water transport in GDLs". Electrochimica Acta, **53** (26) , pp. 7630 – 7637.

[51] Wu, R., Zhu, X., Liao, Q., Wang, H., dong Ding, Y., Li, J., and ding Ye, D., 2010. "A pore network study on the role of micro-porous layer in control of liquid water distribution in gas diffusion layer". International Journal of Hydrogen Energy, **35** (14) , pp. 7588 – 7593.

[52] Ostadi, H., Rama, P., Liu, Y., Chen, R., Zhang, X., and Jiang, K., 2010. "3d reconstruction of a gas diffusion layer and a microporous layer". Journal of Membrane Science, **351** (1?2) , pp. 69 – 74.

[53] Hao, L., and Cheng, P., 2010. "Lattice boltzmann simulations of water transport in gas diffusion layer of a polymer electrolyte membrane fuel cell". Journal of Power Sources, **195** (12) , pp. 3870 – 3881.

[54] Sivertsen, B., and Djilali, N., 2005. "Cfd based modelling of proton exchange membrane fuel cells". Journal of Power Sources, **141** (1) February , pp. 65–78.

[55] Wang, Z., Wang, C., and Chen, K., 2001. "Two-phase flow and transport in the air cathode of proton exchange membrane fuel cells". Journal of Power Sources, **94** (1) February , pp. 40–50.

[56] Harvey, D., Pharoah, J., and Karan, K., 2008. "A comparison of different approaches to modelling the pemfc catalyst layer". Journal of Power Sources, **179** (1) Apr. , pp. 209–219.

[57] You, L., and Liu, H., 2002. "A two-phase flow and transport model for the cathode of PEM fuel cells". *International Journal of Heat and Mass Transfer,* **45** , pp. 2277–2287.

[58] Lin, G., He, W., and Nguyen, T. V., 2004. "Modeling liquid water effects in the gas diffusion and catalyst layers of the cathode of a PEM fuel cell". Journal of the Electrochemical Society, **151** (12) , pp. A1999–A2006.

[59] Secanell, M., Carnes, B., Suleman, A., and Djilali, N., 2007. "Numerical optimization of proton exchange membrane fuel cell cathodes". Electrochimica Acta, **52** (7) , pp. 2668–2682.

[60] Eikerling, M., 2006. "Water management in cathode catalyst layers of pem fuel cells". Journal of the Electrochemical Society, **153** (3) , pp. E58–E70.

[61] Wang, Q., Eikerling, M., Song, D., and Liu, Z., 2004. “Structure and performance of different types of agglomerates in cathode catalyst layers in PEM fuel cells”. *Journal of Electroanalytical Chemistry,* **573** , pp. 61–69.

[62] Secanell, M., Karan, K., Suleman, A., and Djilali, N., 2007. “Multi-variable optimization of PEMFC cathodes using an agglomerate model”. Electrochimica Acta, **52** (22) June , pp. 6318–6337.

[63] Broka, K., and Ekdunge, P., 1997. “Modelling the PEM fuel cell cathode”. Journal of Applied Electrochemistry, **27** (3) March , pp. 281–289.

[64] Siegel, N., Ellis, M., Nelson, D., and Von Spakovsky, M., 2003. “Single domain PEMFC model based on agglomerate catalyst geometry”. Journal of Power Sources, **115** (1) March , pp. 81–89.

[65] Sun, W., Peppley, B. A., and Karan, K., 2005. “An improved two-dimensional agglomerate cathode model to study the influence of catalyst layer structural parameters”. Electrochimica Acta, **50** (16-17) , pp. 3347–3358.

[66] Bultel, Y., Ozil, P., and Durand, R., 1998. “Modified thin film and agglomerate models for active layers of p.e. fuel cells”. Electrochimica Acta, **43** (9) , pp. 1077–1087.

[67] Jaouen, F., Lindbergh, G., and Sundholm, G., 2002. “Investigation of mass-transport limitations in the solid polymer fuel cell cathode - I. Mathematical model”. Journal of the Electrochemical Society, **149** (4) , pp. A437–A447.

[68] Bear, J., 1988. *Dynamics of Fluids in Porous Media.* Dover Publications, Inc.

[69] Burdine, N., 1953. “Relative permeability calculations from pore size distribution data”. Journal of Petroleum Technology, **5** (3) , pp. 71 – 78.

[70] Weber, A., and Hickner, M., 2008. “Modeling and high-resolution-imaging studies of water-content profiles in a polymer-electrolyte-fuel-cell membrane-electrode assembly”. Electrochimica Acta, **53** (26) , pp. 7668 – 7674.

[71] Helmy, R., Kazakevich, Y., Ni, C., and Fadeev, A. Y., 2005. “Wetting in hydrophobic nanochannels:? a challenge of classical capillarity”. Journal of the American Chemical Society, **127** (36) , pp. 12446–12447. PMID: 16144365.

[72] Fadeev, A. Y., and Eroshenko, V. A., 1997. “Study of penetration of water into hydrophobized porous silicas”. Journal of Colloid and Interface Science, **187** (2) , pp. 275–282.

[73] Lefevre, B., Saugey, A., Barrat, J. L., Bocquet, L., Charlaix, E., Gobin, P. F., and Vigier, G., 2004. “Intrusion and extrusion of water in highly hydrophobic mesoporous materials: effect of the pore texture”. Colloids and Surfaces A: Physicochemical and Engineering Aspects, **241** (1-3) , pp. 265 – 272.

[74] Xie, J., More, K. L., Zawodzinski, T. A., and Smith, W. H., 2004. “Porosimetry of meas made by “thin film decal” method and its effects on performance of PEFCs”. Journal of the Electrochemical Society, **151** (11) , pp. A1841–A1846.

[75] El-Dieb, A., and Hooton, R., 1994. “Evaluation of the katz-thompson model for estimating the water permeability of cement-based materials from mercury intrusion porosimetry data”. Cement and Concrete Research, **24** (3) , pp. 443 – 455.

[76] Martnez-Rodrguez, M. J., Cui, T., Shimpalee, S., Seraphin, S., Duong, B., and Zee, J. V., 2012. “Effect of microporous layer on macmullin number of carbon paper gas diffusion layer”. Journal of Power Sources, **207** (0) , pp. 91 – 100.

[77] Fadeev, A. Y., and Eroshenko, V. A., 1997. “Study of penetration of water into hydrophobized porous silicas”. Journal of Colloid and Interface Science, **187** (2) , pp. 275 – 282.

[78] White, F. M., 2006. *Viscous Fluid Flow.* McGraw-Hill.

[79] Pant, L. M., Mitra, S. K., and Secanell, M., 2011. “Mass transport measurements in porous transport layers of a PEM fuel cell”. In ASME 2011 9th International Conference on Nanochannels, Microchannels, and Minichannels, no. ICNMM2011-58181.

[80] Pant, L. M., 2011. Experimental and theoretical investigation of mass transport in porous media of a pem fuel cell. Master’s thesis, University of Alberta.

[81] Froment, G., and Bischoff, K., 1979. *Chemical Reactor Analysis and Design.* Wiley.

[82] Das, P. K., Li, X., and Liu, Z.-S., 2010. “Effective transport coefficients in pem fuel cell catalyst and gas diffusion layers: Beyond bruggeman approximation”. Applied Energy, **87** (9) , pp. 2785 – 2796. ¡ce:title¿Special Issue of the IGEC-IV, the 4th International Green Energy Conference (IGEC-IV), Beijing, China, October 20?22, 2008¡/ce:title¿ ¡ce:title¿Special Issue of the First International Conference on Applied Energy, ICAE?09, Hong Kong, January 5?7, 2009¡/ce:title¿.

[83] Fairweather, J. D., Cheung, P., and Schwartz, D. T., 2010. "The effects of wetproofing on the capillary properties of proton exchange membrane fuel cell gas diffusion layers". Journal of Power Sources, **195** (3) , pp. 787 – 793.

[84] Cheung, P., Fairweather, J. D., and Schwartz, D. T., 2009. "Characterization of internal wetting in polymer electrolyte membrane gas diffusion layers". Journal of Power Sources, **187** (2) , pp. 487 – 492.

[85] Ji, J., Luo, G., and Wang, C.-Y., 2010. "Pore-level liquid water transport through composite diffusion media of pemfc". Journal of The Electrochemical Society, **157** (12) , pp. B1753 – B1761.

[86] Gostick, J. T., Ioannidis, M. A., Fowler, M. W., and Pritzker, M. D., 2007. "Pore network modeling of fibrous gas diffusion layers for polymer electrolyte membrane fuel cells". Journal of Power Sources, **173** (1) , pp. 277 – 290.

[87] Shi, Y., Cheng, S., and Quan, S., 2012. "Fractal-based theoretical model on saturation and relative permeability in the gas diffusion layer of polymer electrolyte membrane fuel cells". Journal of Power Sources, **209** (0) , pp. 130 – 140.

[88] Gostick, J. T., Ioannidis, M. A., Fowler, M. W., and Pritzker, M. D., 2009. "Wettability and capillary behavior of fibrous gas diffusion media for polymer electrolyte membrane fuel cells". Journal of Power Sources, **194** (1) , pp. 433 – 444. XIth Polish Conference on Fast Ionic Conductors 2008.

[89] Pant, L. M., Mitra, S. K., and Secanell, M., 2012. "Absolute permeability and knudsen diffusivity measurements in pemfc gas diffusion layers and micro porous layers". Journal of Power Sources, **206** (0) , pp. 153 – 160.

[90] Parthasarathy, A., Srinivasan, S., Appleby, A. J., and Martin, C. R., 1992. "Temperature dependence of the electrode kinetics of oxygen reduction at the Platinum/Nafion® interface—a microelectrode investigation". Journal of The Electrochemical Society, **139** (9) , pp. 2530–2537.

[91] Li, K., and Horne, R. N., 2001. "Steam-water relative permeability by the capillary pressure method". *International Symposium of the Society of Core Analysis* .

[92] Nam, J. H., and Kaviany, M., 2003. "Effective diffusivity and water-saturation distribution in single- and two-layer pemfc diffusion medium". International Journal of Heat and Mass Transfer, **46** (24) , pp. 4595 – 4611.

Appendix A

Derivation of Expressions to Estimate Effective Transport Properties from PSD Model

A.1 Saturation

A wettability-specific PSD function has the form:

$$\frac{dX(r)}{dr} = \sum_k \left[\frac{f_k}{r\, s_k \sqrt{2\pi}} \exp\left(- \left[\frac{\ln(r) - \ln(r_k)}{s_k \sqrt{2}} \right]^2 \right) \right] \tag{A.1}$$

Following the formulation of the proposed mixed-wettability PSD model, the saturation can be obtained by integrating the change of cumulative volume fraction as a function of effective pore radius for both the hydrophilic and hydrophobic PSD functions:

$$S = \int_0^{r_{c,HI}} \frac{dX(r)_{HI}}{dr}\, dr + \int_{r_{c.HO}}^{\infty} \frac{dX(r)_{HO}}{dr}\, dr \tag{A.2}$$

where $r_{c,HI}$ and $r_{c,HO}$ are the hydrophilic and hydrophobic effective critical radii, respectively. These values cannot be obtained from the Young-Laplace equation. Depending on the capillary pressure, the values for $r_{c,HI}$ and $r_{c,HO}$ are given as:

- If $p_c < 0$ then: $0 < r_{c,HI} \leq \infty$ and $r_{c,HO} = \infty$
- If $p_c \geq 0$ then: $r_{c,HI} = \infty$ and $0 < r_{c,HO} \leq \infty$

If the capillary pressure is less than zero, the hydrophobic pores cannot be invaded by water while the hydrophilic pores can be invaded. If the capillary pressure is zero all the hydrophilic pores must be invaded with liquid water. For capillary pressures greater or equal to zero, the hydrophobic pores will be invaded according to the

Young-Laplace equation. These phenomena can be accurately predicted using the PSD formulation and the proper values $r_{c,HI}$ and $r_{c,HO}$. Also, it can be shown that by evaluating the integrals of Equation (A.2) an exact (algebraic) solution is obtained. The saturation due to the hydrophilic pores can be found from:

$$S_{HI} = \int_{R_1=0}^{R_2=r_{c,HI}} \frac{dX(r)_{HI}}{dr}\, dr \tag{A.3}$$

where

$$\frac{dX(r)_{HI}}{dr} = F_{HI} \sum_k f_{HI,k} \left[\frac{1}{r\, s_{HI,k}\sqrt{2\pi}} \exp\left(- \left[\frac{\ln(r) - \ln(r_{HI,k})}{s_{HI,k}\sqrt{2}} \right]^2 \right) \right] \tag{A.4}$$

To solve Equation (A.3), the Error function and some of its properties must be introduced. The error function is an expression of the form:

$$\operatorname{erf}(x) = \frac{2}{\sqrt{\pi}} \int_0^x \exp\left(-t^2\right) dt \tag{A.5}$$

Some of the important properties of the error function, as can be seen in Figure A.1, are given by:

$$\operatorname{erf}(\infty) = 1 \tag{A.6}$$

$$\operatorname{erf}(-\infty) = -1 \tag{A.7}$$

$$\operatorname{erf}(b) - \operatorname{erf}(a) = \frac{2}{\sqrt{\pi}} \int_a^b \exp\left(-t^2\right) dt \tag{A.8}$$

$$\operatorname{erf}(b) = \frac{1}{\sqrt{\pi}} \int_{-b}^b \exp\left(-t^2\right) dt \tag{A.9}$$

$$\frac{2}{\sqrt{\pi}} \int_x^\infty \exp\left(-t^2\right) dt = 1 - \operatorname{erf}(x) \tag{A.10}$$

Equation (A.3) can be written in a form similar to the Error function. In order to perform this, an appropriate substitution is needed. In this case,

$$t = \frac{\ln(r) - \ln(r_{HI,k})}{s_{HI,k}\sqrt{2}} \tag{A.11}$$

Taking the differential of both sides,

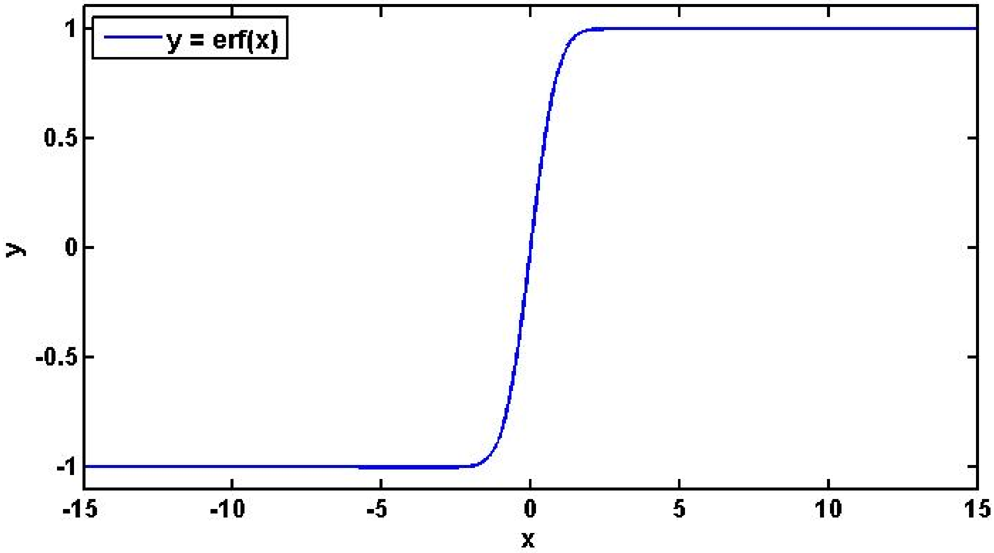

Figure A.1 – Error function.

$$dt = \frac{1}{r}\frac{1}{s_{HI,k}\sqrt{2}}dr \tag{A.12}$$

Substituting back into Equation (A.3)

$$S_{HI} = F_{HI}\int_{t_1'}^{t_2'}\sum_k f_{HI,k}\left[\frac{1}{\sqrt{\pi}}\exp\left(-t^2\right)\right]dt \tag{A.13}$$

where the integration limits t_1' and t_2' indicate that the original limits must be changed accordingly in order to match the substitution made in Equation (A.11).

It is known that in order to find saturation properly, the integration limits of this integral will be different for positive or negative capillary pressures. In order to account for that, different integration scenarios are considered now. Something to keep in mind is that the original integral was a function of the pore radius r. Given the substitution in Equation (A.11) two different scenarios will be considered: an integration from zero to infinity, and an integration from a real positive number to infinity.

When the integration limits are from $r_2 = \infty$ to $r_1 = 0$, the expressions lead to:

$$t_2' = \frac{\ln(r_2) - \ln(r_{HI,k})}{s_{HI,k}\sqrt{2}} \tag{A.14}$$

which is equivalent to

$$t'_2 = \lim_{r \to \infty} \frac{\ln(r) - \ln(r_{HI,k})}{s_{HI,k}\sqrt{2}} = \infty \tag{A.15}$$

Then, the lower limit of the integral is given by

$$t'_1 = \frac{\ln(r_1) - \ln(r_{HI,k})}{s_{HI,k}\sqrt{2}} \tag{A.16}$$

which can then be expressed as

$$t'_1 = \lim_{r \to 0^+} \frac{\ln(r) - \ln(r_{HI,k})}{s_{HI,k}\sqrt{2}} = -\infty \tag{A.17}$$

When the integration limits are from $r_2 = \infty$ to $r_1 = r_{c,HI}$, the upper limit of the integral was already found on the previous scenario. The lower limit is just given by

$$t'_1 = \frac{\ln(r_{c,HI}) - \ln(r_{HI,k})}{s_{HI,k}\sqrt{2}} \tag{A.18}$$

Therefore,

$$S_{HI} = F_{HI} \int_{-\infty}^{\frac{\ln(r_{c,HI}) - \ln(r_{HI,k})}{s_{HI,k}\sqrt{2}}} \sum_k f_{HI,r,k} \left[\frac{1}{\sqrt{\pi}} \exp\left(-t^2\right) \right] dt \tag{A.19}$$

and since the function $\exp(-t^2)$ is even, Equation (A.19) can be written as

$$S_{HI} = F_{HI} \int_{-\frac{\ln(r_{c,HI}) - \ln(r_{HI,k})}{s_{HI,k}\sqrt{2}}}^{\infty} \sum_k f_{HI,r,k} \left[\frac{1}{\sqrt{\pi}} \exp\left(-t^2\right) \right] dt \tag{A.20}$$

From the properties of the Error function, the later expression can be written as

$$S_{HI} = F_{HI} \sum_k \frac{f_{HI,r,k}}{2} \left[1 - \operatorname{erf}\left(-\frac{\ln(r_{c,HI}) - \ln(r_{HI,k})}{s_{HI,k}\sqrt{2}} \right) \right] \tag{A.21}$$

and since the Error function is odd, as shown in Figure A.1:

$$S_{HI} = F_{HI} \sum_k \frac{f_{HI,r,k}}{2} \left[1 + \operatorname{erf}\left(\frac{\ln(r_{c,HI}) - \ln(r_{HI,k})}{s_{HI,k}\sqrt{2}} \right) \right] \tag{A.22}$$

Similarly, for hydrophobic pores the saturation is given as

$$S_{HO} = F_{HO} \int_{\frac{\ln(r_{c,HO}) - \ln(r_{HO,k})}{s_{HO,k}\sqrt{2}}}^{\infty} \sum_k f_{HO,k} \left[\frac{1}{\sqrt{\pi}} \exp\left(-t^2\right) \right] dt \tag{A.23}$$

Using the properties of the Error function and trivial algebra manipulation, can be shown that

$$S_{HO} = F_{HO} \sum_k \frac{f_{HO,k}}{2} \left[1 - \text{erf}\left(\frac{\ln(r_{c,HO}) - \ln(r_{HO,k})}{s_{HO,k}\sqrt{2}} \right) \right] \tag{A.24}$$

By looking at the similarities between Equation A.22 and Equation A.24, a single expression for the saturation of pores with specified wettability can be written as:

$$S_H = F_H \sum_k \frac{f_{H,k}}{2} \left[1 + \phi_H \text{erf}\left(\frac{\ln(r_{c,H}) - \ln(r_{H,k})}{s_{H,k}\sqrt{2}} \right) \right] \tag{A.25}$$

where ϕ_H has a value of 1 for hydrophilic pores, and a value of -1 for hydrophobic pores. The total saturation is then found as

$$S = S_{HI} + S_{HO} \tag{A.26}$$

Finally, at this point is important to know that the following expressions must hold for the PSD functions:

$$0 < F_{HI} < 1 \tag{A.27}$$

$$0 < F_{HO} < 1 \tag{A.28}$$

$$F_{HI} + F_{HO} = 1 \tag{A.29}$$

A.2 Saturated Permeability and Relative Permeability

The concept of relative permeability arose from multiphase flow through porous media. When multiphase flow interactions are taking place on a porous media, each phase experiences a different effective permeability, due mainly to the saturation level. This effective permeability is known as relative permeability. Some of the researchers that studied relative permeability include Weber [3], Li and Horne [91], and also Nam and Kaviany [92]. It was found that the relative liquid and relative gas permeability behave approximately as a high order function of saturation (third or forth order polynomials).

With a relatively simple expression, and as documented by Weber [3], the relative permeability can be obtained by integrating a variation of the PSD with a weighting function. To define permeability, Darcy's law can be used to express the mean velocity of a fluid through a channel as:

$$u_{mean} = -\frac{k}{\mu}\frac{dp}{dx} \tag{A.30}$$

where k is the permeability of the material, μ is the dynamic viscosity of the fluid, and dp/dx is the pressure drop along the length of the pores. Considering one single pore, the pressure driven flow through a cylinder (known as Poiseuille flow through a pipe) leads to a velocity profile of the form:

$$u(r^*) = -\frac{(r^2 - (r*)^2)}{4\mu}\frac{dp}{dx} \tag{A.31}$$

where the term dp/dx is a constant. The total volume flow rate, as obtained from the Poiseuille flow through pipes is given as:

$$Q = -\int_0^r \frac{(r^2 - (r*)^2)}{4\mu}\frac{dp}{dx}dA = -\int_0^r \frac{(r^2 - (r*)^2)}{4\mu}\frac{dp}{dx}(2\pi\, r^*)dr^* \tag{A.32}$$

or,

$$Q = -\int_0^r \frac{(r^2 - (r*)^2)}{4\mu}\frac{dp}{dx}(2\pi\, r^*)dr^* \tag{A.33}$$

and simplifying,

$$Q = -\frac{\pi\, r^4}{8\mu}\frac{dp}{dx} \tag{A.34}$$

The mean velocity of the Poiseuille flow is then defined as:

$$u_{mean} = \frac{Q}{Area} = -\frac{r^2}{8\mu}\frac{dp}{dx} \tag{A.35}$$

Note that on this particular notation, r is the radius of the pore, and r^* is the incremental pore radius of the pore (that goes from 0 to r). In most references in fluid mechanics, the pore radius is represented by r_0 or R, and the incremental pore radius is represented by r. Refer to White [78] for more information about the derivation of the velocity profile of the pressure driven flow through cylindrical channels.

Combining Equation (A.30) and Equation (A.35), it can be shown that the permeability of a single pore is given by

$$\frac{r^2}{8\mu}\frac{dp}{dx} = \frac{k}{\mu}\frac{dp}{dx} \tag{A.36}$$

and simplifying,

$$k = \frac{r^2}{8} \tag{A.37}$$

For multiphase flow in porous media, this effective permeability is the product of the relative permeability and the saturated permeability (the permeability when the porous media is completely saturated with a wetting fluid). Therefore,

$$k_r = \frac{k}{k_{sat}} \tag{A.38}$$

Then, can be assumed that both the saturated permeability and relative permeability behave similarly,

$$k \sim \frac{r^2}{8} \tag{A.39}$$

$$k_{sat} \sim \frac{r^2}{8} \tag{A.40}$$

The assumption above is basically that both the permeability and the saturated permeability are proportional to the pore radius squared. How can the difference between the two be expressed? Since the difference of the permeability and the saturated permeability is basically the permeability at a given level of saturation versus the permeability when the medium is fully saturated, one can argue that the weighting function needed is the change in volume fraction. Accounting for all the pores and not only a single pore, this can be expressed as

$$k = \int_{r_0}^{r_1} \frac{r^2}{8} \frac{dX(r)}{dr} dr \tag{A.41}$$

$$k_{sat} = \int_{0}^{\infty} \frac{r^2}{8} \frac{dX(r)}{dr} dr \tag{A.42}$$

Therefore,

$$k_r = \frac{k}{k_{sat}} = \frac{\int_{r_0}^{r_1} r^2 \frac{dX(r)}{dr} dr}{\int_{0}^{\infty} r^2 \frac{dX(r)}{dr} dr} \tag{A.43}$$

As pointed out by Weber [3], this formulation assumed that the porous material is equivalent to an array of straight cylindrical pores, while in reality their geometry is highly heterogeneous. To account for this, statistical analysis is used. In addition, the effects of residual saturation are not considered on this formulation. The residual saturation, S_o, can be defined as a small amount of liquid that after several injection-drainage cycles, will remain on the porous material, and is hard to be removed by means of capillary effects and evaporation. When $S \leq S_o$ then the liquid (or wetting) phase is almost immobile, and an effective saturation can be defined as:

$$S_e = \frac{S - S_o}{1 - S_o} \tag{A.44}$$

where S is the conventional saturation of the porous media. In order to account for the heterogeneous geometry of the pores, suppose that an array of straight cylindrical capillaries is sliced into several sections, as assumed by Bear [68]. These sections are then randomly arranged, and reassembled. In any slice area A of this later geometry, the area occupied by liquid water is given by:

$$A_{Liq} = \varepsilon_o \, A \, S_e \tag{A.45}$$

where ε_o is the porosity of the material. Any slice contains the same area occupied by liquid water. However, some portions of these areas may not be connected, due to the random interconnection of the pores inside each slice. Thus, using statistical analysis, the probability of having a point on the interface between two neighbouring slices which also lies on liquid water is given by

$$P_1 = \frac{\varepsilon_o \, S_e}{\lambda} \tag{A.46}$$

where λ represents a factor that takes into account the interconnection of the pores. Now, the probability that a point lies in two wet slices simultaneously is given as

$$P_2 = P_1 \, P_1 = \left[\frac{\varepsilon_o \, S_e}{\lambda} \right]^2 \tag{A.47}$$

Therefore, the permeability and the saturated permeability, taking into account the random interconnection of the pores by statistical means, can be expressed as

$$k = \left[\frac{\varepsilon_o \, S_e}{\lambda} \right]^2 \int_{r_0}^{r_1} \frac{r^2}{8} \frac{dX(r)}{dr} dr \tag{A.48}$$

$$k_{sat} = \left[\frac{\varepsilon_o}{\lambda} \right]^2 \int_{0}^{\infty} \frac{r^2}{8} \frac{dX(r)}{dr} dr \tag{A.49}$$

Note that for a fully saturated medium, $S_e = 1$. Therefore, the permeability of the wetting phase can be expressed as

$$k_{r,L} = \frac{1}{8} \left[\frac{\varepsilon_o \, S_e}{\lambda} \right]^2 \frac{\int_{r_0}^{r_1} r^2 \frac{dX(r)}{dr} dr}{\frac{1}{8} \left[\frac{\varepsilon_o}{\lambda} \right]^2 \int_{0}^{\infty} r^2 \frac{dX(r)}{dr} dr} \tag{A.50}$$

This integral can be solved using the Error function, as well as some algebraic manipulation. Consider first the permeability of the liquid (wetting) phase, for the hydrophilic portion of the PSD, the numerator of Equation (A.50),

$$k_{L,HI} = \frac{1}{8}\left[\frac{\varepsilon_o\, S_e}{\lambda}\right]^2 \int_0^{r_{c,HI}} r^2 \frac{dX_{HI}(r)}{dr} dr \tag{A.51}$$

Then, using the definition of the PSD model, the following substitution can be used to relate the liquid relative permeability to the Error function:

$$w = \frac{\ln{(r)} - \ln{(r_{HI,k})}}{s_{HI,k}\sqrt{2}} \tag{A.52}$$

$$dw = \frac{dr}{r\, s_{HI,k}\,\sqrt{2}} \tag{A.53}$$

Using the expanded version of the PSD, is trivial to show that

$$k_{L,HI} = \frac{F_{HI}}{8}\left[\frac{\varepsilon_o\, S_e}{\lambda}\right]^2 \int_{w_1}^{w_2} \sum_k \frac{r^2 f_{HI,k}}{\sqrt{\pi}} \exp{(-w^2)}\, dw \tag{A.54}$$

where

$$r^2 = r^2_{HI,k} \exp{(2\, w\, s_{HI,k}\,\sqrt{2})} \tag{A.55}$$

Combining the latter two equations,

$$\begin{aligned} k_{L,HI} =& \frac{F_{HI}}{8}\left[\frac{\varepsilon_o\, S_e}{\lambda}\right]^2 \int_{w_1}^{w_2} \sum_k \cdots \\ & \exp{(2\, w\, s_{HI,k}\,\sqrt{2})}\frac{r^2_{HI,k} f_{HI,k}}{\sqrt{\pi}} \exp{(-w^2)}\, dw \end{aligned} \tag{A.56}$$

The exponential functions can be rearranged as

$$\begin{aligned} k_{L,HI} =& \frac{F_{HI}}{8}\left[\frac{\varepsilon_o\, S_e}{\lambda}\right]^2 \int_{w_1}^{w_2} \sum_k \cdots \\ & \exp{(-2\, s^2_{HI,k})}\frac{r^2_{HI,k} f_{HI,k}}{\sqrt{\pi}} \exp{(-(w - s_{HI,k}\sqrt{2})^2)}\, dw \end{aligned} \tag{A.57}$$

Now, for convenience a new variable can be defined as:

$$t = w - s_{HI,k}\sqrt{2} \tag{A.58}$$

$$dw = dt \tag{A.59}$$

$$k_{L,HI} = \frac{F_{HI}}{8}\left[\frac{\varepsilon_o\, S_e}{\lambda}\right]^2 \int_{t_1}^{t_2} \sum_k \exp\left(-2\, s_{HI,k}^2\right) \frac{r_{HI,k}^2 f_{HI,k}}{\sqrt{\pi}} \exp\left(-t^2\right) dt \tag{A.60}$$

As for the new integration limits, according to the hydrophilic PSD they are defined as:

$$t_1 = lim_{r \to 0^+}\left[\frac{\ln(r) - \ln(r_{HI,k})}{s_{HI,k}\sqrt{2}} - s_{HI,k}\sqrt{2}\right] = -\infty \tag{A.61}$$

$$t_2 = \left[\frac{\ln(r_{c,HI}) - \ln(r_{HI,k})}{s_{HI,k}\sqrt{2}} - s_{HI,k}\sqrt{2}\right] \tag{A.62}$$

Thus,

$$\begin{aligned} k_{L,HI} =& \frac{F_{HI}}{8}\left[\frac{\varepsilon_o\, S_e}{\lambda}\right]^2 \int_{-\infty}^{\left[\frac{\ln(r_{c,HI}) - \ln(r_{HI,k})}{s_{HI,k}\sqrt{2}} - s_{HI,k}\sqrt{2}\right]} \dots \\ & \sum_k \exp\left(-2\, s_{HI,k}^2\right) \frac{r_{HI,k}^2 f_{HI,k}}{\sqrt{\pi}} \exp\left(-t^2\right) dt \end{aligned} \tag{A.63}$$

Using the properties of the Error function and the fact that the outer summation just means that we have more than one more (so we can integrate and them sum all the distributions), is trivial to see that

$$\begin{aligned} k_{L,HI} =& \frac{F_{HI}}{16}\left[\frac{\varepsilon_o\, S_e}{\lambda}\right]^2 \sum_k \exp\left(-2\, s_{HI,k}^2\right) r_{HI,k}^2 f_{HI,k} \\ & \left[\operatorname{erf}\left(\frac{\ln(r_{c,HI}) - \ln(r_{HI,k})}{s_{HI,k}\sqrt{2}} - s_{HI,k}\sqrt{2}\right) - \operatorname{erf}(-\infty)\right] \end{aligned} \tag{A.64}$$

And since the Error function is odd,

$$\begin{aligned} k_{L,HI} =& \frac{F_{HI}}{16}\left[\frac{\varepsilon_o\, S_e}{\lambda}\right]^2 \sum_k \exp\left(-2\, s_{HI,k}^2\right) r_{HI,k}^2 f_{HI,k} \\ & \left[\operatorname{erf}\left(\frac{\ln(r_{c,HI}) - \ln(r_{HI,k})}{s_{HI,k}\sqrt{2}} - s_{HI,k}\sqrt{2}\right) + \operatorname{erf}(\infty)\right] \end{aligned} \tag{A.65}$$

$$\begin{aligned} k_{L,HI} =& \frac{F_{HI}}{16}\left[\frac{\varepsilon_o\, S_e}{\lambda}\right]^2 \sum_k \exp\left(-2\, s_{HI,k}^2\right) r_{HI,k}^2 f_{HI,k} \\ & \left[\operatorname{erf}\left(\frac{\ln\left(r_{c,HI}\right) - \ln\left(r_{HI,k}\right)}{s_{HI,k}\sqrt{2}} - s_{HI,k}\sqrt{2}\right) + 1\right] \end{aligned} \tag{A.66}$$

By changing the limits of integration for those corresponding to the hydrophobic portion of the PSD, as well as the definition of the hydrophobic PSD itself, is easy to see that

$$\begin{aligned} k_{L,HO} =& \frac{F_{HO}}{16}\left[\frac{\varepsilon_o\, S_e}{\lambda}\right]^2 \sum_k \exp\left(-2\, s_{HO,k}^2\right) r_{HO,k}^2 f_{HO,k} \\ & \left[-\operatorname{erf}\left(\frac{\ln\left(r_{c,HO}\right) - \ln\left(r_{HO,k}\right)}{s_{HO,k}\sqrt{2}} - s_{HO,k}\sqrt{2}\right) + 1\right] \end{aligned} \tag{A.67}$$

Similarly, is also trivial to show that the fraction corresponding to the saturated permeability that is used to compute the relative permeability can be obtained from

$$k_{sat} = \frac{1}{16}\left[\frac{\varepsilon_o}{\lambda}\right]^2 \sum_k \exp\left(-2\, s_k^2\right) r_k^2 f_k \left[\operatorname{erf}\left(\infty\right) + \operatorname{erf}\left(\infty\right)\right] \tag{A.68}$$

$$k_{sat} = \frac{1}{16}\left[\frac{\varepsilon_o}{\lambda}\right]^2 \sum_k \exp\left(-2\, s_k^2\right) r_k^2 f_k \left[1 + 1\right] \tag{A.69}$$

$$k_{sat} = \frac{1}{8}\left[\frac{\varepsilon_o}{\lambda}\right]^2 \sum_k \exp\left(-2\, s_k^2\right) r_k^2 f_k \tag{A.70}$$

where the lack of wettability subscripts indicates that the factors defining the PSD correspond to the global PSD (hydrophilic plus hydrophobic PSDs). Therefore, the liquid relative saturation can be defined as

$$k_{r,L} = \frac{k_{L,HI} + k_{L,HO}}{k_{sat}} \tag{A.71}$$

Similarly, since the effective saturation that defines the gas (non-wetting) phase is given by

$$1 - S_e \tag{A.72}$$

and also the limits of integration are changes (from $[0,\ r_c]$ to $[r_c,\ \infty]$, since the liquid wetting phase is non-wetting for gases), is easy to show that

$$k_{r,G} = \frac{k_{G,HI} + k_{G,HO}}{k_{sat}} \tag{A.73}$$

where $k_{G,HI}$ is given as:

$$\begin{aligned} k_{G,HI} =& \frac{F_{HI}}{16} \left[\frac{\varepsilon_o \left(1 - S_e\right)}{\lambda} \right]^2 \sum_k \exp\left(-2\, s_{HI,k}^2\right) r_{HI,k}^2 f_{HI,k} \\ & \left[-\mathrm{erf}\left(\frac{\ln\left(r_{c,HI}\right) - \ln\left(r_{HI,k}\right)}{s_{HI,k}\sqrt{2}} - s_{HI,k}\sqrt{2} \right) + 1 \right] \end{aligned} \tag{A.74}$$

and $k_{G,HO}$ can be estimated from

$$\begin{aligned} k_{G,HO} =& \frac{F_{HO}}{16} \left[\frac{\varepsilon_o \left(1 - S_e\right)}{\lambda} \right]^2 \sum_k \exp\left(-2\, s_{HO,k}^2\right) r_{HO,k}^2 f_{HO,k} \\ & \left[\mathrm{erf}\left(\frac{\ln\left(r_{c,HO}\right) - \ln\left(r_{HO,k}\right)}{s_{HO,k}\sqrt{2}} - s_{HO,k}\sqrt{2} \right) + 1 \right] \end{aligned} \tag{A.75}$$

A.3 Total Pore Wall Surface Area

Recall from Weber [3, 21] that the saturation of a porous layer can be found from

$$S = \frac{V(r)}{V} \tag{A.76}$$

and the later can be expressed as:

$$S = \frac{\pi L \int r^2\, n(r) dr}{\pi L \int_0^\infty r^2\, n(r) dr} \tag{A.77}$$

where L is the length of the pores and $n(r)$ express the number of pores of radius r. Therefore, this can be seen as a summation of the volumes of all the pores of a given radius. Now, recall that for a straight cylinder the lateral surface area for a given pore radius is given by:

$$A(r) = 2\pi L \int r n(r)\, dr \tag{A.78}$$

and the volume is given by:

$$V(r) = \pi L \int r^2 n(r) dr \tag{A.79}$$

From the latter, can be seen that the lateral surface area normalized by the total volume of the pores is given by :

$$a_{wall}(r) = \frac{2\pi L \int rn(r)\,dr}{\pi L \int_0^\infty r^2 n(r)\,dr} \tag{A.80}$$

and by simplifying this leads to:

$$a_{wall}(r) = \frac{2 \int rn(r)\,dr}{\int_0^\infty r^2 n(r)\,dr} = \int \frac{1}{r}\frac{dX(r)}{dr}\,dr \tag{A.81}$$

The solution for the later expression can be found from:

$$a_{wall} = \int_{r_0}^{r_1} \frac{2}{r}\frac{dX(r)_H}{dr}\,dr \tag{A.82}$$

An exact expression can be obtained from Equation (A.82). For this, and since the integral of a sum is the sum of the integrals (given that the functions are continuous everywhere in the domain), a wettability-specific PSD function can be used to derive the final expression, and then the wettability-specific pore-size distribution functions can be included.

Combining Equation (A.82) and Equation (A.3):

$$a_{wall} = \int_{r_0}^{r_1} \sum_k \left[\frac{2\,f_k}{s_k\, r^2 \sqrt{2\pi}} \exp\left(- \left[\frac{\ln(r) - \ln(r_k)}{s_k \sqrt{2}} \right]^2 \right) \right] dr \tag{A.83}$$

To solve Equation (A.83), a new variable u is defined as:

$$u = \frac{\ln(r) - \ln(r_k)}{s_k \sqrt{2}} \tag{A.84}$$

Therefore, the differential is found to be:

$$du = \frac{dr}{r\, s_k\, \sqrt{2}} \tag{A.85}$$

and also another useful relation between the new variable u and r is given as:

$$r = r_k \exp\left(u\, s_k\, \sqrt{2}\right) \tag{A.86}$$

Using the later expressions, Equation (A.83) can be expressed in terms of the Error function. Using equations (A.84) to (A.86), Equation (A.83) can be manipulated to lead:

$$a_{wall} = \int_{u_0}^{u_1} \sum_k \left[\frac{2\,f_k}{r\sqrt{\pi}} \exp\left(-u^2\right) \right] du \tag{A.87}$$

$$a_{wall} = \int_{u_0}^{u_1} \sum_k \left[\frac{2\,f_k}{r_k \exp\left(u\, s_k\, \sqrt{2}\right) \sqrt{\pi}} \exp\left(-u^2\right) \right] du \tag{A.88}$$

$$a_{wall} = \int_{u_0}^{u_1} \sum_k \left[\frac{2\, f_k}{r_k \sqrt{\pi}} \exp\left(-u^2 - u\, s_k\, \sqrt{2} \right) \right] du \tag{A.89}$$

where u_0 and u_1, as the reader may expect, depend on the previous integration limits r_0 and r_1. Also, is trivial to see that

$$-\, u^2 - u\, s_k\, \sqrt{2} = -\left(u + \frac{s_k}{\sqrt{2}} \right)^2 + \frac{s_k^2}{2} \tag{A.90}$$

Therefore,

$$a_{wall} = \int_{u_0}^{u_1} \sum_k \left[\frac{2\, f_k}{r_k \sqrt{\pi}} \exp\left[-\left(u + \frac{s_k}{\sqrt{2}} \right)^2 + \frac{s_k^2}{2} \right] \right] du \tag{A.91}$$

$$a_{wall} = \int_{u_0}^{u_1} \sum_k \left[\frac{2\, f_k}{r_k \sqrt{\pi}} \exp\left(\frac{s_k^2}{2} \right) \exp\left[-\left(u + \frac{s_k}{\sqrt{2}} \right)^2 \right] \right] du \tag{A.92}$$

By inspecting Equation (A.92), the Error function can be recovered. First, a new variable is defined as:

$$x = u + \frac{s_k}{\sqrt{2}} \tag{A.93}$$

$$dx = du \tag{A.94}$$

Thus, Equation (A.92) is written in terms of x as:

$$a_{wall} = \int_{x_0}^{x_1} \sum_k \left[\frac{2\, f_k}{r_k \sqrt{\pi}} \exp\left(\frac{s_k^2}{2} \right) \exp\left[-x^2 \right] \right] dx \tag{A.95}$$

if the original integration limits are taken to be $r_0 = 0$ and $r_1 = r_c$, and recovering the Error function, the new expression is given as:

$$a_{wall} = \sum_k \left\{ \frac{f_k}{r_k} \exp\left(\frac{s_k^2}{2} \right) \left[1 + \operatorname{erf}\left(\frac{\ln(r_c) - \ln(r_k)}{s_k \sqrt{2}} + \frac{s_k}{\sqrt{2}} \right) \right] \right\} \tag{A.96}$$

If the original integration limits are taken to be $r_0 = r_c$ and $r_1 = \infty$, and recovering the Error function, the new expression is instead given as

$$a_{wall} = \sum_k \left\{ \frac{f_k}{r_k} \exp\left(\frac{s_k^2}{2} \right) \left[1 - \operatorname{erf}\left(\frac{\ln(r_c) - \ln(r_k)}{s_k \sqrt{2}} + \frac{s_k}{\sqrt{2}} \right) \right] \right\} \tag{A.97}$$

Now, the situation described by Equation (A.96) corresponds to the case where the hydrophilic pores are filling, and the situation described in Equation (A.97) corresponds to the case where the hydrophobic pores are filling, as documented on prior reports. Thus, the wettability-specific pore walls surface area per unit volume are given by expressions of the form:

$$a_{wall,HI} = \sum_k \frac{F_{HI}\, f_{k,HI}}{r_{k,HI}} \exp\left(\frac{s_{k,HI}^2}{2}\right) \left[1 + \operatorname{erf}\left(\frac{\ln(r_{c,HI}) - \ln(r_{k,HI})}{s_{k,HI}\sqrt{2}} + \frac{s_{k,HI}}{\sqrt{2}}\right)\right] \tag{A.98}$$

for the hydrophilic pores,

$$a_{wall,HO} = \sum_k \frac{F_{HO}\, f_{k,HO}}{r_{k,HO}} \exp\left(\frac{s_{k,HO}^2}{2}\right) \left[1 - \operatorname{erf}\left(\frac{\ln(r_{c,HO}) - \ln(r_{k,HO})}{s_{k,HO}\sqrt{2}} + \frac{s_{k,HO}}{\sqrt{2}}\right)\right] \tag{A.99}$$

for the hydrophobic pores, and the total pore walls surface area per unit volume can be found, using the PSD model, as:

$$a_{wall} = a_{wall,HI} + a_{wall,HO} \tag{A.100}$$

A.4 Liquid-Gas Interfacial Surface Area per Unit Volume

To obtain the liquid-gas interfacial surface area per unit volume, some geometrical considerations must be used. The cross-sectional area of a single capillary is given as:

$$area = \pi r^2 \tag{A.101}$$

The pore volume is given as:

$$Volume = \pi r^2\, L = a\, L \tag{A.102}$$

where L is the length of the pore. Using these expressions, the ratio of cross sectional area over the pore volume is given as:

$$\frac{area}{Volume} = \frac{1}{L} \tag{A.103}$$

The last expression can be integrated in order to take into account the filling of the pores,

$$\frac{a(r)}{V_T} = \int_0^{r_{c,HI}} \frac{1}{L}\frac{dX_{HI}}{dr}dr + \int_{r_{c,HO}}^{\infty} \frac{1}{L}\frac{dX_{HO}}{dr}dr \tag{A.104}$$

Eikerling [60] documented that for conventional catalyst layers, a linear relation between pore size and average pore length. The suggested form is given as:

$$L = 4\,r \tag{A.105}$$

The cross sectional area of the pores per unit volume is defined as:

$$\frac{a(r)}{V_T} = \int_0^{r_{c,HI}} \frac{1}{4\,r}\frac{dX(r)_{HI}}{dr}dr + \int_{r_{c,HO}}^{\infty} \frac{1}{4\,r}\frac{dX(r)_{HO}}{dr}dr \tag{A.106}$$

This integral is very similar to the integral used to define the wetted pore wall area. Using a similar approach and substitutions we get that:

$$\begin{aligned}\frac{a(r)_{HI}}{V_T} =& F_{HI}\sum_k \frac{f_{k,HI}\exp\left(\frac{s_{k,HI}^2}{2}\right)}{8\,r_{k,HI}} \\ &\left[1 + \operatorname{erf}\left(\frac{\ln(r_{cr}) - \ln(r_{k,HI})}{s_{k,HI}\sqrt{2}} + \frac{s_{k,HI}\sqrt{2}}{2}\right)\right]\end{aligned} \tag{A.107}$$

The effects of pore interconnectivity can be included using a probability function Pb such that,

$$\begin{aligned}\frac{a(r)_{HI}}{V_T} =& Pb\,F_{HI}\sum_k \frac{f_{k,HI}\exp\left(\frac{s_{k,HI}^2}{2}\right)}{8\,r_{k,HI}} \\ &\left[1 + \operatorname{erf}\left(\frac{\ln(r_{cr}) - \ln(r_{k,HI})}{s_{k,HI}\sqrt{2}} + \frac{s_{k,HI}\sqrt{2}}{2}\right)\right]\end{aligned} \tag{A.108}$$

For the hydrophobic pores the cross sectional area per unit volume can be estimated from an expression of the form:

$$\begin{aligned}\frac{a(r)_{HO}}{V_T} =& Pb\,F_{HO}\sum_k \frac{f_{k,HO}\exp\left(\frac{s_{k,HO}^2}{2}\right)}{8\,r_{k,HO}} \\ &\left[1 - \operatorname{erf}\left(\frac{\ln(r_{cr}) - \ln(r_{k,HO})}{s_{k,HO}\sqrt{2}} + \frac{s_{k,HO}\sqrt{2}}{2}\right)\right]\end{aligned} \tag{A.109}$$

Therefore, the expression for the liquid-vapour interfacial surface area per unit volume corresponding to all the pores is given by:

$$a(r)_T = \frac{a(r)}{V_T} = \frac{a(r)_{HI}}{V_T} + \frac{a(r)_{HO}}{V_T} \tag{A.110}$$

A.5 Average Knudsen Radius

In order to define an expression for the average Knudsen radius, the approach followed was to start with very simple geometric relations for a straight cylinder, and then use the PSD formulation to define the final expression. Consider the volume of a cylinder of radius r and height h,

$$V = \pi\, r^2\, h \tag{A.111}$$

The lateral surface area (or area of the walls) for the same cylinder would be:

$$A_{wall} = 2\,\pi\, r\, h \tag{A.112}$$

From Equation (A.111) and Equation (A.112), the cylinder radius can be found from:

$$r = 2\frac{V}{A_{wall}} \tag{A.113}$$

By looking at the cumulative differential volume and pore wall area, and dividing by the total volume of all the pores V_T, the pore radius can be found from:

$$r = 2\frac{\dfrac{1}{V_T}\dfrac{dV(r)}{dr}}{\dfrac{1}{V_T}\dfrac{da_{wall}(r)}{dr}} \tag{A.114}$$

Using integration, the average pore radius can be estimated from:

$$r_{Kn} = 2\frac{\displaystyle\int_{r_{crit}}^{\infty}\frac{1}{V_T}\frac{dV_{HI}(r)}{dr}dr + \int_{0}^{r_{crit}}\frac{1}{V_T}\frac{dV_{HO}(r)}{dr}dr}{\displaystyle\int_{r_{crit}}^{\infty}\frac{1}{V_T}\frac{da_{wall,HI}(r)}{dr}dr + \int_{0}^{r_{crit}}\frac{1}{V_T}\frac{da_{wall,HO}(r)}{dr}dr} \tag{A.115}$$

Therefore, the final expression presented in Section 2.4 to estimate the average Knudsen radius can be found from:

$$r_{Kn} = \frac{C_1 + C_2}{C_3 + C_4} \tag{A.116}$$

where,

$$C_1 = F_{HI} \sum_k \frac{f_{HI,r,k}}{2} \left[1 - \operatorname{erf}\left(\frac{\ln(r_{c,HI}) - \ln(r_{HI,k})}{s_{HI,k}\sqrt{2}} \right) \right] \tag{A.117}$$

$$C_2 = F_{HO} \sum_k \frac{f_{HO,k}}{2} \left[1 + \operatorname{erf}\left(\frac{\ln(r_{c,HO}) - \ln(r_{HO,k})}{s_{HO,k}\sqrt{2}} \right) \right] \tag{A.118}$$

$$C_3 = \sum_k \frac{F_{HI}\, f_{k,HI}}{r_{k,HI}} \exp\left(\frac{s_{k,HI}^2}{2} \right) \left[1 - \operatorname{erf}\left(\frac{\ln(r_{c,HI}) - \ln(r_{k,HI})}{s_{k,HI}\sqrt{2}} + \frac{s_{k,HI}}{\sqrt{2}} \right) \right] \tag{A.119}$$

$$C_4 = \sum_k \frac{F_{HO}\, f_{k,HO}}{r_{k,HO}} \exp\left(\frac{s_{k,HO}^2}{2} \right) \left[1 + \operatorname{erf}\left(\frac{\ln(r_{c,HO}) - \ln(r_{k,HO})}{s_{k,HO}\sqrt{2}} + \frac{s_{k,HO}}{\sqrt{2}} \right) \right] \tag{A.120}$$

Appendix B

Effective GDL Properties

This section studies the effects of PSD parameters on GDL effective properties. The PSD used for this study corresponds to the SGL Sigracet 34BA presented in Table 2.1. The GDL configurations tested can be seen in Figure 2.46 and Figure 2.47, the description of each GDL configuration is presented in Table B.1.

Table B.1 – PSD functions for the GDL configurations tested in this study.

GDL number	Percent HI pores	Percent HO pores
1	0	100
2	10 (small pores)	90 (large pores)
3	20 (small pores)	80 (large pores)
4	30 (small pores)	70 (large pores)
5	40 (small pores)	60 (large pores)
6	50 (small pores)	50 (large pores)
7	10 (large pores)	90 (small pores)
8	20 (large pores)	80 (small pores)
9	30 (large pores)	70 (small pores)
10	40 (large pores)	60 (small pores)
11	50 (large pores)	50 (small pores)

The wetted pore wall surface area per unit volume corresponding to the first six GDL configurations is presented in Figure B.1. As the amount of hydrophilic pores increases, the wetted pore wall surface area profiles increases for both positive and negative capillary pressures. This indicates that the wetted pore wall surface area per unit volume benefits significantly from the addition of small hydrophilic pores.

Figure B.2 presents the wetted pore wall surface area corresponding to GDL 1, and GDL 7 to 10. For negative capillary pressures, adding large hydrophilic pores

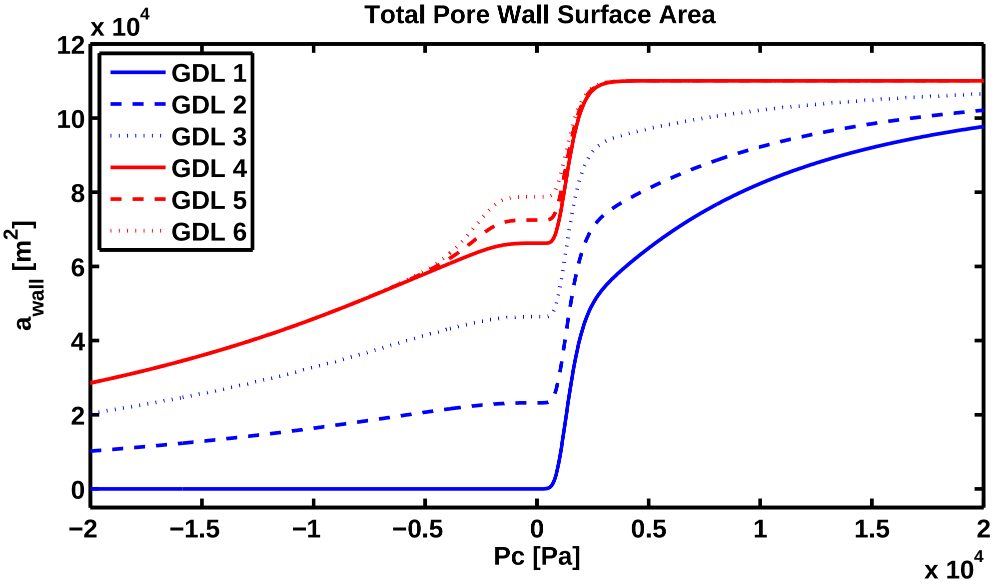

Figure B.1 – Wetted pore wall surface area per unit volume profiles for tested GDL cases with small hydrophilic pores plotted against capillary pressure.

increases the value of wetted pore wall surface area per unit volume. For positive capillary pressure values, adding large hydrophilic pores does not impact the wetted pore wall surface area per unit volume.

The liquid-gas interfacial surface area per unit volume profiles for the first six GDL configurations, plotted against capillary pressure, are presented in Figure B.3. Note that adding small hydrophilic pores to the GDL will cause the liquid-gas interfacial surface area per unit volume to increase faster for negative capillary pressures, and consequently, to increase slower for positive capillary pressure values.

The liquid-gas interfacial surface area per unit volume profiles corresponding to the GDL configurations with large hydrophilic pores, plotted against capillary pressure, are presented in Figure B.4. For negative capillary pressures, the interfacial surface area profiles increase faster as more hydrophilic pores are added to the GDL. For positive capillary pressures, adding large hydrophilic pores has a very modest impact on the interfacial surface area profiles.

The liquid-gas interfacial surface area per unit volume profiles, plotted against saturation, is presented in Figure B.5 for the small hydrophilic pores, and Figure B.6 for large hydrophilic pores. From the figures can be observed that for low saturation values, the GDLs with highest evaporation rates are GDL 4, GDL 5, and GDL 6.

Additionally, by comparing Figures B.3 to B.6, the liquid-gas interfacial surface area values of the GDL with the ones corresponding to MPLs in Figures 2.37 to 2.40, is observed that the potential evaporation rates for MPLs are much greater than the

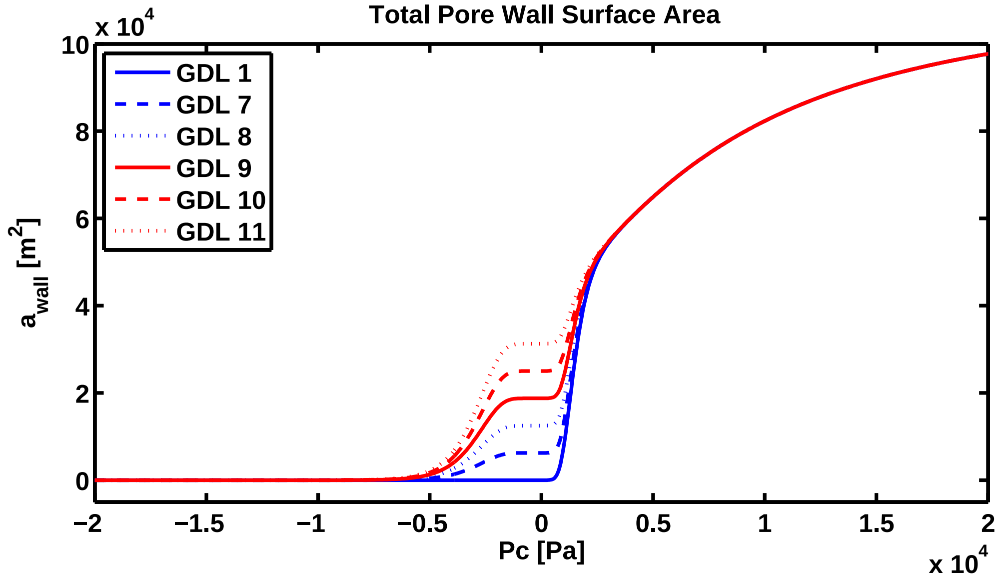

Figure B.2 – Pore wall surface area per unit volume profiles for tested GDL cases with large hydrophilic pores plotted against capillary pressure.

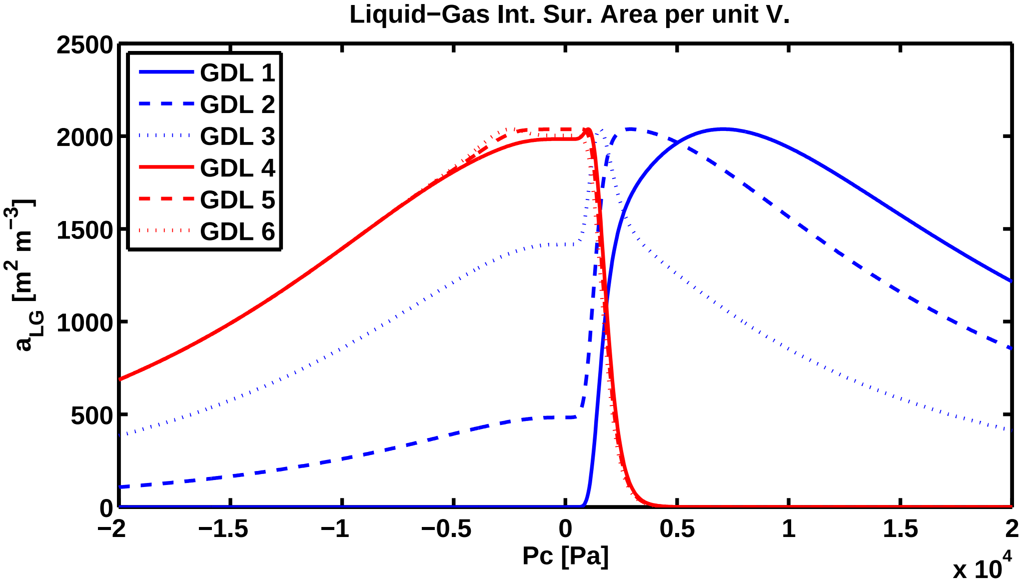

Figure B.3 – Liquid-gas interfacial surface area per unit volume profiles for tested GDL cases with small hydrophilic pores plotted against capillary pressure.

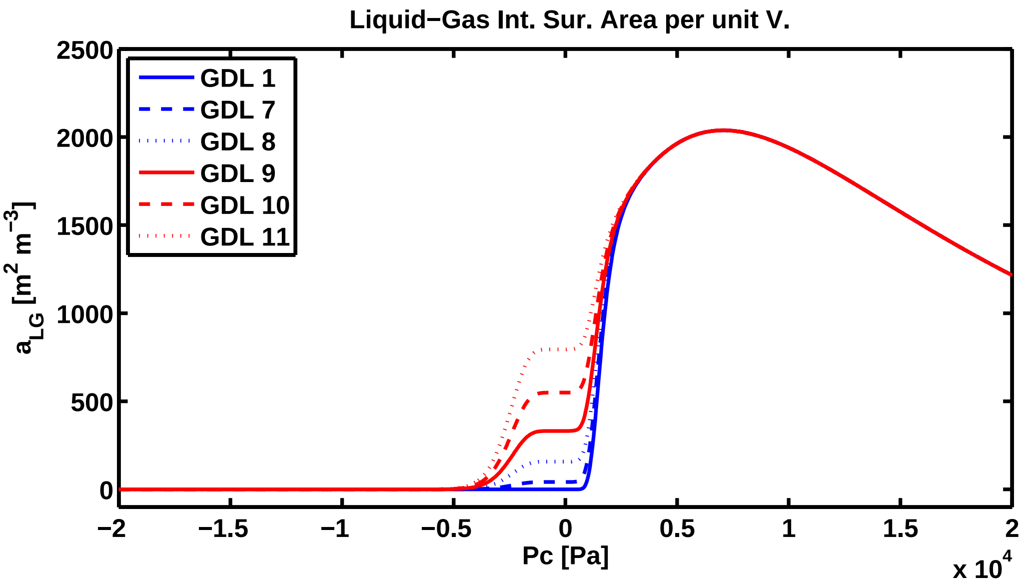

Figure B.4 – Liquid-gas interfacial surface area per unit volume profiles for tested GDL cases with large hydrophilic pores plotted against capillary pressure.

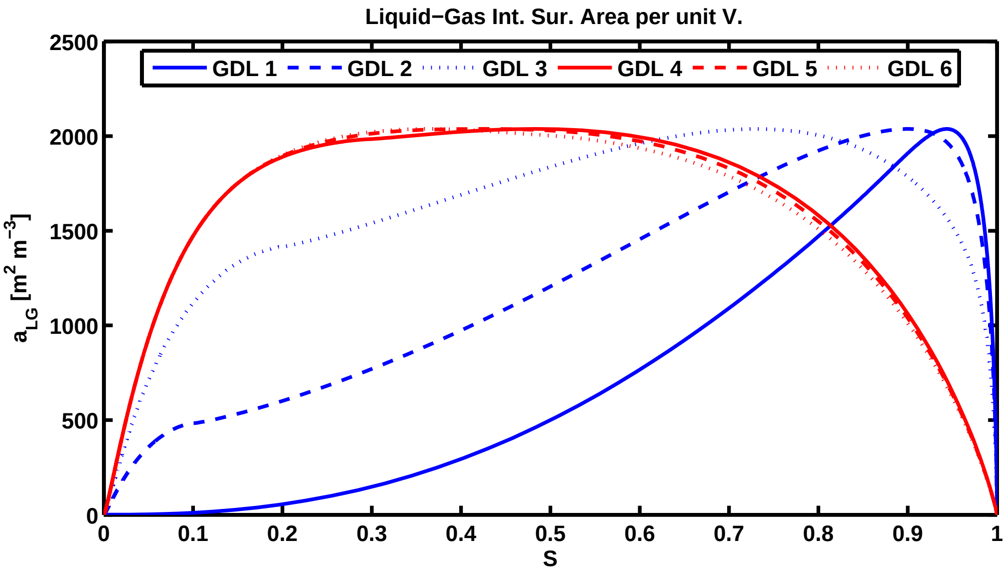

Figure B.5 – Liquid-gas interfacial surface area per unit volume profiles for tested GDL cases with small hydrophilic pores plotted against saturation.

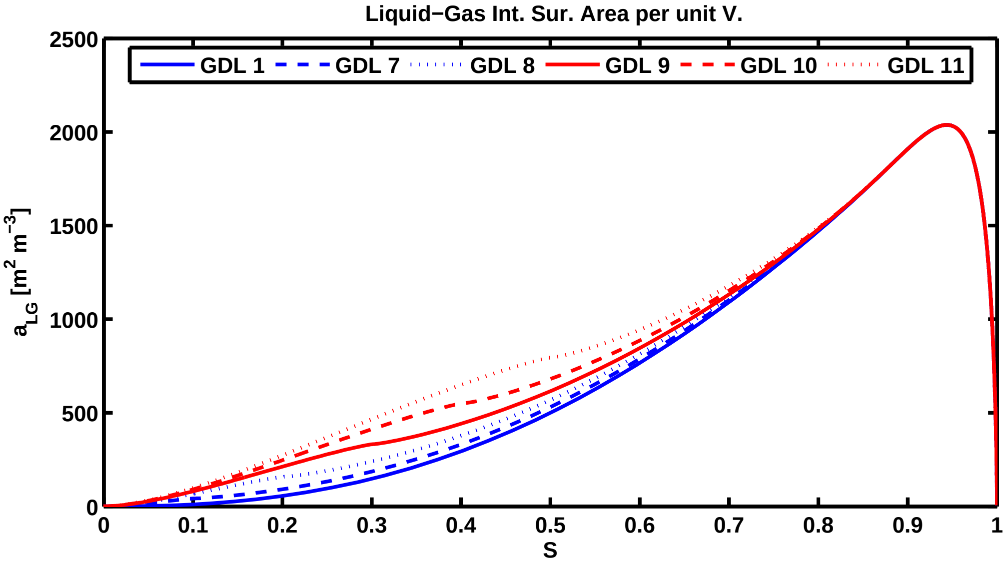

Figure B.6 – Liquid-gas interfacial surface area per unit volume profiles for tested GDL cases with large hydrophilic pores plotted against saturation.

evaporation rates for GDLs, due th the much smaller average pore sizes of MPLs. This provides more evidence to the claim that GDLs cannot evaporate the water produced by the electrochemical reactions taking place at the cathode side of a PEMFC.

Appendix C

Description of Matlab Files

A_pore.m

Function that estimates the pore wall surface area from PSD model.

CCL_main.m

Main driver program for the conventional cathode catalyst layer model.

CCL_1D_validation.m

Main driver program for the conventional cathode catalyst layer model used for the validation and comparison studies.

D_eff_Brug.m

Function that estimated the effective diffusion coefficient based on Bruggeman approximation.

D_eff_per.m

Function that estimated the effective diffusion coefficient based on percolation theory.

effective_sat.m

Function that estimates effective saturation.

int_surfaceA.m

Function that estimates the liquid-gas interfacial surface area per unit volume from PSD model.

k_rL.m

Function that estimates the liquid relative permeability from PSD model.

k_rG.m

Function that estimates the gas relative permeability from PSD model.

KnudsenDPSD.m

Function that estimates the Knudsen diffusion coefficient from PSD model.

MPL_main.m

Main driver program for the Microporous layer model.

plot_PSD_profile.m

Function that plots PSD and effective properties estimated in terms of capillary pressure and (when applicable) saturation.

rKn.m

Function that estimates average Knudsen radius from PSD model.

S_DPSD.m

Function that estimates saturation from PSD model.

S_GDL.m

Function that estimates saturation of a GDL, based on a given capillary pressure.

set_PSD.m

Function that inputs all PSD parameters to a driver program.